Investigating neutrino oscillations and diffuse cosmic neutrino fluxes with the KM3NeT neutrino telescope

Der Naturwissenschaftlichen Fakultät
der Friedrich-Alexander-Universität
Erlangen-Nürnberg
zur

Erlangung des Doktorgrades Dr. rer. nat.

vorgelegt von

Dominik Stransky

aus Erlangen

FRIEDRICH-ALEXANDER
UNIVERSITÄT
ERLANGEN-NÜRNBERG
NATURWISSENSCHAFTLICHE
FAKULTÄT

ERLANGEN CENTRE
FOR ASTROPARTICLE
PHYSICS

Als Dissertation genehmigt
von der Naturwissenschaftlichen Fakultät
der Friedrich-Alexander-Universität Erlangen-Nürnberg

Tag der mündlichen Prüfung:	07.01.2019
Vorsitzender des Promotionsorgans:	Prof. Dr. Georg Kreimer
Gutachter:	Prof. Dr. Ulrich Katz PD Dr. Ira Jung-Richardt

Abstract

KM3NeT is a neutrino telescope under construction in the Mediterranean Sea. Among the main goals is the discovery and subsequent study of sources of high-energy neutrinos. Furthermore, the determination of the mass ordering of the three known neutrino types is envisaged which is possible via oscillations of atmospheric neutrinos on their path through Earth. For these goals, two separate detectors are being built: the ARCA detector for high-energy neutrino astronomy, and the ORCA detector dedicated to the determination of the mass ordering.

This work presents contributions to both detectors. Based on numerical calculations, neutrino oscillations in the Earth have been analysed in order to predict the susceptibility of the ORCA detector to systematic uncertainties both in the Earth model and in fundamental oscillation parameters describing the neutrino oscillations. Furthermore, the calculation of oscillation probabilities still represents a major bottleneck in the CPU time consumption of ORCA sensitivity studies. A dedicated interpolation algorithm has therefore been developed with the aim to reduce the corresponding computing time by calculating all needed oscillation probabilities in advance. The amount of data needed for these interpolations has been estimated as well. The final computing time needed to run the ORCA sensitivity studies is expected to be reduced by these measures by around three orders of magnitude.

In order to increase the sensitivity of the ARCA detector to an isotropic high-energy cosmic neutrino flux, a machine learning algorithm for the classification of neutrino events has been developed. The studies achieve unprecedented sensitivity in the shower channel, a major neutrino event class. The “rediscovery” of the cosmic neutrino signal measured and published by the IceCube collaboration is possible within less than one year observation time. In particular, considering the strongest published signal flux, an observation with $5\,\sigma$ significance is possible in less than 0.3 years with 50% observation probability, meaning that the chance for a random background fluctuation giving a similar signature is below $2.87 \cdot 10^{-5}\,\%$. Compared to previous ARCA sensitivity analyses in the shower channel, the time needed for such a significant observation is reduced by at least 25% up to about 50% depending on the assumed signal flux hypothesis. Furthermore, besides the potential determination of the so-called prompt atmospheric neutrino flux, the capabilities of the ARCA detector to constrain the spectral shape of an isotropic cosmic neutrino flux has been analysed for the first time within the KM3NeT collaboration.

In addition, part of the work performed during the doctoral studies included tutoring of diverse student classes, the maintenance and administration of a Mac client-server system (about 100 users) as well as the work with several Linux systems including an HPC system.

Zusammenfassung

Untersuchung von Neutrinooszillationen und diffusen kosmischen Neutrinoflüssen mit dem KM3NeT Neutrinoteleskop

KM3NeT ist ein Neutrinoteleskop im Mittelmeer, das sich derzeit in der ersten Konstruktionsphase befindet. Ziel ist unter anderem der Nachweis und die Untersuchung von Quellen kosmischer Neutrinos und dadurch die Identifikation von Quellen höchstenergetischer kosmischer Strahlung. Des Weiteren soll mit Hilfe des KM3NeT-Experiments die Massenrangordnung bzw. Massenhierarchie der drei bekannten Neutrinoarten ermittelt werden. Dies ist möglich durch Oszillationen niedrigenergetischer atmosphärischer Neutrinos beim Durchgang durch die Erde. Zwei separate Detektoren sind für die genannten Ziele vorgesehen: der ARCA Detektor für die Hochenergie-Neutrinoastronomie, und der ORCA Detektor für die Bestimmung der Massenhierarchie.

Diese Arbeit stellt Beiträge zu beiden Detektoren vor. Basierend auf numerischen Berechnungen wurden Neutrinooszillationen in der Erde analysiert, um die Sensitivität des ORCA Detektors auf systematische Unsicherheiten sowohl im Erdmodell als auch in den fundamentalen Oszillationsparametern, die die Neutrinooszillationen beschreiben, vorherzusagen. Außerdem ist die Berechnung der Oszillationswahrscheinlichkeiten sehr zeitaufwändig und stellt einen zeitlichen Engpass bei der Durchführung von Sensitivitätsstudien zu ORCA dar. Daher wurde ein dedizierter Interpolationsalgorithmus entwickelt, mit dem Ziel, die benötigte Rechenzeit zu reduzieren und die Oszillationswahrscheinlichkeiten bereits im Voraus zu berechnen. Die dazu nötige Datenmenge wurde ebenfalls abgeschätzt. Die schließlich für die Sensitivitätsstudien benötigte Rechenzeit reduziert sich dadurch um etwa drei Größenordnungen.

Durch Verwendung eines Algorithmus zur Neutrinoereignisklassifikation – beruhend auf maschinellem Lernen – wurde die Sensitivität des ARCA Detektors in Bezug auf einen isotropen kosmischen Neutrinofluss untersucht. Mit Hilfe von sogenannten Schauerereignissen, einem bedeutenden Neutrinoereignistyp, wurde eine noch nie dagewesene Sensitivität erreicht. So ist die signifikante Detektion des von der IceCube Kollaboration gemessenen und veröffentlichten kosmischen Neutrinosignals in weniger als einem Jahr Beobachtungszeit möglich. Insbesondere wird mit einer Wahrscheinlichkeit von 50% einer der stärkeren veröffentlichten Signalflüsse in weniger als 0.3 Jahren mit einer Signifikanz von $5\,\sigma$ beobachtet. Das bedeutet, dass die Wahrscheinlichkeit, dass ein ähnliches Signal alleine durch Hintergrundfluktuationen erzeugt wird, kleiner ist als $2.87 \cdot 10^{-5}\,\%$. Verglichen mit bisherigen ARCA Sensitivitätsanalysen im Schauerkanal wurde die benötigte Zeit für solch

eine signifikante Beobachtung um mindestens 25% bis zu ca. 50% reduziert, abhängig vom angenommenen kosmischen Neutrinofluss. Außerdem wurde, zum ersten Mal innerhalb der KM3NeT Kollaboration, sowohl die Sensitivität des ARCA Detektors auf die spektralen Eigenschaften solch eines isotropen kosmischen Neutrinoflusses untersucht als auch die Sensitivität auf den sogenannten prompten atmosphärischen Neutrinofluss.

Des Weiteren waren umfangreiche Tutorentätigkeiten, die Verwaltung eines Mac Client-Server Systems (ca. 100 Nutzer) und die Arbeit mit diversen Linux Systemen inklusive eines HPC Systems Teil der Arbeit während der Promotion.

Contents

Part I

Introduction

This part motivates the work performed for this thesis in Chapter 1, introduces the relevant physics in Chapter 2 and the KM3NeT experiment in Chapter 3.

Chapter 1

Motivation

Neutrinos are fundamental particles only interacting through gravity and the weak force. They can therefore travel large distances without being absorbed. For example, billions of billions of neutrinos travel through the Earth unaffectedly every second. Because of this low interaction probability, they are often referred to as ghost particles. On the other hand, for the same reason, neutrinos offer unique possibilities in astronomy and astroparticle physics. A long standing mystery in these fields is the origin of the highest-energy cosmic rays. Cosmic rays were discovered in 1911 by Victor Hess [1] and are particles (protons and other nuclei of atoms) permanently bombarding the Earth from outer space. A tiny fraction reaches energies up to roughly 10^{20} eV or 50 J (see Chapter 29 of [2]), which is for instance the energy needed to lift one litre of water by five metres from the surface of the Earth. The cosmic sources that are able to produce single particles with such high energies are yet to be identified.

Unfortunately, detecting the charged cosmic rays gives no information on the position of their sources on the sky. The reason for this is the deflection of the charged particles by inter- and extra-galactic magnetic fields, whereupon most of these particles lose their directional information. Neutrinos, however, are electrically neutral and thus travel through space undeflectedly, always pointing back to their source. They are produced in the same acceleration processes as the charged cosmic rays. The classical way of finding celestial bodies – detection of electromagnetic radiation or their high energy version, called gamma rays – yields no distinct evidence to a cosmic ray source as electromagnetic radiation does not always have the same formation processes as the cosmic rays. In addition, gamma rays very likely undergo absorption on their way to Earth as they travel through interstellar clouds and dust. Opposed to that, cosmic neutrinos travel through space mostly unabsorbed. A detection of high-energy neutrinos would therefore reveal unique information about the Universe.

A major effort in this direction has been achieved with the detection of neutrinos of cosmic origin in 2013 with the IceCube experiment [3]. However, as of now, no single cosmic neutrino sources could be identified.

Due to the low neutrino interaction cross-section, it is also a difficult task to determine the fundamental neutrino properties. Therefore, it is not a surprise that neutrinos nowadays, 88 years after their first prediction by Wolfgang Pauli [4] in 1930 and 62 years after the first detection [5] in 1956, are not fully understood. It is known that neutrinos come in three different so-called flavour states – electron-, muon- and tau-neutrinos – that are produced in weak interactions. In the standard model of particle physics [2] neutrinos are massless. However, with the detection of neutrino oscillations in 1998 [6] it became clear that these flavour states are superpositions of three different mass states and therefore must have a mass. Neutrino oscillations describe the fact that neutrinos change flavour during propagation. Today, the neutrino masses are still unknown. Nevertheless, by measuring neutrino oscillations in matter, as e.g. in Earth, it is possible to determine the ordering of the neutrino masses. Today, only the order of two of the mass states is known, and it is an ongoing task to determine the full neutrino mass ordering also known as the neutrino mass hierarchy.

KM3NeT is a distributed neutrino telescope under construction at the bottom of the Mediterranean Sea with the major objectives of determining the neutrino mass hierarchy as well as performing neutrino astronomy, i.e. finding and subsequently studying cosmic neutrino sources to possibly reveal highest-energy cosmic-ray accelerators. As these two goals tackle different neutrino energy regimes, two distinct detector configurations are envisaged [7] in the ongoing building phase-2: ORCA (Oscillation Research with Cosmics in the Abyss) for the determination of the mass hierarchy at lower energies (1 GeV to 100 GeV), and ARCA (Astroparticle Research with Cosmics in the Abyss) for neutrino astronomy at very high energies (up to 10^8 GeV). Due to the low neutrino interaction probability, it is inevitable to instrument large volumes in order to detect a sufficient amount of neutrinos. For ORCA roughly 0.004 km^3, for ARCA around 1 km^3 of seawater will be instrumented with roughly 64 000 and 128 000 photo sensors, respectively. These volumes correspond to cubes with a height of 160 m and 1 km, respectively. The photo sensors are used to detect neutrinos by measuring the Cherenkov light produced from charged secondary particles generated in neutrino interactions with the surrounding media.

The remainder of this part of the thesis describes the fundamental physics relevant for the physics goals of KM3NeT in Chapter 2, and the KM3NeT experiment with its two detectors in Chapter 3.

The work performed for this thesis contributed to both parts of KM3NeT. As part of feasibility studies, it has been investigated if and how the determination of the neutrino mass hierarchy will be affected by uncertainties in the quantities describing the neutrino oscillations, the so-called neutrino oscillation parameters. In addition, since a precise treatment of the uncertainties requires the neutrino oscillation probabilities to be known in the relevant neutrino oscillation parameter space, a method of calculating and interpolating these oscillation probabilities has been developed. These studies are described in Part II.

For the ARCA detector, sensitivity studies have been performed to assess the capabilities of KM3NeT to detect a diffuse cosmic neutrino flux. The preparations needed and done for this are described in Part III and the sensitivity study and its results are described in Part IV. It utilises a machine learning algorithm, a cut-and-count analysis, and spectral fitting. The latter aims to reach high sensitivity to the spectrum of the cosmic neutrino flux and therefore to differentiate between several spectral hypotheses of the diffuse cosmic flux.

Chapter 2

Neutrinos

In this chapter, the main physics related to high-energy neutrinos will be described, including their production, propagation, interaction and detection. The energy range discussed here includes neutrinos from 1 GeV up to 10^9 GeV. Regarding the descriptions, this range will be subdivided into a lower-energy part ($E < 100$ GeV) and a higher-energy part ($E > 100$ GeV) where appropriate, as these are the energy ranges relevant for ORCA and ARCA, respectively, for which the work presented in this thesis was performed. For comprehensive discussion of lower-energy neutrinos ($E < 1$ GeV), e.g. produced in the Sun or in radioactive decays on Earth see [8].

A major part of this thesis includes the determination of the KM3NeT sensitivity to diffuse fluxes of neutrinos. These fluxes will therefore be described in more detail than e.g. the expected fluxes from individual galactic objects.

2.1 Neutrino production

The main production processes of high-energy neutrinos are the decay of charged mesons like pions and kaons and the subsequent decay of muons:

$$\pi^-(K^-) \rightarrow \mu^- + \nu_\mu \tag{2.1}$$

$$\mu^- \rightarrow e^- + \bar{\nu}_e + \nu_\mu \tag{2.2}$$

and the corresponding charge-conjugate decays. Another contribution is the decay of neutrons:

$$n \rightarrow p + e^- + \bar{\nu}_e. \tag{2.3}$$

The neutrons and charged mesons are produced in the interactions of cosmic rays. Depending on where the interactions happen, the resulting neutrino fluxes can be categorised as described in the following.

2.1.1 Cosmic fluxes

Cosmic neutrino fluxes are produced when cosmic rays interact at their sources or during their travel through the intergalactic medium. Among the important processes leading to pion production are the reaction with ambient photons

$$p + \gamma \to \Delta^+ \to \begin{cases} n + \pi^+ \\ p + \pi^0 \end{cases} \tag{2.4}$$

$$p + \gamma \to \begin{cases} n + N_+\pi^+ + N_-\pi^- + N_0\pi^0 \\ p + N_+\pi^+ + N_-\pi^- + N_0\pi^0 \end{cases} \tag{2.5}$$

and the reaction with ambient matter X

$$p + X \to N_+\pi^+ + N_-\pi^- + N_0\pi^0 + Y. \tag{2.6}$$

where Y may be anything consistent with conservation laws. The average numbers of produced pions, N_+, N_-, N_0, depend on the interaction type and energy [8]. The neutrinos are subsequently produced via pion or neutron decay.

In many theoretical predictions of cosmic neutrino fluxes [9], neutrinos from pion or kaon decays dominate the neutrino spectrum leading to an initial flavour ratio of approximately $\nu_e : \nu_\mu : \nu_\tau = 1:2:0$ (neutrinos and antineutrinos) according to Eqs. (2.1) and (2.2). Neutrino oscillations transform this ratio to roughly $1:1:1$ incident on Earth. However, other models such as muon-damped or neutron-beam sources lead to different flavour compositions. In the first case the muons lose most of their energy before decaying, leading to an initial high-energy neutrino flavour composition of $0:1:0$. In the extreme of the second case, only high-energy neutrons escape the sources leading to a composition of $1:0:0$. The compositions for the extreme cases would transform on their way to Earth roughly like $0:1:0 \to 0.2:0.4:0.4$ and $1:0:0 \to 0.6:0.2:0.2$. Sensitivity to the neutrino flavours is therefore important for the purpose of constraining physical source models. More about the different cosmic flavour ratio models and the resulting energy spectrum can be found in [9]. For more on neutrino oscillations see Section 2.2.

Cosmic rays interacting at their source form neutrino point sources. Candidates are supernova remnants (SNR) for Galactic neutrinos and active galactic nuclei (AGN) and gamma ray bursts (GRBs) for neutrinos of extra-galactic origin. Point sources will not be further addressed in this work, instead see e.g. [10].

Cosmic ray interactions with intergalactic media give rise to a diffuse cosmic neutrino flux. In addition, a diffuse flux is also produced by the sum of unresolved neutrino point sources distributed over the sky. Diffuse fluxes will be described in more detail in the following.

Diffuse neutrino fluxes

From the pion production reactions (Eq. (2.4) to (2.6)) follow relations between the flux of cosmic rays and the flux of the produced neutrinos and gamma rays (stemming from decays of neutral pions). Theoretical predictions (see e.g. [11–13]) for fluxes of cosmic neutrinos are therefore based on observations of gamma rays and cosmic rays. The predicted neutrino fluxes depend on assumptions about the dominating production channel of the cosmic particles.

A popular upper limit on cosmic neutrinos is given by Waxman and Bahcall [11]. They assume optically thin sources in a way that high-energy nucleons can escape the sources to produce the observed cosmic-ray flux. It is normalised to the cosmic ray flux at about 10^{10} GeV which is in this model assumed to be originating from the beta decay of the escaping neutrons. The dominant process is taken to be the resonant photoproduction (Eq. (2.4)). Furthermore, an E^{-2} cosmic-ray injection spectrum is assumed which can be derived from the "first-order Fermi acceleration" [14]. This mechanism describes the energy gain of particles via repeated reflection between shock fronts [15]. The resulting limit on the neutrino flux is given by $E^2\Phi = 1.4-6.8\cdot 10^{-8}\,\mathrm{GeV\,cm^{-2}\,s^{-1}\,sr^{-1}}$ for the all-flavour neutrino flux. The uncertainty reflects different source evolution models.

Another diffuse neutrino flux is given by the so-called cosmogenic neutrinos. They are produced when cosmic rays interact with cosmological photon backgrounds on their way through the universe. Predictions of the corresponding neutrino flux are in the range $E^2\Phi = 10^{-11} - 10^{-7}\,\mathrm{GeV\,cm^{-2}\,s^{-1}\,sr^{-1}}$ for energies between roughly 10^6 and 10^{10} GeV. The large uncertainty is due to different assumptions about the unknowns that go into the predictions. Among them are the source evolution, chemical composition and the maximum acceleration energy of the cosmic rays. For details see [16].

As mentioned above, unresolved point sources can always contribute to a potential diffuse neutrino flux. Further contributions to diffuse neutrino fluxes are given by extended sources like the Galactic Plane [17] or the Fermi Bubbles [18]. Another possibility are neutrinos from “top-down scenarios”. In these scenarios highest-energy cosmic rays are assumed to originate from decays of long-lived super-heavy particles. Measurements of the ultra-high-energy photon flux by the Pierre Auger Observatory, however, severely constrain such scenarios [19]. Furthermore, theories about dark matter predict neutrinos from the annihilation of dark-matter particles such as WIMPs (weakly interacting massive particles). For a more detailed overview see [20].

The IceCube Collaboration [21] recently detected a flux of cosmic neutrinos consistent with an isotropic distribution across the sky. Its detector at the South Pole is taking data in its full configuration since 2011. Several studies have been performed [3,22–27], whose results are combined in [28,29]. These studies were sensitive to astrophysical neutrinos with energies exceeding 20-100 TeV. The analysis providing first evidence for cosmic neutrinos [3], published in 2013, presented the following all-flavour flux:

$$\Phi(E) = 3.6 \cdot 10^{-18} \cdot \left(\frac{E}{100\,\mathrm{TeV}}\right)^{-2} \left(\mathrm{cm^2\,s\,sr\,GeV}\right)^{-1}. \tag{2.7}$$

This flux was taken as a basis for the sensitivity study of ARCA presented in this thesis.

The more recently published *“combined analysis”* [28] (2015) provided a best-fit all-flavour neutrino flux of

$$\Phi(E) = 6.7 \cdot 10^{-18} \cdot \left(\frac{E}{100\,\mathrm{TeV}}\right)^{-2.5} \left(\mathrm{cm^2\,s\,sr\,GeV}\right)^{-1} \tag{2.8}$$

valid for neutrino energies E from 25 TeV to 2.8 PeV.

Another analysis [30] from 2016 sensitive to muon neutrinos between roughly 200 TeV and 7.8 PeV from the northern hemisphere found a harder spectrum for the diffuse flux than the *combined analysis* but similar to the one of Eq. (2.7):

$$\Phi(E) = 2.7 \cdot 10^{-18} \cdot \left(\frac{E}{100\,\mathrm{TeV}}\right)^{-2.13} \left(\mathrm{cm^2\,s\,sr\,GeV}\right)^{-1} \tag{2.9}$$

This result, here multiplied by three to represent the all-flavour flux (see also below), is in tension with the *combined analysis* at $3.3\,\sigma$. This may indicate a possible break in the power-law spectrum somewhere around 100 TeV or a possible North-South asymmetry in neutrino arrival directions[1].

---

[1] A tension of $3.3\,\sigma$ means here that the probability that both results are caused by the same isotropic neutrino flux is only around 0.1%.

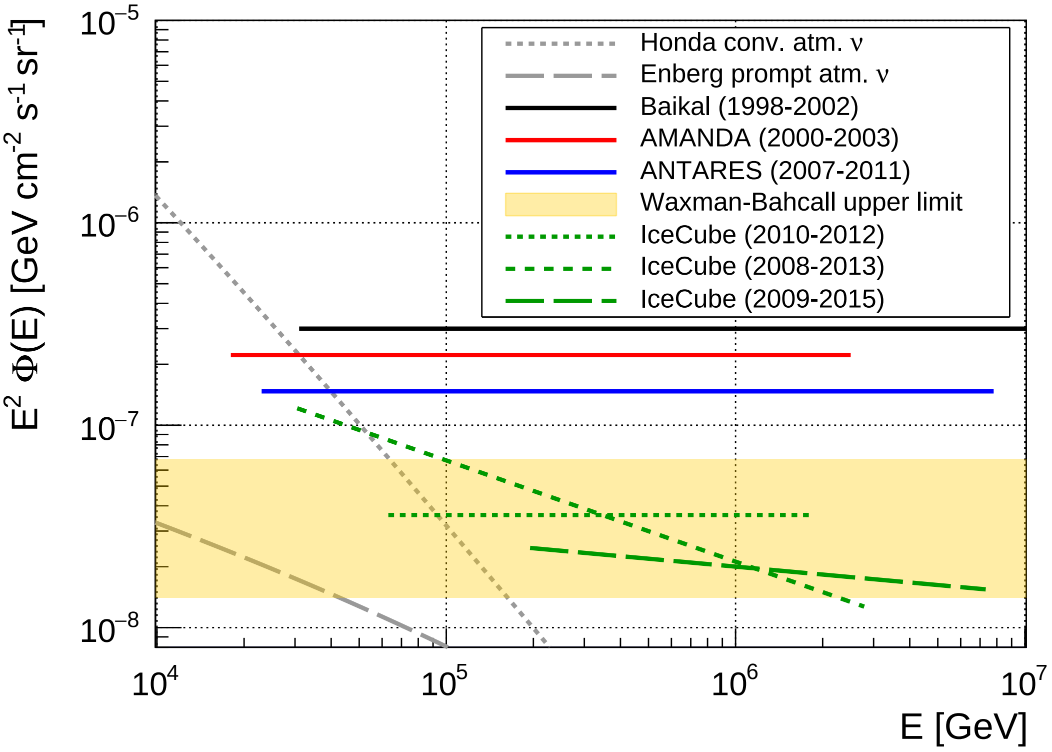

Figure 2.1: *Experimental diffuse flux upper limits from the Baikal Neutrino Telescope [32], AMANDA [34] and ANTARES [36] with best-fit fluxes from three different IceCube measurement periods (2010-2012 [3], 2008-2013 [28] and 2009-2015 [30], given in Eq. (2.7) to (2.9), respectively), all drawn in their valid energy range. Also shown is the theoretical upper limit by Waxman and Bahcall [11] and predictions for the conventional and prompt atmospheric neutrino fluxes, from Honda [39] and Enberg [40], respectively, which form a main background in cosmic neutrino searches. The fluxes and upper limits correspond to the sum of all neutrino flavours assuming a cosmic-neutrino flavour ratio of* $\nu_e : \nu_\mu : \nu_\tau = 1:1:1$ *incident on Earth.*

These three best-fit fluxes assume an isotropic flux with flavour ratio $\nu_e : \nu_\mu : \nu_\tau = 1:1:1$ incident on Earth. The flavour composition as measured by IceCube is consistent with pion-decay sources as well as muon-damped sources. However, neutron-beam sources are disfavoured with 3.6 σ significance [28].

The fluxes are used as reference fluxes regarding the sensitivity of KM3NeT to diffuse neutrino fluxes as presented in Part IV of this thesis. They are shown in Figure 2.1 together with experimental upper limits determined by the neutrino telescopes Baikal [31,32], AMANDA [33,34] and ANTARES [35,36]. The Waxman-Bahcall limit is also shown and is in the range of the IceCube best-fit result from 100 TeV to 2 PeV.

Several analyses of the IceCube data have been performed to search for correlations between known γ-ray sources and the measured neutrino spectrum (see e.g. [37]). So far no significant detection has been made. For instance, an analysis of blazars [38] as possible sources came to the conclusion that at most 50% of the observed astrophysical neutrino flux is caused by this special kind of AGN. However, as these blazars are distributed over almost the full sky, KM3NeT won't be able to distinguish potential neutrinos stemming from these sources from an isotropic distribution before a diffuse flux has been "rediscovered".

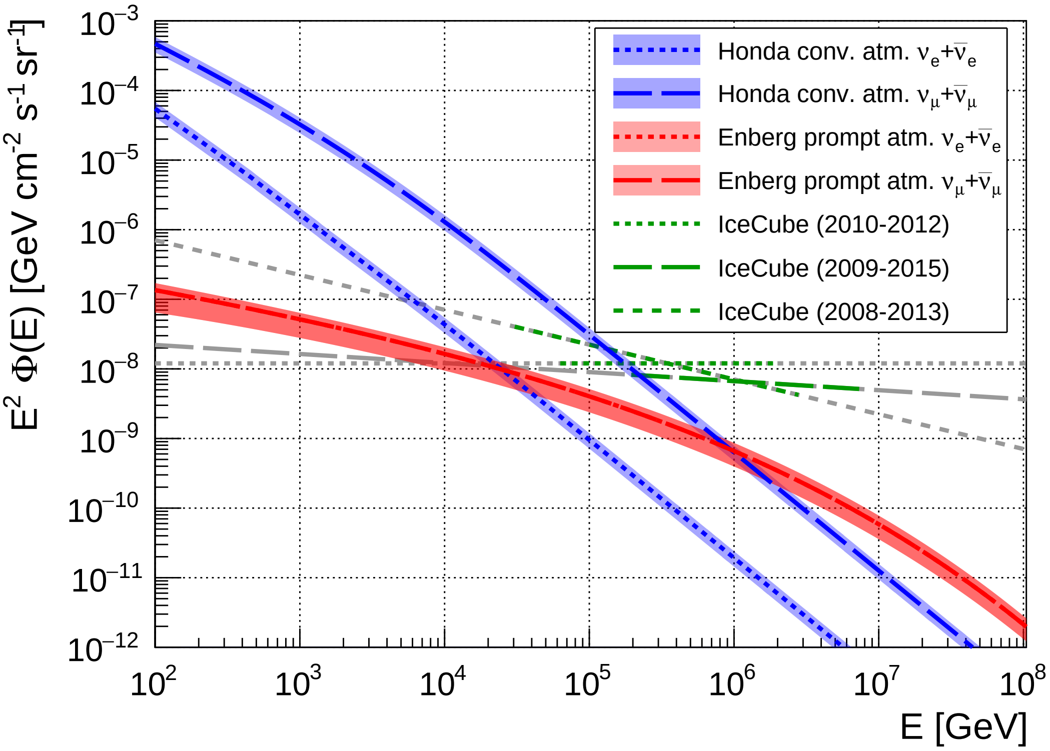

Figure 2.2: *The atmospheric conventional and prompt neutrino fluxes as calculated by Honda et al. [39] and Enberg et al. [40], respectively. Uncertainties are given as shaded bands. The uncertainty for the conventional neutrino flux is taken as ±25% [42] while for the prompt neutrino flux the uncertainties as derived by Enberg et al. [40] are used. For comparison, also three IceCube best-fit fluxes per flavour are shown (green in the valid energy range, gray elsewhere, see also Figure 2.1). Always the sum of neutrinos and antineutrinos is considered.*

2.1.2 Atmospheric fluxes

Atmospheric neutrinos represent one of the main background sources for searches for cosmic neutrinos. Nevertheless, they allow for the investigation of neutrino properties as foreseen with ORCA. They are produced in extensive air showers, initiated when cosmic rays interact with atomic nuclei in the Earth's atmosphere. They are called "conventional" if they are created through pion and kaon decays. These mesons may interact with the surrounding matter, thus losing energy before decaying, whereupon the resulting spectrum is much steeper than the initial cosmic ray spectrum.

With rising energy of the cosmic ray particles, also charmed mesons occur which may also decay into neutrinos. The resulting neutrino flux is called "prompt" atmospheric neutrino flux since these mesons have much lower lifetimes than pions and kaons, and decay before undergoing secondary interactions. This is also the main reason for the resulting spectrum being much harder than that of the conventional atmospheric neutrino flux. For more details on the prompt neutrino flux see [41].

In this work the Honda [39] and Enberg [40] models are used as reference for the conventional and prompt flux, respectively. Corrections based on calculations presented in [27] are taken into account. Both fluxes are shown in Figure 2.1 together with the high-energy diffuse cosmic neutrino flux measurements. In Figure 2.2 the atmospheric neutrino fluxes are shown separated by neutrino

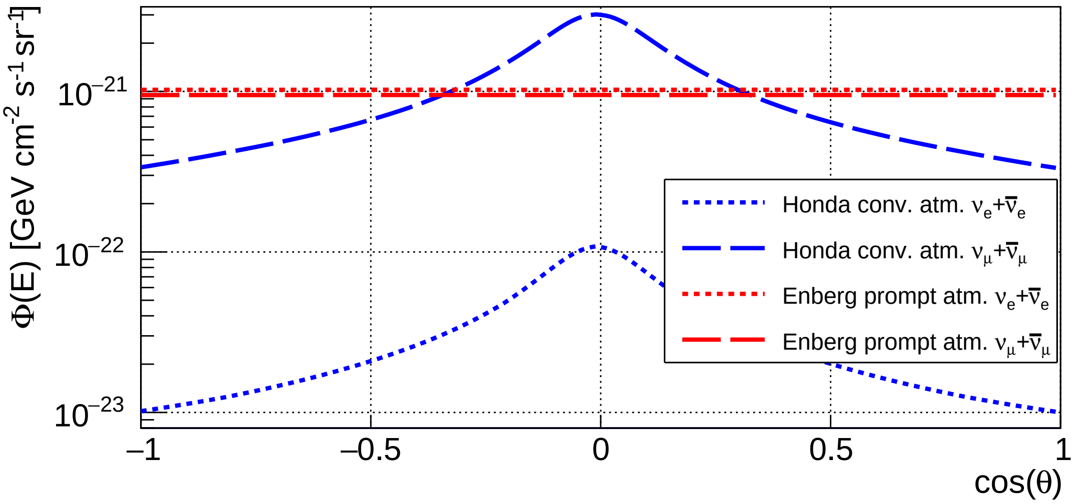

Figure 2.3: *The atmospheric conventional and prompt neutrino fluxes at 1 PeV as a function of cosine of zenith angle.*

type.

For the conventional flux, the electron neutrino component is strongly suppressed. This is due to the fact that, first, for each electron neutrino two muon neutrinos are generated (see Eq. (2.2)) and, second and more importantly, the parent muons lose a large fraction of their energy before decaying. This leads to the fact that the dominating part of the atmospheric electron-neutrino spectrum is caused by three-body kaon decays. Here, the chiral suppression of $e\,\nu_e$ production caused by the weak interaction is much weaker. The $\nu_\mu : \nu_e$ ratio reaches values up to 60 (10^5 GeV). For the prompt flux the flavour ratio is close to unity since the charmed mesons decay almost equally likely into electrons or muons[2].

The prompt flux begins to dominate the atmospheric spectrum at around 30 TeV for electron neutrinos and around 1 PeV for muon neutrinos. The IceCube best-fit fluxes are well above the predicted prompt neutrino fluxes for energies higher than 100 TeV. In fact, the data of IceCube is consistent with a vanishing prompt component [28]. Note, though, that high-energy atmospheric neutrinos coming from above are distinguishable from cosmic neutrinos as the atmospheric neutrinos are likely accompanied by atmospheric muons of the same extensive air shower. This can be used to “veto” atmospheric neutrinos or to probe specifically the prompt component of the atmospheric flux at energies where the prompt flux dominates [43,44].

The atmospheric neutrino fluxes as a function of zenith angle θ as incident at sea level at the geographic position of the KM3NeT detector are shown in Figure 2.3. The conventional flux near the horizon ($\cos\theta = 0$) is about one order of magnitude higher than the flux from near-vertical directions which is due to the development of the cosmic ray air showers in the atmosphere. For neutrinos from above and below, the density of the atmosphere as seen from the parent particles increases faster so that these particles lose energy faster than for neutrinos from the horizon and their respective parent particles. Thus the neutrinos from above stem in average from cosmic rays with higher energies where the respective flux is smaller. This effect is negligible for the prompt neutrinos since their parent particles only have a very short lifetime.

---

[2] The flux of prompt tau neutrinos is negligible since the decay into a tau neutrino is only allowed for a small fraction of the charmed mesons [40].

Parameter	Hierarchy	
	Normal	Inverted
$\sin^2\theta_{12}/10^{-1}$	3.07	3.07
$\sin^2\theta_{13}/10^{-2}$	2.41	2.44
$\sin^2\theta_{23}/10^{-1}$	3.86	3.92
$\Delta m^2_{21}/10^{-5}\,\mathrm{eV}^2$	7.54	7.54
$\Delta m^2_{31}/10^{-3}\,\mathrm{eV}^2$	2.45	2.40
δ/π	1.08	1.09

Table 2.1: *Best-fit oscillation parameters according to Fogli et al. [50] which in general depend on the assumed neutrino mass hierarchy.*

2.2 Neutrino oscillations

Neutrino mass eigenstates are distinct from the eigenstates of the weak interaction. This leads to neutrino oscillations governed by the neutrino mixing matrix (PMNS-matrix[3])

$$U = \begin{pmatrix} U_{e1} & U_{e2} & U_{e3} \\ U_{\mu 1} & U_{\mu 2} & U_{\mu 3} \\ U_{\tau 1} & U_{\tau 2} & U_{\tau 3} \end{pmatrix} = \begin{pmatrix} 1 & 0 & 0 \\ 0 & c_{23} & s_{23} \\ 0 & -s_{23} & c_{23} \end{pmatrix} \times \begin{pmatrix} c_{13} & 0 & \mathrm{e}^{-i\delta} s_{13} \\ 0 & 1 & 0 \\ -\mathrm{e}^{i\delta} s_{13} & 0 & c_{13} \end{pmatrix} \times \begin{pmatrix} c_{12} & s_{12} & 0 \\ -s_{12} & c_{12} & 0 \\ 0 & 0 & 1 \end{pmatrix}, \tag{2.10}$$

with $c_{ij} = \cos\theta_{ij}$, $s_{ij} = \sin\theta_{ij}$, θ_{12}, θ_{13}, θ_{23} the three mixing angles and δ the CP phase[4]. This matrix relates the mass eigenstates $|\nu_k\rangle$, $k \in \{1,2,3\}$, to the flavour eigenstates $|\nu_\alpha\rangle$, $\alpha \in \{e,\mu,\tau\}$:

$$|\nu_k\rangle = \sum_{\alpha\in\{e,\mu,\tau\}} U_{\alpha k}\,|\nu_\alpha\rangle\,. \tag{2.11}$$

As of now, the neutrino masses are unknown. However, with the measurement of solar, reactor and atmospheric neutrinos [6,48,49], it was possible to determine the mass squared differences $\Delta m^2_{21} \equiv \Delta m^2_{\mathrm{sol}} \approx 7.5 \cdot 10^{-5}\,\mathrm{eV}^2$ and $|\Delta m^2_{31}| \approx |\Delta m^2_{\mathrm{atm}}| \approx 2.5 \cdot 10^{-3}\,\mathrm{eV}^2$ with $\Delta m^2_{kk'} := m^2_k - m^2_{k'}$ and neutrino masses m_k of the mass eigenstates $|\nu_k\rangle$. The sign of the large mass squared difference $\Delta m^2_{\mathrm{atm}}$ and therefore the neutrino mass hierarchy is still unknown, i.e. the ordering of the mass eigenstates. The two possibilities are shown in Figure 2.4. The hierarchy is referred to as normal if $\Delta m^2_{31} > 0$ and inverse if $\Delta m^2_{31} < 0$.

The best-fit oscillation parameters – mass squared differences, mixing angles and CP phase – according to a global analysis, carried out by Fogli et al. [50], of the results of several experiments are summarised in Table 2.1.

In the remainder of this section, neutrino oscillations will be discussed in detail. Firstly, oscillations in vacuum are described from which it will become clear why cosmic neutrinos (sum of neutrinos and antineutrinos) from pion-decay sources arrive at Earth with approximately a uniform flavour ratio. It follows the description of oscillations in matter and specifically in the Earth. Due to matter effects in the Earth it is possible to determine the sign of Δm^2_{31} with atmospheric neutrinos and thus the neutrino mass hierarchy.

---

[3] Named after Pontecorvo [45,46], Maki, Nakagawa and Sakata [47].

[4] Two Majorana phases irrelevant to neutrino oscillations have been neglected.

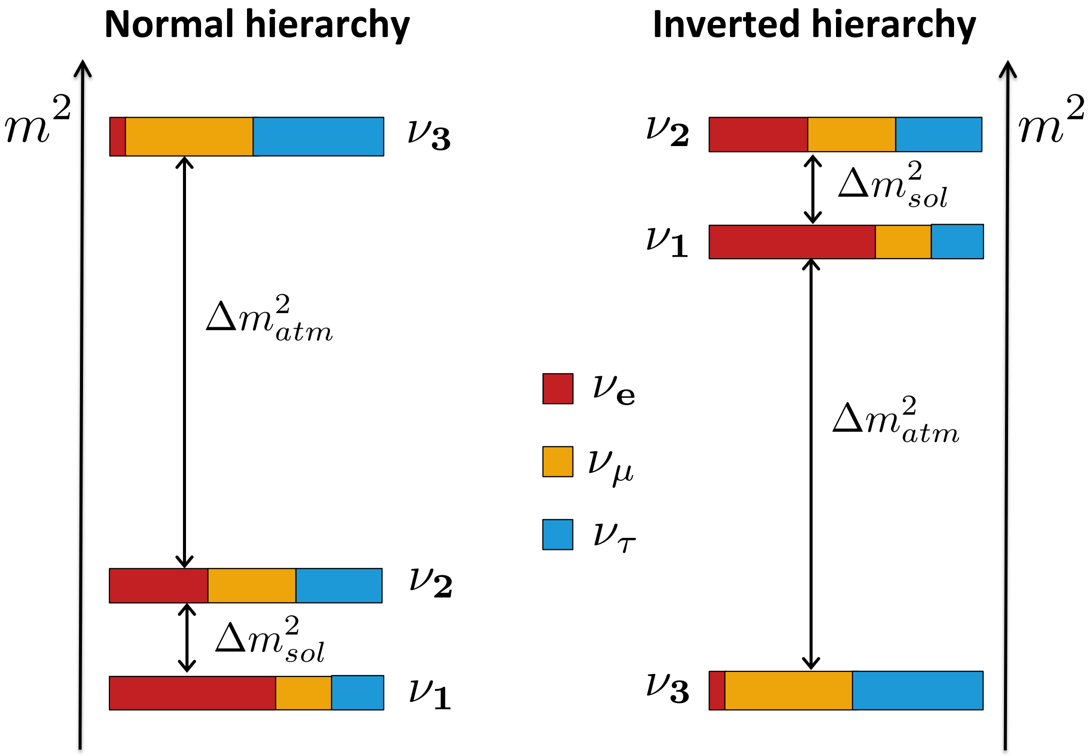

Figure 2.4: *Sketch of the two possible mass hierarchies (m^2-axis not to scale). The colours indicate the flavour content of each mass eigenstate. Figure taken from [7].*

2.2.1 Neutrino oscillations in vacuum

The Schrödinger-type equation of motion for a free neutrino of mass m_k and energy E_k in mass eigenstate $|\nu_k\rangle$ is given by[5]

$$i\frac{\partial}{\partial t}|\nu_k(t)\rangle = E_k\,|\nu_k(t)\rangle\,, \tag{2.12}$$

which can be solved to get

$$|\nu_k(t)\rangle = \exp\left(-iE_k t\right)|\nu_k(0)\rangle\,. \tag{2.13}$$

For relativistic neutrinos, $E_k \gg m_k$ and therefore roughly equal momentum $p_k \approx E$ for $k \in \{1,2,3\}$ for the three mass eigenstates can be assumed and the energies can be approximated by $E_k = \sqrt{p_k^2 - m_k^2} \approx p_k + \frac{m_k^2}{2p_k} \approx E + \frac{m_k^2}{2E}$. In addition, with the neutrinos travelling almost at the speed of light, the propagation in time t can be replaced by the propagation in space x. Therefore, Eq. (2.13) can be written as

$$|\nu_k(x)\rangle = \exp\left(-i\frac{m_k^2}{2E}x\right)|\nu_k(0)\rangle\,, \tag{2.14}$$

---

[5] In natural units where $\hbar = c = 1$.

where an overall phase factor E, which is the same for all mass eigenstates, has been ignored. It follows for the flavour eigenstate α:

$$|\nu_\alpha(x)\rangle = \sum_{k=1}^{3} U^*_{\alpha k} \, |\nu_k(x)\rangle = \sum_{k=1}^{3} U^*_{\alpha k} \exp\left(-i\frac{m_k^2}{2E}x\right)|\nu_k(0)\rangle \,. \tag{2.15}$$

The probability for a neutrino of flavour α to oscillate into a neutrino of flavour β after travelling a distance L is then given by evaluating $P(\nu_\alpha \rightarrow \nu_\beta) \equiv |\langle\nu_\alpha|\nu_\beta(L)\rangle|^2$ which gives

$$P(\nu_\alpha \rightarrow \nu_\beta) = \sum_{k=1}^{3} |U_{\alpha k}|^2 |U_{\beta k}|^2 + 2\mathrm{Re} \sum_{j<k} U_{\alpha j} U^*_{\alpha k} U_{\beta k} U^*_{\beta j} \exp\left(-i\frac{\Delta m_{kj}^2}{2E}L\right), \tag{2.16}$$

with the three mass squared differences $\Delta m_{kj}^2 = m_k^2 - m_j^2$.

From the oscillatory terms in Eq. (2.16), oscillation lengths can be defined as the length at which the argument becomes 2π, respectively:

$$\begin{aligned} L_{21} &= 4\pi E/|\Delta m_{21}^2| = 32.9 \cdot 10^3\,\text{km} \cdot E/\text{GeV}, \\ L_{31} &= 4\pi E/|\Delta m_{31}^2| = 1.00 \cdot 10^3\,\text{km} \cdot E/\text{GeV}, \\ L_{32} &= 4\pi E/|\Delta m_{32}^2| = 1.04 \cdot 10^3\,\text{km} \cdot E/\text{GeV}, \end{aligned} \tag{2.17}$$

with the values from Table 2.1 for normal hierarchy with $\Delta m_{32}^2 \equiv \Delta m_{31}^2 - \Delta m_{21}^2$. It follows that over large distances ($L \gg 10^5\,\text{km} \cdot E/\text{GeV}$) even small differences in energy produce large phase shifts. Given the finite energy resolution of any real detector and the fact that also the emission regions of cosmic neutrino sources may well be larger than the oscillation lengths, the oscillatory terms in Eq. (2.16) average out. Therefore, only averaged oscillation probabilities are observable for cosmic neutrinos:

$$\langle P(\nu_\alpha \rightarrow \nu_\beta)\rangle = \sum_{k=3}^{3} |U_{\alpha k}|^2 |U_{\beta k}|^2. \tag{2.18}$$

With the best-fit mixing angles from Table 2.1 and the CP phase $\delta = \pi$ which is close to its best-fit value, the mixing matrix becomes roughly:

$$U = \begin{pmatrix} U_{e1} & U_{e2} & U_{e3} \\ U_{\mu 1} & U_{\mu 2} & U_{\mu 3} \\ U_{\tau 1} & U_{\tau 2} & U_{\tau 3} \end{pmatrix} \approx \begin{pmatrix} 0.82 & 0.55 & -0.16 \\ -0.35 & 0.70 & 0.62 \\ 0.45 & -0.45 & 0.77 \end{pmatrix}, \tag{2.19}$$

and the averaged probabilities calculated from these values are given in Table 2.2.

Thus, the sum of cosmic neutrinos and antineutrinos produced according to Eqs. (2.1) and (2.2) oscillate from a flavour ratio of $\nu_e : \nu_\mu : \nu_\tau = 1:2:0$ to 1.03 : 1.05 : 0.92 incident on Earth, which is close to 1 : 1 : 1. For muon-damped or neutron-beam sources the flavours oscillate on their way to Earth like 0 : 1 : 0 → 0.24 : 0.41 : 0.35 and 1 : 0 : 0 → 0.55 : 0.24 : 0.21.

If neutrinos travel through matter, e.g. atmospheric neutrinos travelling through Earth, they cannot be regarded as free particles any more and the oscillation probabilities are modified. This modification of the oscillation probabilities depends on the neutrino mass hierarchy and is as such the central physics case for the ORCA experiment. The main aspects will be described in the following section.

	ν_e	ν_μ	ν_τ
ν_e	55%	24%	21%
ν_μ	24%	41%	35%
ν_τ	21%	35%	44%

Table 2.2: *Averaged probabilities for the oscillation of one given neutrino type into another.*

2.2.2 Neutrino oscillations in matter

Expressing the neutrino state vector as $|\Psi\rangle = a_e\,|\nu_e\rangle + a_\mu|\nu_\mu\rangle + a_\tau|\nu_\tau\rangle$, the corresponding equation of motion according to Eqs. (2.11) and (2.12) can be written as

$$i\frac{\partial}{\partial t}\begin{pmatrix} a_e \\ a_\mu \\ a_\tau \end{pmatrix} = \frac{1}{2E} U \begin{pmatrix} m_1^2 & 0 & 0 \\ 0 & m_2^2 & 0 \\ 0 & 0 & m_3^2 \end{pmatrix} U^\dagger \begin{pmatrix} a_e \\ a_\mu \\ a_\tau \end{pmatrix} \tag{2.20}$$

with U from Eq. (2.10) and the approximations given after Eq. (2.13).

In matter, coherent forward scattering of electron neutrinos off electrons creates an effective potential $V = \sqrt{2}G_F n_e$ for the electron neutrinos. For electron antineutrinos, V is replaced by $-V$. Here, G_F is the Fermi coupling constant and n_e is the number density of electrons. Thus, in matter Eq. (2.20) gets modified to

$$\begin{aligned} i\frac{\partial}{\partial t}\begin{pmatrix} a_e \\ a_\mu \\ a_\tau \end{pmatrix} &= \frac{1}{2E}\left[U \begin{pmatrix} m_1^2 & 0 & 0 \\ 0 & m_2^2 & 0 \\ 0 & 0 & m_3^2 \end{pmatrix} U^\dagger + \begin{pmatrix} 2EV & 0 & 0 \\ 0 & 0 & 0 \\ 0 & 0 & 0 \end{pmatrix} \right] \begin{pmatrix} a_e \\ a_\mu \\ a_\tau \end{pmatrix} \\ &= \frac{1}{2E} U_M \begin{pmatrix} m_{M,1}^2 & 0 & 0 \\ 0 & m_{M,2}^2 & 0 \\ 0 & 0 & m_{M,3}^2 \end{pmatrix} U_M^\dagger \begin{pmatrix} a_e \\ a_\mu \\ a_\tau \end{pmatrix} \end{aligned} \tag{2.21}$$

where the last equation follows after diagonalisation. The effective neutrino masses squared are then given by $m_{M,k}^2$ and the effective mixing matrix by U_M which incorporates the effective mixing angles in matter $\theta_{M,ij}$. In general, the electron density $n_e = n_e(x) = n_e(t)$ is an unknown function of space x, or equivalently of time t for relativistic neutrinos. Therefore, also the matrix $U_M = U_M(t)$ and the mass squared differences $m_{M,k}^2 = m_{M,k}^2(t)$ will depend on time and Eq. (2.21) cannot be solved analytically. Furthermore, the expressions for the effective neutrino masses and mixing angles in matter as a function of their vacuum counterpart are very extensive and will therefore not be given here, see instead [51].

For the sake of clarity, it is convenient to use the two-flavour case to illustrate the main feature of matter oscillations. This gives a good approximation for many practical cases and is applicable due to $|\Delta m_{21}^2| \ll |\Delta m_{31}^2| \approx |\Delta m_{32}^2|$ and $|U_{e3}| \ll 1$. In this approximation, there exists only one mixing angle θ and mass squared difference Δm^2. The respective diagonalisation of the two-flavour version of Eq. (2.21) yields for the effective mixing angle in matter θ_M the following expression:

$$\sin 2\theta_M = \frac{\sin 2\theta}{\sqrt{\cos^2 2\theta\,(1 - A/A_R)^2 + \sin^2 2\theta}} \tag{2.22}$$

with $A = 2EV$ and $A_R = \Delta m^2 \cos 2\theta$. This expression exhibits a resonance at $A = A_R$ where the mixing becomes maximal: $\sin 2\theta_M = 1$. This is often referred to as the MSW resonance after Mikheyev, Smirnov and Wolfenstein [52–54]. The resonance value A_R depends on the sign of the mass squared difference and this is where the sensitivity to the neutrino mass hierarchy arises from. Recalling that $A \rightarrow -A$ for antineutrinos, the resonance may be reached both for neutrinos given positive mass squared difference and for antineutrinos given negative mass squared difference.

Writing the electron number density as $n_e = Y_e \rho / m_N$ with Y_e as the mean number of electrons per nucleon, ρ the matter density and m_N the nucleon mass, the neutrino energy E_R at the resonance is derived to be:

$$E_R = \frac{\Delta m^2 \cos 2\theta}{2\sqrt{2} G_F \, Y_e / m_N} \, \rho^{-1}. \tag{2.23}$$

In the case of atmospheric neutrino oscillations with neutrino energies $\gtrsim 2\,\text{GeV}$, the above approximation conditions ($|\Delta m^2_{21}| \ll |\Delta m^2_{31}| \approx |\Delta m^2_{32}|$) mean that the 1-2 mixing (with an oscillation length of several times the Earth diameter) can be neglected compared to the 1-3 and 2-3 mixing (see Eq. (2.17)). Instead, two-flavour neutrino mixing governed by θ_{13} and Δm^2_{31} can be used as an approximation[6] [55]. Considering, according to [56], the density in the Earth's mantle, ranging from 2.7 to 5.5 g/cm^3, and in the core, ranging from 9.9 to 12.5 g/cm^3, and approximating Y_e by 0.5, the resonance energies corresponding to these regions are given by:

$$\begin{aligned} 5.6\,\text{GeV} &< E_R < 11.5\,\text{GeV}, && \text{for the Earth's mantle,} \\ 2.5\,\text{GeV} &< E_R < 3.1\,\text{GeV}, && \text{for the Earth's core.} \end{aligned} \tag{2.24}$$

The width of the resonance ΔE_R where $\sin 2\theta_M$ drops to 1/2 can be derived to be $\Delta E_R = 2E_R \tan 2\theta_{13}$ which is 3.6 to 7.4 GeV for the mantle and 1.6 to 2.0 GeV for the core. Correspondingly, given the neutrino energy E one can derive the resonance matter density ρ_R by swapping E and ρ in Eq. (2.23). The density width of the resonance is then $2\rho_R \tan 2\theta_{1,3}$ which is 2.9 g/cm^3 and 7.4 g/cm^3 considering the average density of the mantle and core, respectively. Thus for any neutrino, given normal mass hierarchy (or antineutrino, given inverted hierarchy), between roughly 2 and 15 GeV travelling through the Earth's mantle and core the 1-3 mixing gets enhanced considerably.

It has been pointed out by Akhmedov [57] that neutrino mixing can be enhanced by another matter effect referred to as parametric resonance. The requirements for this resonance to happen are neutrinos travelling through layers of alternating (constant) density ρ_1 and ρ_2 with thicknesses L_1 and L_2, respectively. For such a density profile, the equation of motion (Eq. (2.21)) can be solved analytically and it can be shown that under special conditions for the densities, layer thicknesses and neutrino energy, the probability $P(\nu_\alpha \rightarrow \nu_\beta)$ for $\alpha \neq \beta$ after traversing this periodic density profile can be maximal even for small mixing angles in both vacuum and matter. In fact, neutrinos travelling through the Earth's core traverse approximately one and a half periods of such a density profile when the densities of the Earth's mantle and core are approximated by their average densities. Akhmedov showed that in this case the enhancement of the neutrino mixing is especially favoured when the neutrino energy is between the MSW resonance energies of the two considered density layers. This implies that also the parametric resonance is sensitive to the neutrino mass ordering.

---

[6] The two-flavour mixing occurs between ν_e and the mixed flavour $\sin\theta_{23}\nu_\mu + \cos\theta_{23}\nu_\tau$ [55].

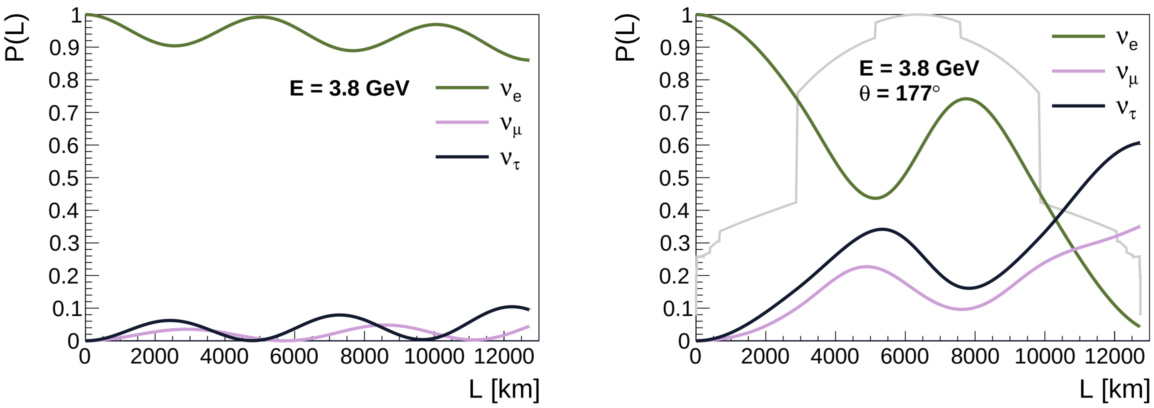

Figure 2.5: *The probability of a 3.8 GeV electron neutrino to oscillate into an electron (green), muon (pink) or tau neutrino (black) over the travelled distance assuming normal mass hierarchy. The left part shows the oscillation probability for propagation in vacuum, the right for propagation through the Earth for a zenith angle of 177°. The oscillations of electron neutrinos into other flavours get enhanced significantly in the Earth. On the right, the relative Earth density profile [56] used for the calculation is also indicated (the maximum corresponds to about 12 g/cm^3). See Section 4.1 for details on the calculation of the oscillation probabilities.*

An example of how the oscillation gets modified due to the presence of the Earth matter is illustrated in Figure 2.5 for a starting electron neutrino with $E = 3.8$ GeV. The propagation in vacuum is compared to the propagation through Earth at a zenith angle of $\theta = 177°$ assuming normal neutrino mass hierarchy. As can be seen especially in the vacuum case and as already mentioned above, the oscillations due to Δm^2_{21} are negligible for such a distance. On the other hand it shows how the, in vacuum almost negligible, 1-3-mixing gets enhanced in matter.

The effect of the parametric resonance according to analytic formulae of Akhmedov is illustrated in Figure 2.6. For these formulae the Earth was approximated by a two-layer sphere, representing mantle and core, with constant densities 4.5 g/cm^3 and 11.5 g/cm^3, respectively. The effects of the parametric resonance are compared to the outcome of a numerical solution of the neutrino equation of motion taking into account a more detailed and realistic Earth model (for details see Section 4.1). This numerical calculation therefore takes fully into consideration the effects of both the parametric resonances and MSW resonances. In the full calculation, the two different resonance phenomena are not strictly separable anymore because of the varying Earth density and the underlying, highly non-linear problem. The differences in the resulting oscillation probability are also shown in the figure. These differences are both due to the MSW resonance and result from the much more realistic treatment of the Earth.

From the relatively large differences up to about 70% at some energies and zenith angles, it follows that both effects play an important role though some of the differences result also from the different Earth models. To what extend deviations in the Earth model may change the oscillation probabilities is analysed and discussed in Section 4.4.

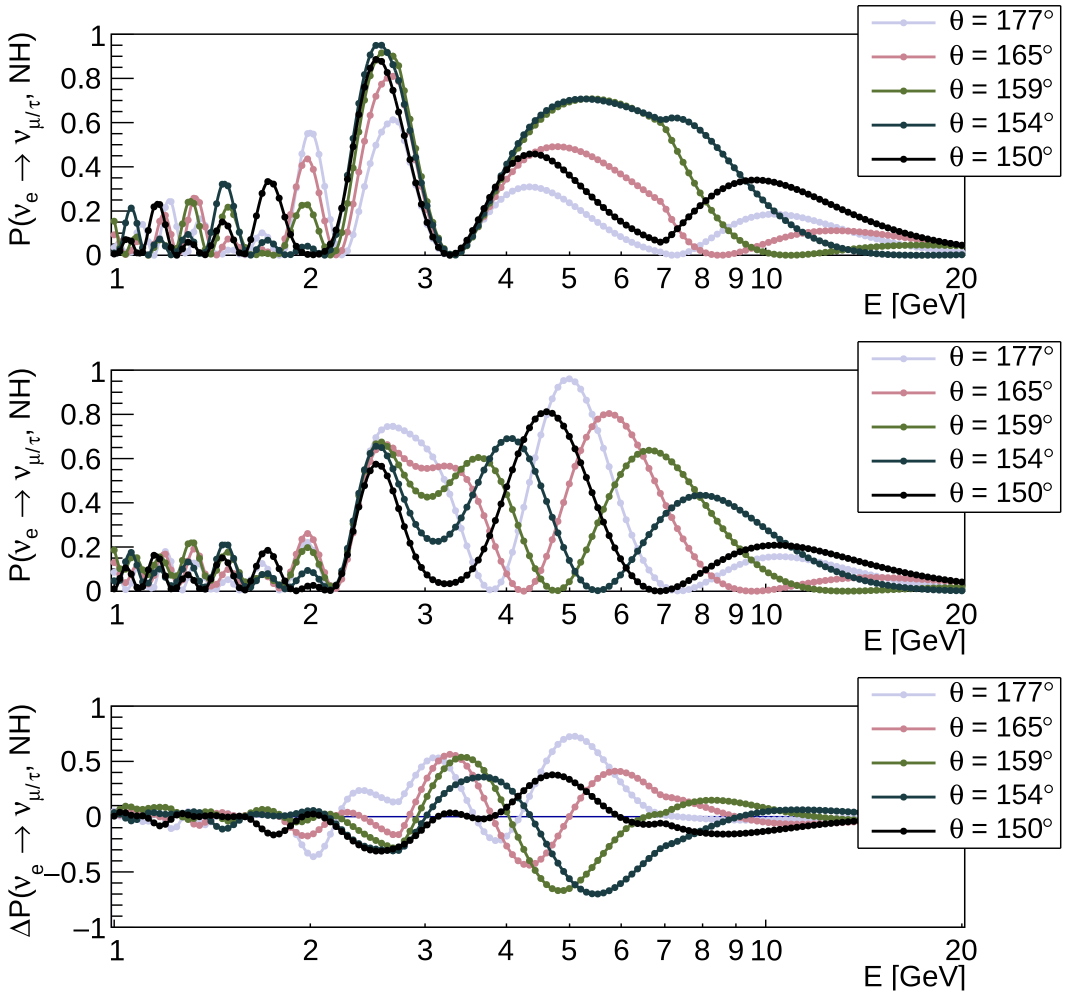

Figure 2.6: *Top: The oscillation probability $P(\nu_e \rightarrow \nu_{\mu/\tau}) = 1 - P(\nu_e \rightarrow \nu_e)$ according to the parametric resonance effect after the starting electron neutrino has passed through the Earth for different zenith angles calculated via analytic formulas from [57] approximating the Earth mantle and core with constant densities of 4.5 g/cm^3 and 11.5 g/cm^3, respectively. The main effect happens around 2.5 GeV and at energies between 4 to 8 GeV. Note that at these energies and path lengths $P(\nu_e \rightarrow \nu_{\mu/\tau}) \approx 0$ in vacuum due to $\theta_{13} \ll 1$.*
Middle: The oscillation probabilities calculated by numerically solving the neutrino equation of motion with a more detailed Earth model (see Section 4.1 for details).
Bottom: Difference between middle and top.

2.3 Neutrino interactions with matter

The neutrino nucleon interactions relevant at lower energies are quasi-elastic scattering, resonance production and deep-inelastic scattering (DIS). From energies above some 10 GeV, DIS becomes the dominating process. In general, charged-current and neutral-current (CC and NC) interactions are distinguished. In the former, a W boson is exchanged and therefore a charged lepton produced. The latter are mediated by a Z boson which leads to a neutrino in the final state of the same type as the incident one. In both cases a hadronic shower X is produced. The reactions can be summarised

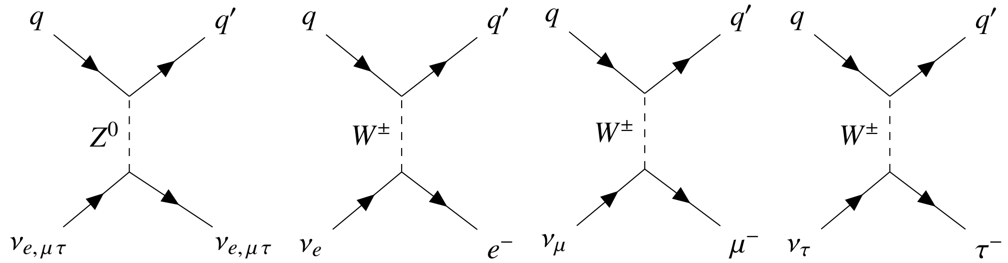

Figure 2.7: *Feynman diagrams for neutral-current (left) and charged-current neutrino interactions with a quark q of a nucleon (deep-inelastic scattering). For antineutrinos the corresponding arrow directions are inverted.*

as

$$\begin{aligned} \overset{(-)}{\nu}_l + N &\to l^\mp + X \quad \text{(CC)} \\ \overset{(-)}{\nu}_l + N &\to \overset{(-)}{\nu}_l + X \quad \text{(NC)} \end{aligned} \tag{2.25}$$

with $l \in \{e, \mu, \tau\}$ and where N represents a nucleon. For neutrinos/antineutrinos a negatively/positively charged lepton is produced in the CC interaction. Figure 2.7 shows the corresponding Feynman diagrams.

Given the lepton's energy loss $\nu = E_\nu - E_l$ in the target's rest frame, with E_ν and E_l as the energy of the initial neutrino and of the outgoing lepton, respectively, the cross-section for these interactions is given in terms of the Bjorken scaling variables $x = Q^2/2M_N\nu$ and $y = \nu/E_\nu$ as (see e.g. [58])

$$\frac{\mathrm{d}^2\sigma}{\mathrm{d}x\,\mathrm{d}y} = \frac{G_F^2 M_N E_\nu}{\pi} \begin{cases} 2\left(\frac{M_W^2}{Q^2+M_W^2}\right)^2 \left[xq(x,Q^2) + x\bar{q}(x,Q^2)(1-y)^2\right] & \text{(CC)} \\ \frac{1}{2}\left(\frac{M_Z^2}{Q^2+M_Z^2}\right)^2 \left[xq^0(x,Q^2) + x\bar{q}^0(x,Q^2)(1-y)^2\right] & \text{(NC).} \end{cases} \tag{2.26}$$

Here, G_F is the Fermi constant, M_N, M_W and M_Z are the nucleon mass and the masses of the W and Z boson, respectively, and $Q^2 = 2xyE_\nu M_N$ is the negative four-momentum transfer squared. The parton distribution functions (PDFs) q and $\bar{q}$ represent the quark and antiquark distributions of the nucleon including all relevant quark flavours. The PDFs q^0 and $\bar{q}^0$ also include the chiral couplings important for the neutral current interactions. Detailed expressions for the PDFs are given in [58]. For antineutrinos, the cross-sections are given by replacing each quark distribution function with the corresponding antiparticle distribution and vice versa.

The total cross-section for neutrinos (per nucleon), obtained by integrating over x and y [59], is shown in Figure 2.8 for very high energies. Uncertainties at highest energies are due to unknowns in the PDFs. Below roughly 10 TeV the total cross-section rises approximately linear with neutrino energy. For higher energies, the Q^2 dependencies become important resulting in a rise proportional to about $E_\nu^{0.4}$ [20].

The Bjorken variable y, also known as inelasticity, gives the energy fraction transferred from the incoming neutrino to the hadronic shower. From this fraction, the energy deposited in the surrounding medium can be inferred which is important for energy reconstruction. For NC interactions, only energy from the hadronic system is deposited while the remaining fraction (1-y) is carried away by the outgoing neutrino. In CC events, potentially the total energy is deposited, though outgoing long-range leptons (muons and high-energy taus) may take energy away from the sensitive detector volume. The mean inelasticity varies between 0.2 and 0.5. It is shown in Figure 2.9 as a function of neutrino energy.

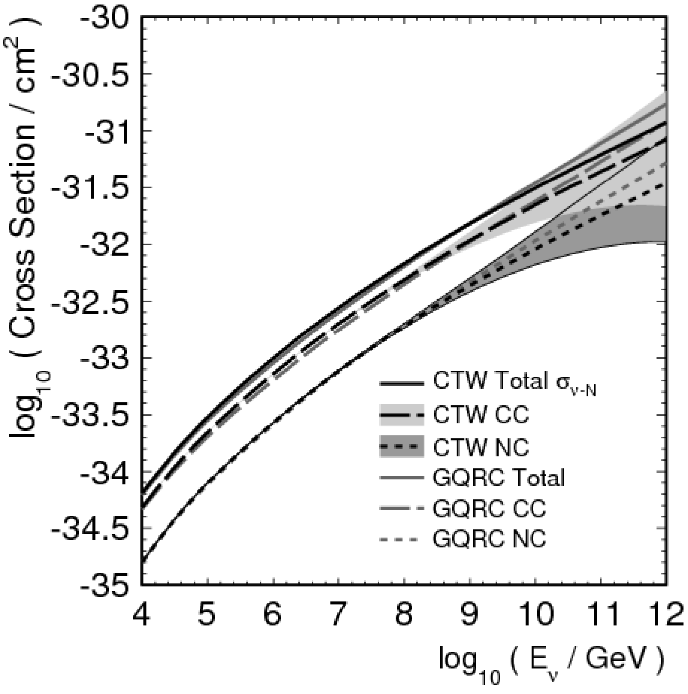

Figure 2.8: *The high-energy neutrino charged-current (CC) and neutral-current (NC) cross-section as a function of neutrino energy for neutrino-nucleon deep-inelastic scattering as derived by Connolly et al.[59] (CTW) where the figure is taken from. It is compared to earlier calculations (GQRS) [58]. Uncertainties are shown as bands.*

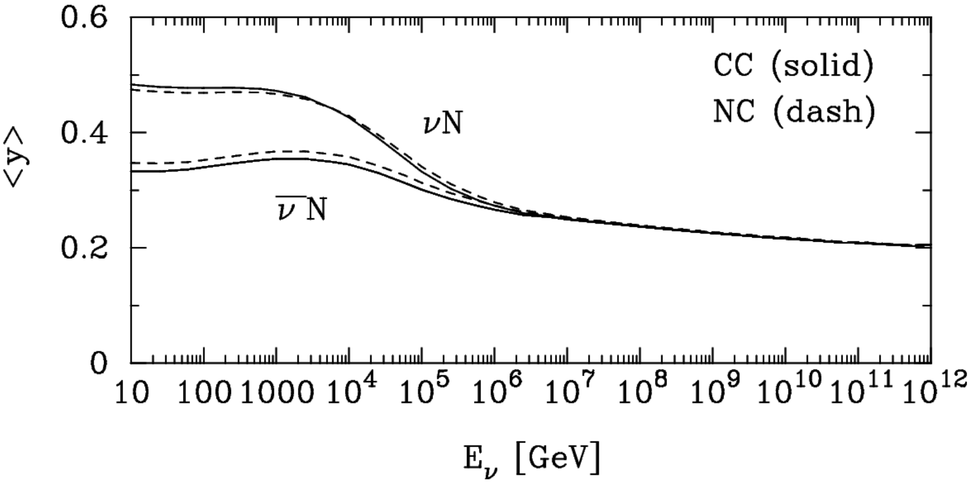

Figure 2.9: *Mean inelasticity as a function of incident neutrino energy for CC (solid) and NC (dashed) interactions. Figure taken from [60].*

In the energy range of a few PeV, electron antineutrinos may interact resonantly with electrons by generating a W^- boson which subsequently decays into leptons, or a quark-antiquark pair which produces a hadronic shower:

$$\bar{\nu}_e + e^- \to W^- \to \begin{cases} \bar{\nu}_l + l^- \\ (q + \bar{q}) \to X, \end{cases} \tag{2.27}$$

where again $l \in \{e, \mu, \tau\}$. This resonant W^- production is also called the Glashow resonance and peaks at $E_\nu = 6.3$ PeV [60]. The cross-section at this energy has a value of $5.4 \cdot 10^{-32}$ cm^2 exceeding the DIS cross-section at this energy by over two orders of magnitude. The Glashow resonance plays therefore a notable role in neutrino telescopes sensitive in this very-high-energy region [61]. It gives a unique sensitivity to the electron-antineutrino-content of the investigated neutrino flux.

As neutrino telescopes such as KM3NeT also look for neutrinos crossing the Earth from below, neutrino absorption in the Earth has to be considered. At energies above some TeV absorption becomes relevant. For instance considering DIS, at 1 TeV/1 PeV the interaction lengths are roughly 10^6 km/10^4 km in water (compare this to the Earth diameter of roughly 12 000 km). For neutrinos with energies above 10 PeV, more than 90% are absorbed for zenith angles larger than 120°. For more details see e.g. [58,60,62].

Note though that each neutrino absorbed in a neutral current interaction produces a neutrino of the same type but with lower energy (regeneration effect). These neutrinos travel further through the Earth potentially reaching the detector. The energy loss yE_ν is in general small enough so that the neutrinos are still important for neutrino astronomy. The regeneration effect also applies to tau neutrinos absorbed in charged-current interactions, where the outgoing tau will produce a high-energy tau neutrino when decaying.

2.4 Neutrino detection

The charged secondary particles created in neutrino interactions produce Cherenkov light if their velocities exceed the speed of light in a surrounding dielectric medium [63]. The detection of this Cherenkov light is the principle of high-energy neutrino detection which will be presented in this section. Water (liquid or solid) serves as an ideal choice for the detector medium, occurring naturally in large volumes and being transparent in a large part of the Cherenkov light spectrum.

The spectral distribution for the number of Cherenkov photons with wavelength λ emitted by a charged particle (charge $\pm ze$) with velocity $v = \beta c$ per path length x is given by

$$\frac{\mathrm{d}N}{\mathrm{d}x\,\mathrm{d}\lambda} = \frac{2\pi z^2 \alpha}{\lambda^2} \cdot \left(1 - \frac{1}{\beta^2 n^2}\right) \tag{2.28}$$

with α the fine structure constant and n the index of refraction of the surrounding medium. The Cherenkov light is emitted under the characteristic angle θ_C given by

$$\cos\theta_C = \frac{1}{\beta n}, \tag{2.29}$$

which amounts to roughly 41° in water with $\beta = 1$ and $n = 1.33$. From Eq. (2.28), the number of photons emitted in the transparency window of water (400 nm $\leq \lambda \leq$ 700 nm) can be determined to roughly 200 per cm [20].

These photons are measured to reconstruct the energy deposit and the mean angle of the charged secondaries and therefore infer the energy and angle of the primary neutrino. In an electromagnetic or hadronic shower, the number of generated relativistic particles is by approximation proportional to the shower energy. Therefore, also the number of emitted Cherenkov photons is roughly proportional to the shower energy. The photons are emitted in every direction although with a strong peak at the Cherenkov angle with respect to the shower direction.

The energy of a high-energy muon can be inferred from its energy losses. The average energy loss per path length is a function of the muon energy E and can be written as

$$-\mathrm{d}E/\mathrm{d}x = a(E) + b(E)\,E, \tag{2.30}$$

where $a(E)$ is the loss due to ionisation and $b(E)$ accounts for e^+e^- pair production, bremsstrahlung and photonuclear losses (see Chapter 34 of [2]). At high energies the latter term dominates. It is responsible for stochastic generation of electromagnetic and hadronic showers along the muon track. From these the total muon energy loss can be determined and from that the energy of the muon. Note though that muons (> 10 GeV) and very-high-energy taus (> 10 PeV) have mean track lengths of the order of kilometres. They can reach the active detector volume from far outside having lost a large fraction of their energy. Therefore the reconstructed energy in these cases may only serve as a lower limit for the parent-neutrino energy.

Depending on the type of charged secondaries produced in a neutrino interaction, different event topologies can be distinguished based on the emitted light pattern. These will be described briefly in the following.

Event topologies

In general track-like and shower-like events are distinguished. A hadronic shower is produced in every neutrino-nucleon DIS interaction. In charged-current (CC) electron-neutrino interactions, the outgoing electron creates an extra electromagnetic shower. The showers have typical extensions of the order of metres, and can be considered quasi point-like compared to the average distances between the light detectors of typical underwater high-energy neutrino telescopes. The light output of these events is approximately spherical, centred around the shower maximum and peaked at the Cherenkov angle[7]. Besides CC electron-neutrino events, such purely shower-like events happen for all neutral-current interactions. In addition, tau-neutrino CC events can be purely shower-like when the intermediate tau decays immediately into a shower. This event class therefore represents a major fraction of all event topologies.

Purely track-like events occur when muons (or ultra-high-energy taus) produced in reactions outside of the active detector volume go through the detector leaving behind a cone of Cherenkov light. The muons might also be produced in the decay of intermediate taus outside of the detector. Due to the large track length, a very good precision on the reconstruction of the muon direction is possible. Produced in a high-energy neutrino interaction, the outgoing muon is nearly collinear with the parent neutrino. However, track-like events are also caused by atmospheric muons. Coming from above, these produce down-going tracks. Therefore, neutrino searches in general only look for up-going tracks.

Figure 2.10 shows examples for a characteristic shower-like and track-like event as simulated for the KM3NeT/ARCA detector (see Section 3.1).

Apart from these two event classes, there exist intermediate topologies. Among them are showers with an outgoing track (starting tracks), or very-high-energy taus producing a second shower

---

[7] For instance, the minimum distance between two detection modules in ARCA is roughly 40 m. See also Chapter 3. For ORCA, where the minimum distance is around 10 m, the approximation of spherical light output reaches its limits.

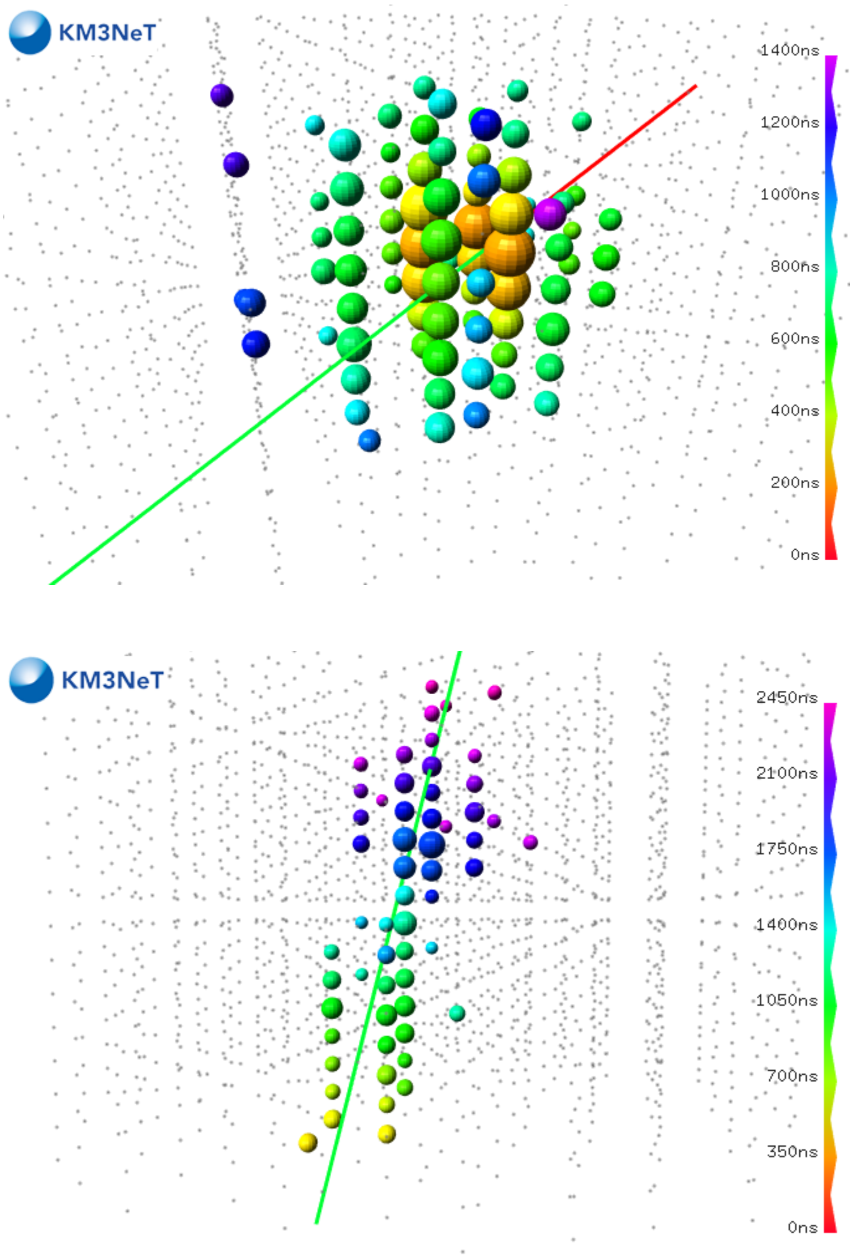

Figure 2.10: *Event signatures for a shower event (ν_e-CC, top) and track event (ν_μ-CC, bottom) as simulated for the KM3NeT/ARCA detector (see Section 3.1). The coloured spheres depict light detectors with recorded photon signals above a given amplitude, the size of a sphere refers to the amplitude, the colour to the hit time with respect to the neutrino interaction. Grey dots represent light detectors with no such hits. In the top picture, the incoming neutrino is shown as a red track, the outgoing-electron direction as a green track. In the bottom picture, the green track refers to the up-going muon resulting from the neutrino interaction.*

when decaying (double-bang). At energies above some PeV the distance between both showers is of the order of tens of metres and the bangs become separable. However, such double-bang events are only important for high-energy-neutrino detectors like KM3NeT/ARCA. They are the only event class that directly allows the inference of the neutrino flavour. In general, the neutrino flavour content can only be determined on a statistical basis.

Chapter 3

The KM3NeT experiment

KM3NeT[8] is a neutrino detector under construction in the Mediterranean Sea. It builds upon the experience gained with ANTARES [35], the first deep sea neutrino telescope and predecessor of KM3NeT which proved the feasibility of doing neutrino astronomy in the deep sea. Two separate detector configurations are envisaged: the ARCA (Astroparticle Research with Cosmics in the Abyss) detector for high-energy neutrino astronomy, and the ORCA (Oscillation Research with Cosmics in the Abyss) detector dedicated to the determination of the neutrino mass ordering.

The detectors are planned to be built in three phases. Phase-1, which is still ongoing, includes prototype construction and testing (see e.g. [64,65]) as well as optimisation of the deployment and installation. A first construction is also part of Phase-1: 31 strings will be deployed, expectedly 24 of these for ARCA and seven for ORCA. The first detection unit (DU) or string has been installed successfully in December 2015. In addition, the development of necessary software tools is comprised in this phase. The second phase (Phase-2) has the goal of completing the ARCA and ORCA detectors by 2020. In Phase-3, KM3NeT is planned to contain seven building blocks in total, six of them for high-energy neutrino astronomy. These building blocks will be distributed off-shore Toulon (France), Capo Passero (Sicily, Italy) and Pylos (Peloponnese, Greece).

A KM3NeT building block, schematically depicted in Figure 3.1, comprises 115 vertical strings anchored at the sea floor. The strings are equipped equidistantly with 18 digital optical modules (DOMs) each. One DOM consists of 31 photomultiplier tubes (PMTs) attached spherically (see Figure 3.2) and is therefore often called multi-PMT DOM. This new technology provides significantly more photo-sensitive area and directional information as compared to single PMT optical modules as used e.g. in the ANTARES and IceCube neutrino telescopes. The PMTs utilised in KM3NeT are able to measure single photons with nanosecond timing accuracy needed for neutrino detection in the deep sea. The spacing of the DOMs on a string is variable as is the horizontal spacing of the strings on the sea floor. This allows targeting a specific neutrino energy range, which is needed for the different science goals of ORCA and ARCA. ORCA will be densely instrumented to be able to resolve neutrino events in the energy range of 1-100 GeV. On the other hand a large instrumented detector volume is needed to be sensitive to the expected neutrino fluxes from tens of TeV up to some PeV, the targeted energy range for ARCA. Strings are held vertical by a submerged buoy, minimising horizontal displacement produced by the sea current. Nevertheless, acoustic position calibrations are done regularly as well as optical time calibration and orientation calibration via a compass and a tilt-meter within a DOM.

More about the detailed design of the detector elements and the physics goals can be read in

---

[8] http://www.km3net.org, KM3NeT: km^3-sized Neutrino Telescope

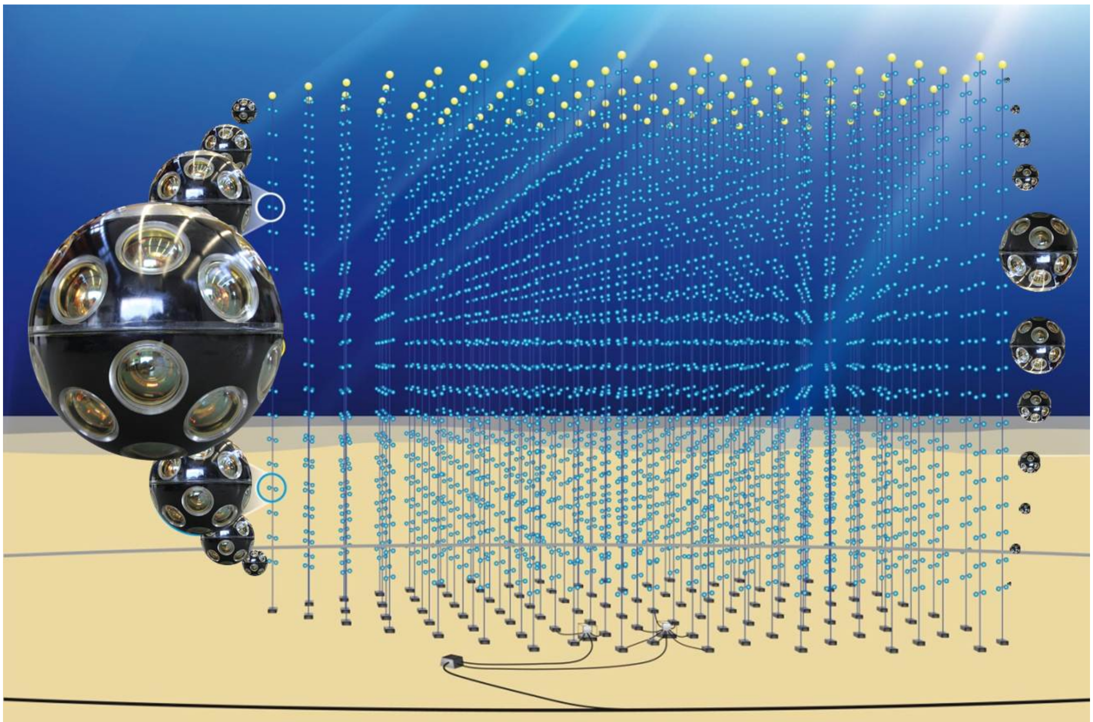

Figure 3.1: *Artist's impression of a KM3NeT building block including magnifications of single DOMs. Picture taken from [66].*

Figure 3.2: *The KM3NeT DOM with 12 PMTs in two rows on the upper hemisphere 18 PMTs in three rows on the lower hemisphere and one PMT pointing directly downwards. Picture taken from [7].*

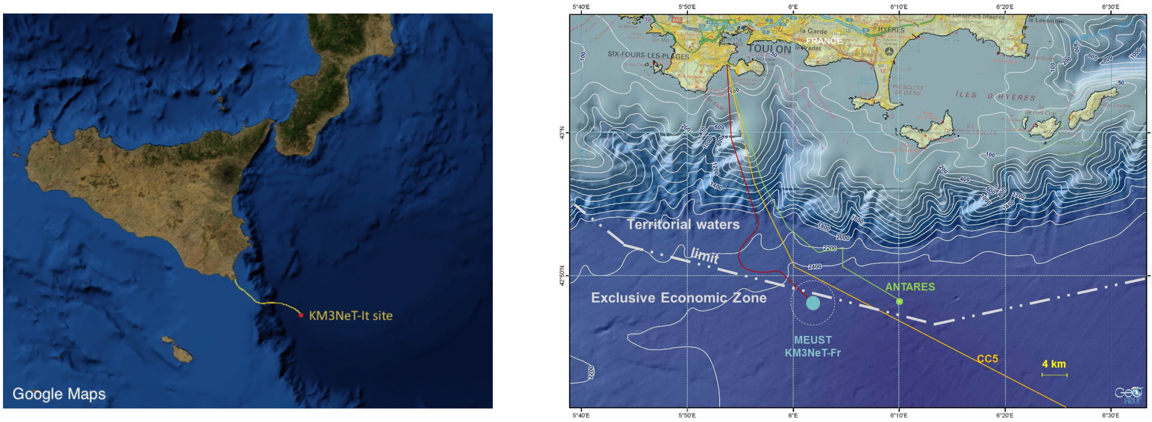

Figure 3.3: *The KM3NeT Italy site (left) near Sicily and the France site (right) near Toulon where the ARCA and ORCA detectors will be built in depths of about 3500 m and 2450 m, respectively. Pictures taken from [7].*

the Letter of Intent for ARCA and ORCA [7] published in July 2016. In the following sections, some of the unique features of ARCA and ORCA will be presented as well as their science goals. At the end of this chapter sources of non-neutrino background present in the deep sea will be explained.

3.1 Astroparticle Research with Cosmics in the Abyss (ARCA)

The ARCA detector will comprise two building blocks at the KM3NeT-Italy site at a depth of 3500 m, about 100 km offshore from Porto Palo di Capo Passero, Sicily (Figure 3.3, left). It has the main goal of detecting neutrinos of cosmic origin and therefore to observe the diffuse cosmic flux measured by IceCube as well as subsequently finding galactic and extra-galactic neutrino point sources. The IceCube measurements imply that diffuse cosmic neutrinos begin to dominate at some tens $(\nu_e + \bar{\nu}_e)$ to a few hundred TeV $(\nu_\mu + \bar{\nu}_\mu)$ over the major background of atmospheric neutrinos (see Figure 2.2, p. 21). The detector is designed to instrument the largest possible volume while retaining sensitivity to neutrinos at these energies. The DOMs on a string have a distance of 36 m starting 80 m above the sea floor. The strings have a total length of roughly 700 m and are spaced 95 m apart horizontally on average. The instrumented volume of one ARCA building block can be approximated by a cylinder of 0.61 km height and 0.50 km radius and therefore a volume of 0.48 km^3. With roughly 1 km^3, the total instrumented volume of ARCA is comparable to that of IceCube.

3.2 Oscillation Research with Cosmics in the Abyss (ORCA)

ORCA has the main goal of determining the neutrino mass hierarchy by measuring atmospheric neutrinos undergoing neutrino oscillations on their way through Earth. Matter effects may alter the outcome of neutrino oscillations depending on the neutrino energy and its specific way through Earth, i.e. the neutrino angle of incidence with respect to the detector. Resonant matter effects revealing the neutrino mass hierarchy happen in the range of 1-20 GeV (see also Sections 2.2.2 and 4.1). To be able to detect and reconstruct neutrino interactions of a few GeV, the sole building block used for ORCA has to be built much denser than an ARCA building block. The average horizontal spacing between the ORCA strings will be about 20 m with a total string length of 200 m. The DOMs on a string will have a distance of 9 m leading to a total instrumented volume around

$3.6 \cdot 10^6\,\mathrm{m}^3$ or 3.6 Mton water. The detector will be installed at the KM3NeT-France site at a depth of 2450 m, about 40 km offshore from Toulon, France (Figure 3.3, right).

3.3 Background sources

It has already been pointed out in Section 2.1 that atmospheric neutrinos form a major background for ARCA but are, on the other hand, the target neutrinos for ORCA.

A transient background for both experiments is given by occasional bursts of bioluminescence varying in intensity and duration. The probability of a burst depends on the site and the sea current. Short bursts can be filtered in real-time. The total inefficiency of the detectors caused by bioluminescence is expected to be negligible [7].

In the following, the further background sources common to ARCA and ORCA, namely ^{40}K decays and atmospheric muons, will be described together with filters that are defined to reduce the background resulting from ^{40}K while keeping as many relevant signal events as possible.

3.3.1 ^{40}K background and filtering

The beta decay of ^{40}K present in the deep sea forms a permanent source of photon hits in the PMTs. The electron emitted in the beta decay is faster than the speed of light in water and therefore emits Cherenkov light. The rate of single photon hits resulting from this, plus the PMT dark count rate, is 6-8 kHz per PMT. This rate is reduced by the definition of filters. The level-one filter (L1) corresponds to two or more photon hits on a DOM in different PMTs coincident within typically[9] 20 ns. The resulting L1 trigger rate is then just about 1000 Hz per optical module [7].

3.3.2 Atmospheric muons

Atmospheric muons are created in cosmic-ray air showers in the atmosphere. Many muons are created in a single high-energy air shower and thus they mostly arrive at the detector as bundles of more than one muon. As they lose energy during their travel and eventually are stopped and/or decay, less muons arrive at the detector the greater the depth of the detector. Thus, atmospheric muons typically arrive at the detector from the upper hemisphere, with an estimated trigger rate of roughly 50 Hz for ARCA. See [68] for a comprehensive description of features of the atmospheric muon flux relevant for KM3NeT including depth-dependence and bundle multiplicity.

As an example, the rate of atmospheric muons reaching the ARCA detector as a function of energy and zenith angle is shown in Figure 3.4 compared with the rate of muons resulting from muon-neutrino charged-current interactions in the vicinity of the detector. Both types of events produce a track in the detector (see also Section 2.4). However, the rate of atmospheric muons coming from above is up to six orders of magnitude larger than e.g. the rate induced by the IceCube signal flux. Hence, neutrino searches in the track channel typically look for upward-going tracks. Here, atmospheric muons misreconstructed as upward-going still have to be taken into account.

Furthermore, very-high-energy atmospheric muons may scratch the edge of the detector or may undergo catastrophic energy losses mimicking shower events. This can be seen in Figure 3.5 which displays a simulated event of the former case looking like a shower happening at the edge of the instrumented volume. Although such events happen very rarely, atmospheric muon bundles are a critical source of background in shower analyses, too, and may not be neglected (see Chapter 9).

---

[9] The trigger settings allow a variation of the coincidence time window.

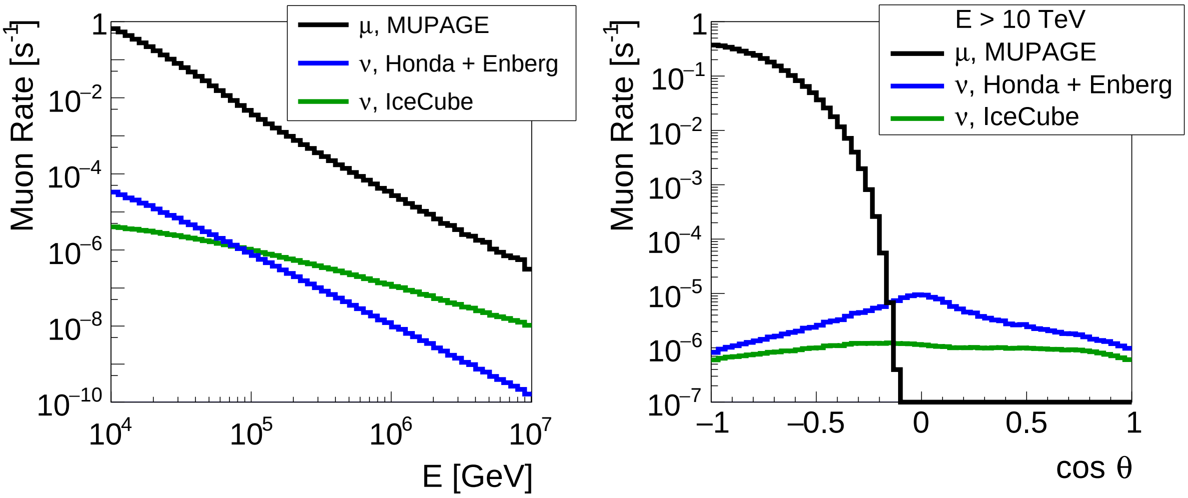

Figure 3.4: *The expected muon rate at the ARCA detector induced from atmospheric muons according to the MUPAGE parameterisation [67] (black), from charged-current interactions of atmospheric muon-neutrinos according Honda [39] and Enberg [40] (blue), and of cosmic muon-neutrinos according to the flux (Eq. (2.8)) as measured by IceCube [28] (green), see also Section 2.1. The rate is shown as a function of total muon-bundle energy or parent neutrino energy (left) and as a function of zenith angle (right) of the respective particle for corresponding energies greater than 10 TeV. The rates of neutrino events is calculated from simulations (see Chapter 6).*

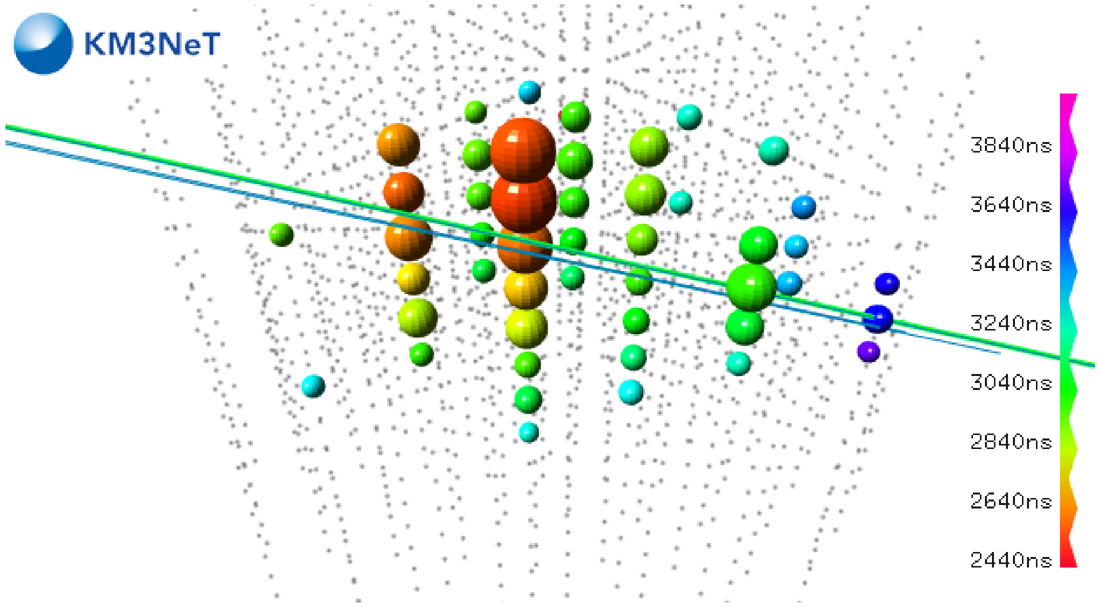

Figure 3.5: *A simulated atmospheric muon event consisting of a bundle of six muons with a total bundle energy of 1.0 PeV scratching the ARCA detector and looking like a shower event. For the interpretation of the image see also Figure 2.10 (p. 34).*

Part II

Neutrino oscillation investigations for ORCA

This part is related to the ORCA detector of the KM3NeT experiment and is based on neutrino oscillations in matter discussed in Section 2.2.2. It is divided into two chapters. Chapter 4 is about the investigation of neutrino oscillation probabilities taking into account oscillation parameter uncertainties and uncertainties in the model describing the Earth. These investigations have been initiated as part of ORCA feasibility studies. At that time the ORCA detector was just about to be planned. The output of these investigations was used as input for comprehensive and dedicated sensitivity studies regarding the potential of ORCA to measure the neutrino mass hierarchy.

It was soon realised that in order to perform dedicated ORCA sensitivity studies, oscillation probabilities need to be known to a high precision in the whole relevant parameter space. The calculation of these oscillation probabilities is computationally very demanding. Taking the kinetic parameters of energy and neutrino zenith angle and the six neutrino oscillation parameters, this parameter space has already eight dimensions. With this in mind, an algorithm was needed that is capable of producing the required oscillation probabilities for an arbitrary set of parameters in a computationally efficient manner. This includes interpolation of oscillation probabilities and also a sophisticated way of determining the points in the parameter space from which to interpolate from. These studies are presented in Chapter 5.

Chapter 4

Oscillation probabilities in the scope of uncertainties

This chapter investigates the effects of uncertainties in the neutrino oscillation parameters and in the Earth's density distribution on neutrino oscillations through the Earth. The primary goal is to make qualitative statements about how the parameter uncertainties affect the sensitivity of ORCA to the neutrino mass hierarchy.

If neutrino oscillation probabilities are insensitive to changes in a parameter, then the mass hierarchy sensitivity of ORCA will be insensitive to systematic uncertainties in that parameter. Conversely, if neutrino oscillation probabilities are sensitive to parameter changes, this may reduce the mass hierarchy sensitivity but on the other hand allow ORCA to constrain that parameter.

Ideally, these estimates would include detector and event simulations, event reconstructions, and likelihood fits which account for variations of the parameters relevant for oscillation probabilities. However, at the time the work presented in this chapter was conducted, there were no detector simulations, and therefore such an analysis was impossible. Instead, this work was part of initial feasibility studies. It gave valuable input on the development of complete sensitivity studies by highlighting important and negligible parameters, thereby reducing the number of parameters that had to be accounted for in the studies presented in the KM3NeT Letter of Intent [7].

The studies target the oscillation probabilities of atmospheric neutrinos in the energy range from 1 to 20 GeV and zenith angle range from 90° to 180°. This phase space region includes the resonant matter effects which are the crucial phenomenon allowing ORCA to be sensitive to the neutrino mass hierarchy (see also Section 2.2.2). The matter effects become significant for zenith angles greater than roughly 110° and energies between 3 and 10 GeV.

Section 4.1 presents the calculation of oscillation probabilities. This includes a description of the Earth model utilised, and illustrates how the oscillation probabilities differ between normal and inverted hierarchy. In Section 4.2 the methods are defined that quantify the impact of the different parameters on the oscillation probabilities. These methods are applied to infer the effect of oscillation parameter uncertainties in Section 4.3 and the effect of Earth model uncertainties in Section 4.4. Finally, a summary and conclusions are given in Section 4.5.

Layer name	r [km]	B [km]	ρ [g/cm^3]	θ	$\cos\theta$
Inner core	1222	1222	13	169°	-0.98
Outer core	3480	2258	11	147°	-0.84
Lower mantle	5701	2221	5.0	117°	-0.45
Transition zone 1	5771	70	4.0	115°	-0.42
Transition zone 2	5971	200	3.8	110°	-0.35
Transition zone 3	6151	180	3.5	105°	-0.26
LVZ/LID	6347	196	3.4	95.0°	-0.087
Crust 1	6356	9	2.9	93.9°	-0.069
Crust 2	6368	12	2.6	91.8°	-0.031
Ocean	6371	3	1.0	90.0°	0

Table 4.1: *The layers of the PREM together with their outer radius r, thickness B, approximate mean density ρ, and zenith angle θ with respective $\cos\theta$ of a neutrino path grazing the transition zone between the given layer and the next one (with respect to a hypothetical detector at sea level).*

4.1 Neutrino oscillations in the Earth

Oscillations of atmospheric neutrinos in the Earth lead to a characteristic pattern for the probability of the final neutrino state depending on energy and incident zenith angle. Such patterns are illustrated in Figure 4.1 for neutrinos and in Figure 4.2 for antineutrinos via so-called oscillograms. The studies presented in the following sections are based on such oscillograms.

An oscillogram as defined here shows the probability for a neutrino of certain flavour to oscillate into a given flavour after travelling through the Earth, for the energy and zenith angle range considered. It consists of 150 intervals in the energy range from 1 to 20 GeV and 300 intervals in the zenith angle range from 90° and 180°. The intervals are distributed equidistantly over the logarithm of the energy and the cosine of the zenith angle ($-1 < \cos\theta < 0$). Thus, in total 45,000 data points are generated per oscillogram. The higher number of data points with respect to the zenith angle is chosen in consideration of the discontinuous Earth density profile (see below).

Due to the finite energy and direction resolution of the ORCA detector, the high-frequency pattern at small energies and large zenith angles will wash out to a large extent. Going to higher energies and smaller zenith angles, fewer minima and maxima occur on the oscillograms due to the longer oscillation length and the shorter distance covered in the Earth, respectively.

Comparing Figure 4.1 and 4.2, it becomes clear that the patterns for neutrinos (antineutrinos) at normal mass hierarchy are essentially the same as those for antineutrinos (neutrinos) at inverted mass hierarchy. This should be kept in mind for the following sections when the effect of different parameter uncertainties are discussed. This phenomenon follows from the underlying neutrino equation of motion in matter (Section 2.2.2). Nevertheless, a net asymmetry in the combined $(\nu + \bar{\nu})$ event rates will be measurable in ORCA. This is mainly due to the fact that in the targeted energy range, the CC neutrino interaction cross sections are different by about a factor of two [7,69].

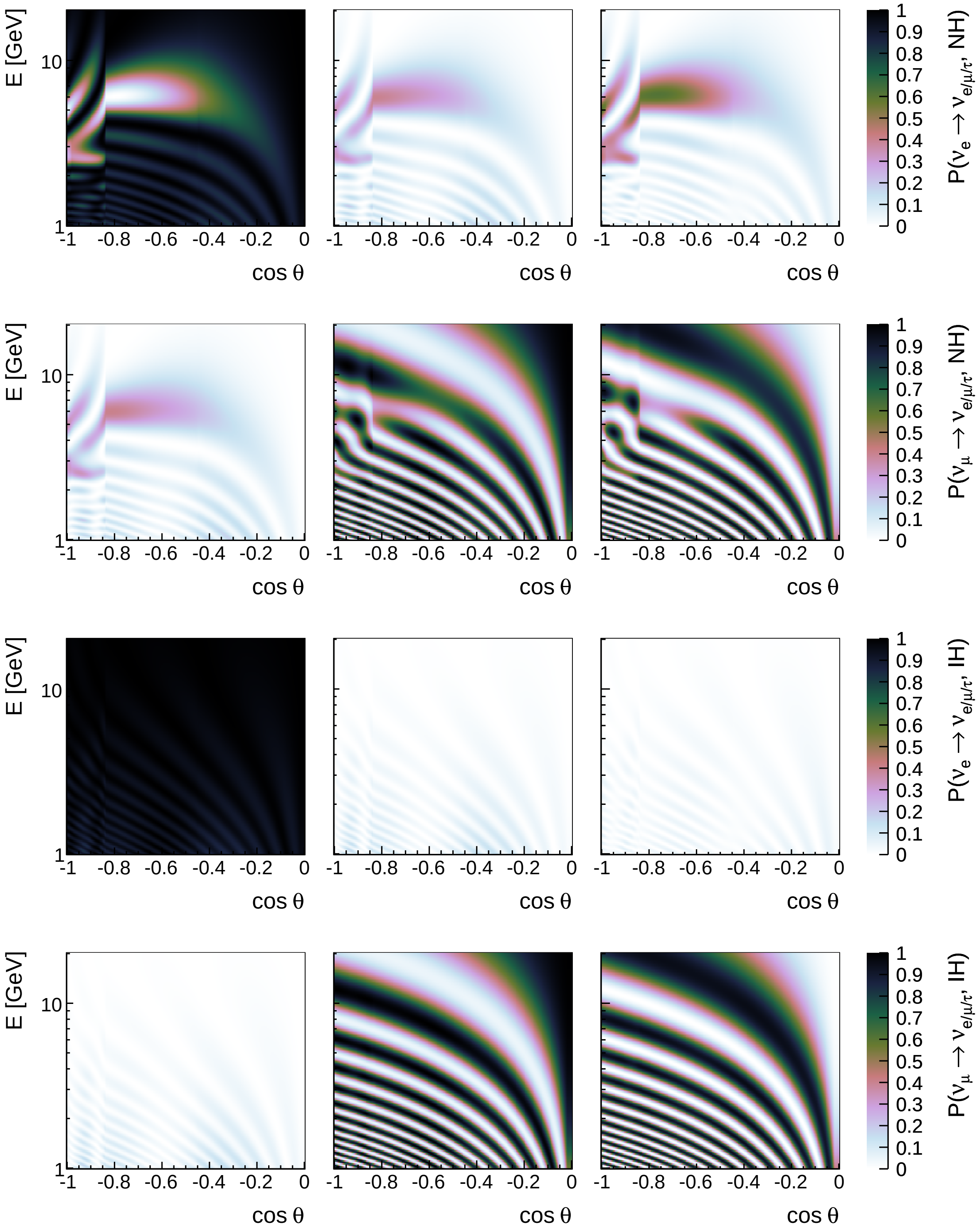

Figure 4.1: *Oscillograms showing the probability of atmospheric neutrinos to oscillate into electron (left), muon (middle) and tau neutrinos (right column) after traversing the Earth, as functions of energy and of the cosine of the zenith angle. The top two rows show the probability for assumed normal mass hierarchy (NH), the bottom two rows for inverted hierarchy (IH) for incident electron and muon neutrinos (top and bottom, respectively). Comparing the cases for normal and inverted hierarchy, the effect of resonances in the Earth are clearly visible (here for NH), especially in the energy range from 3 to 9 GeV and cosine of zenith angle below -0.45. For antineutrinos (see Figure 4.2) the resonance effects occur for IH.*

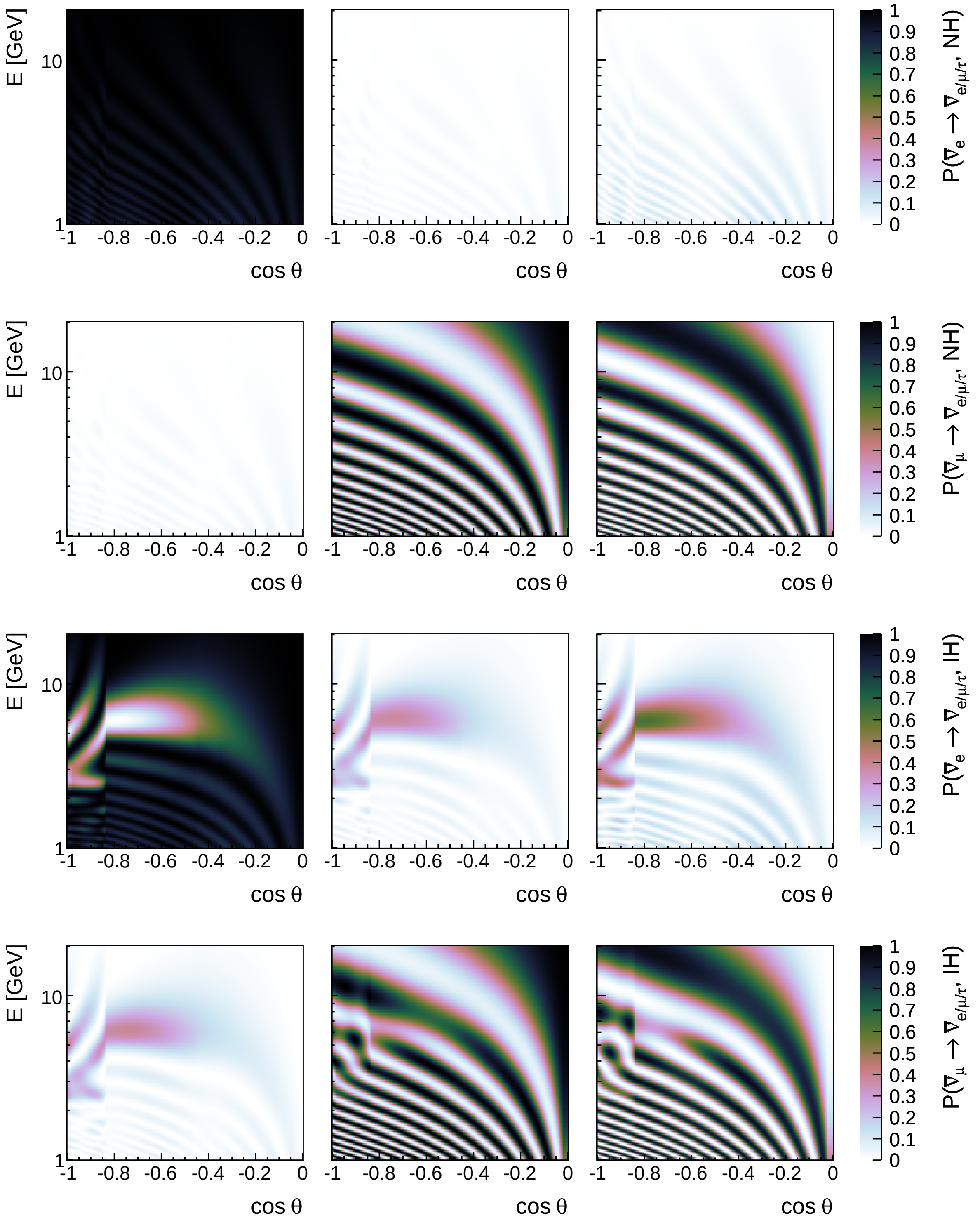

Figure 4.2: *The same as Figure 4.1 for antineutrinos instead of neutrinos. The resonance effects occur here for IH.*

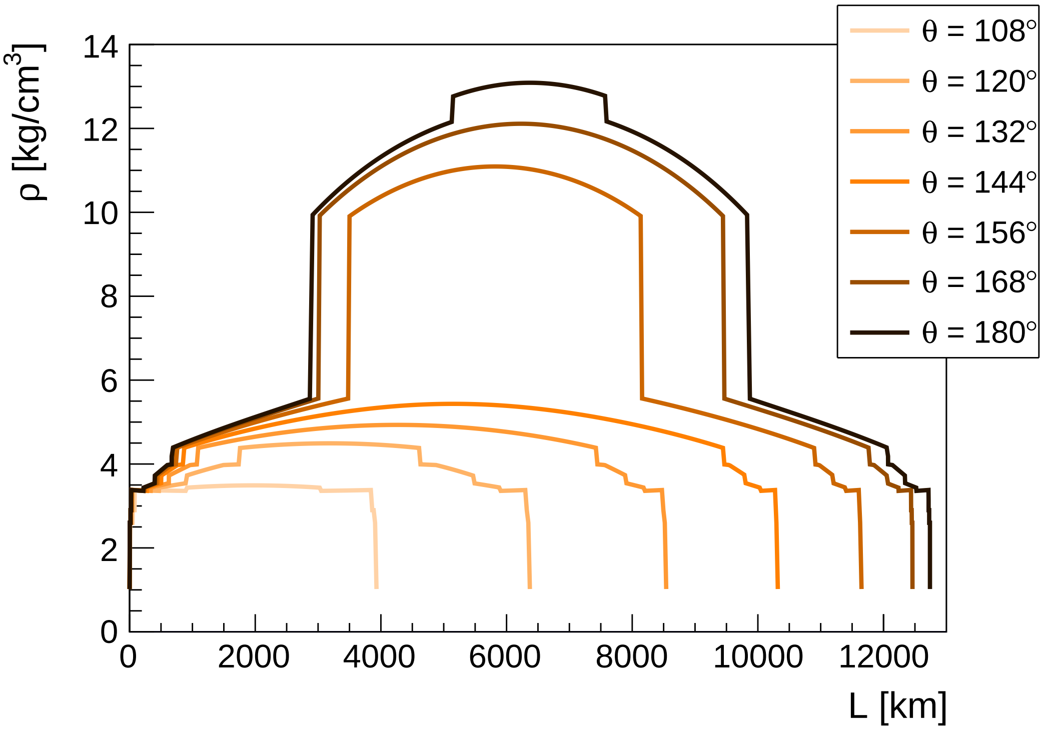

Figure 4.3: *The density profile of the Earth along a neutrino path for various zenith angles. At zenith angles bigger than 117°* ($\cos\theta <$ *-0.45) the path traverses the lower mantle which is the region where matter effects begin to matter. From angles exceeding 147° and 169°* ($\cos\theta <$ *-0.84 and* $\cos\theta <$ *-0.98), also the outer and inner core is crossed, respectively.*

The Earth model used here is the *Preliminary Reference Earth Model* (PREM) [56]. Therein, the density distribution is assumed to be spherically symmetric with a total of ten different density layers distributed over two main structures, the Earth core and the Earth mantle. Within each of the ten layers the density profile is approximated by polynomials of third degree or less. A summary of the main features is given in Table 4.1 including outer radii and mean density of single layers.

Depending on the zenith angle, the neutrino path through the Earth traverses only part of the different layers and a different density profile. Zenith angles corresponding to paths “touching” a certain layer are also given in the table. Figure 4.3 illustrates the density profile for different zenith angles.

For the matter effects on neutrino oscillations, the electron number density is essential (see Section 2.2). Having the Earth matter density, it is determined from the electron fraction Y_e in the Earth matter. For the inner and outer Earth core, expected to mainly consist of iron, the electron fraction is approximated by $Y_e = 0.466$ [70]. The mantle on the other hand consists of a variety of different rock types. Here the electron fraction is roughly given by $Y_e = 0.494$ [71].

The oscillation probabilities are calculated by solving the differential equation of motion (first equation of Eqs. (2.21)) numerically in *Python* via the *SciPy* [72] integration package *odeint*, which is a wrapper for the ODEPACK Fortran library [73]. The corresponding code has been provided by courtesy of Patrick Toale who wrote it for the PINGU experiment [74] of the IceCube collaboration.

To assess the precision of the numerical calculation, the calculated oscillation probabilities were compared by Patrick Toale with those as calculated by Soebur Razzaque (written in Fortran) [75]. The differences between both methods are smaller than 10^{-4}.

The code allows the variation of the six neutrino oscillation parameters. To adapt it to ORCA, only the depth of the detector had to be adjusted. The code has then been extended to include the possibility of varying parameters that describe the Earth. This includes changing the electron densities of single layers by a given factor, shifting the position of layer boundaries and smoothing the transition between layers.

The computation time depends strongly on the neutrino energy and zenith-angle: the number of space (or time) steps along the neutrino path evaluated for the numerical calculation is roughly 980 for a 1 GeV neutrino coming straight from below ($\theta = 180°$) whereas the number of function evaluations is around 2200. These numbers decrease with higher energy and smaller zenith angle, e.g. to 340 and 880, respectively, for a zenith angle of $\theta = 135°$ and energy $E = 10$ GeV. The generation of the data needed for the oscillograms corresponding to one incident neutrino type (e.g. one row in Figure 4.1, 45 000 data points per oscillogram) takes roughly one and a half hours on a single “Intel Xeon X5650” CPU.

The oscillograms calculated with this code are used to quantify the impact of oscillation and Earth parameters on the neutrino oscillation probabilities as shown in the next section.

4.2 Uncertainty impact measures

In order to characterise the influence of single parameters on the oscillation probabilities, several measures are defined in the following based on the oscillograms introduced in the previous section. In total variations of 34 parameters are considered. These are the six oscillation parameters introduced in Section 2.2, and 28 parameters describing the Earth: the density of each of the ten PREM layers, the position of the nine boundaries between two adjacent layers, and the smoothness of the nine density transitions between two layers. The considered ranges for the oscillation parameters are the respective $3\,\sigma$ uncertainty ranges (see Section 4.3). For the Earth parameters, ranges are chosen based on uncertainty estimates (see Section 4.4).

Given ν_e, ν_μ and ν_e, ν_μ, ν_τ as the initial and final neutrino and antineutrino states, respectively, and the two possible mass hierarchies, a total of 24 different channels have to be considered to measure the influence of a single parameter. In order to simplify the following descriptions, the set of these 24 types of channels shall be called Q, an element of this set q. Then, the set can be written as $Q = \{\overset{(-)}{\nu}_x \rightarrow \overset{(-)}{\nu}_y, H\}$ with $x \in \{e, \mu\}$, $y \in \{e, \mu, \tau\}$ and $H \in \{\text{NH}, \text{IH}\}$, where NH stands for normal hierarchy and IH for inverted hierarchy. The oscillation probabilities for given x, y, H and particle or antiparticle (ν or $\bar{\nu}$) are then written as

$$P_q(p; E, \theta) \equiv P(\overset{(-)}{\nu}_x \rightarrow \overset{(-)}{\nu}_y, H; p; E, \theta) \tag{4.1}$$

with E the neutrino energy, θ the zenith angle, and p the respective parameter under consideration, i.e. one of the 34 parameters mentioned above. The dependence on the other parameters is omitted here.

In order to derive the final measures, additional definitions are made. Denoting the bounds of the considered range of a parameter p by p_- and p_+, the *local effective difference* (LED)

$$\mathsf{LED}_q(E,\theta) = \int_{p_-}^{p_+} \frac{\partial P_q(p;E,\theta)}{\partial p}\,\mathrm{d}p = P_q(p_+;E,\theta) - P_q(p_-;E,\theta) \tag{4.2}$$

gives the effective change of the oscillation probability within the considered parameter range. The LED can take both negative and positive values. However, it does not take into account oscillatory behaviour of the integrand. To take that into account, the *local absolute difference* (LAD) is defined:

$$\mathsf{LAD}_q(E,\theta) = \int_{p_-}^{p_+} \left| \frac{\partial P_q(p;E,\theta)}{\partial p} \right| \mathrm{d}p. \tag{4.3}$$

It holds $\mathsf{LAD}_q(E,\theta) \geq |\mathsf{LED}_q(E,\theta)|$, i.e. a large LED indicates a large impact of that parameter, a small LAD a small impact in the specified oscillation channel at the given energy and zenith angle[10].

To account for the total change of a given type of oscillogram over the whole $E-\cos\theta-$plane considered, the *global effective difference* (GED) is defined as the normalised sum of the LED over all data points in an oscillogram:

$$\mathsf{GED}_q = \frac{1}{N_E N_\theta} \sum_{i=1}^{N_E} \sum_{j=1}^{N_\theta} \mathsf{LED}_q(E_i,\theta_i), \tag{4.4}$$

where, $N_E = 150$ and $N_\theta = 300$ are the number of data points along the respective kinetic variable and E_i and θ_i stand for the energy and zenith angle related to the i-th data point. Here, a large value indicates a large impact of the parameter for the considered type of oscillation. Nevertheless, positive and negative values of the LED may cancel out and produce a very small GED even though differences in some regions of the oscillogram might be large.

Therefore, similarly to the LAD, the *global absolute difference* (GAD) is defined taking into account such differences including also oscillatory behaviour. It is given by the normalised sum of the LAD over the $E-\cos\theta-$plane:

$$\mathsf{GAD}_q = \frac{1}{N_E N_\theta} \sum_{i=1}^{N_E} \sum_{j=1}^{N_\theta} \mathsf{LAD}_q(E_i,\theta_i). \tag{4.5}$$

A small value of the GAD means a small impact of the considered parameter for the type of oscillation q. Similarly to the local differences, also for global differences $\mathsf{GAD}_q \geq |\mathsf{GED}_q|$.

With the above definitions, six measures are defined that are used for the descriptions in the following sections:

- The maximum of the LED over energy, zenith angle and oscillation channel, *maximum local effective difference* (MLED):

$$\mathsf{MLED} = \max_{\substack{q\in Q,\\ E\in[E_{\mathsf{min}},E_{\mathsf{max}}],\\ \theta\in[\theta_{\mathsf{min}},\theta_{\mathsf{max}}]}} \left\{ \left| \mathsf{LED}_q(E,\theta) \right| \right\} \tag{4.6}$$

---

[10] To numerically calculate the LAD, a number of 31 data points were produced along a given parameter dimension.

with $E_{\text{min}} = 1$ GeV, $E_{\text{max}} = 20$ GeV and $\theta_{\text{min}} = 90°$, $\theta_{\text{max}} = 180°$. A large MLED indicates a high impact of the corresponding parameter. However, the impacted energy and zenith-angle region might be small. Therefore, it still needs to be compared with global measures (below) to make definite statements.

- The maximum of the LAD over energy, zenith angle and oscillation channel, *maximum local absolute difference* (MLAD):

  $$\text{MLAD} = \max_{\substack{q\in Q,\\ E\in[E_{\text{min}},E_{\text{max}}],\\ \theta\in[\theta_{\text{min}},\theta_{\text{max}}]}} \left\{ \text{LAD}_q(E,\theta) \right\} \tag{4.7}$$

  A small value of the MLAD unambiguously implies that the corresponding parameter has no large influence. If it has a large value, a comparison with global measures is necessary.

- The maximum of the GED over oscillation channels, *maximum global effective difference* (MGED):

  $$\text{MGED} = \max_{q\in Q} \left\{ \left| \text{GED}_q \right| \right\} \tag{4.8}$$

  A large value of the MGED signals a large impact. If its value is small, a comparison with other measures is needed as it may result from large LEDs cancelling out each other.

- The maximum of the GAD over oscillation channels, *maximum global absolute difference* (MGAD):

  $$\text{MGAD} = \max_{q\in Q} \left\{ \text{GAD}_q \right\} \tag{4.9}$$

  As with the MLAD, a small value of the MGAD signals a small influence. The MGAD can be large even tough the MGED is small. In such a case a more thorough investigation is needed.

- The GED averaged over oscillation channel, *average global effective difference* (AGED):

  $$\text{AGED} = \frac{1}{24} \sum_{q\in Q} \left| \text{GED}_q \right| \tag{4.10}$$

- The GAD averaged over oscillation channel, *average global absolute difference* (AGAD):

  $$\text{AGAD} = \frac{1}{24} \sum_{q\in Q} \text{GAD}_q \tag{4.11}$$

  The AGED and AGAD measure the total impact of a parameter. They therefore also help to compare the general impact of different parameters.

These six measures will be used in the following sections to draw conclusions about the importance of the considered parameters. Note that by definition these measures are greater than or equal to zero and the measures based on the LED can have a maximum value of unity.

Oscillation Parameter	3σ range	
	Normal Hierarchy	Inverted Hierarchy
$\sin^2\theta_{12}/10^{-1}$	$2.59 - 3.59$	$2.59 - 3.59$
$\sin^2\theta_{13}/10^{-2}$	$1.69 - 3.13$	$1.71 - 3.15$
$\sin^2\theta_{23}/10^{-1}$	$3.31 - 6.37$	$3.35 - 6.63$
$\Delta m^2_{21}/10^{-5}\,\mathrm{eV}^2$	$6.99 - 8.18$	$6.99 - 8.18$
$\Delta m^2_{31}/10^{-3}\,\mathrm{eV}^2$	$2.23 - 2.66$	$2.13 - 2.57$
δ_{cp}/π	$0 - 2$	$0 - 2$

Table 4.2: *The 3σ ranges of the oscillation parameters according to Fogli et al. [50] which in general depend on the assumed neutrino mass hierarchy. For the CP phase δ_{cp} no value is disfavoured at the 3σ level.*

4.3 Oscillation parameter uncertainties

For the investigation of the effect of the uncertainties in oscillation parameters on the oscillation probabilities, the 3σ ranges as determined by Fogli et al. [50] have been used. They are shown in Table 4.2 and were up-to-date at the time this study was performed[11]. Each oscillation parameter has been investigated separately. As only two of the three mass squared differences are independent, Δm^2_{21} and Δm^2_{31} are used for the description.

Tables 4.3 and 4.4 summarise the influences of the different oscillation parameters by showing the measures based on the LED and LAD, respectively, as defined in the previous section. In the following, the impact of each parameter will be described in detail. Keep in mind that the most relevant kinetic region for resonant matter effects and thus for the mass hierarchy determination is given by 3 GeV $< E <$ 9 GeV and $\cos\theta <$ -0.45 (see also Figure 4.1, p. 47). This range will in the following be referred to as *resonance region*. Also recall that resonant matter effects happen for neutrinos given normal mass hierarchy (NH) and antineutrinos given inverted mass hierarchy (IH).

Impact of $\sin^2\theta_{12}$

The MLED due to the θ_{12} uncertainty is the same as the respective MLAD and relatively small, MLED = MLAD = 13%. Both are reached at energy $E = 1.02$ GeV and cosine of zenith angle $\cos\theta =$ -0.92 for $\nu_\mu \rightarrow \nu_\mu$, NH.

The local differences for this type of oscillation are shown in Figure 4.4 in the $E - \cos\theta -$plane. It can be seen that the strongest impact is at low energies where the oscillations will be totally washed out. This is also the case for the other oscillation channels. Thus, also the differences will be washed out and no notable effect will be detectable in this region for ORCA. In general for θ_{12} it holds |LED| = LAD, thus no oscillatory behaviour of the oscillation probabilities as a function of θ_{12} in its 3σ range.

The MGED and the AGED are around 0.1% and 0.05%, respectively, and the local differences in the *resonance region* around 3% at maximum. Therefore, implications on determining the mass

---

[11] See the end of this Section for a brief discussion of the effects of updated constraints on oscillation parameters on the work presented here.

	E [GeV]	$\cos\theta$	MLED	MGED	AGED
$\sin^2\theta_{12}$	1.02	-0.92	$P(\nu_\mu \to \nu_\mu, \text{NH})$ 12.7%	$P(\bar{\nu}_e \to \bar{\nu}_\tau, \text{IH})$ 0.109%	0.0545%
$\sin^2\theta_{13}$	3.8	-0.94	$P(\nu_e \to \nu_e, \text{NH})$ 53.8%	$P(\bar{\nu}_e \to \bar{\nu}_\tau, \text{IH})$ 3.08%	1.42%
$\sin^2\theta_{23}$	6.0	-0.82	$P(\bar{\nu}_\mu \to \bar{\nu}_\mu, \text{IH})$ 34.0%	$P(\bar{\nu}_\mu \to \bar{\nu}_e, \text{IH})$ 5.06%	2.14%
Δm^2_{21}	1.00	-0.99	$P(\bar{\nu}_\mu \to \bar{\nu}_\mu, \text{NH})$ 13.2%	$P(\nu_\mu \to \nu_e, \text{NH})$ 0.217%	0.0996%
Δm^2_{31}	3.3	-0.85	$P(\nu_\mu \to \nu_\mu, \text{NH})$ 95.3%	$P(\bar{\nu}_\mu \to \bar{\nu}_\mu, \text{NH})$ 0.457%	0.241%
δ_{cp}	1.90	-0.81	0%	0%	0%

Table 4.3: *Measures based on the local effective differences (LED) as defined in Section 4.2 for each oscillation parameter. The second and third column give the energy and cosine of zenith angle where the maximum local effective difference (MLED) is reached. The remaining three columns give, from left to right, the MLED, the maximum global effective difference (MGED) and the average global effective difference (AGED). For the MLED and MGED, also the channel is given for which the maximum is reached. For comparison see Table 4.4.*

	E [GeV]	$\cos\theta$	MLAD	MGAD	AGAD
$\sin^2\theta_{12}$	1.02	-0.92	$P(\nu_\mu \to \nu_\mu, \text{NH})$ 12.7%	$P(\nu_\mu \to \nu_\tau, \text{IH})$ 1.20%	0.477%
$\sin^2\theta_{13}$	3.8	-0.94	$P(\nu_e \to \nu_e, \text{NH})$ 53.8%	$P(\nu_e \to \nu_e, \text{NH})$ 7.01%	2.65%
$\sin^2\theta_{23}$	6.0	-0.82	$P(\bar{\nu}_\mu \to \bar{\nu}_\mu, \text{IH})$ 34.0%	$P(\bar{\nu}_\mu \to \bar{\nu}_\mu, \text{IH})$ 12.4%	4.81%
Δm^2_{21}	1.00	-0.99	$P(\bar{\nu}_\mu \to \bar{\nu}_\mu, \text{NH})$ 13.2%	$P(\bar{\nu}_\mu \to \bar{\nu}_\mu, \text{NH})$ 1.35%	0.517%
Δm^2_{31}	1.00	-1.00	$P(\nu_\mu \to \nu_\mu, \text{IH})$ 389%	$P(\nu_\mu \to \nu_\tau, \text{IH})$ 64.3%	24.1%
δ_{cp}	1.04	-0.84	$P(\nu_\mu \to \nu_\mu, \text{NH})$ 37.4%	$P(\nu_\mu \to \nu_e, \text{NH})$ 5.58%	3.10%

Table 4.4: *Measures based on the local absolute differences (LAD) as defined in Section 4.2 for each oscillation parameter. The second and third column give the energy and cosine of zenith angle where the maximum local absolute difference (MLAD) is reached. The remaining three columns give, from left to right, the MLAD, the maximum global absolute difference (MGAD) and the average global absolute difference (AGAD). For the MLAD and MGAD, also the channel is given for which the maximum is reached. For comparison see Table 4.3.*

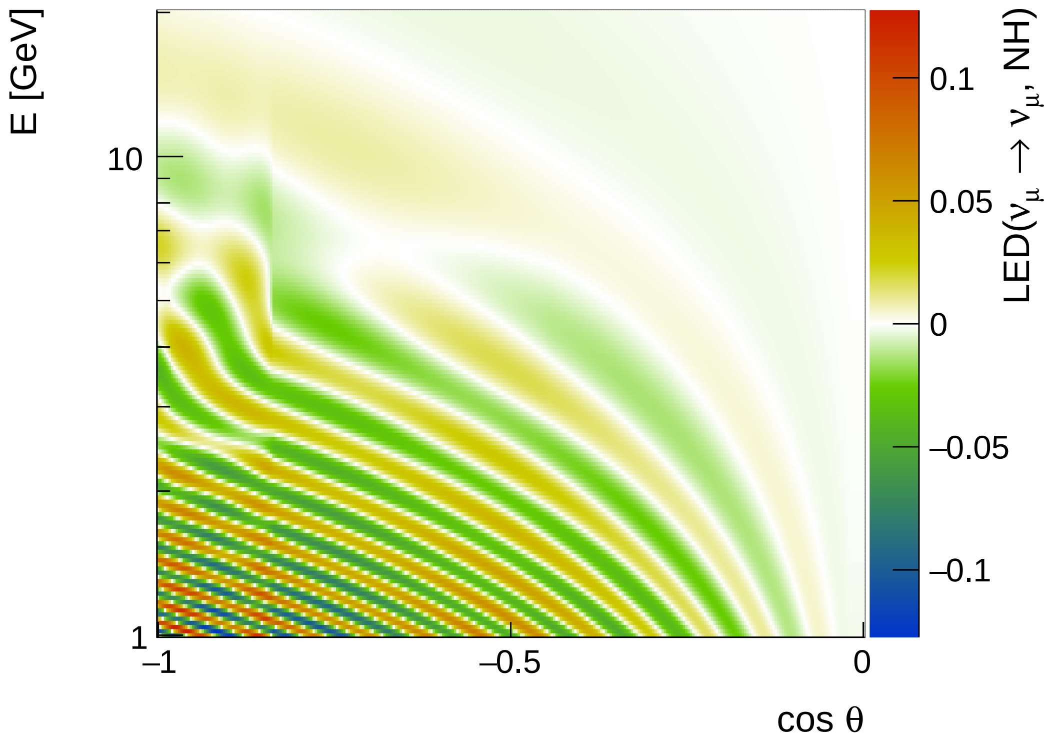

Figure 4.4: *The local effective differences originating from a change of θ_{12} as defined in Eq. (4.2) over the $E-\cos\theta-$plane in the case of $\nu_\mu \to \nu_\mu$, NH. The largest differences appear at low energies. In the resonance region, the changes are only around a few percent.*

hierarchy for ORCA are negligible. In turn, ORCA will have virtually no sensitivity to θ_{12}.

The main reason why the effects are so small is that θ_{12} plays only a minor role in the high-frequency oscillations due to large mass squared differences. However, these are the important ones for the neutrino mass hierarchy determination with ORCA. In fact, in the approximation $\Delta m^2_{31} = \Delta m^2_{32}$ the high-frequency oscillations are completely independent of θ_{12}. On the other hand, θ_{12} has a major influence on the oscillations governed by the small mass squared difference. This also explains why the impact decreases with higher energy as the low-frequency oscillations become more and more negligible with higher energy.

Impact of $\sin^2\theta_{13}$

In spite of the mixing angle θ_{13} being rather small, a change within the 3σ ranges affects the oscillation probabilities significantly. This is because of the resonant amplification of the 3-1-mixing due to the matter effects in Earth. Thus, a change in θ_{13} leads to a change of the characteristic pattern in the oscillograms emerging from the matter effects in the cases the resonances are passed.

The MLAD is the same as the MLED reaching 54% in the *resonance region* for $P(\nu_e \to \nu_e, \text{NH})$. The LEDs for this case are shown in Figure 4.5. It becomes clear that the largest deviations arise for neutrinos travelling through the Earth's core. For such neutrino paths, resonance effects happen both in the mantle and core and over a wide energy range from roughly 2 to 10 GeV. Also for paths going only through the Earth's mantle ($\cos\theta >$ -0.84), the differences are still significant with values up to 20% over a large area around $E = 6$ GeV. Therefore, an incorporation of the θ_{13} uncertainty is

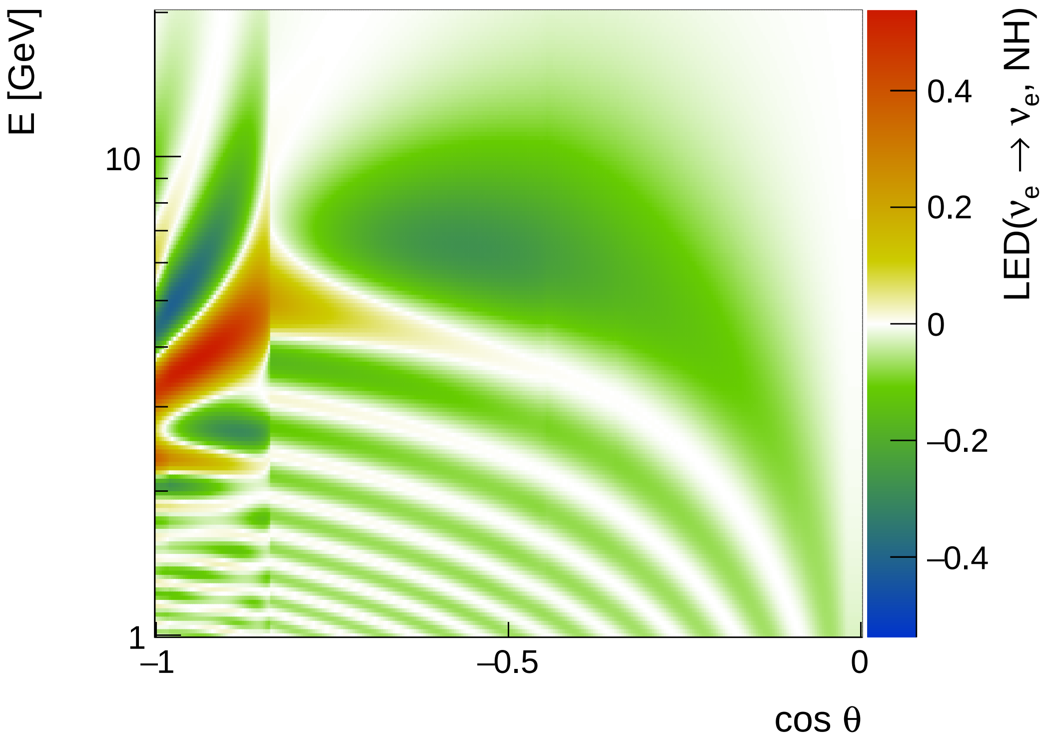

Figure 4.5: *The local effective differences originating from a change of θ_{13} as defined in Eq. (4.2) over the $E-\cos\theta-$plane in the case of $\nu_e \to \nu_e$, NH. The largest differences occur for neutrino paths going through the Earth's core, where resonance effects are most prominent.*

expected to reduce the sensitivity to the mass hierarchy.

The MGED is rather small with a value of 3.1% (reached for $\bar{\nu}_e \to \bar{\nu}_\tau$, IH), i.e. the positive and negative changes cancel out to a certain degree. The AGED has a value of only 1.4%, the AGAD of 2.7%. All this indicates that the total number of neutrinos of a given type at the position of the ORCA detector is not much influenced by a change of θ_{13}. Thus, the possible sensitivity of ORCA to θ_{13} will depend on the energy and direction resolution of the detector.

Impact of $\sin^2\theta_{23}$

With a change of θ_{23} within its 3σ range, the shape of the characteristic oscillatory pattern is only hardly modified but the amplitudes change to a large extent especially in the *resonance region*. Again the MLED is equal to the MLAD and amounts to 34% and is realised for $P(\bar{\nu}_\mu \to \bar{\nu}_\mu$, IH). The LEDs for this case are shown in Figure 4.6. It can be seen that all are of the same sign.

Related to this, it is also worth noting that $P(\bar{\nu}_e \to \bar{\nu}_e$, IH) is independent of θ_{23}, i.e. the differences (LAD) when changing θ_{23} are zero. Additionally, the LED in the other two cases, $P(\bar{\nu}_e \to \bar{\nu}_\mu$, IH) and $P(\bar{\nu}_e \to \bar{\nu}_\tau$, IH), are over most part of the $E-\cos\theta-$plane of the same sign (just like in Figure 4.6), however positive and negative, respectively. Furthermore, the LED in the case $P(\bar{\nu}_\mu \to \bar{\nu}_\tau$, IH) are very small and the changes in the channels ($\bar{\nu}_{e,\mu} \to \bar{\nu}_\mu$, IH) cancel out mostly. Thus, in total for IH, a change of θ_{23} keeps the number of muon antineutrinos constant. However, it leads to an effective increase of electron antineutrinos and a decrease of tau antineutrinos. The same argument holds for neutrinos and normal mass hierarchy. Therefore, an experiment like ORCA can increase its

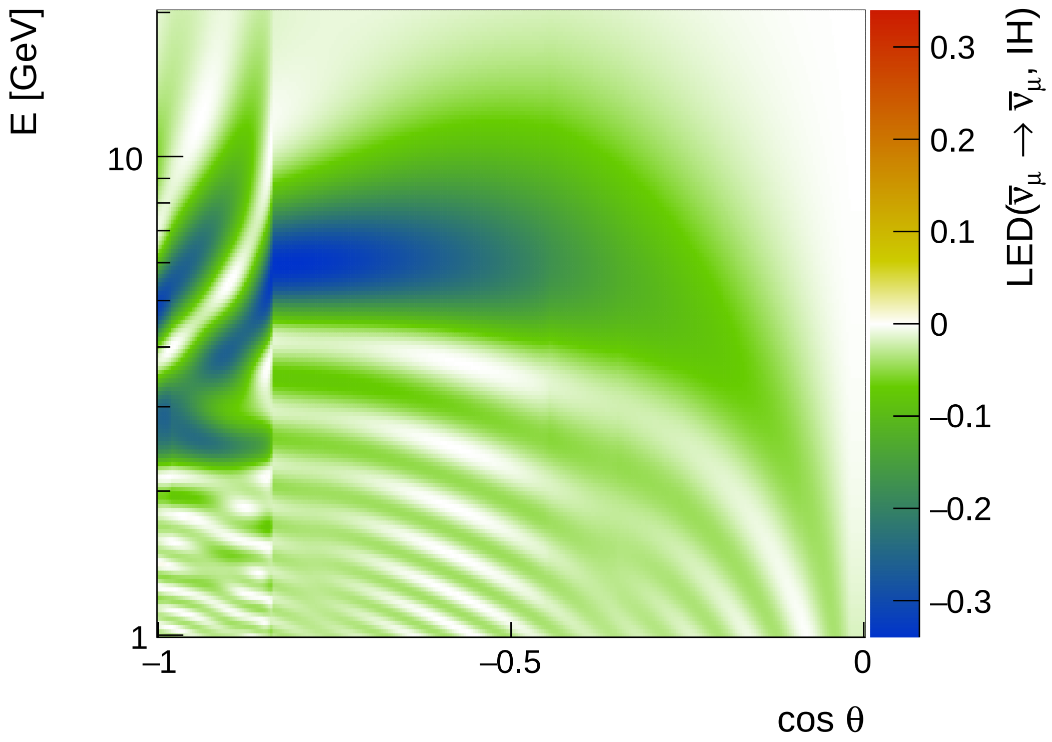

Figure 4.6: *The local effective differences originating from a change of θ_{23} as defined in Eq. (4.2) over the $E-\cos\theta-$plane in the case of $\bar{\nu}_\mu \rightarrow \bar{\nu}_\mu$, IH. Large differences even above 30% occur and all differences have the same sign over the whole $E-\cos\theta-$plane.*

sensitivity to θ_{23} by being able to efficiently distinguish electron from tau (anti)neutrinos.

In the cases where the MSW-resonance conditions are not realised (neutrinos at IH and antineutrinos at NH), the local differences are negligible, reaching values of up to 2% above 2 GeV and up to around 7% below 2 GeV. The effects below 2 GeV won't be a measurable as the differences will wash out given the finite energy resolution of the detector.

Impact of Δm^2_{21}

The small mass squared difference Δm^2_{21} mainly affects the long oscillation lengths which hardly play any role for the neutrino oscillations relevant for ORCA. Thus, a change in Δm^2_{21} has only little effect which mainly arises due to the fact that, leaving Δm^2_{31} constant, a change in Δm^2_{21} also leads to a change in Δm^2_{32}. Due to Δm^2_{32} being large compared to the changes, the effects are negligible in the kinetic region considered here.

At low energies and high zenith angles where many oscillations happen along the path, the differences are maximal: MLED = 13% at $E = 1.0$ GeV and $\cos\theta = -1.0$ for $\bar{\nu}_\mu \rightarrow \bar{\nu}_\mu$, NH. This is a channel without resonance and the LEDs for this case are shown in Figure 4.7. The larger differences in the low energy/large zenith-angle region will wash out. Above 3 GeV, the LAD is below 3%. Thus, the effect of the Δm^2_{21} uncertainty on the determination of the neutrino mass hierarchy is negligible for ORCA.

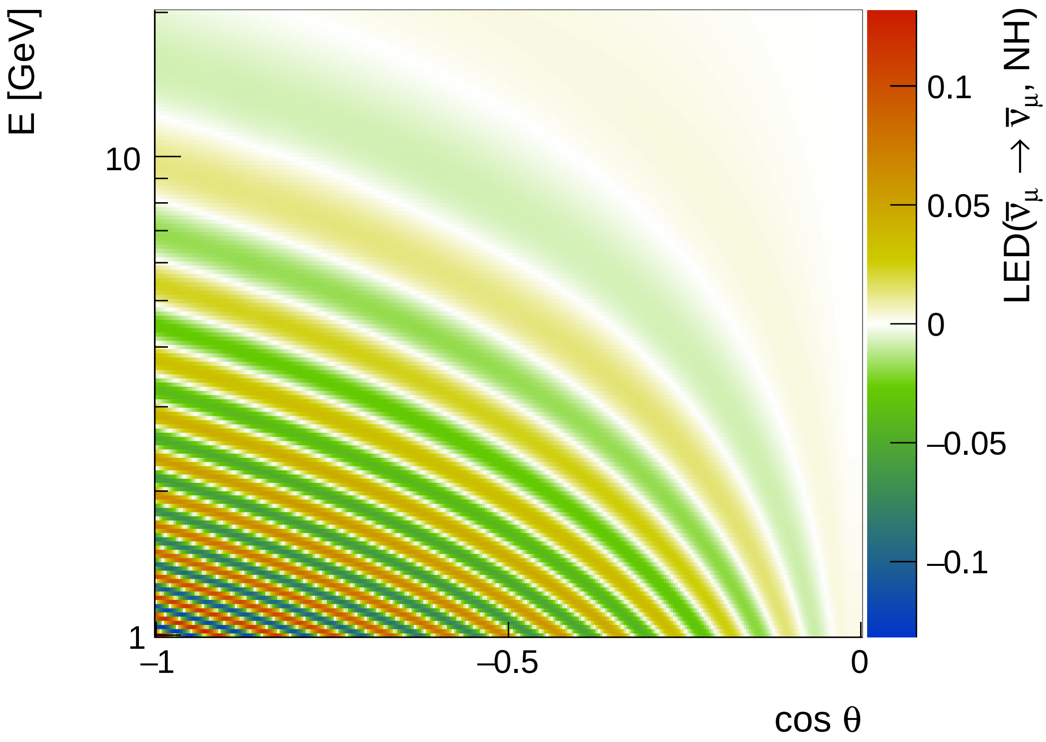

Figure 4.7: *The local effective differences originating from a change of Δm^2_{21} as defined in Eq. (4.2) over the $E-\cos\theta-$plane in the case of $\bar{\nu}_\mu \to \bar{\nu}_\mu$, NH. The largest differences occur at small energies and large zenith angles in a fast changing pattern which will wash out due to the finite resolution of the detector.*

Impact of Δm^2_{31}

The large mass squared difference Δm^2_{31} is responsible for the high-frequency oscillations. Therefore, a variation has a large influence on the oscillation probabilities relevant for ORCA. The local absolute differences are shown in Figure 4.8, the effective differences in Figure 4.9, both in the case of $\nu_\mu \to \nu_\mu$, NH. The MLAD reached at the border at $E = 1.0$ GeV and $\cos\theta = -1.0$ has a value of 389%. The MLED is 95% reached at $E = 3.3$ GeV and $\cos\theta = -0.85$.

These large differences for low energies are most easily explained when looking at the two-flavour vacuum-oscillation scheme with the approximation $\Delta m^2_{21} \to 0$. Here, the oscillation probabilities depend on $\Delta m^2_{31}/E$ and therefore an increase of the large mass squared difference by a given factor leads to the same result as decreasing the energy by the same factor. Hence, it becomes clear by looking at standard oscillograms (Figure 4.1, p. 47), why at low energies the absolute differences become much larger than 100%. The relation between energy and the large mass squared difference still holds qualitatively at higher energies. Thus a difference in Δm^2_{31} is equivalent to a systematic uncertainty in the energy resolution. An example where this can be seen is shown in Figure 4.10. This figure also shows that due to the aforementioned reasons there is also no discrimination power at low energies and large zenith angles with respect to Δm^2_{31}.

In the *resonance region*, the differences have values around 80% and are very high. They thus could interfere with the sensitivity to the neutrino mass hierarchy. On the other hand, by looking at events with energies above 10 GeV, it should be possible to get a handle on the large mass squared

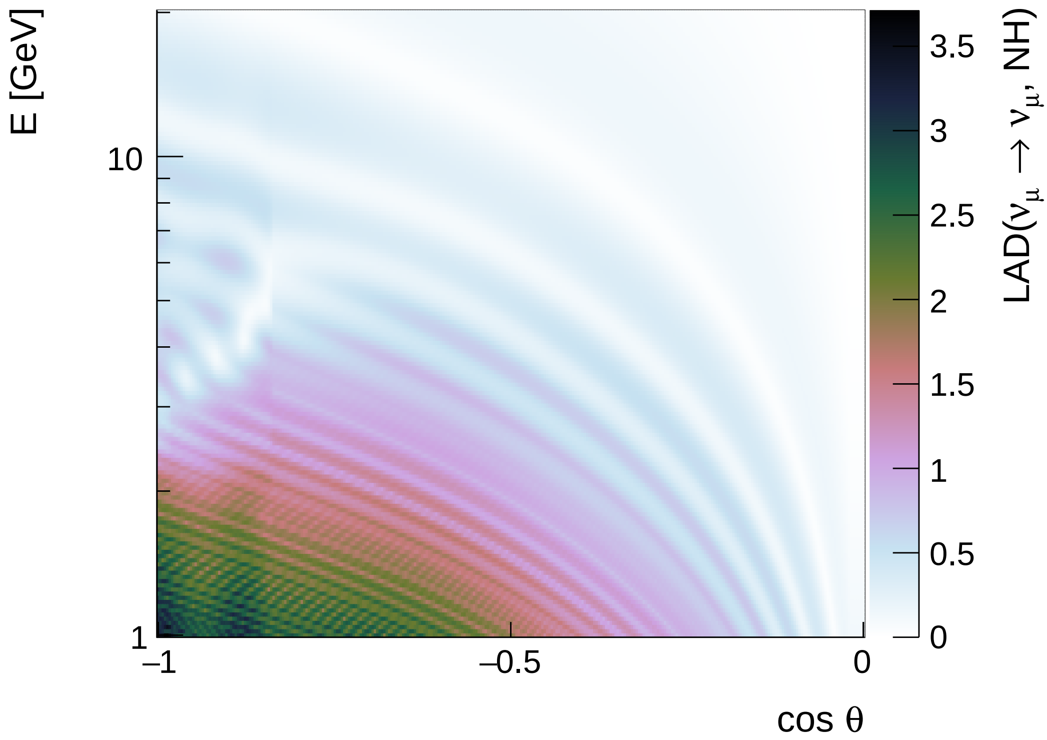

Figure 4.8: *The local absolute differences originating from a change of Δm^2_{31} as defined in Eq. (4.3) over the $E-\cos\theta-$plane in the case of $\nu_\mu \to \nu_\mu$, NH. The differences accumulate up to about 390% at small energies and large zenith angles. For comparison see Figure 4.9.*

difference and reduce the uncertainty.

Impact of δ_{cp}

The CP phase δ_{cp} is completely unconstrained at the $3\,\sigma$ level so that the $3\,\sigma$ range is defined here from 0 to 2π. Thus, the oscillation probabilities being a cyclic function of δ_{cp}, the LED are zero everywhere and the absolute differences have to be considered. They are shown in Figure 4.11 for $P(\nu_\mu \to \nu_\mu, \text{NH})$. As with most other oscillation parameters, the largest differences appear at lower energies (Table 4.4). There are many regions in the $E-\cos\theta-$plane where the absolute difference is rather large.

To get a feeling of the actual change of the oscillation probabilities, consider that in general the oscillation probability as a function of the CP phase goes through a single minimum and maximum. The difference between these extrema is then the half of the absolute difference which is below 20% at the maximum. In the *resonance region*, the difference between maximum and minimum is below 7%. The MGAD is 5.6%, the AGAD 3.1%. Taking into account the cyclic behaviour, it follows that the impact of the CP phase is rather small and ORCA will not have a high sensitivity to it. On the other hand the effect on the sensitivity to the mass hierarchy has to be handled with care.

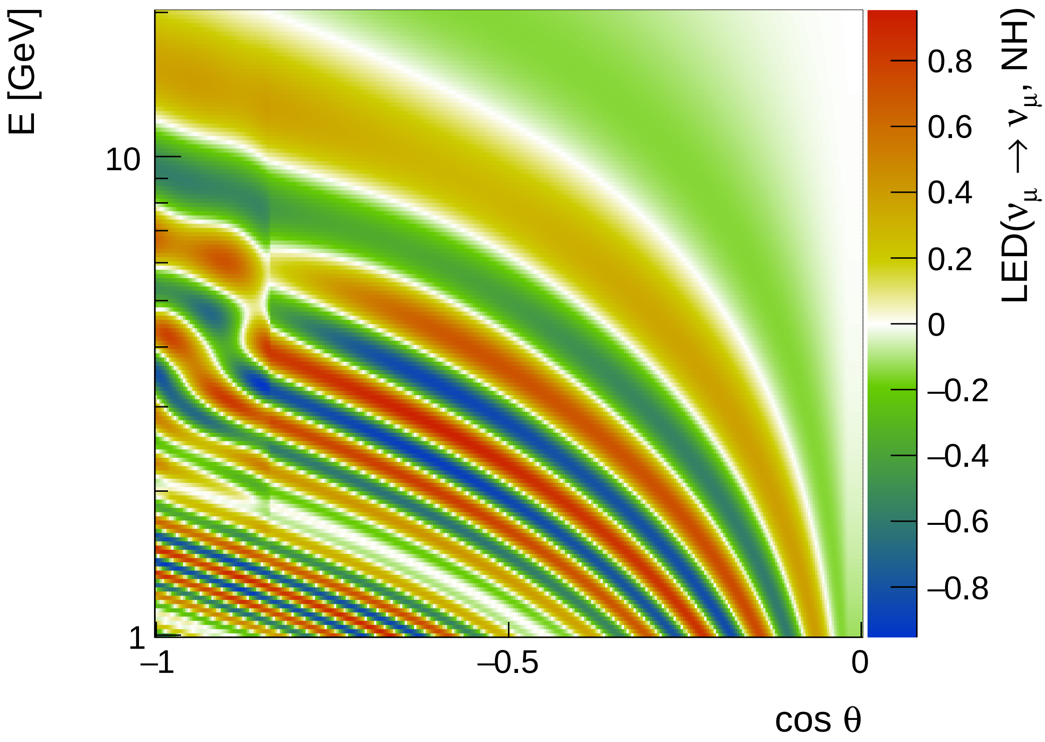

Figure 4.9: *The local effective differences originating from a change of Δm^2_{31} as defined in Eq. (4.2) over the $E - \cos\theta -$plane in the case of $\nu_\mu \rightarrow \nu_\mu$, NH. Large differences occur over the whole $E - \cos\theta -$plane. For comparison see Figure 4.8.*

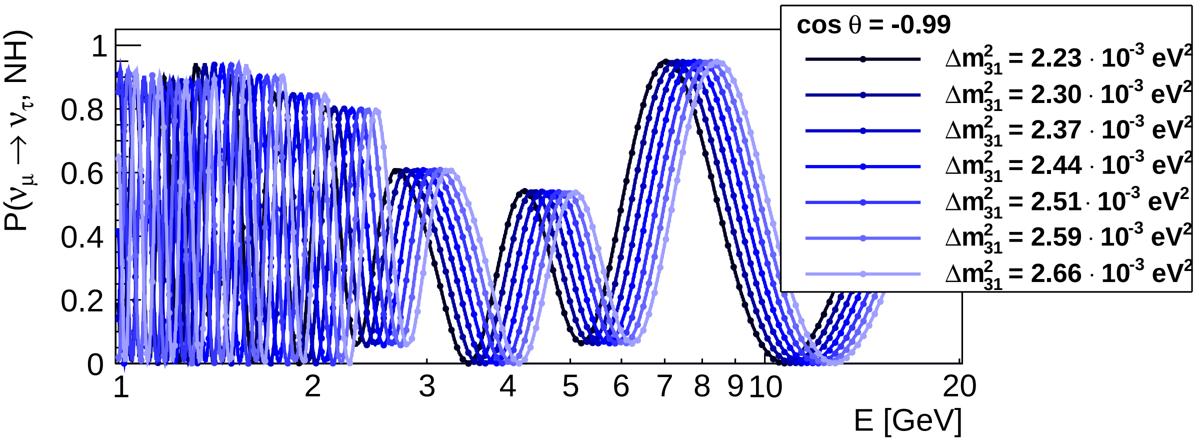

Figure 4.10: *The oscillation probability $P(\nu_\mu \rightarrow \nu_\tau$, NH) as a function of energy at $\cos\theta$ = -0.99 for different values of Δm^2_{31} in its 3σ range. At energies between 1 and 2 GeV, the curves are not distinguishable. At high energies, the differences between the different curves are still rather large and the shift in energy between the curves becomes clear.*

Impact of new constraints on oscillation parameters

It has been mentioned in the beginning of this Section that the oscillation parameter constraints given in Table 4.2 were the up-to-date ones at the time this study was performed. The ones up-to-

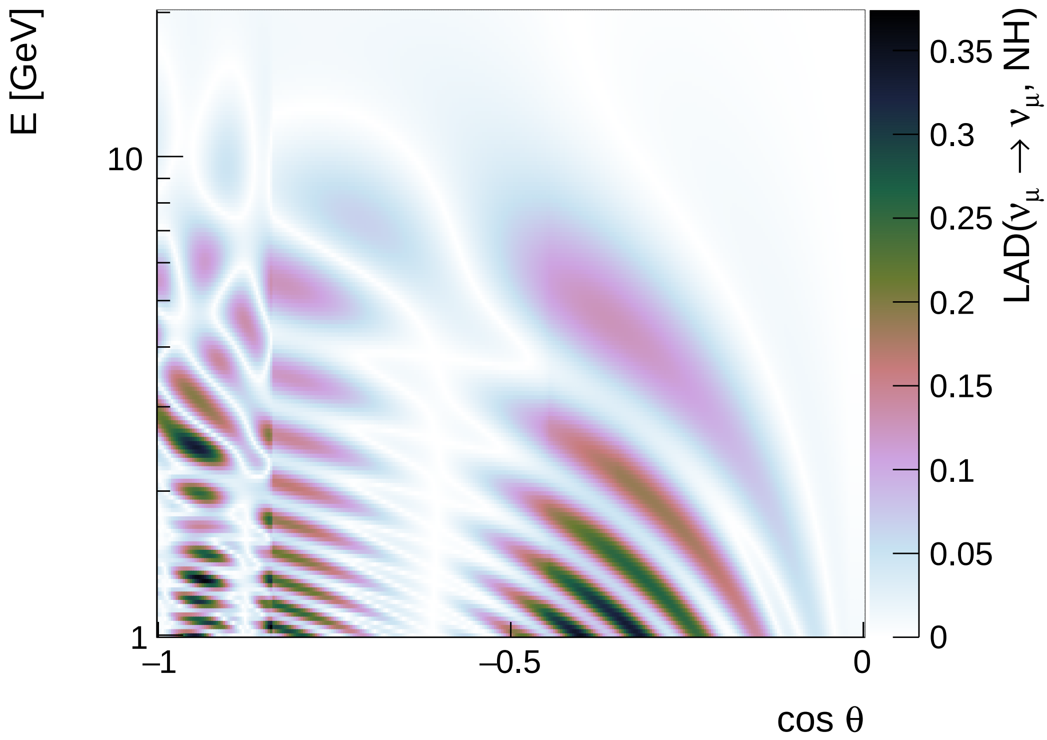

Figure 4.11: *The local absolute differences originating from a change of δ_{cp} as defined in Eq. (4.3) over the $E-\cos\theta-$plane in the case of $\nu_\mu \rightarrow \nu_\mu$, NH. Most effect happens at low energies around $\cos\theta$ = -0.4 and for paths going through the Earth's core.*

date at the time of this writing are given in [76]. They show only slightly stricter constraints except for the θ_{13} mixing angle and the large mass squared difference Δm^2_{31}.

For both assumed mass hierarchies, the allowed 3σ range for θ_{13} decreased by 57%, for the large mass squared difference by roughly 40%. A corresponding change is expected in the impact of these parameter on the oscillation probabilities, i.e. local differences in the *resonance region* will still be around 25% for θ_{13} and 40% for Δm^2_{31}. Therefore, the impact of these parameters will still play an important role.

4.4 Uncertainties in the Earth model

The influence of three different classes of parameters have been investigated: 1) the electron number density of the different Earth layers taking into account the uncertainties in both matter density and chemical composition, 2) the border positions between layers, and 3) the smoothness of the transition between layers generally described as sudden jumps.

As mentioned in Section 4.1, to model the interior of the Earth, the preliminary reference Earth model (PREM [56]) is used. Intended to be preliminary, the authors refrained from giving a precise estimation of possible errors for the density distribution. According to [77], the densities of the Earth's interior, averaged over 100 km, are expected to be correctly described by the PREM to within 5% at nearly all depths in the Earth.

Little information on the precision of the layer thicknesses is given. E.g. in [56], it is stated that three different studies agreed on the Earth's core radius within 0.2% without giving errors on the single studies.

Density jumps between different layers are expected to have a 1-2% precision [56]. However, there is not much information on the size of the range within which the density jump occurs. In [77], it is mentioned that there is strong evidence that the density jump between the inner and outer core and the outer core and lower mantle happens within less than 3 km which is small compared to the thickness of these layers.

Another uncertainty important for neutrino oscillations arises from the chemical composition of the different layers, as the relevant quantity affecting matter oscillations is the electron number density. For the core the uncertainty in the electron fraction is about 1% [70].

With this in mind, it was chosen to vary the density within ±9%, the border positions within ±9% relative to the thicknesses of adjacent layers, and the transition between two layers has been smoothed according to the thicknesses of adjacent layers (see below for the exact definition of the variations). These rather large ranges allow for an ample study of the respective effects on the oscillation probabilities. With the change of the parameters the conservation of the Earth mass (known to 0.01% precision [78]) has been neglected. The resulting change in oscillation probabilities allows for an estimate of the sensitivity of ORCA to PREM parameters, and conversely, also of the precision needed for ORCA in the Earth model description.

In the following sections, the effects of the parameter variations will be described in detail. As the parameters are changed layer by layer, only neutrinos whose paths go through the specific layer are affected by a change. Hence, the deeper a layer the smaller the affected zenith angle range. In addition, as the outer layers are rather thin, effects due to the outer layers will turn out to be negligible.

4.4.1 Density changes

The densities in the different layers are varied in steps of ±3% up to ±9%. The largest impact is expected for the core layers and the lower mantle as these are the largest layers and their densities are in the relevant range for the resonant matter effects of the oscillations (Section 2.2.2). Furthermore, changing the density in the lower mantle affects neutrino zenith angles up to $\cos\theta = -0.45$, whereas for the inner and outer core only zenith angles up to $\cos\theta = -0.98$ and $\cos\theta = -0.84$ are affected (see also Table 4.1, p. 46).

Tables 4.5 and 4.6 list the measures based on the effective and absolute differences, respectively, defined in Section 4.2. The largest local differences are reached for changes in the outer core with values up to nearly 90%. For both the inner core and the lower mantle these differences only reach up to roughly 50%. On the other hand, the global difference is the largest for changes of the density in the lower mantle due to the reasons mentioned above. Changes in the layers above the lower mantle have only minor impact as their thicknesses are much smaller than the relevant neutrino oscillation length.

How the density change in the outer core affects the oscillations of $\nu_e \to \nu_e$ for normal hierarchy (largest MLED) is illustrated in Figure 4.12. It shows the corresponding oscillograms for a density change of -9% and +9%, respectively. In the latter case, the density of the outer core reaches the density of the inner core and the kink in the oscillogram at $\cos\theta = -0.98$ vanishes. Note though that this adjustment of the density contradicts the PREM in such a way that the core then only consists of one density layer. Realistic deviations from the PREM in these layers are therefore expected to be much smaller.

Since the core layers only influence a rather small zenith angle range, it is not expected for ORCA to have a very good sensitivity to their densities considering each layer separately. Also the influence on the sensitivity to the mass hierarchy should be small. The same is true for the layers above the lower mantle. For the lower mantle on the other hand, or when looking at a combination of several layers, the influence is larger and detailed analyses are advisable.

Earth layer	E [GeV]	$\cos\theta$	MLED	MGED	AGED
Inner core	3.7	-1.00	$P(\nu_\mu \to \nu_\tau, \text{NH})$ 45.2%	$P(\bar{\nu}_e \to \bar{\nu}_\tau, \text{IH})$ 0.0507%	0.0192%
Outer core	3.4	-0.98	$P(\nu_e \to \nu_e, \text{NH})$ 87.3%	$P(\bar{\nu}_e \to \bar{\nu}_\tau, \text{IH})$ 0.547%	0.207%
Lower mantle	5.4	-0.81	$P(\bar{\nu}_e \to \bar{\nu}_e, \text{IH})$ 49.8%	$P(\bar{\nu}_e \to \bar{\nu}_e, \text{IH})$ 1.02%	0.247%
Transition zone 1	4.7	-0.44	$P(\bar{\nu}_e \to \bar{\nu}_e, \text{IH})$ 8.26%	$P(\nu_e \to \nu_\tau, \text{NH})$ 0.0288%	0.0117%

Table 4.5: *Same as Table 4.3 (p. 54) for changes in the density of the respective layer. For comparison, see Table 4.6.*

Earth layer	E [GeV]	$\cos\theta$	MLAD	MGAD	AGAD
Inner core	3.7	-1.00	$P(\nu_\mu \to \nu_\tau, \text{NH})$ 45.2%	$P(\bar{\nu}_e \to \bar{\nu}_e, \text{IH})$ 0.195%	0.0649%
Outer core	3.4	-0.98	$P(\nu_e \to \nu_e, \text{NH})$ 87.3%	$P(\nu_e \to \nu_e, \text{NH})$ 3.06%	0.995%
Lower mantle	5.4	-0.81	$P(\bar{\nu}_e \to \bar{\nu}_e, \text{IH})$ 49.8%	$P(\bar{\nu}_e \to \bar{\nu}_e, \text{IH})$ 5.13%	1.60%
Transition zone 1	4.7	-0.44	$P(\bar{\nu}_e \to \bar{\nu}_e, \text{IH})$ 8.26%	$P(\bar{\nu}_e \to \bar{\nu}_e, \text{IH})$ 0.201%	0.0679%

Table 4.6: *Same as Table 4.4 (p. 54) for changes in the density of the respective layer. For comparison, see Table 4.5.*

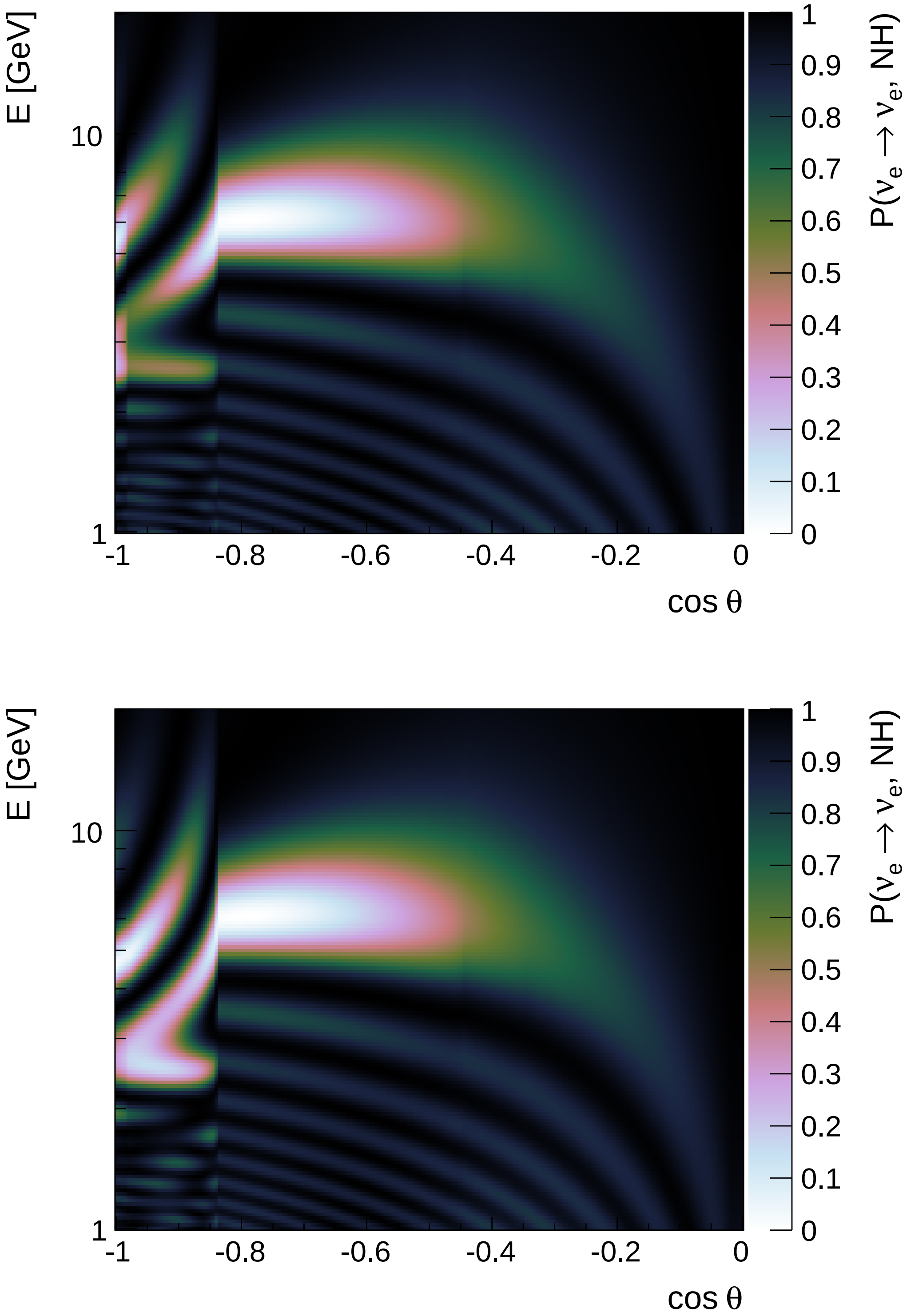

Figure 4.12: *Oscillograms for a density change in the outer core of -9% (top) and +9% (bottom) in the case of $\nu_e \rightarrow \nu_e$, NH. Oscillation probabilities for neutrinos going through the Earth's core* ($\cos\theta < 0.82$) *change significantly.*

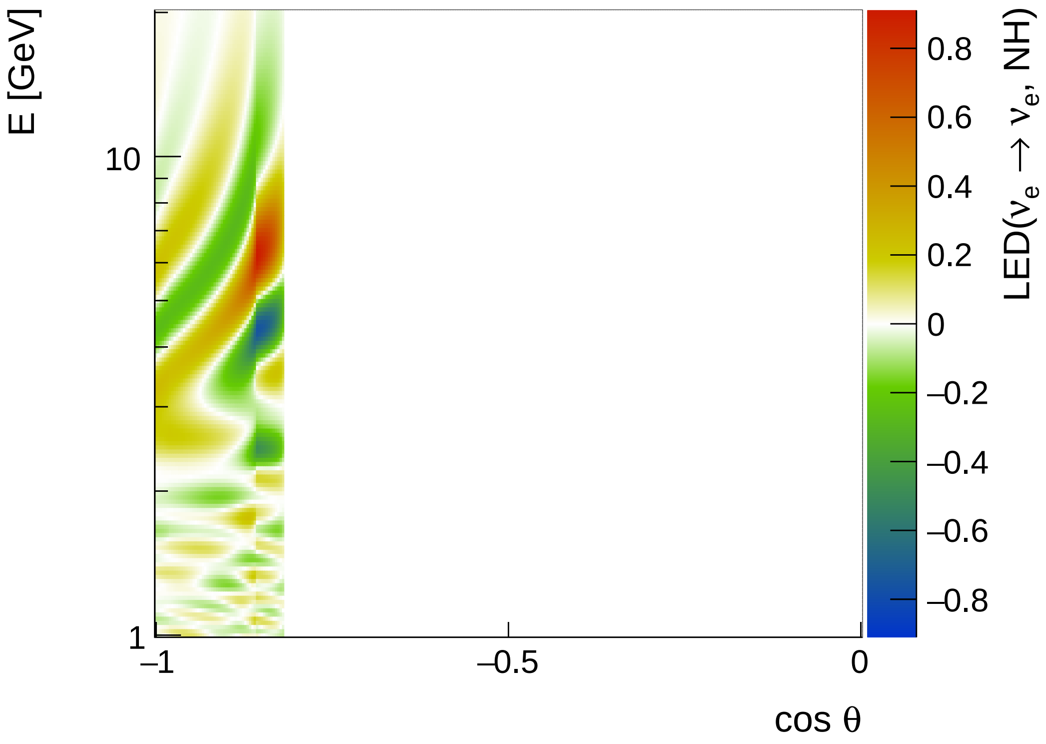

Figure 4.13: *The local effective differences as defined in Eq. (4.2) over the $E - \cos\theta$-plane originating from a shift of the core-mantle border in the case of $\nu_e \to \nu_e$, NH. Neutrinos not going through the Earth's core are therefore unaffected (-0.82$\lesssim \cos\theta < 0$). The largest differences appear in the region of the border change (-0.87$\lesssim \cos\theta \lesssim$ -0.82).*

4.4.2 Border shifts

In order to investigate the effects of different border positions, they are shifted on a percent basis. The position change is given as a fraction s of the thickness of the layer the border is moved towards to. The fraction has been varied between ±9% in steps of ±3%. Thus, given the position of the border between layer i and $i + 1$ by the outer radius r_i of the inner layer, the new position r'_i is given as

$$r'_i = \begin{cases} r_i + s \cdot (r_{i+1} - r_i) & \text{for } 0\% \leq s \leq 9\%, \\ r_i + s \cdot (r_i - r_{i-1}) & \text{for } -9\% \leq s < 0\%. \end{cases}$$

For instance regarding the ±3%-shift for the border between the inner and outer core[12], the border is shifted 36.7 km towards the inner core for -3% and 67.7 km towards the outer core for +3%.

Therefore, the position of the border between the outer core and lower mantle receives the largest absolute change as these two have the largest thicknesses with 2258 km and 2221 km, respectively. Additionally, since the density jump between these two layers is the most profound one and the densities in these layers are most decisive for the resonant matter effects, it is expected that this border change has the largest impact.

---

[12] The thickness of the inner core being 1222 km and of the outer core 2258 km (Table 4.1, p. 46).

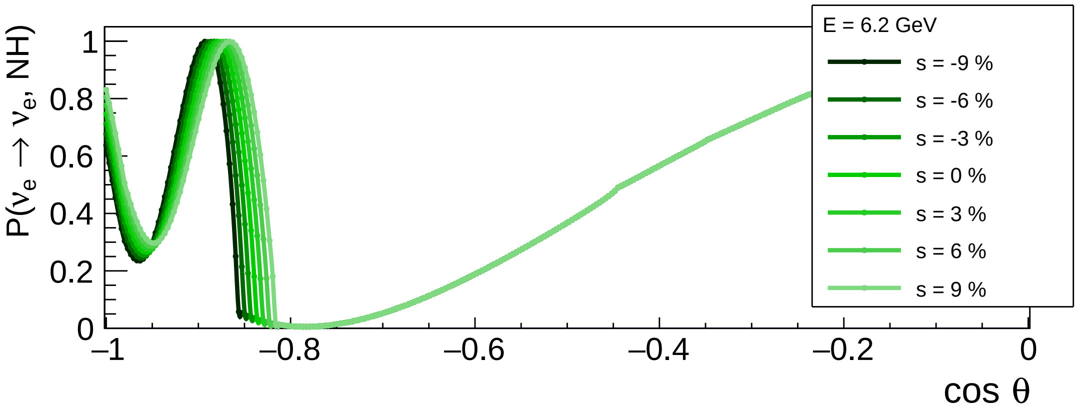

Figure 4.14: *The oscillation probability $P(\nu_e \rightarrow \nu_e, \mathrm{NH})$ as a function of the zenith angle at $E = 6.2\,\mathrm{GeV}$ for different shifts s of the mantle-core border (see text for the definition of the shift). With increasing size of the Earth's core the oscillatory pattern generated by neutrinos going through the core broadens with respect to the zenith angle. Neutrinos not going through the core are unaffected.*

The differences defined in Eqs. (4.6) to (4.11) measuring the effect of the changes are summarised in Table 4.7 and 4.8. Indeed, with an MLED of 91%, the change of the border position between the outer core and lower mantle has the largest effect. The fact that only neutrinos with zenith angles large enough are affected reduces the global effect. Nevertheless, with an MGED of 0.26% and an AGED of 0.068% the largest global differences occur compared to changes in other layers. The MGED and AGED for the change of the adjacent borders are 0.010% and 0.0038% (inner core - outer core), and 0.035% and 0.015% (lower mantle - transition zone), respectively. Consequently, these changes seem negligible. For all other layers, being relatively thin, the changes become even less important as the borders are shifted only by a rather small amount.

In the oscillograms, the change of the border position between the outer core and lower mantle lead to a shift of the kink around $\cos\theta = -0.85$. Consequently, most of the changes of the oscillation probabilities happen in this region. This is illustrated in Figure 4.13. It also shows the significant changes in oscillation probability reaching values up to ±30% for neutrinos travelling through most of the Earth's core.

In Figure 4.14 the oscillation probability $P(\nu_e \rightarrow \nu_e, \mathrm{NH})$ is shown as a function of the zenith angle for different border shifts, at an energy of 6.2 GeV. It can be seen that border changes result not only in a shift of the kink but also in a broadening of the overall oscillation pattern at zenith angles corresponding to neutrinos travelling through the core. A useful fact for the experiment if zenith angle resolutions are well enough.

4.4.3 Transition smoothing

In order to model the smoothing of the border transitions, the density distribution in the Earth is written with the help of sigmoid functions in the following way:

$$\rho(r) = \sum_{i=1}^{9} \frac{\rho_i(r) - \rho_{i+1}(r)}{\exp\left(\frac{r-r_i}{w_i}\right) + 1} + \rho_{10}(r). \qquad (4.12)$$

Here, $\rho_i(r)$ is the polynomial given by the PREM describing the density in layer i which has outer radius r_i according to Table 4.1 (p. 46), so that $\rho_1(r)$ describes the inner core, $\rho_2(r)$ the outer core etc.

Earth layer	E [GeV]	$\cos\theta$	MLED	MGED	AGED
Inner core	3.5	-0.98	$P(\nu_e \to \nu_e, \text{NH})$ 8.36%	$P(\bar{\nu}_e \to \bar{\nu}_\tau, \text{IH})$ 0.0101%	0.00377%
Outer core	4.6	-0.85	$P(\nu_e \to \nu_e, \text{NH})$ 91.0%	$P(\nu_e \to \nu_e, \text{NH})$ 0.264%	0.0679%
Lower mantle	4.3	-0.50	$P(\bar{\nu}_e \to \bar{\nu}_e, \text{IH})$ 9.18%	$P(\nu_e \to \nu_\tau, \text{NH})$ 0.0351%	0.0153%
Transition zone 1	4.6	-0.42	$P(\bar{\nu}_e \to \bar{\nu}_e, \text{IH})$ 0.0512%	$P(\nu_e \to \nu_\tau, \text{NH})$ $9.44 \cdot 10^{-5}$%	$3.85 \cdot 10^{-5}$%

Table 4.7: *Same as Table 4.3 (p. 54) for changes in the position of the outer border of the respective layer. For comparison, see Table 4.8.*

Earth layer	E [GeV]	$\cos\theta$	MLAD	MGAD	AGAD
Inner core	3.5	-0.98	$P(\nu_e \to \nu_e, \text{NH})$ 8.36%	$P(\nu_e \to \nu_e, \text{NH})$ 0.0395%	0.0131%
Outer core	4.6	-0.85	$P(\nu_e \to \nu_e, \text{NH})$ 91.0%	$P(\bar{\nu}_e \to \bar{\nu}_e, \text{IH})$ 2.42%	0.779%
Lower mantle	4.3	-0.50	$P(\bar{\nu}_e \to \bar{\nu}_e, \text{IH})$ 9.18%	$P(\bar{\nu}_e \to \bar{\nu}_e, \text{IH})$ 0.347%	0.116%
Transition zone 1	4.6	-0.42	$P(\bar{\nu}_e \to \bar{\nu}_e, \text{IH})$ 0.0512%	$P(\bar{\nu}_e \to \bar{\nu}_e, \text{IH})$ $7.63 \cdot 10^{-4}$%	$2.60 \cdot 10^{-4}$%

Table 4.8: *Same as Table 4.4 (p. 54) for changes in the position of the outer border of the respective layer. For comparison, see Table 4.7.*

This functional form allows for a representation of the full density distribution in a single function. In addition a simple variation of the “smoothness” w_i of the transition from layer i to layer $i+1$ is possible. In the limit $w_i \to 0$, $\forall\, i$, the formula reproduces the density distribution of the PREM.

In order to relate the smoothnesses w_i to transition widths, the following considerations are made. Given the w are reasonably small

$$w_i \ll |r_{i\pm1} - r_i| \;\forall\, i, \tag{4.13}$$

so that

$$\exp\left(\frac{r_{i-1} - r_i}{w_i}\right) \approx 0, \qquad \exp\left(\frac{r_{i+1} - r_i}{w_i}\right) \gg 1, \tag{4.14}$$

their values only affect the density distribution in a small range around the border between the two adjacent layers. Looking now at the density distribution around a single layer boundary given by j, i.e. $r \approx r_j$, the following abbreviations are used:

$$\rho_j := \rho_j(r_j) \approx \rho_j(r), \tag{4.15}$$

$$\rho_{j+1} := \rho_{j+1}(r_j) \approx \rho_{j+1}(r), \tag{4.16}$$

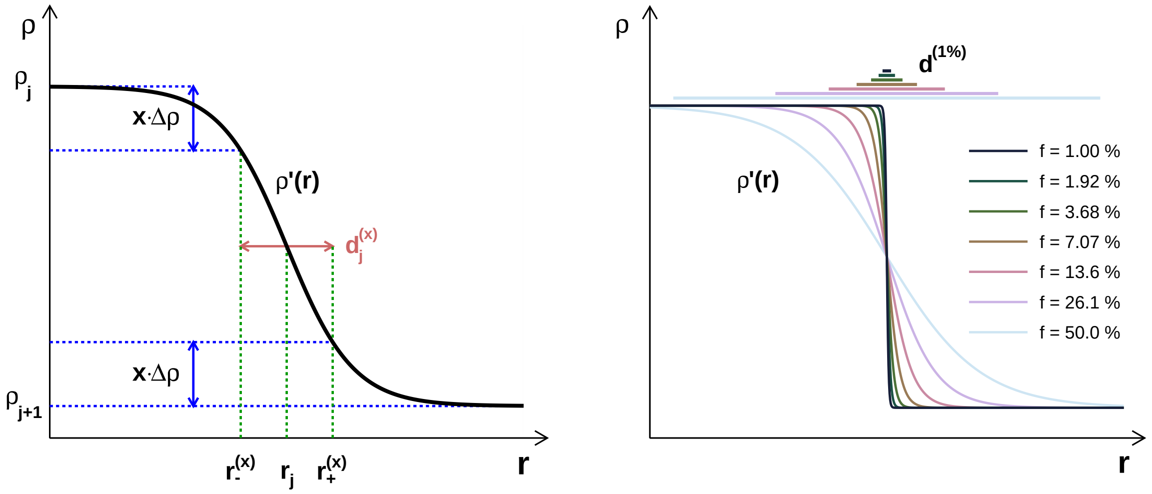

Figure 4.15: *Definition of the transition width* $d_j^{(x)}$ *for a given* x *(left) and the qualitative density distribution around a single layer boundary for different values of* f *including depictions of the corresponding 1%-transition width* $d^{(1\%)}$ *(right). See text for details.*

i.e. the density distribution for a single layer is near the layer boundary approximated by its value at the boundary. Using these approximations, the density distribution $\rho'(r)$ around the boundary can be written as

$$\rho'(r) = \frac{\rho_j - \rho_{j+1}}{\exp\left(\frac{r-r_j}{w_j}\right) + 1} + \rho_{j+1}. \tag{4.17}$$

The behaviour of this function is illustrated in Figure 4.15 (left). At the layer boundary r_j its value is given by $(\rho_j + \rho_{j+1})/2$. For smaller and larger r, the function symmetrically approaches ρ_j and ρ_{j+1}, respectively. It is therefore reasonable to define a transition width as the range within which the density deviates more than a given factor $x < 0.5$ times the density difference $\Delta\rho = \rho_j - \rho_{j+1}$ from ρ_j for $r < r_j$ and from ρ_{j+1} for $r > r_j$. This is depicted in the figure by two values of r denoted as $r_-^{(x)}$ and $r_+^{(x)}$. Thus,

$$\rho'(r_-^{(x)}) = \frac{\Delta\rho}{\exp\left(\frac{r_-^{(x)}-r_j}{w_j}\right) + 1} + \rho_{j+1} = \rho_j - x\,\Delta\rho, \tag{4.18}$$

$$\rho'(r_+^{(x)}) = \frac{\Delta\rho}{\exp\left(\frac{r_+^{(x)}-r_j}{w_j}\right) + 1} + \rho_{j+1} = \rho_{j+1} + x\,\Delta\rho. \tag{4.19}$$

The transition width for a given x is then defined as $d_j^{(x)} := r_+^{(x)} - r_-^{(x)}$. Solving Eqs. (4.18) and (4.19) for $r_-^{(x)}$ and $r_+^{(x)}$, respectively, yields

$$r_-^{(x)} = r_j - w_j \ln\left(\frac{1-x}{x}\right), \tag{4.20}$$

$$r_+^{(x)} = r_j + w_j \ln\left(\frac{1-x}{x}\right). \tag{4.21}$$

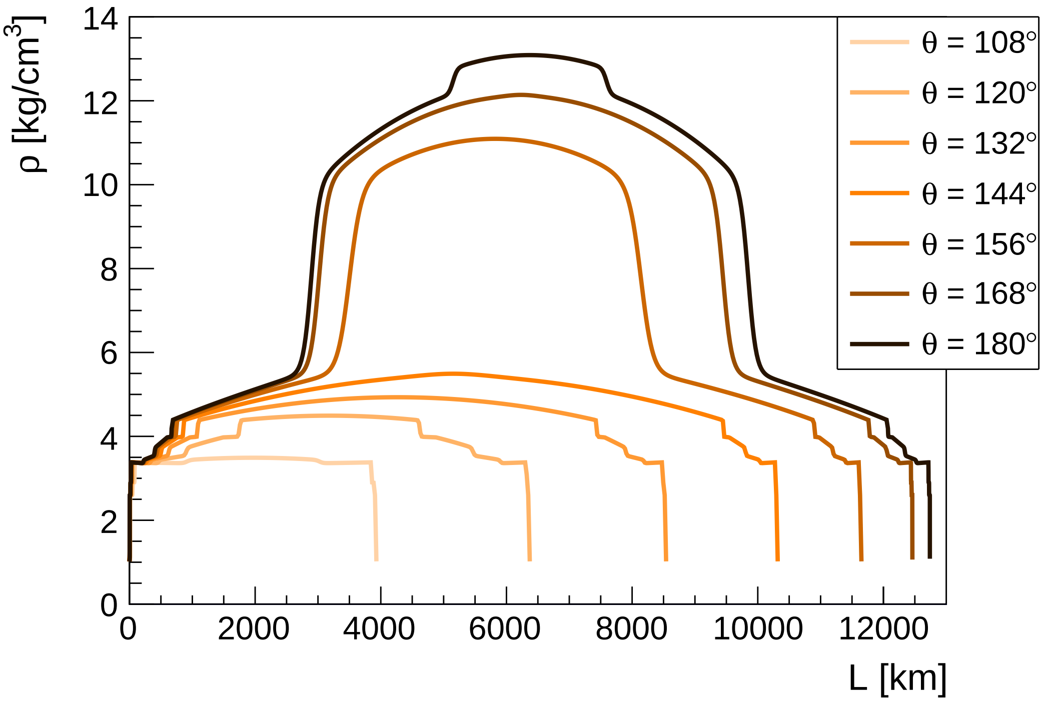

Figure 4.16: *Smoothed density profiles for different neutrino zenith angles for $f = 25\%$, i.e. the 1%-transition width is for each boundary equal to a quarter of the thickness of the thinner adjacent layer. Compare also Figure 4.3 (p. 49).*

Thus, the transition width as a function of w_j is given by

$$d_j^{(x)} = 2\, w_j \, \ln\left(\frac{1-x}{x}\right). \tag{4.22}$$

Going back to an arbitrary boundary given by i, it is for example:

$$d_i^{(1\%)} = 9.19\, w_i, \quad d_i^{(10\%)} = 4.39\, w_i, \quad d_i^{(20\%)} = 2.77\, w_i, \quad d_i^{(40\%)} = 0.81\, w_i. \tag{4.23}$$

Thus taking for instance $w_i = 10$ km, the central 98% of the density change from one layer to another happens within 91.9 km, the central 80% within 43.9 km etc.

To investigate the impact of different transition widths on the oscillation probabilities, the 1%-transition-width $d_i^{(1\%)}$ is chosen to be a given fraction f of the thinner adjacent layer:

$$d_i^{(1\%)} = \begin{cases} f \cdot (r_{i+1} - r_i) & \text{for} \quad r_{i+1} - r_i \le r_i - r_{i-1}, \\ f \cdot (r_i - r_{i-1}) & \text{for} \quad r_{i+1} - r_i > r_i - r_{i-1}. \end{cases} \tag{4.24}$$

Seven different values for f are considered defined from 1% to 50% on a logarithmic scale to cover a wide range while at the same time having a higher density of points near the more realistic cases of very small transition widths[13]. Figure 4.15 (right) illustrates qualitatively the transition at a

---

[13] Considering that the density jumps between inner and outer core and between outer core and lower mantle are expected to happen within a few kilometres [77], even the smallest transition width fraction of 1% overestimates this considerably.

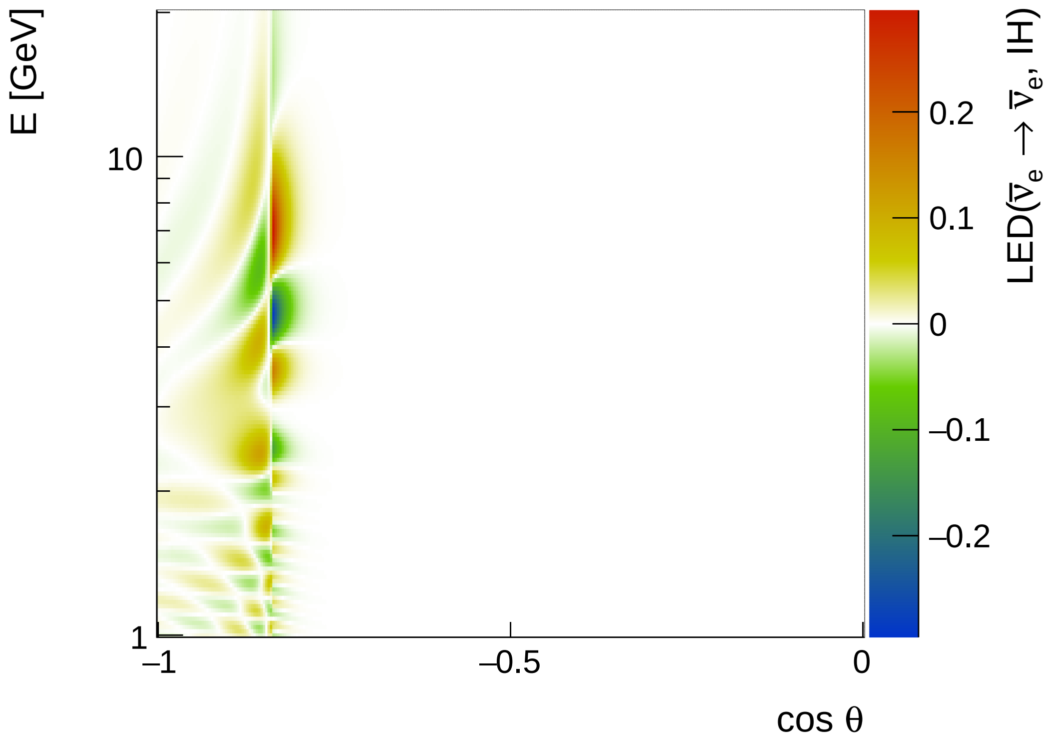

Figure 4.17: *The local effective differences as defined in Eq. (4.2) over the $E-\cos\theta-$plane originating from a smoothing of the core-mantle transition in the case of $\bar{\nu}_e \to \bar{\nu}_e$, IH. Only neutrinos whose paths go along the transition zone are affected. Oscillation probabilities for neutrinos that just pass the transition zone ($\cos\theta \gtrsim -1$) receive hardly any change.*

single layer for different values of f. The corresponding 1%-transition widths are also indicated. In Figure 4.16 the density profiles for different zenith angles are illustrated for the case of $f = 25\%$ for all transitions.

Figure 4.17 shows the differences (LED) that occur when changing the 1%-transition-width between the outer core and the lower mantle from 1% to 50% of the outer-core thickness for $\bar{\nu}_e \to \bar{\nu}_e$, IH. It can be seen that neutrinos that move along this transition zone are mostly affected ($\cos\theta \approx$ -0.84) with differences up to nearly 30%. Neutrinos that move through the inner core ($\cos\theta <$ -0.98) receive a change of at most 1%. The reason is that along the transition zone a relatively long part of the corresponding profile is changed as compared to paths perpendicular to the transition zone.

In the oscillograms, the smoothing of the transition removes the respective kink. This is illustrated in Figure 4.18, which shows the oscillation probability as a function of cosine of zenith angle at 7.2 GeV for different levels of core-mantle-transition smoothing. It is also noticeable that 1%-transition-widths up to around 160 km ($f = 7\%$ of the outer core thickness) produce negligible changes compared to a sudden density jump. Recall that the core-mantle-transition according to the PREM is expected to happen within a few kilometres [77].

Smoothing the transitions between the other layers has the same qualitative effect for the cases where matter resonances play a role (neutrinos with NH, antineutrinos with IH). Quantitatively, the impacts of smoothing are negligible due to the respective layers being very thin. This is summarised

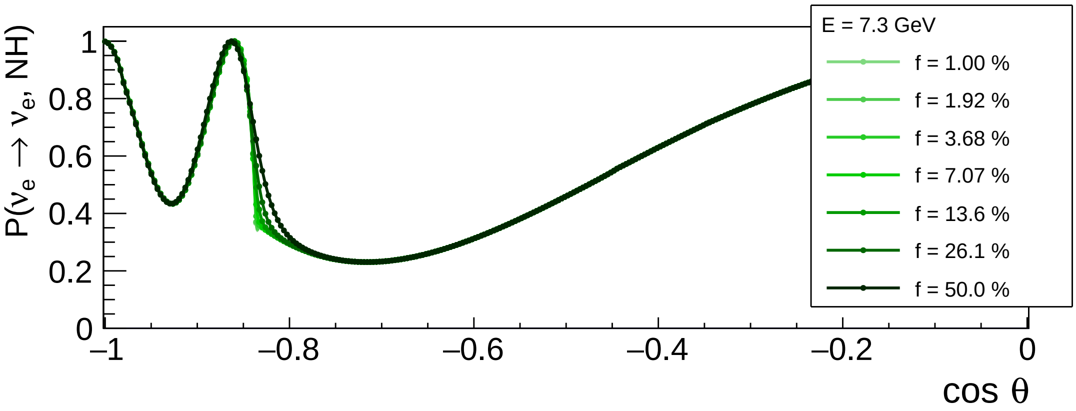

Figure 4.18: *The oscillation probability $P(\nu_e \to \nu_e, NH)$ as a function zenith angle at $E = 7.2\,\mathrm{GeV}$ for different mantle-core transition widths given via f (see Eq. (4.24)). The kink at $\cos\theta = -0.84$ due to the density jump vanishes if the transition is smoothed. Oscillation probabilities for neutrinos going through the Earth's core receive no noticeable change.*

in Table 4.9 and 4.10, which list the differences defined in Section 4.2 up to the transition between the first and second transition zone.

In the cases where no matter resonances occur, smoothing the transition between layers has no noteworthy effect, not even for the most extreme change, with local effective differences well below 1%.

To sum up, possible uncertainties in the density transitions are completely negligible for ORCA determining the neutrino mass hierarchy, and anything different from sudden density jumps will be very hard to detect.

Earth layer	E [GeV]	$\cos\theta$	MLED	MGED	AGED
Inner core	4.5	-0.98	$P(\nu_e \to \nu_e, \mathrm{NH})$ 1.40%	$P(\nu_e \to \nu_\tau, \mathrm{NH})$ $2.84 \cdot 10^{-4}$%	$1.13 \cdot 10^{-4}$%
Outer core	6.3	-0.83	$P(\bar{\nu}_e \to \bar{\nu}_e, \mathrm{IH})$ 29.6%	$P(\bar{\nu}_e \to \bar{\nu}_e, \mathrm{IH})$ 0.144%	0.0346%
Lower mantle	4.7	-0.44	$P(\bar{\nu}_e \to \bar{\nu}_e, \mathrm{IH})$ 0.225%	$P(\nu_e \to \nu_\mu, \mathrm{NH})$ $1.56 \cdot 10^{-5}$%	$8.50 \cdot 10^{-6}$%
Transition zone 1	4.6	-0.43	$P(\bar{\nu}_e \to \bar{\nu}_e, \mathrm{IH})$ 0.00540%	$P(\nu_e \to \nu_\tau, \mathrm{NH})$ $1.53 \cdot 10^{-5}$%	$6.24 \cdot 10^{-6}$%

Table 4.9: *Same as Table 4.3 (p. 54) for smoothing the transition between the given and the next layer. For comparison, see Table 4.10.*

Earth layer	E [GeV]	$\cos\theta$	MLAD	MGAD	AGAD
Inner core	4.5	-0.98	$P(\nu_e \to \nu_e, \mathrm{NH})$ 1.40%	$P(\nu_e \to \nu_e, \mathrm{NH})$ 0.00342%	0.00114%
Outer core	6.3	-0.83	$P(\bar{\nu}_e \to \bar{\nu}_e, \mathrm{IH})$ 29.6%	$P(\bar{\nu}_e \to \bar{\nu}_e, \mathrm{IH})$ 0.380%	0.120%
Lower mantle	4.7	-0.44	$P(\bar{\nu}_e \to \bar{\nu}_e, \mathrm{IH})$ 0.225%	$P(\bar{\nu}_e \to \bar{\nu}_e, \mathrm{IH})$ $6.91 \cdot 10^{-4}$%	$2.38 \cdot 10^{-4}$%
Transition zone 1	4.6	-0.43	$P(\bar{\nu}_e \to \bar{\nu}_e, \mathrm{IH})$ 0.00540%	$P(\nu_e \to \nu_e, \mathrm{NH})$ $1.17 \cdot 10^{-4}$%	$4.42 \cdot 10^{-5}$%

Table 4.10: *Same as Table 4.4 (p. 54) for smoothing the transition between the given and the next layer. For comparison, see Table 4.9.*

4.5 Summary

The effects of uncertainties and variations in the neutrino oscillation parameters and in the model describing the Earth density have been investigated. The focus was on how the ability of ORCA to measure the neutrino mass hierarchy might be affected. The results, summarised below, were valuable input of initial feasibility and sensitivity studies of the ORCA experiment (see the KM3NeT Letter of Intent [7]) as uncertainties in two of the oscillation parameters as well as in the Earth model could be neglected.

Regarding the oscillation parameters, the uncertainties of the mixing angle θ_{12} and the small mass squared difference Δm^2_{21} will not lead to any deterioration of the sensitivity to the neutrino mass hierarchy. On the other hand, the characteristic oscillatory pattern depends crucially on the values of the other two mixing angles θ_{13} and θ_{23}. The incorporation of their uncertainties into a detailed study therefore reduces the sensitivity to the neutrino mass hierarchy as compared to assuming fixed values (see KM3NeT Letter of Intent [7] where this has been done). The same is true for the CP phase δ_{cp}, the impact of its uncertainty being comparable to that of θ_{13} and θ_{23}. Considering a measurement of θ_{23}, it has also been pointed out that the sensitivity to θ_{23} is expected to increase with the ability to distinguish electron from tau neutrinos[14].

A variation of the large mass squared difference Δm^2_{31} within its $3\,\sigma$ range has the largest effect on the oscillation probabilities. Such a variation leads to an energy shift of the complete oscillatory pattern. Therefore, the uncertainty in Δm^2_{31} is equivalent to a systematic uncertainty in the energy resolution. On the other hand, by exploiting oscillation maxima and minima above 10 GeV it might be possible to reduce this uncertainty.

Earth model parameters have been changed on a per-layer basis. Considered parameters were the density, the position of the layer boundaries and the steepness of the density jumps at the layer boundaries. As sophisticated error estimations for such parameters are scarce, the variations have been done within an arbitrary range to get an impression of their effect on the oscillation probabilities. The lower mantle and outer core being the largest layers, changes in the parameters describing these two layers have the largest effect. In general, significant changes only appear for variations larger than known uncertainties [77].

The electron number density plays the most important role. Variations of more than about 5% begin to have a significant effect. It should be noted here that some authors (e.g. [79,80]) approximate the electron fraction in the Earth's core by $Y_e = 0.5$ as opposed to $Y_e = 0.466$ used here. This corresponds to a deviation of roughly 7% that should not be neglected.

Among layer boundary shifts, shifting the core-mantle border has the largest effect. The larger the shift the larger the zenith angle range affected by the shift. This is mainly due to the fact that the neutrino path length through the core, which is important for the resonant matter effects, receives a respective alteration. A shift of more than about 50 km, a value much larger than given through expected uncertainties [56], produces significant changes.

A smoothing of the density transition produces changes that are negligible even for a very extreme smoothing. The smoothing only affects a very small zenith angle range, namely those zenith angles that describe neutrinos moving along the transition. This result also shows that for the calculation of oscillation probabilities, an approximation of the Earth interior with a given number ($\gtrsim 40$)

---

[14] Distinguishing electron from tau neutrinos in the ORCA energy regime is not an easy task and will only be possible on a statistical basis as their event topologies are very similar most of the time (see Section 2.4).

of layers with constant density is appropriate; this is implemented in a procedure established in the last years to speed up the calculation of oscillation probabilities (see e.g. [7]).

It has been mentioned that the performed studies were done to get a qualitative output on how sensitivities are affected. To be able to give sophisticated, quantitative statements, detailed studies need to be performed including detector simulations and statistical sensitivity analyses. In addition, considering a comprehensive incorporation of all possible effects, the oscillation probabilities need to be known in the entire six-dimensional parameter space formed by the six neutrino oscillation parameters. The parameter space gets even larger when also Earth parameter uncertainties shall be included. The following chapter is about an approach to calculate these oscillation probabilities with a dedicated interpolation method.

Chapter 5

Interpolation of oscillation probabilities

For a comprehensive analysis of the sensitivity of ORCA to the neutrino mass hierarchy and the oscillation parameters and to fully evaluate the influence of the uncertainties of the oscillation parameters, the oscillation probabilities need to be known in the full eight-dimensional[15] parameter space to a good precision. The parameter space gets even larger if Earth model uncertainties shall also be considered.

The numerical solution to derive the neutrino oscillation probabilities is a bottle neck regarding the time consumption for ORCA sensitivity studies (see e.g. [7]). This chapter presents an attempt to overcome this bottle neck by interpolating oscillation probabilities in the full $3\,\sigma$ oscillation parameter space based on the oscillograms defined in Section 4.1.

For this purpose, a sophisticated interpolation method was developed to meet the high precision requirements without having to produce unnecessary data. This method is described in Section 5.1, its exemplary application in Section 5.2.

The application lead to an estimate of how many oscillograms need to be calculated to be able to interpolate the oscillation probabilities with a precision of at most 0.1% in the full parameter space. The derivation of this estimate and the results are described in Section 5.3.

Section 5.4 highlights possibilities to improve this estimate and the developed methods, and Section 5.5 gives a summary of this chapter.

5.1 Interpolation method

The aim is to find the value of a function of arbitrary dimension at an arbitrary point in the multi-dimensional parameter space. About the function, only the values at certain parameter values (data points) are known. In order to find the unknown values the function needs to be approximated by interpolating from the given data points.

Here, the underlying principle of the interpolation method is a d-dimensional Taylor expansion of K-th order around each given data point via the I nearest data points, with $d, K, I \in \mathbb{N}$. The data points are used to approximate the unknown derivatives. The final interpolation between two given data points is then done by taking a weighted mean of the respective Taylor expansions. As no appropriate mathematical descriptions have been found after an extensive literature search, the corresponding formulae have been derived from scratch as shown in the following.

---

[15] The eight dimensions comprise the six oscillation parameters and energy and zenith angle.

Derivation of the interpolation formulae

For the derivation of the interpolation formulae, the unknown function to be approximated is written as $f_h := f(x+h)$ with $x, h \in \mathbb{R}^d$. The Taylor expansion in multi-index notation for n is then given as

$$f_h = \sum_{n \leq N} \frac{h^n}{n!} f^{(n)} + R_{N+1} \tag{5.1}$$

with the remainder R_{N+1}

$$R_{N+1} = \sum_{|n|=N+1} \frac{h^n}{n!} f_{th}^{(n)} = O(h^{N+1}) \tag{5.2}$$

and the abbreviations

$$f^{(n)} := \frac{\partial^n f}{\partial x^n}(x) \tag{5.3}$$

$$f_{th}^{(n)} := \frac{\partial^n f}{\partial x^n}(x+th) \tag{5.4}$$

$$O(h^{N+1}) := \sum_{|n|=N+1} O(h^n) \tag{5.5}$$

with $t \in [0,1]$ and $N \in \mathbb{N}$ as the order of the Taylor expansion[16]. Multi-index notation for n includes the following definitions (see also [81]):

$$|n| := n_1 + \cdots + n_d, \qquad n! := n_1! \cdot \cdots \cdot n_d!, \qquad x^n := x_1^{n_1} \cdot \cdots \cdot x_d^{n_d},$$

$$\frac{\partial^n f}{\partial x^n}(x) := \frac{\partial^{n_1}}{\partial x_1^{n_1}} \cdots \frac{\partial^{n_d}}{\partial x_d^{n_d}} f$$

Now looking at Eq. (5.1), the goal is to approximate the derivatives $f^{(n)}$ from the data points given as (h_i, f_{h_i}) in the vicinity of $f_{h=0}$. In order to accomplish that, a linear combination of the f_{h_i} with coefficients a_i is introduced in the following way, where the f_{h_i} are written as their Taylor expansions:

$$\begin{aligned}\sum_{i=1}^{I} a_i f_{h_i} &= \sum_{i=1}^{I} a_i \left(\sum_{n \leq N} \frac{h_i^n}{n!} f^{(n)} + O(h_i^{N+1}) \right) \\ &= \sum_{n \leq N} \left(\sum_{i=1}^{I} a_i h_i^n \right) \frac{f^{(n)}}{n!} + \sum_{i=1}^{I} O(h_i^{N+1}). \end{aligned} \tag{5.6}$$

This expression is solved in the following for a certain derivative $f^{(m)}$ (m in multi-index notation) that is to be calculated. For this purpose the sum over n is split to get:

$$\sum_{i=1}^{I} a_i f_{h_i} = \sum_{i=1}^{I} a_i f^{(0)} + \sum_{i=1}^{I} a_i h_i^m \frac{f^{(m)}}{m!} + \sum_{\substack{n \leq N \\ 0 \neq n \neq m}} \left(\sum_{i=1}^{I} a_i h_i^n \right) \frac{f^{(n)}}{n!} + \sum_{i=1}^{I} O(h_i^{N+1}). \tag{5.7}$$

---

[16] As a reminder, for two functions f and g, $f = O(g)$ means that f does not grow faster than g, with the Landau symbol O.

Solving for $f^{(m)}$ yields:

$$f^{(m)} = \frac{m!}{\sum_{i=1}^{I} a_i h_i^m} \left[\sum_{i=1}^{I} a_i \left(f_{h_i} - f_0 \right) - \sum_{\substack{n \leq N \\ 0 \neq n \neq m}} \left(\sum_{i=1}^{I} a_i h_i^n \right) \frac{f^{(n)}}{n!} \right] + \sum_{i=1}^{I} O(h_i^{N+1-m}), \tag{5.8}$$

where it has been used that $f^{(0)} \equiv f_0$ and for the remainder it holds

$$\frac{m!}{\sum\limits_{i=1}^{I} a_i h_i^m} \cdot \sum_{i=1}^{I} O(h_i^{N+1}) = \sum_{i=1}^{I} O(h_i^{N+1-m}). \tag{5.9}$$

In this expression the exact values of the derivatives on the right side are still unknown. Thus, for the $f^{(m)}$ to be well approximated, the sum right in front of the unknown derivatives needs to be zero so that they can be ignored. This provides a proper condition for the a_i:

$$\sum_{i=1}^{I} a_i h_i^n = 0, \qquad \text{for } n \leq N, 0 \neq n \neq m \tag{5.10}$$

This leads to a homogeneous system of linear equations with the vector $\boldsymbol{a} = (\ldots, a_i, \ldots) \in \mathbb{R}^I$ and the matrix $H_m \in \mathbb{R}^{(R,I)}$ (with the number of rows R) containing the rows $(h_1^n, \ldots, h_I^n)$ for $n \leq N, 0 \neq n \neq m$:

$$H_m \boldsymbol{a} = \mathbf{0}. \tag{5.11}$$

An analytical solution for $\boldsymbol{a}$ in one dimension is derived below. The job is done once solutions $\boldsymbol{a}_m$ have been found for $\boldsymbol{a}$ for all $m \leq N$. The approximative formula for the derivatives then reads

$$f^{(m)} \approx \frac{m!}{\sum_{i=1}^{I} a_{m,i} h_i^m} \sum_{i=1}^{I} a_{m,i} \left(f_{h_i} - f_0 \right), \tag{5.12}$$

and the corresponding polynomial approximating the function f_h:

$$f_h \approx f_0 + \sum_{n \leq N} \frac{\sum_{i=1}^{I} a_{n,i} \left(f_{h_i} - f_0 \right)}{\sum_{i=1}^{I} a_{n,i} h_i^n} h^n. \tag{5.13}$$

Note that here, the sum over n can be stopped at any value K smaller than N which therefore determines the degree of the approximative polynomial. The choice of N is important for the matrix equation (Eq. (5.11)) and determines the order up to which the unknown derivatives are negligible (see text before Eq. (5.10)). Therefore, the choice of N is crucial for the precision of the approximation formula.

In order to get a minimum for the number of data points (beyond the expansion point) needed to approximate up to the order given by N, the linear system of equations (Eq. (5.11)) has to be considered. To make it non-trivially solvable, a necessary requirement is for the number of rows R to be smaller than the number of columns given by the number of data points I: $R < I$. The number of rows R in the matrix is given as[17]:

$$R = \binom{d+N}{N} - 2. \tag{5.14}$$

---

[17] Recall that multi-index notation is used in n. Therefore, the number of rows can be calculated by considering a "drawing with replacement" urn problem (without distinguishing the draw order). It is equivalent to the sum of the first N elements in the $(d-1)$-th diagonal of Pascal's triangle minus one (because the row with $n = m$ is missing in H_m).

This therefore gives the minimum number of data points $I_{\text{min}} = R + 1$ needed as a function of N and d.

The approximation formula (Eq. (5.13)) incorporates several inconveniences: for high d and N, the solution of the matrix equations and the formula itself contains a huge number of computation steps that make it impractical. Another aspect concerns the choice of data points. For some choices, the matrix might not be solvable or the remainders (Eq. (5.9)) can assume large values[18]. Additionally, numerical instabilities have been encountered trying to solve the linear systems of equations (Eq. (5.11)) for $d > 1$.

For these reasons, it was decided to work in one dimension. For this case, a handy analytical expression could be found for the $\boldsymbol{a}_m$ as shown in the following.

Solution to Equation 5.11 in one dimension

Recall that $I + 1$ is the number of given or chosen data points to use for the Taylor expansion and N determines the precision of the approximation and is limited by the number of chosen data points. In the case $I = 1$, only the first derivative is to be approximated and Eq. (5.12) gives the standard approximation $f^{(1)} \approx (f_{h_1} - f_0)/h_1$. Therefore, in the following $I > 1$ is assumed.

In one dimension, the matrix equation $H_m \boldsymbol{a} = \boldsymbol{0}$ takes the following form

$$\begin{pmatrix} h_1^1 & h_2^1 & \dots & h_{I-1}^1 & h_I^1 \\ \vdots & \vdots & & \vdots & \vdots \\ h_1^{m-1} & h_2^{m-1} & \dots & h_{I-1}^{m-1} & h_I^{m-1} \\ h_1^{m+1} & h_2^{m+1} & \dots & h_{I-1}^{m+1} & h_I^{m+1} \\ \vdots & \vdots & & \vdots & \vdots \\ h_1^N & h_2^N & \dots & h_{I-1}^N & h_I^N \end{pmatrix} \begin{pmatrix} a_1 \\ a_2 \\ \vdots \\ a_{I-1} \\ a_I \end{pmatrix} = \begin{pmatrix} 0 \\ 0 \\ \vdots \\ 0 \\ 0 \end{pmatrix}. \tag{5.15}$$

Within a column of the matrix the exponent increases by one up to N from top to bottom, and the exponent m is missing. The matrix has N - 1 rows and I columns (see also Eq. (5.14)). For mutually distinct h_i, its rank is given by $\min\{N-1, I\}$. So choosing $N = I > 1$, the system has a non-trivial solution and one value of the a_i can be chosen freely. Furthermore, this gives the maximum precision achievable with $I + 1$ data points. Thus, from now on $N = I$ unless stated otherwise so that the matrix has one more column than rows.

Putting the terms corresponding to a_1 (i.e. a_1 times the first column of H_m) on the right side of the equation, the system of equations can be written in the following form:

$$\begin{pmatrix} h_2^1 & \dots & h_{I-1}^1 & h_I^1 \\ \vdots & & \vdots & \vdots \\ h_2^{m-1} & \dots & h_{I-1}^{m-1} & h_I^{m-1} \\ h_2^{m+1} & \dots & h_{I-1}^{m+1} & h_I^{m+1} \\ \vdots & & \vdots & \vdots \\ h_2^N & \dots & h_{I-1}^N & h_I^N \end{pmatrix} \begin{pmatrix} a_2 \\ \vdots \\ a_{I-1} \\ a_I \end{pmatrix} = -a_1 \begin{pmatrix} h_1 \\ \vdots \\ h_1^{m-1} \\ h_1^{m+1} \\ \vdots \\ h_1^N \end{pmatrix}, \tag{5.16}$$

so that the matrix on the left is a square matrix. Given that its determinant is non-zero, Cramer's rule [82] can be applied. For this purpose, the square matrix which one gets from H_m by removing

---

[18] An appropriate choice of data points in multiple dimensions will not be discussed here.

column i is denoted as $H_{m,i}$. Then, the solutions $a_{m,i}$ to the a_i for $i > 1$ can be written for all m as a function of a_1 according to Cramer's rule as

$$a_{m,i} = -a_1 \frac{(-1)^i \det H_{m,i}}{\det H_{m,1}}, \tag{5.17}$$

where a_1 can be chosen freely. Again, this solution is only valid if $\det H_{m,1} \neq 0$. Then, choosing $a_1 = -\det H_{m,1}$ for all m gives

$$a_{m,i} = (-1)^i \det H_{m,i}. \tag{5.18}$$

So the remaining task is to determine the determinants. Calculating these with standard algorithms is computationally very intensive. A relatively simple analytical expression has been found for the determinants[19] that allows a faster calculation:

$$\det H_{m,i} = \prod_{\substack{j=1 \\ j\neq i}}^{I} h_j \prod_{\substack{1\leq k<l\leq I \\ k\neq i\neq l}} (h_l - h_k) \sum_{\substack{1\leq p_1<\ldots<p_{I-m}\leq I \\ p_q\neq i\,\forall q}} \prod_{q=1}^{I-m} h_{p_q}. \tag{5.19}$$

It follows that for the determinants to be non-zero, it is sufficient that all data points differ from one another (and from the expansion point), i.e. $h_j \neq h_k$ for all $j \neq k$ and $h_j \neq 0$ for all j where $1 \leq j,k \leq I$. The expression will be proven in the following.

Proof of Equation 5.19

The proof is performed via induction over the number of rows/columns given by I. It is sufficient to show the special case of $i = I$ which corresponds to the case where the column with h_I is missing from the matrix. Then defining $J := I - 1$ and denoting $H_m(J)$ as the matrix with J columns (and rows), the induction is performed over J and it remains to show

$$\det H_m(J) \equiv \begin{vmatrix} h_1^1 & \cdots & h_J^1 \\ \vdots & & \vdots \\ h_1^{m-1} & \cdots & h_J^{m-1} \\ h_1^{m+1} & \cdots & h_J^{m+1} \\ \vdots & & \vdots \\ h_1^N & \cdots & h_J^N \end{vmatrix} = \prod_{j=1}^{J} h_j \prod_{1\leq k<l\leq J} (h_l - h_k) \sum_{1\leq p_1<\ldots<p_{J+1-m}\leq J} \prod_{q=1}^{J+1-m} h_{p_q}. \tag{5.20}$$

which is therefore the induction hypothesis. The determinants for all $H_{m,i}$ follow from this as a mere renaming of the components of h.

---

[19] Actually, a similar approach for the $a_{m,i}$ can be used for any number of dimensions d to arrive at Eq. (5.18). However, no simple expression for the determinants has been found for $d > 1$.

Starting with the base cases $J = 1$ ($N = 2$) and for illustration purposes $J = 2$ ($N = 3$), one gets

$$\det H_1(1) = \left| h_1^2 \right| = h_1^2 = \prod_{j=1}^{1} h_j \prod_{1 \le k < l \le 1} (h_l - h_k) \sum_{1 \le p_1 \le 1} \prod_{q=1}^{1} h_{p_q}, \tag{5.21}$$

$$\det H_2(1) = \left| h_1 \right| = h_1 = \prod_{j=1}^{1} h_j \prod_{1 \le k < l \le 1} (h_l - h_k) \sum_{1 \le 1} \prod_{q=1}^{0} h_{p_q}, \tag{5.22}$$

$$\det H_1(2) = \begin{vmatrix} h_1^2 & h_2^2 \\ h_1^3 & h_2^3 \end{vmatrix} = h_1^2 h_2^2 (h_2 - h_1) = \prod_{j=1}^{2} h_j \prod_{1 \le k < l \le 2} (h_l - h_k) \sum_{1 \le p_1 < p_2 \le 2} \prod_{q=1}^{2} h_{p_q}, \tag{5.23}$$

$$\det H_2(2) = \begin{vmatrix} h_1 & h_2 \\ h_1^3 & h_2^3 \end{vmatrix} = h_1 h_2 (h_2^2 - h_1^2) = \prod_{j=1}^{2} h_j \prod_{1 \le k < l \le 2} (h_l - h_k) \sum_{1 \le p_1 \le 2} \prod_{q=1}^{1} h_{p_q}, \tag{5.24}$$

$$\det H_3(2) = \begin{vmatrix} h_1 & h_2 \\ h_1^2 & h_2^2 \end{vmatrix} = h_1 h_2 (h_2 - h_1) = \prod_{j=1}^{2} h_j \prod_{1 \le k < l \le 2} (h_l - h_k) \sum_{1 \le 2} \prod_{q=1}^{0} h_{p_q}, \tag{5.25}$$

with the sum over the empty product defined as unity (last term in Eqs. (5.22) and (5.25)).

Now, the inductive step starts with subtracting h_{J+1} times the row above for each row but the m-th, and for the m-th row subtracting h_{J+1}^2 times the row above:

$$\det H_m(J+1) \equiv \begin{vmatrix} h_1 & \dots & h_J & h_{J+1} \\ h_1^2 & \dots & h_J^2 & h_{J+1}^2 \\ \vdots & & \vdots & \vdots \\ h_2^{m-1} & \dots & h_J^{m-1} & h_{J+1}^{m-1} \\ h_2^{m+1} & \dots & h_J^{m+1} & h_{J+1}^{m+1} \\ h_2^{m+2} & \dots & h_J^{m+2} & h_{J+1}^{m+2} \\ \vdots & & \vdots & \vdots \\ h_2^{N+1} & \dots & h_J^{N+1} & h_{J+1}^{N+1} \end{vmatrix} = \begin{vmatrix} h_1 & \dots & h_J & h_{J+1} \\ h_1(h_1 - h_{J+1}) & \dots & h_J(h_J - h_{J+1}) & 0 \\ \vdots & & \vdots & \vdots \\ h_1^{m-2}(h_1 - h_{J+1}) & \dots & h_J^{m-2}(h_J - h_{J+1}) & 0 \\ h_1^{m-1}(h_1^2 - h_{J+1}^2) & \dots & h_J^{m-1}(h_J^2 - h_{J+1}^2) & 0 \\ h_1^{m+1}(h_1 - h_{J+1}) & \dots & h_J^{m+1}(h_J - h_{J+1}) & 0 \\ \vdots & & \vdots & \vdots \\ h_1^N(h_1 - h_{J+1}) & \dots & h_J^N(h_J - h_{J+1}) & 0 \end{vmatrix} \tag{5.26}$$

$$= (-1)^J h_{J+1} \prod_{j=1}^{J} (h_j - h_{J+1}) \begin{vmatrix} h_1 & \dots & h_J \\ \vdots & & \vdots \\ h_1^{m-2} & \dots & h_J^{m-2} \\ h_1^{m-1}(h_1 + h_{J+1}) & \dots & h_J^{m-1}(h_J + h_{J+1}) \\ h_1^{m+1} & \dots & h_J^{m+1} \\ \vdots & & \vdots \\ h_1^N & \dots & h_J^N \end{vmatrix} . \tag{5.27}$$

In the last step, standard rules for determinants have been used. The last expression is equivalent to the sum of two determinants and it follows:

$$\det H_m(J+1) = h_{J+1} \prod_{j=1}^{J} (h_{J+1} - h_j) \left(\begin{vmatrix} h_1 & \dots & h_J \\ \vdots & & \vdots \\ h_1^{m-2} & \dots & h_J^{m-2} \\ h_1^{m} & \dots & h_J^{m} \\ h_1^{m+1} & \dots & h_J^{m+1} \\ \vdots & & \vdots \\ h_1^{N} & \dots & h_J^{N} \end{vmatrix} + h_{J+1} \begin{vmatrix} h_1 & \dots & h_J \\ \vdots & & \vdots \\ h_1^{m-2} & \dots & h_J^{m-2} \\ h_1^{m-1} & \dots & h_J^{m-1} \\ h_1^{m+1} & \dots & h_J^{m+1} \\ \vdots & & \vdots \\ h_1^{N} & \dots & h_J^{N} \end{vmatrix} \right) \tag{5.28}$$

$$= h_{J+1} \prod_{j=1}^{J} (h_{J+1} - h_j) \left(\det H_{m-1}(J) + h_{J+1} \det H_m(J) \right). \tag{5.29}$$

Using the induction hypothesis one arrives at:

$$\begin{aligned} \det H_m(J+1) &= \prod_{j=1}^{J+1} h_j \prod_{1 \le k < l \le J+1} (h_l - h_k) \left(\sum_{1 \le p_1 < \ldots < p_{J+1-m+1} \le J} \prod_{q=1}^{J+1-m+1} h_{p_q} + h_{J+1} \sum_{1 \le p_1 < \ldots < p_{J+1-m} \le J} \prod_{q=1}^{J+1-m} h_{p_q} \right) \\ &= \prod_{j=1}^{J+1} h_j \prod_{1 \le k < l \le J+1} (h_l - h_k) \sum_{1 \le p_1 < \ldots < p_{J+2-m} \le J+1} \prod_{q=1}^{J+2-m} h_{p_q}, \end{aligned} \tag{5.30}$$

as it was to be shown.

Summary and usage

To summarise, the following formulae are used to approximate the function f around a given data point at $(x_0, f_0 \equiv f(x_0))$ in one dimension $(x_0, h \in \mathbb{R})$:

$$f(x_0 + h) \approx f_0 + \sum_{n=1}^{K} \frac{\sum_{i=1}^{I} a_{n,i} (f_i - f_0)}{\sum_{i=1}^{I} a_{n,i} h_i^n} h^n, \tag{5.31}$$

$$a_{n,i} = (-1)^i \prod_{\substack{j=1 \\ j \ne i}}^{I} h_j \prod_{\substack{1 \le k < l \le I \\ k \ne i \ne l}} (h_l - h_k) \sum_{\substack{1 \le p_1 < \ldots < p_{I-n} \le I \\ p_q \ne i \, \forall q}} \prod_{q=1}^{I-n} h_{p_q}, \tag{5.32}$$

where K gives the degree of the used polynomial and is limited by I: $K \le I$. The I nearest data points around x_0 are used given by $(x_0 + h_i, f_i \equiv f(x_0 + h_i))$.

Up until now, only the formulae to approximate the function around a single(!) given data point have been derived. To interpolate between two different data points, a linearly weighted mean of the two interpolations around these data points is used. For this purpose, the function that approximates $f(x) = f(x_m + h)$ according to Eq. (5.31) around a given data point $(x_m, f(x_m))$ shall be called $g_m(x)$. Given M data points in total and assuming $x_m < x_{m+1} \; \forall \, m \in \{1, \ldots, M-1\}$, the interpolation formula $P_m(x)$, $x_m \le x \le x_{m+1}$, between the two points given by m and $m+1$ reads:

$$P_m(x) = \frac{1}{x_{m+1} - x_m} \left[g_m(x) \cdot (x_{m+1} - x) + g_{m+1}(x) \cdot (x - x_m) \right] \tag{5.33}$$

and it is $P_m(x_m) = g_m(x_m) = P_{m-1}(x_m)$ and $P_m(x_{m+1}) = g_{m+1}(x_{m+1}) = P_{m+1}(x_{m+1}) \; \forall \, m \in [1, M-1]$.

5.2 Application

In the interpolation algorithm the number I of data points used for the interpolation (besides the expansion point) and the order K of the Taylor expansion can essentially be chosen freely. This section discusses the precision of the interpolation method as a function of I and K, and takes the neutrino oscillation probability as a function of $\cos\theta$ as an example. The desired precision (see also next section) is 0.1%.

Figures 5.1 and 5.2 show such examples and demonstrate effectiveness and applicability of the derived method. The interpolation is done with respect to $\cos\theta$, in the range $-1 < \cos\theta < -0.2$, for the oscillation probability $P(\nu_\mu \to \nu_\mu, \text{NH})$ at $E = 1.23\,\text{GeV}$ which includes many oscillations. A number of 50 data points distributed equidistantly over $\cos\theta$ are used for the interpolation. The precision is checked in the middle between two points by computing the difference between the oscillation probability, calculated by solving the equation of motion, and the interpolation result at that point.

Figure 5.1 shows how the precision changes when increasing I and K with the condition $I = K$. With $I = K = 4$, a precision better than 1% is achieved over most part of the considered zenith angle range. Only for some angles corresponding to neutrinos passing the Earth's core the differences exceed 1%. Increasing I and K to six improves the precision to better than 0.5% with the exception of two data points. The first one near the edge of $\cos\theta \approx -1$ where the precision is expected to suffer from the asymmetrically distributed data points used for the interpolation. The second one is near a zenith angle corresponding to the mantle-core transition (see Table 4.1, p. 46) where the precision suffers from the kink in the oscillation probabilities which is not visible at these energies with the naked eye. The precision reaches values better than the desired value of 0.1% over many parts of the zenith angle range when increasing I and K further to 8. Relatively large deviations remain near the mantle-core transition indicating that more data points are needed there.

Figure 5.2 shows how the precision changes as a function of I for higher values of I up to 16. Here, the degree of the interpolating polynomials are kept constant at $K = 8$. Increasing I to 12 improves the precision to values better than 0.01% in most of the zenith angle space with $\cos\theta > -0.78$. In two regions which correspond to the layer transitions in the upper mantle at $\cos\theta = -0.45$ and $\cos\theta = -0.35$ (see also Table 4.1, p. 46), the precision has significantly worse values. At $\cos\theta < -0.78$, the precision gets worse in general (not visible in the figure) compared to the case of $I = 8$. The precision stays essentially the same near angles corresponding to Earth layer transitions when I gets increased to 16. Near the edge of $\cos\theta = -1$, the interpolation does not work properly anymore. However, for $-0.72 < \cos\theta < -0.55$ the precision gets even better[20] than 0.001%.

Finally, it is important to know how fast the interpolation works. The generation of an oscillogram with 895x1795 points via interpolating from an oscillogram with 150x300 points (between two points, five points are interpolated for both dimensions) takes about 37 seconds for $I = K = 8$. This yields an average number of 42 000 points interpolated per second. Given that the average number of points calculated by solving the equation of motion is about 7.1 per second, a speed-up by a factor of around 6000 is achieved. Taking $I = K = 6$, and thus a reduced precision, increases the speed-up to a factor of roughly 75 000. This also shows how strongly the time needed for the interpolation depends on the chosen numbers for I and K. For I and $K > 12$, the interpolation method becomes impractical[21].

---

[20] Note that with such a good interpolation precision the overall precision is limited by the method of solving the neutrino equation of motion (see also Section 4.1).

[21] Here, all reference computations were performed on a single “Intel Xeon X5650” CPU.

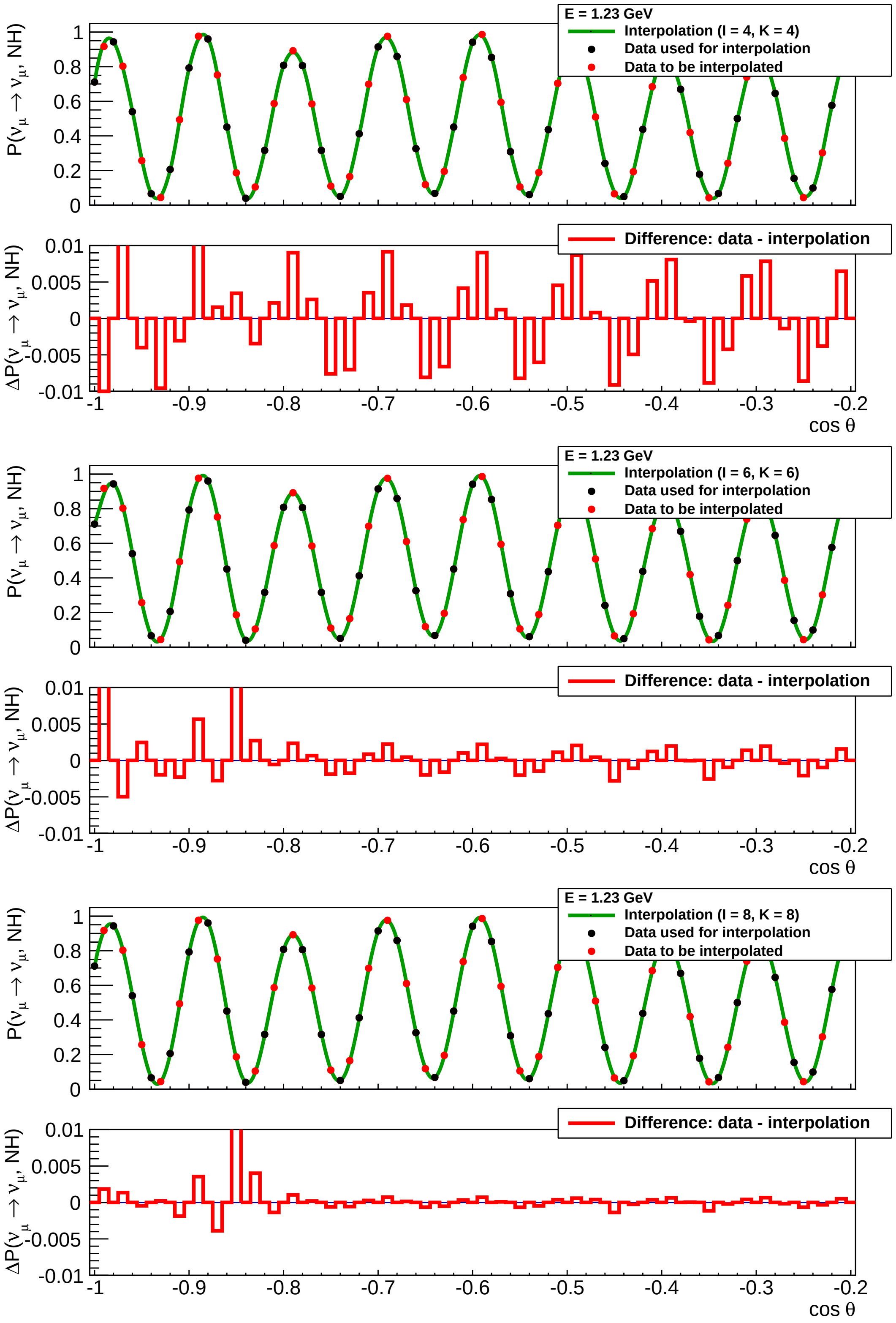

Figure 5.1: *Interpolation example of $P(\nu_\mu \rightarrow \nu_\mu, NH)$ with respect to $\cos\theta$ at E =1.23 GeV for the case of $I = K = 4$ (top), $I = K = 6$ (middle) and $I = K = 8$ (bottom). Data points used for the interpolation in general are shown as black dots, data points that are to be interpolated as red dots, and the interpolation is shown in green. For each case, also the differences between the data points and the interpolation are shown. In the case of $I = K = 8$, a precision of better than 0.1% is reached for most part of the zenith angle space. See discussion in the text.*

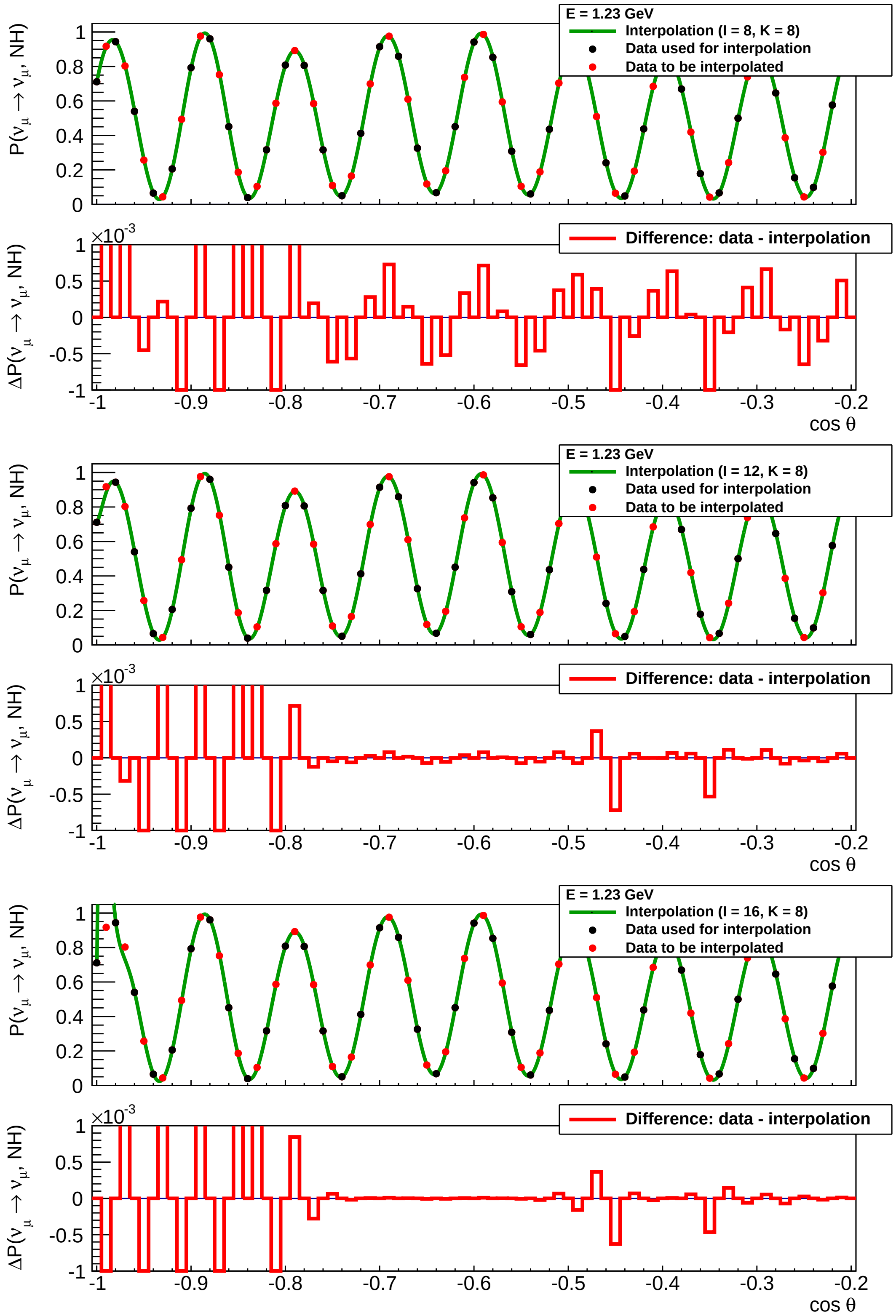

Figure 5.2: *Interpolation example of* $P(\nu_\mu \rightarrow \nu_\mu, NH)$ *with respect to* $\cos\theta$ *at* E *=1.23 GeV for* $K = 8$ *and* $I = 8$ *(top),* $I = 12$ *(middle) and* $I = 16$ *(bottom). Data points used for the interpolation in general are shown as black dots, data points that are to be interpolated as red dots, and the interpolation is shown in green. For each case, also the differences between the data points and the interpolation are shown. In the case of* $I = 16$*, a precision of better than 0.001% is reached for -0.72 <* $\cos\theta$ *< -0.55. See discussion in the text.*

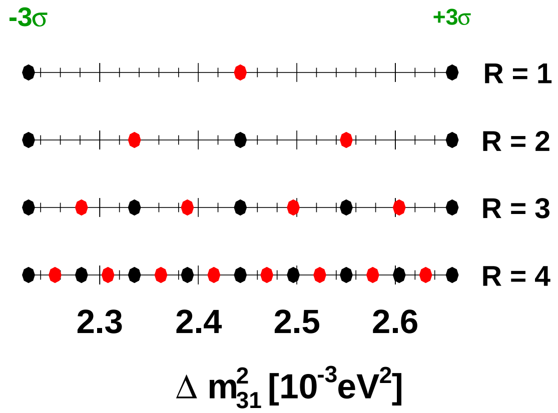

Figure 5.3: *Illustration of the data production method. As an example, the 3σ range for the Δm^2_{31}-axis is shown with increasing order R of data production. See text for details.*

5.3 Results

The interpolation method is used to get an estimate of how many oscillograms must be calculated to interpolate oscillation probabilities up to a precision of 0.1% in the six-dimensional oscillation parameter space defined by their 3σ ranges (see Table 4.2, p. 53). That is, the difference between the interpolated oscillation probability and the one calculated by solving the equation of motion must be smaller than 0.1% in the full parameter space. The order and the number of data points for the interpolation are chosen to be $K = 4$ and $I = 8$, respectively.

As mentioned previously, the interpolation is only performed along one dimension. The multi-dimensional interpolation is done by interpolating along one dimension at a time. First, within the oscillograms (with respect to $\log E$, then $\cos\theta$), and then between the oscillograms of different oscillation parameter values. The order there is θ_{12}, θ_{13}, θ_{23}, Δm^2_{21}, Δm^2_{31}, δ_{cp}. Though the order might influence the final result, no detailed studies on this topic have been performed.

Recall that an oscillogram as defined here gives the oscillation probabilities for one neutrino to oscillate into another neutrino for a given neutrino mass hierarchy in the $E - \cos\theta -$plane for $1 \le E/\text{GeV} \le 20$ and $-1 \le \cos\theta < 0$. Here, 100 data points distributed equidistantly along both the logarithm of the energy and cosine of the zenith angle were chosen.

To get the estimate, data is produced only for $P(\nu_\mu \to \nu_x, \text{NH})$, $x \in \{e, \mu, \tau\}$. For the production, a grid is defined with a spacing as illustrated in Figure 5.3 for each parameter. As a starting point, $3 = 2^1 + 1$ uniformly distributed points for each parameter are used, two at the edges of the 3σ range and one in the middle. This means, at the beginning a number of $3^6 = 729$ oscillograms are created. Then, it is checked if the 665 oscillograms corresponding to the middle points in the six-dimensional space can well be interpolated by the 64 oscillograms at the edges. Thereafter, the precision is checked by taking the maximum difference between an interpolated oscillogram and the oscillogram that is supposed to be interpolated. If this difference exceeds 0.1% for the interpolation along a given dimension, additional oscillograms are created for that dimension so that $5 = 2^2 + 1$ equidistant points are covered. Now, it is checked if the oscillograms at the second and fourth point are well interpolated. This is done up to $2^R + 1$, $R \in \mathbb{N}$ points until the precision is good enough with R as the the "production order".

The final result is illustrated in Figure 5.4 and Table 5.1. It can be seen that for the unimpactful

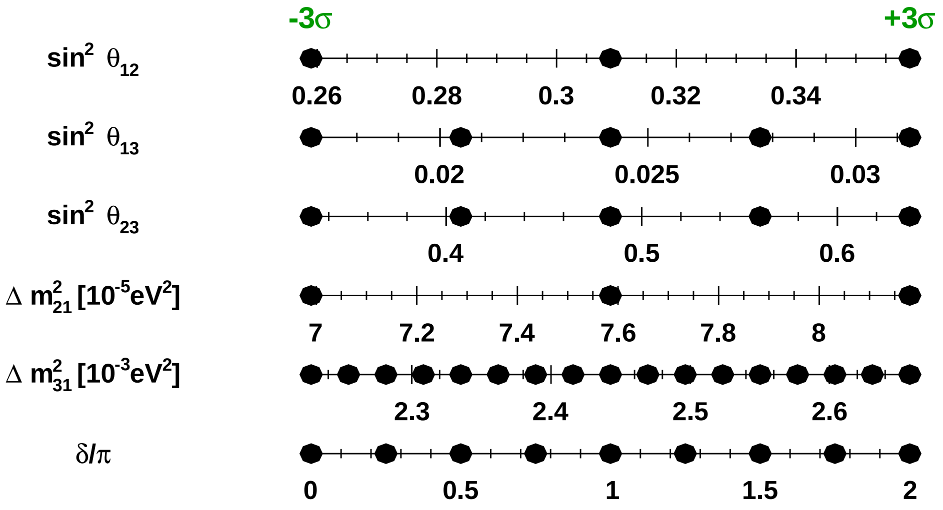

Figure 5.4: *Illustration of the final result for the estimate of data points that need to be covered to interpolate oscillation probabilities in the full six-dimensional 3σ space with the interpolation method developed in this chapter. Shown are the axis for the six oscillation parameters with dots indicating which points need to be covered in the parameter space to achieve an estimated precision of better than 0.1% in the full parameter space. See also Table 5.1.*

Oscillation parameter	R	N	Precision	R	N	Precision
$\sin^2\theta_{12}$	0	2	0.2%	1	3	0.005%*
$\sin^2\theta_{13}$	1	3	0.3%	2	5	0.004%*
$\sin^2\theta_{23}$	1	3	0.4%	2	5	0.003%*
Δm^2_{21}	0	2	0.1%	1	3	0.0008%*
Δm^2_{31}	3	9	6%	4	17	0.01%*
δ_{cp}	2	5	0.1%	3	9	0.0005%*

	Number of oscillograms	
Per channel	1 620	34 425
Total	12 960	275 400

Table 5.1: *Number of oscillograms that need to be created to interpolate all oscillation probabilities in the 3σ range of the six oscillation parameters. The top table shows how many data points along each dimension need to be covered to achieve the given precision in the interpolation along that dimension for two cases. In the second case, the * indicates that this precision has not been checked in the complete parameter space as not enough computing time was available and therefore gives only an estimate. Assuming this estimate is true everywhere, the precision requirement (0.1%) would be fulfilled in the full parameter space. The bottom table shows the number of oscillograms that need to be created per channel (starting neutrino type and hierarchy) and in total for the two cases.*

parameters θ_{12} and Δm^2_{21} (see also Section 4.3) only few points are needed. Along the Δm^2_{21} dimension, two points suffice to fulfil the precision requirement of 0.1% while for θ_{12} with two points it is almost fulfilled. For three points, the precision is already far better with values below 0.01%. For the two other mixing angles θ_{13} and θ_{23} which have a larger impact, five points are needed to get the necessary precision. The CP phase δ_{cp} has a similar impact on the oscillation probabilities but needs nine points along its dimension. For the most impactful parameter, the large mass squared difference Δm^2_{31}, 17 points need to be covered to achieve the required precision in the full parameter space. This large number originates from the strong variations in oscillation probabilities with Δm^2_{31} at low energies.

As mentioned above, these numbers were only checked for one neutrino type and hierarchy ($\nu_\mu \to \nu_x$, NH). For this channel, following the numbers above, 34 425 oscillograms need to be calculated. Assuming these numbers are true for all other channels, this number increases to 275 400. Recall that the creation of one oscillogram takes roughly 1.5 hours computing time with the numerical method utilised here to solve the equation of motion. Thus, the total computing time amounts to roughly 50 years. If one wants to check the achieved precision in the full parameter space, roughly $2^6 = 64$ times more oscillograms need to be produced making the required computing time impractical. Thus, it is very much desirable to improve the methodology of calculating oscillation probabilities. This can be done in various ways, some of which will be discussed in the next section.

5.4 Possible improvements

In the previous section, it has been shown that with the used interpolation algorithm, the computation time needed to produce sufficient oscillograms is of the order of some tens of years. To reduce this time, a more sophisticated procedure is needed for the calculation of the oscillation probabilities. This section discusses possibilities to achieve this.

The first possibility would be an optimisation of the grid starting with distribution of data points in the $E-\cos\theta-$plane. Considering the fact that the oscillations in vacuum depend on $1/E$, data points should be distributed equidistantly with respect to $1/E$ (as opposed to $\log E$ utilised here)[22].

Regarding the interpolation in $\cos\theta$ space, the examples of Figure 5.1 and 5.2 show that more data points need to be produced around zenith angles corresponding to layer transitions (i.e. the kinks in the oscillograms).

The grid in the $E-\cos\theta-$plane can be further optimised by letting the number of generated data points along zenith angle vary as a function of energy, and along energy vary as a function of zenith angle (as opposed to a constant number utilised here). Looking at an oscillogram like e.g. Figure 4.1 (p. 47), many oscillations occur at steep zenith angles and low energies, and only few or none at near horizontal angles and large energies. Regarding this, initial studies have been performed. Preliminary results show for instance that at $E = 20\,\text{GeV}$, ten data points within $-1 \leq \cos\theta \leq 0$ might suffice, while at $\cos\theta = 0$ only four points along $1 \leq E/\text{GeV} \leq 20$ are needed. The number of points needed for a complete oscillogram might be reducible by a factor of about two.

Similar arguments apply to the grid in the oscillation parameter space. As has been shown in Section 4.3, the oscillation probabilities show strong dependence on some of the oscillation parameters at low energies and zenith angles. Thus, the optimal six-dimensional grid should be denser

---

[22] The equivalent of this has already been done for the zenith angle: the length of the neutrino path through Earth, which is directly related to the number of oscillation periods in vacuum, is determined by the cosine of the zenith angle. Therefore, an equidistant distribution of data point with respect to the cosine of the zenith angle is reasonable.

there.

A further possibility of improvement concerns the interpolation method. Given the fact that oscillation probabilities and therefore oscillations are to be interpolated, a good ansatz might be to consider trigonometric interpolation. In trigonometric interpolation, Fourier polynomials are used for the interpolation. In general, this is applicable for a strict periodic function where several periods are gone through. Therefore, it is best applicable with respect to energy and zenith angles in regions of the parameter space where matter effects are negligible and where many oscillations happen, and with respect to the large mass squared difference at low energies. Note though, as mentioned above, for the interpolation with respect to energy and zenith angle, the oscillation probability should then be modelled as a function of $1/E$ and $\cos\theta$. Furthermore, another possibility could be to combine several interpolation methods.

Another possibility concerns solving the equation of motion and the Earth model. In the last years, and also used in ORCA sensitivity studies (see e.g. [7]), algorithms have been developed to solve the neutrino equation of motion that model the Earth as a number of layers with constant density. In Section 4.4, the investigation of the dependence of the oscillation probabilities on the transition smoothness showed implicitly that this is an appropriate approximation as the oscillation probabilities are rather independent of the way of a density change over a distance of smaller than roughly 100 km. Thus, the relatively slight density change within a layer can be modelled via steps of constant density. Compared to the numerical solution employed here, a speed-up by a factor of about 10 to 100 is possible [83]. However, further in-depth precision comparisons have to be performed.

5.5 Summary

In this chapter a method has been derived to interpolate oscillation probabilities in the eight-dimensional parameter space given by the six oscillation parameters and the neutrino energy and zenith angle. The ultimate goal is the reduction of the computing time needs during ORCA sensitivity studies where the calculation of the oscillation probabilities is a major bottleneck.

The formulae used for the interpolation have been derived based on Taylor expansions around given data points. They show high flexibility as the number of data points used for the expansion can be chosen freely and the order of the expansion is only limited by the chosen number of data points. At the same time a very high precision is achievable with these formulae as shown in Section 5.2.

The interpolation in the oscillation parameter space was based on oscillograms. An estimate for the total number of oscillograms needed to incorporate the full $3\,\sigma$ space of the oscillation parameters has been determined. Also the parameters that need the most oscillograms to be calculated (along their dimension) have been identified. The results were in agreement with the studies presented in Chapter 4. However, the total number of oscillograms needed, several 100 000, to achieve a precision[23] of better than 0.1% requires very large computational resources of more than 50 CPU years with the method derived here[24]. Therefore, several possibilities for improvement have been

---

[23] The precision requirement of 0.1% was chosen conservatively. The expected precision of the ORCA detector regarding neutrino event rates in the $E-\cos\theta-$plane is of the order of a few percent [7]. Systematic errors introduced via the calculation of the oscillation probabilities should therefore be much less which is achieved with the chosen precision requirement.

[24] The reference CPU here corresponds to an “Intel Xeon X5650”.

identified and discussed in Section 5.4. Among them is the optimisation of the grid of data points in the full eight-dimensional parameter space, as for most parameters it holds that more points are needed at low energies and fewer at high energies. This will not only reduce the required CPU time but also the required disk space.

Regarding the final computation time needed during the sensitivity studies, the oscillation probabilities then do not have to be produced by solving the equation of motion any more. Instead, a pre-defined set of oscillation probabilities in the eight-dimensional parameter space would be produced in advance, and the remaining oscillation probabilities would be interpolated on the fly from this pre-generated data. Comparing both methods the average time needed to calculate the oscillation probability for a single point in the parameter space is reduced by at least three orders of magnitude[25].

---

[25] This assumes the treatment of the Earth as many layers of constant density as done in current sensitivity analyses [7,83]. The computing time would be reduced by at least five orders of magnitude in comparison to the calculations where the Earth is treated exactly according to the PREM.

Part III

Preparations for the ARCA diffuse flux sensitivity analysis

This part is about the key elements of the diffuse flux sensitivity analysis for ARCA. This includes event simulation (Chapter 6) and event reconstruction (Chapter 7). The different event reconstruction algorithms yield parameters that describe single reconstructed events and are the basic ingredients of the sensitivity analysis. The preprocessing of these parameters is described in Chapter 8. One aspect of the preprocessing is finding the parameters which are helpful for the classification of signal and background events. The classification uses a machine learning algorithm based on "boosted decision trees". It is described in the last chapter of this part (Chapter 9). The result of the classification is then used to evaluate the sensitivity of ARCA to diffuse neutrino fluxes as described in Part IV.

With the measurements by IceCube published in 2013 [3] including the detection of 28 high-energy shower events and giving evidence for a diffuse cosmic neutrino flux, the importance of the shower channel for high-energy neutrino telescopes was established. For this reason, the procedures and methods as described in Chapter 8 and 9 were initially developed and optimised for detecting neutrinos in the shower channel (shower search). They were afterwards extended also for a search in the track channel (track search). Intermediate results for both searches will be described in parallel.

The analysis was optimised with respect to the all-flavour diffuse flux as first published by IceCube [3]. In order to prevent a bias towards very-high-energy events (not observed by IceCube) a cut-off at 3 PeV was added (compare Eq. (2.7)):

$$\Phi(E) = 3.6 \cdot 10^{-18} \cdot \left(\frac{E}{100\,\mathrm{TeV}}\right)^{-2} \cdot \exp\left(-\frac{E}{3\,\mathrm{PeV}}\right) \left(\mathrm{cm}^2\,\mathrm{s}\,\mathrm{sr}\,\mathrm{GeV}\right)^{-1}.$$

Throughout this part of the thesis, whenever signal events are mentioned, events according to this flux are considered.

Chapter 6

Simulation

A complete simulation of the ARCA experiment is fundamental to assess the expected performance of the telescope. This chapter describes the simulations utilised for the work presented in this thesis. The simulation data have been generated by the KM3NeT collaboration from existing tools that have been adjusted taking into account the special design and location of the ARCA detector as described in Section 3.1. Each building block is treated identically and independently, i.e. the simulations are performed for one building block.

The simulation chain consists of three main parts that are described in the following sections: 1) the generation of physics events like neutrino interactions and atmospheric muons passing the detector, including the production of secondary particles[26]; 2) the propagation of the secondary particles and the production and propagation of Cherenkov photons; and 3) the simulation of the detector response, covering the light detection process and the subsequent event triggering. In this last part also the omnipresent ^{40}K background is taken into account.

Section 6.1 presents the event generation including the treatment of secondary particles. Section 6.2 describes the Cherenkov light production and detection. The event weighting scheme for the neutrino events, allowing for the calculation of the event rate for an arbitrary neutrino flux, is described in Section 6.3.

6.1 Event generation

For the event generation the detector volume is approximated by a cylinder with radius of 504 m and height of 612 m. Two cylindrical volumes surrounding the detector are defined called *“can”* and *“generation volume”*.

The *can* is the relevant volume for Cherenkov light production. It extends the detector in radius and above by roughly 200 m. Below, it is limited by the seabed which is roughly 80 m below the lowest DOMs. Cherenkov processes outside the can produce insufficient light to contribute to a significant detection.

The *generation volume* is the volume within which neutrino interactions are simulated and is chosen so that events outside of it only have a negligible chance of being detected. Its size depends on the neutrino type and interaction channel. For shower events the generation volume is chosen equal to the can, whereas for events with a long track the generation volume exceeds the can by up to several kilometres, according to the energy-dependent track range.

---

[26] Secondary particles describe here all particles relevant for the Cherenkov light production.

production type		$N_{\text{sim}}/10^5$	T_{live}
atm. μ	$E > 10$ TeV	250	87 days
	$E > 50$ TeV	80	36 months
$(\nu_e + \bar{\nu}_e)$ CC		20	$> 10^4$ years
$(\nu_\mu + \bar{\nu}_\mu)$ CC		$2.0 \cdot 10^5$	
$(\nu_{e,\mu} + \bar{\nu}_{e,\mu})$ NC		40	
$(\nu_\tau + \bar{\nu}_\tau)$ CC → shower		$2.0 \cdot 10^5$	
$(\nu_\tau + \bar{\nu}_\tau)$ CC → μ		$2.0 \cdot 10^6$	
$(\nu_\tau + \bar{\nu}_\tau)$ NC		100	
EAS	10-50 TeV	610	17 minutes
	50-200 TeV	410	170 minutes
	200-1000 TeV	200	14 hours
	1-5 PeV	28	28 hours
	5-20 PeV	16	12 days
	20-100 PeV	11	120 days
	100-500 PeV	4.9	39 months
	500-2000 PeV	2.2	32 years
	2-10 EeV	1.5	320 years

Table 6.1: *Rounded numbers of simulated events and corresponding livetime for the three types of event production used in this work: atmospheric muons, neutrinos and extensive air showers (EAS). The neutrino production is subdivided according to the interaction type: charged current (CC) and neutral current (NC). The tau-neutrino CC production is further separated according to the decay mode of the outgoing tau (shower or muon). The given livetime for neutrinos holds for energies above 10 TeV.*

In the following, the event generation for the different event types is explained in detail. This also includes a separate production for atmospheric neutrino events in coincidence with muons from the same cosmic air shower. For these the full extensive air showers (EAS) are simulated. Table 6.1 gives a summary of the numbers of simulated events and the corresponding livetimes for each production.

Neutrinos

In the standard neutrino event production, neutrino interactions of all types (ν_e, ν_μ, ν_τ, charged current (CC) and neutral current (NC)) are simulated with the GENHEN software package [84] in the energy range from 10^2 to 10^8 GeV. GENHEN takes into account neutrino absorption in the

Earth[27]. The neutrinos are forced to interact in the generation volume and the interaction products relevant for Cherenkov light production are stored. For events outside the can, the secondary long-range particles (muons and taus) are propagated to the surface of the can. In case of muons this is done using MUSIC [85] whereas taus are propagated as minimally ionising particles and decayed with TAUOLA [86]. If the secondary particles do not reach the can the event is discarded. In order to account for the much larger generation volume for the track channel compared to the shower channel, the number of simulated events is chosen appropriately larger (see Table 6.1). The simulated livetime corresponds to more than 10^4 years for both the atmospheric and cosmic neutrino flux for energies larger than 10 TeV.

The events are generated isotropically and according to an energy spectrum with spectral index $\gamma = -1.4$. Afterwards, the events can be reweighted to an arbitrary flux (see Section 6.3). The deep-inelastic scattering cross-section is implemented via the LEPTO code [87] using the CTEQ6D [88] parton distribution functions. The Glashow resonance is taken into account using the leading-order electroweak cross-section.

For each event, the interaction parameters as well as the four-momenta and generation positions of the neutrino and secondary particles are stored for further processing.

Atmospheric muons

The atmospheric muon background is simulated with MUPAGE [67,68]. With this Monte Carlo generator, atmospheric muon events are generated according to a parameterisation of the energy- and zenith-angle-dependent underwater flux of atmospheric muons for a given under-water depth. Muon bundles and the corresponding energy distribution of the muons within a bundle are also accounted for.

Two samples with different lower energy thresholds are used, $E > 10$ TeV and $E > 50$ TeV, with livetimes of roughly three months and three years, respectively (see Table 6.1). Here, E corresponds to the total energy of a muon bundle. The muon events are stored on the surface of the can. The information of a single event includes the bundle multiplicity as well as the four-momentum and generation position of every single muon in the bundle.

Extensive air showers

In order to account for the fact that atmospheric neutrinos coming from above are very likely accompanied by muons from the same extensive air shower (EAS), a separate simulation has been performed with CORSIKA [89]. The main purpose of this simulation is to estimate the “self-veto” [43,44] capabilities of ARCA. Self-veto refers here to the fact that neutrinos accompanied by muons can be identified as atmospheric neutrinos. Therefore, this effect helps to differentiate between atmospheric and cosmic neutrinos.

CORSIKA simulates atmospheric air showers according to a given spectrum of cosmic rays entering the atmosphere. Neutrinos and muons created in the air showers are recorded for further processing when they reach sea level. Muons are propagated to and through the can with MUSIC [85] and an accompanying neutrino is then forced to interact within the instrumented volume. The event is properly weighted so that it can be used together with the GENHEN simulations described above (see also Section 6.3).

---

[27] Note that, in the present simulation chain, neutrinos emerging from interactions of neutrinos on their way through Earth (regeneration effects) are ignored.

The simulations were performed for zenith angles smaller than 87° (above the horizon) and have been divided into nine regions regarding the energy of the incident cosmic rays. The number of simulated events and corresponding livetimes are listed in Table 6.1.

The status of these simulations is still preliminary as only neutrino interactions within the instrumented volume are simulated and interacting neutrinos are required to have an energy above 10 TeV. In addition, the statistics at highest simulated energies is rather small. Therefore, these simulations are used only when explicitly mentioned.

6.2 Light production and detection

In order to simulate the number and detection time of Cherenkov photons detected by the optical modules, tabulated results from full GEANT 3.21 [90] simulations of the charged secondary particles are used. These include simulations of relativistic muons and electromagnetic showers. The light production from hadronic or mixed showers is scaled to purely electromagnetic showers according to the particle types present in the shower and according to the energy of these particles. The Cherenkov light spectrum according to Eq. (2.28) and the wavelength-dependent absorption and scattering lengths at the KM3NeT/ARCA site are taken into account [84,91].

The simulation of the photon detection process is described in detail in [92]. It includes the characteristics and geometry of the digital optical module, the photo-multiplier tubes (PMTs) employed and the internal electronics. In particular, it accounts for the absorption in the glass sphere and optical gel, the physics of the reflection cone [93] as well as the photon detection probability as a function of the photon angle of incidence which also includes the quantum efficiency of the PMTs.

Hits in the PMTs are recorded by their start time and time over threshold (ToT). The ToT is the time during which the electronic signal caused by incident photons exceeds a given threshold and is therefore related to the signal strength. The exact dependence on the number of photoelectrons ejected in a short time window has been measured in the laboratory [94]. This also includes saturation effects setting in at around 40 simultaneous photoelectrons. In addition, a transit-time spread is simulated based on a Gaussian with a standard deviation of 1 ns. The transit time corresponds to the time between the electron being ejected from the photocathode and the actual measurement of the signal at the anode and is subject to statistical fluctuations.

After the hits of an event are generated, hits from ^{40}K-background noise are added. This noise corresponds to a rate of 5 kHz single hits per PMT as well as (2, 3, 4)-fold coincidences with rates of (500, 50, 5) Hz per DOM, in agreement with measurements of the prototype detection unit [65]. The noise hits are added to the event during a time window of ±500 ns around the event. On the complete set of hits from an event, the standard trigger algorithms are applied as they would be on real data.

6.3 Effective area and event weighting

For a given type of neutrino and corresponding flux $\Phi(E,\theta)$ depending on energy E and zenith angle θ, the expected event rate R is given by the following integral:

$$R = -2\pi \iint A_{\mathrm{eff}}(E,\theta)\,\Phi(E,\theta)\,\mathrm{d}\cos\theta\,\mathrm{d}E. \tag{6.1}$$

For this expression it is assumed that the detector is symmetric with respect to the azimuth angle which is true for ARCA in good approximation. The effective area $A_{\mathrm{eff}}(E,\theta)$, reflecting the detector response, is given by:

$$A_{\text{eff}}(E,\theta) = P_{\text{Earth}}(E,\theta)\,\sigma(E) \int\limits_{V_{\text{active}}} \rho_N(\boldsymbol{r})\,\varepsilon(E,\theta,\boldsymbol{r})\,\mathrm{d}V\,, \tag{6.2}$$

where $P_{\text{Earth}}(E,\theta)$ is the probability for a neutrino to traverse the Earth unabsorbed, $\sigma(E)$ is the total neutrino interaction cross-section per nucleon. The integration is performed over the active volume V_{active} of the detector, i.e. the volume within which detectable neutrino interactions occur. For simulation purposes it is chosen equal to the generation volume V_{gen}. The quantities in the integrand are the nucleon density $\rho_N(\boldsymbol{r})$ and the detection efficiency $\varepsilon(E,\theta,\boldsymbol{r})$. Both are in general functions of the position $\boldsymbol{r}$. The nucleon density can be calculated from the matter density $\rho(\boldsymbol{r})$ and mean nucleon mass m_N of the target material[28] $\rho_N(\boldsymbol{r}) = \rho(\boldsymbol{r})/m_N$. The detection efficiency gives the probability that an event is detected.

The detection efficiency is evaluated based on the Monte Carlo simulations described in the previous sections. The effective area and the expected event rate are then evaluated by means of Monte Carlo integration (see e.g. [95]). The neutrino events are generated with an energy spectrum according to a power law[29] with spectral index $\gamma = -1.4$: $\mathrm{d}N_{\text{gen}} \propto E^{-1.4}\,\mathrm{d}E = -2.5\,\mathrm{d}(E^{-0.4})$. With respect to the generation volume and the cosine of zenith angle, the events are generated uniformly distributed. Using Eq. (6.2), the expected event rate (Eq. (6.1)) from neutrinos in an energy and zenith angle phase space given via $[E_{\text{min}}, E_{\text{max}}]$ and $[\theta_{\text{min}}, \theta_{\text{max}}]$, is written as:

$$R = 5\pi \int\limits_{E_{\text{min}}}^{E_{\text{max}}} \int\limits_{\cos\theta_{\text{min}}}^{\cos\theta_{\text{max}}} \int\limits_{V_{\text{gen}}} P_{\text{Earth}}(E,\theta)\,\sigma(E)\,\rho_N(\boldsymbol{r})\,\varepsilon(E,\theta,\boldsymbol{r})\,\Phi(E,\theta)\,E^{1.4}\,\mathrm{d}V\,\mathrm{d}\cos\theta\,\mathrm{d}(E^{-0.4}), \tag{6.3}$$

and via Monte Carlo integration it follows:

$$R = \frac{S}{N_{\text{gen}}} \sum_{i=1}^{N_{\text{gen}}} P_{\text{Earth}}(E_i,\theta_i)\,\sigma(E_i)\,\rho_N(\boldsymbol{r}_i)\,\varepsilon(E_i,\theta_i,\boldsymbol{r}_i)\,\Phi(E_i,\theta_i)\,E_i^{1.4}, \tag{6.4}$$

with S given by:

$$S = 5\pi\,V_{\text{gen}}\,(\cos\theta_{\text{max}} - \cos\theta_{\text{min}})\left(E_{\text{max}}^{-0.4} - E_{\text{min}}^{-0.4}\right), \tag{6.5}$$

and N_{gen} is the number of events generated in the phase space defined above. E_i, θ_i and $\boldsymbol{r}_i$ are the energy, zenith angle, and interaction vertex position of the i-th event, respectively. The detection efficiency $\varepsilon(E_i,\theta_i,\boldsymbol{r}_i)$ takes now values of either 1 or 0 depending on whether the event is detected or not. The detection can be associated with any selection criterion, e.g. the event gets triggered or is well reconstructed. Thus, the event rate can be evaluated for any set of selection cuts (see also Chapter 10).

With the definition of a corresponding event weight w_i

$$w_i = S\,P_{\text{Earth}}(E_i,\theta_i)\,\sigma(E_i)\,\rho_N(\boldsymbol{r}_i)\,\varepsilon(E_i,\theta_i,\boldsymbol{r}_i)\,E_i^{1.4}, \tag{6.6}$$

---

[28] Strictly speaking, the mathematical expression of Eq. (6.2) only takes into account neutrino-nucleon interactions. For electron antineutrinos, however, also the interactions with electrons are relevant (Glashow resonance, Section 2.3). These can be incorporated by adjusting the total neutrino cross-section: $\sigma = \sigma_N + 10/18\ \sigma_{e^-}$ as there are approximately 10 electrons per 18 nucleons in sea water (with σ_N the neutrino-nucleon and σ_{e^-} the neutrino-electron cross-section).

[29] This is done to have a reasonable number of simulated events in each energy decade.

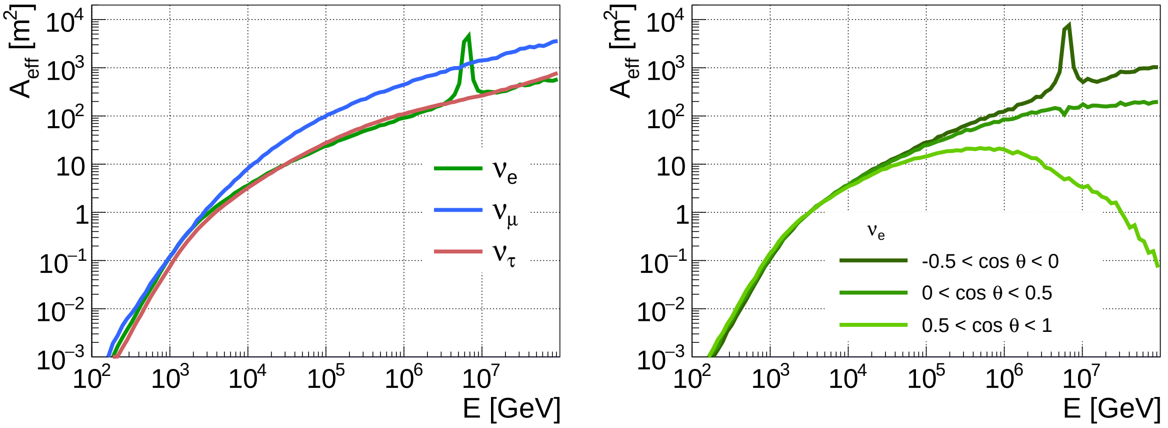

Figure 6.1: *Effective area at reconstruction level (see also next chapter) for the three neutrino types averaged over zenith angle (left) and for electron neutrinos averaged over three different zenith angle bands (right).*

the event rate can be calculated as follows:

$$R = \frac{1}{N_{\text{gen}}} \sum_{i=1}^{N_{\text{gen}}} w_i \, \Phi(E_i, \theta_i). \tag{6.7}$$

Thus, with the help of the event weights the simulations can be used to calculate the event rate for an arbitrary flux.

In addition, with the same integration method a mean effective area can be calculated for the defined integration range:

$$A_{\text{eff}} = \frac{V_{\text{gen}}}{N_{\text{gen}}} \sum_{i=1}^{N_{\text{gen}}} P_{\text{Earth}}(E_i, \theta_i) \, \sigma(E_i) \rho_N(\boldsymbol{r}_i) \, \varepsilon(E_i, \theta_i, \boldsymbol{r}_i). \tag{6.8}$$

The effective area at reconstruction level (see also next chapter) as a function of energy, averaged over zenith angle and over ν and $\bar{\nu}$, for the three neutrino types is shown in Figure 6.1 (left). In order to illustrate neutrino absorption in the Earth at high energies and large zenith angles, Figure 6.1 (right) shows the corresponding effective area for electron neutrinos averaged over three different zenith angle bands. At low energies and small zenith angles, the energy dependence follows mainly that of the neutrino cross-section (see also Figure 2.8, p. 31). The effective area is largest for muon neutrinos as the emerging muon from charge-current events may reach the detector from far away so that the detection probability ε is non-zero.

EAS-simulation reweighting

It has been mentioned in Section 6.1 that simulations of extensive air showers (EAS) are used to estimate the rate of atmospheric neutrinos accompanied by muons of the same air shower. From these simulations, also the fractions of atmospheric neutrinos accompanied or unaccompanied by muons are determined. In order to take the neutrino events accompanied by muons into account properly, a reweighting is performed. First of all, such an event is reweighted according to the probability for any of the high-energy neutrinos present in the air shower to interact. Then, given the fractions of accompanied and unaccompanied events, the standard GENHEN production of (unaccompanied) neutrinos coming from above is down-weighted so that the sum of both productions represents the total expected rate of atmospheric neutrino events. As only neutrino energies above 10 TeV and events within the instrumented volume are considered for this separate production, low-energy events and events outside the instrumented volume from the standard production are kept unmodified. For more details see [96]. Due to the preliminary status of these simulations, their results are only used when explicitly mentioned.

Chapter 7

Event reconstruction

Being able to determine the energy and direction of an event is essential for performing neutrino astronomy. Furthermore, distinguishing different event topologies is essential for background reduction and neutrino flavour identification. All of this is done in ARCA with the help of event reconstruction algorithms. In this chapter, the available reconstruction algorithms will be described, for shower (Section 7.1) and track reconstruction (Section 7.2). The reconstruction parameters that they provide and which are discussed in Section 7.3 are used later in this work (Chapter 9) to distinguish signal from background events. More detailed descriptions of the reconstruction algorithms can be found in [97,98].

7.1 Shower reconstruction

The main characteristics of a shower event are the vertex position and time, the deposited energy and the direction. Three independent algorithms have been developed within the KM3NeT collaboration for the purpose of reconstructing these parameters (see also [98]). These algorithms will be denoted *Shower Reconstruction Algorithm 1-3* in the following, or in short SR1-3. Shower Reconstruction Algorithm 1 has been specifically designed for the ARCA experiment and exhibits the best performance. The other two were originally developed for the ANTARES experiment in the SeaTray [99] framework and have afterwards been adapted to the ARCA detector design. Building upon the experience with ANTARES, they provide many parameters that are helpful for the identification of the event topology (Section 2.4). They prove also very useful in background suppression.

For the reconstruction of the vertex position (space and time), in all three algorithms the Cherenkov light is assumed to originate from a point source given as the hypothetical interaction vertex (spherical light emission). From this assumption, a *time residual* t_r is defined. It is given for each hit as the time difference between the measured hit time t_m and the expected hit time t_e:

$$t_r = t_\mathrm{m} - t_\mathrm{e} \tag{7.1}$$

In order to find the reconstructed vertex, the time residuals are minimised according to an M-estimator (see below). Each algorithm uses a proper hit selection aiming to reject noise hits that would otherwise disturb the minimisation. The time residuals are also important for event discrimination purposes. After the vertex has been reconstructed, the direction and energy are reconstructed. In the following, the procedures for each of the three reconstruction algorithms are described.

7.1.1 Algorithm 1

Shower Reconstruction Algorithm 1 focuses on energy and direction reconstruction of showers within the instrumented detector volume. It takes full advantage of the directional information provided by the KM3NeT multi-PMT DOM design. Nevertheless, it is kept simple thereby ensuring a fast reconstruction. This is accomplished via hit-merging: Hits in a time window of 350 ns on the same PMT are merged into a single hit. The merged hit is assigned the time of the first hit. Given the merged hits, coincidences of two hits on the same DOM within 20 ns on different PMTs are selected for further processing. Time residuals are calculated from the merged hits. For the vertex reconstruction, a minimisation of the time residuals is performed using the following M-estimator:

$$M = \sum_{i=1}^{N_{\text{hits}}} \sqrt{1 + t_{r,i}^2}. \tag{7.2}$$

Here, N_{hits} is the number of selected hits and $t_{r,i}$ is the time residual of the i-th hit. With this method the shower maximum, which is shifted a few metres from the actual interaction vertex, is found with a precision of better than 0.5 m for showers with energies between 100 TeV and 1 PeV and "well contained" within the instrumented detector volume [98]. Here, "well contained" means that the distance between the interaction vertex and the detector centre is smaller than 380 m in radius and smaller than 260 m in height. Recall that the detector borders are at roughly 500 m in radius and 300 m in height.

For the direction and energy reconstruction a maximum-likelihood fit is performed based on counting the PMTs in a DOM that have a merged hit. The probability of a hit PMT in a given DOM can be modelled as a function of the following four event parameters:

- the shower energy,
- the distance between the interaction vertex and the DOM centre,
- the angle between the shower direction and a straight line from the interaction vertex to the DOM centre,
- the orientation of the hit PMT with respect to a straight line from the interaction vertex to the DOM centre.

From Monte Carlo simulations the mean number of detected photons as a function of the three latter parameters is determined. The linear dependence on the shower energy is incorporated via a simple parameterisation [100]. Afterwards, the mean number of expected noise hits in a 1000 ns time window around the Cherenkov-light front (-100 ns to +900 ns) is added to get the expected total number of hits μ_i on the i-th PMT. Using the probability to observe zero events, $P_i = e^{-\mu_i}$, for the i-th PMT, the log-likelihood is defined as:

$$\log L = \sum_{i}^{\text{empty PMTs}} \log(P_i) + \sum_{i}^{\text{hit PMTs}} \log(1 - P_i). \tag{7.3}$$

The first sum is evaluated over all PMTs with no hit, the second one over all PMTs having at least one hit. The likelihood is maximised with respect to the shower direction and energy. The achieved resolution for contained (definition like above) events above 50 TeV reaches 10% in energy and 2° in direction (see also Section 10.2.3 and [98]).

7.1.2 Algorithm 2

Shower Reconstruction Algorithm 2 is based on four consecutive steps of hit selections and fitting [101]. In the first step, a first-guess vertex position is chosen as the mean space-time position of triggered hits. The second step performs a hit selection rejecting hits that are not causally correlated with the first-guess vertex. With the hits of the second selection a time-residual minimisation is performed to find the final vertex position. The M-estimator used for this purpose is equivalent to that used in SR1 (Eq. (7.2)).

The last step consists of the energy and direction reconstruction. The energy is estimated from the total charge of selected hits taking into account the distances between hit PMTs and vertex position. The direction estimate is derived from the mean light direction of all selected hits. This method achieves a mean vertex resolution of 6 m and an energy resolution of less than 0.4 units in $\log E$ [98]. The precision on the direction reconstruction, however, is negligible compared to the other algorithms.

7.1.3 Algorithm 3

Shower Reconstruction Algorithm 3 starts with a selection of hits with ToT greater than 25 ns to reduce the number of noise hits. Then, hits in coincidence with the selected hits are added to the sample. The earliest hit in the sample is used as a first guess for the vertex position. To improve this guess a simple scan fit is performed giving a pre-fit vertex. With the help of this vertex estimate a final hit selection is performed by applying a time-residual cut and further constraints [102].

The selected hits are used for a final reconstruction of the vertex and the subsequent energy and direction reconstruction, each of them based on maximum-likelihood approaches. For the maximum-likelihood fits, probability density functions (PDFs) are used that were generated from Monte Carlo simulations. The PDFs give the probability that a hit stems from a certain shower hypothesis. The PDF for the vertex reconstruction has two parameters: 1) the distance between a DOM and the vertex, and 2) the photon propagation time from the vertex to the DOM. For the energy and direction reconstruction a PDF as a function of three parameters is used: 1) the light emission direction with respect to the initial neutrino direction, 2) the amount of light measured in the PMTs and 3) the shower energy. For more details see [102]. The mean vertex resolution achieved amounts to 5 m, the energy resolution to roughly 20% and the direction resolution to about 5° [98].

7.2 Track reconstruction

The aim of a track reconstruction (TR) is to reconstruct the trajectory of a muon going through the detector. The direction of the trajectory can then be related to the direction of the parent neutrino[30]. From the number of hits consistent with the trajectory, the muon energy can be estimated (see also Eq. (2.30)). This energy can be taken as a minimum energy of the parent neutrino. For the work presented in this thesis, a single track reconstruction was used which will be described in the following. The algorithm has been developed for the ANTARES experiment and then adopted to the design of the ARCA detector. For more details see also [97,103].

The reconstruction algorithm begins with a hit selection aiming for a high fraction of signal hits. This is achieved by looking for space-time coincidences in the hit pattern among PMTs of the same

---

[30] In the case the muon was created in a neutrino interaction.

event class	atm. μ ($E_\mu > 10\,\text{TeV}$)	conventional atm. ν	prompt atm. ν	signal ν
event rate [y^{-1}]	48 000 000	80 000	460	400

Table 7.1: *Expected rates in ARCA at reconstruction level (signal events according to the flux given on page 93). Recall that the rate of atmospheric muons corresponds to those with bundle energy E_μ exceeding 10 TeV. More atmospheric muons with lower bundle energy are expected to be reconstructed.*

DOM, among adjacent and next-to-adjacent DOMs on the same string, and among DOMs on neighbouring strings. The search for coincidences takes into account the travel speed of the muon and the speed of light in sea water as well as the probability of random coincidences from noise.

After the initial hit selection, four consecutive fitting steps are performed to reconstruct the muon direction. At first, a parameterised straight line representing the muon track is fitted assuming that hits occur along the track. The corresponding system of equations, which is in general overdetermined, is solved by introducing hit position uncertainties and minimising the resulting chi-squared [103]. This pre-fit is improved with an M-estimator fit minimising the time residuals according to Eq. (7.2). Here, the time residuals are calculated assuming that the hits stem from direct Cherenkov photons coming from the muon track. The last two steps improve the result by introducing a full-sky scan of the muon direction and applying maximum-likelihood fits to the corresponding tracks. The likelihood fits are based on probability density functions (PDFs) for the time residuals. In the first of these two fitting steps, a PDF without considering noise hits is used. The second fitting step improves the result by using a PDF taking noise hits into accounts.

With the resulting track, a median angular resolution of 0.2° for incoming muons above 10 TeV is achieved (see also Section 10.2.3 and [97]). The muon energy is estimated from the number of hits consistent with the fitted track. The resolution for contained muons above 10 TeV reaches roughly 0.3 units in $\log E_\mu$ [97].

Furthermore, a track length is calculated by back-projecting photon hits onto the fitted track and taking the first and last of those hits as start and end point. The start point is also used as a pseudo-vertex position which, in case of an incoming muon, refers to the entry point of the track in the detector rather than the position of the neutrino interaction vertex.

7.3 Reconstruction parameters

The reconstruction algorithms produce several reconstruction parameters for each event. These parameters are the basis for the ARCA sensitivity study presented in this thesis and are used for the discrimination of signal from background. They can be classified as “standard reconstruction parameters” that are produced in each reconstruction algorithm, and other parameters especially designed for the respective reconstruction algorithm.

In the following, only events at reconstruction level are considered, i.e. the events have to pass the hit selection of all four reconstruction algorithms[31]. Table 7.1 lists the expected event rates at reconstruction level in ARCA for different event classes. As mentioned at the beginning of this part, for signal events the flux given on page 93 is considered.

Before the reconstruction parameters are discussed, probability distribution functions are defined as described in the following. These are helpful to illustrate significant differences in parameter

---

[31] Note that many shower events pass the hit selection of the track reconstruction algorithm, and vice versa, since the hit selections are designed rather loose in order to also allow low-energy events to pass the hit selections.

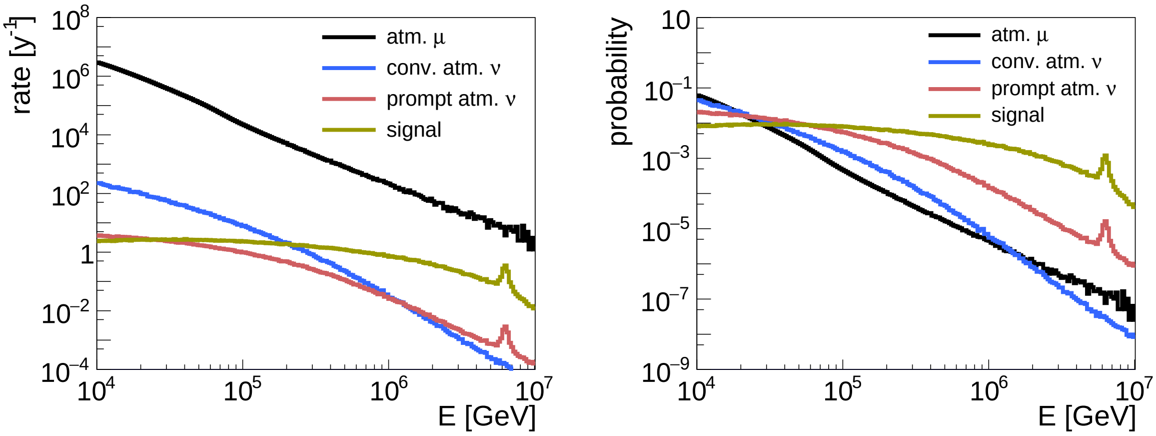

Figure 7.1: *Event rate distributions (left) and corresponding PDFs (right) with respect to energy for atmospheric muons, atmospheric conventional and prompt neutrinos, and signal neutrinos.*

distributions of different event classes.

Probability distribution functions

The expected rate of reconstructed atmospheric muons is several orders of magnitude higher than the respective rate of neutrinos. This is illustrated in Figure 7.1 (left) where the respective event rates as a function of energy[32] are shown. It is expected that event rate distributions with respect to any parameter will in most parts be dominated by atmospheric muons so that differences in the shape of their distributions are hard to recognise. This drawback is overcome by using probability distribution functions (PDFs) for the respective event classes. To get the PDF for each event class, the respective event rate distribution is normalised to unity within the given parameter range. The resulting PDFs for the above example are shown in Figure 7.1 (right).

Thus the PDFs, here implemented as histograms, give the conditional probability $P(p;C)$ that the considered parameter p has a value between p_i and p_{i+1} corresponding to the edges of bin i for an event of event class[33] C (e.g. atmospheric muons or different type of neutrino events) for each bin i with $1 \leq i \leq N_{\text{bins}}$. The number of bins N_{bins} is chosen to be 200 over the considered parameter ranges unless stated otherwise. The bin size is kept constant with respect to the parameter scale considered (either linear or logarithmic). Such PDFs will be used in the following sections and chapters wherever appropriate.

7.3.1 Standard reconstruction parameters

Standard reconstruction parameters are the reconstructed vertex, direction and energy. All of these are useful for background reduction purposes on a statistical basis as will be demonstrated in the following.

Atmospheric muons, representing the main background, enter the detector from above and from outside the detector. Therefore, their reconstructed vertex tends to be outside of the instrumented volume. In contrast to that, the reconstructed vertices of neutrino events are distributed mostly within

---

[32] Muon bundle energy for atmospheric muons, parent neutrino energy for all neutrino events.

[33] As the PDF is normalised over a finite parameter range, a further condition (besides having event class C) is that the parameter value is within that parameter range.

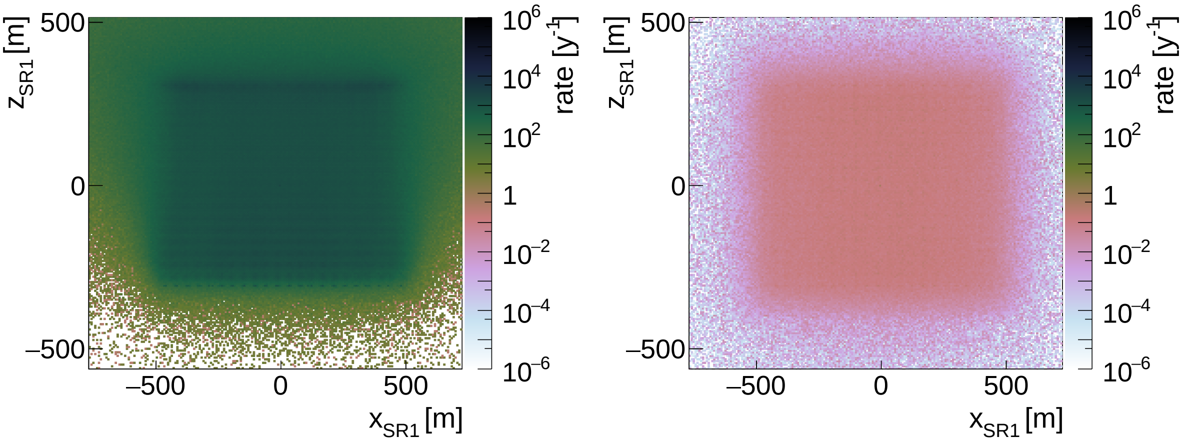

Figure 7.2: *Expected event rates in ARCA for atmospheric muons (left) and signal neutrinos (right) versus x- and z-coordinate, x_{SR1} and z_{SR1}, of the reconstructed vertex as given by SR1 (Shower Reconstruction Algorithm 1).*

this volume[34]. This can be seen in Figure 7.2 which shows the event rate for atmospheric muons and signal neutrino events as a function of reconstructed vertex from SR1 (*Shower Reconstruction Algorithm 1*).

Because of the cylindrical symmetry of the detector, it is obvious to translate the x- and y-component of the reconstructed vertex into a single parameter: the horizontal distance from the detector centre $r = \sqrt{x^2 + y^2}$.

For the same symmetry reasons, only the reconstructed zenith angle θ and not the azimuth angle is considered from the direction reconstruction. Recall that all considered fluxes are independent of the azimuth angle. Generally, the zenith angle is used to discriminate down-going atmospheric muon tracks from up-going tracks induced by neutrinos coming from below. Also in shower analyses, the reconstructed zenith angle is useful to discriminate neutrino events from atmospheric muons on a statistical basis: because of the dominating muon event rate, an event reconstructed as down-going is much more likely a muon event than an event reconstructed as up-going.

The usefulness of the energy reconstruction follows from the energy spectra of the considered fluxes (e.g. Figure 2.2, p. 21). The reconstructed energy, and parameters which are highly correlated with the deposited energy, are therefore a crucial ingredient for the discrimination of signal neutrinos from atmospheric neutrinos.

For the purpose of event discrimination, two further parameters are defined that are described in the following: the *containment* and the *pointing*.

The *containment* c is defined as the maximum perpendicular distance between the reconstructed vertex and the surface of the instrumented volume of the detector. Denoting as r', z'_{min}, z'_{max} the radius and z-components of the boundaries of the instrumented volume, and z, r the components of the reconstructed vertex, c is given by:

$$c = \max(\ r - r',\ z'_{\text{min}} - z,\ \ z - z'_{\text{max}}\ ) \tag{7.4}$$

Here, c is negative for events inside the instrumented volume. The definition of the *containment* combines the discrimination power of the reconstructed vertex into a single parameter.

---

[34] Recall that the instrumented volume has a radius of roughly 500 m and is limited in z-direction by roughly ±300 m

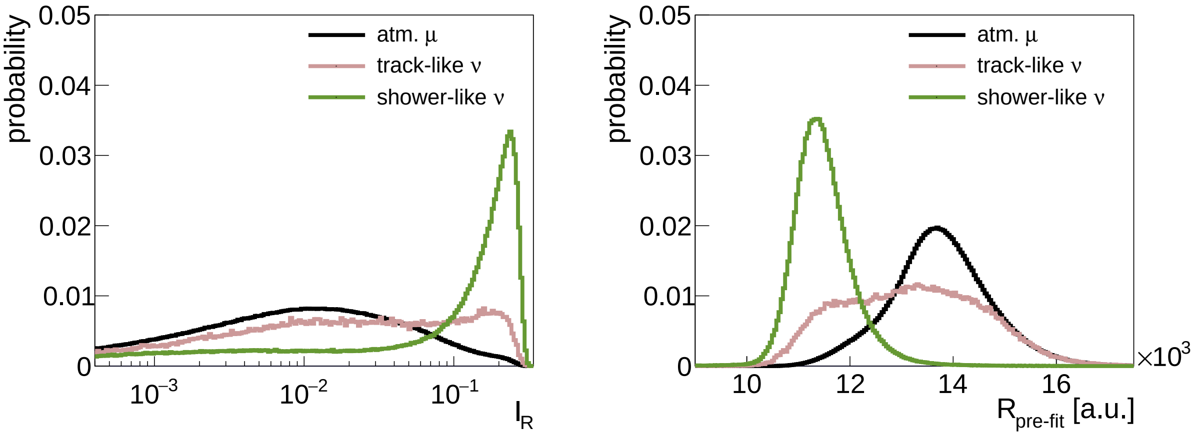

Figure 7.3: *PDFs of the inertia ratio I_R (left) and the residual parameter $R_{\text{pre-fit}}$ (right) for atmospheric muons (black), track-like (red) and shower-like (green) signal neutrino events.*

The *pointing* γ is defined as the angle between the reconstructed direction and a vector pointing from the reconstructed vertex to the detector centre. As atmospheric muons always enter the detector from outside, they have smaller pointing on average than shower events.

Thus, there are in total six considered standard parameters for each reconstruction algorithm (vertex: z, r, c; direction: θ, γ; and energy E). Besides these standard parameters, each reconstruction algorithm provides parameters that assess the quality of respective fits, and parameters based on the distribution of selected hits in the detector. Important ones are described in the following.

7.3.2 Other parameters

SR1 provides as additional parameter solely the likelihood value from the fit. Among the important parameters provided by SR2, two are given by the value of the M-estimator for the pre-fit vertex and the final vertex position (see Eq. (7.2)). These parameters assume larger values the more the hit distribution differs from a distribution that would follow from the assumed spherical light emission. In addition, at both stages a so-called residual parameter is calculated from the time residuals, denoted as $R_{\text{pre-fit}}$ and R_{final}. It measures the agreement of the hit distribution in space-time with the assumption of spherical light emission. For perfect agreement its value is zero and the value gets larger for decreasing agreement. The exact definition is given in [104].

Another useful parameter of SR2 is given by the *inertia ratio* I_R. From the selected hits an inertia tensor of hits is defined in analogy to the tensor of inertia in classical mechanics. The hits are treated as mass points where instead of a mass the hit amplitude is used. From the three eigenvalues λ_i, $i \in \{1, 2, 3\}$ of the inertia tensor, the *inertia ratio* is calculated as follows:

$$I_R = \min_{i\in\{1,2,3\}} \frac{\lambda_i}{\lambda_1 + \lambda_2 + \lambda_3}. \tag{7.5}$$

For almost spherical hit distributions as expected from showers, the eigenvalues have similar values and I_R is close to 1/3. For elongated distributions as they may result from tracks, I_R assumes smaller values down to almost zero.

Figure 7.3 shows the PDFs of I_R and $R_{\text{pre-fit}}$ for atmospheric muons, track-like and shower-like signal neutrino events in ARCA. Track-like neutrino events are here defined as muon neutrino CC in-

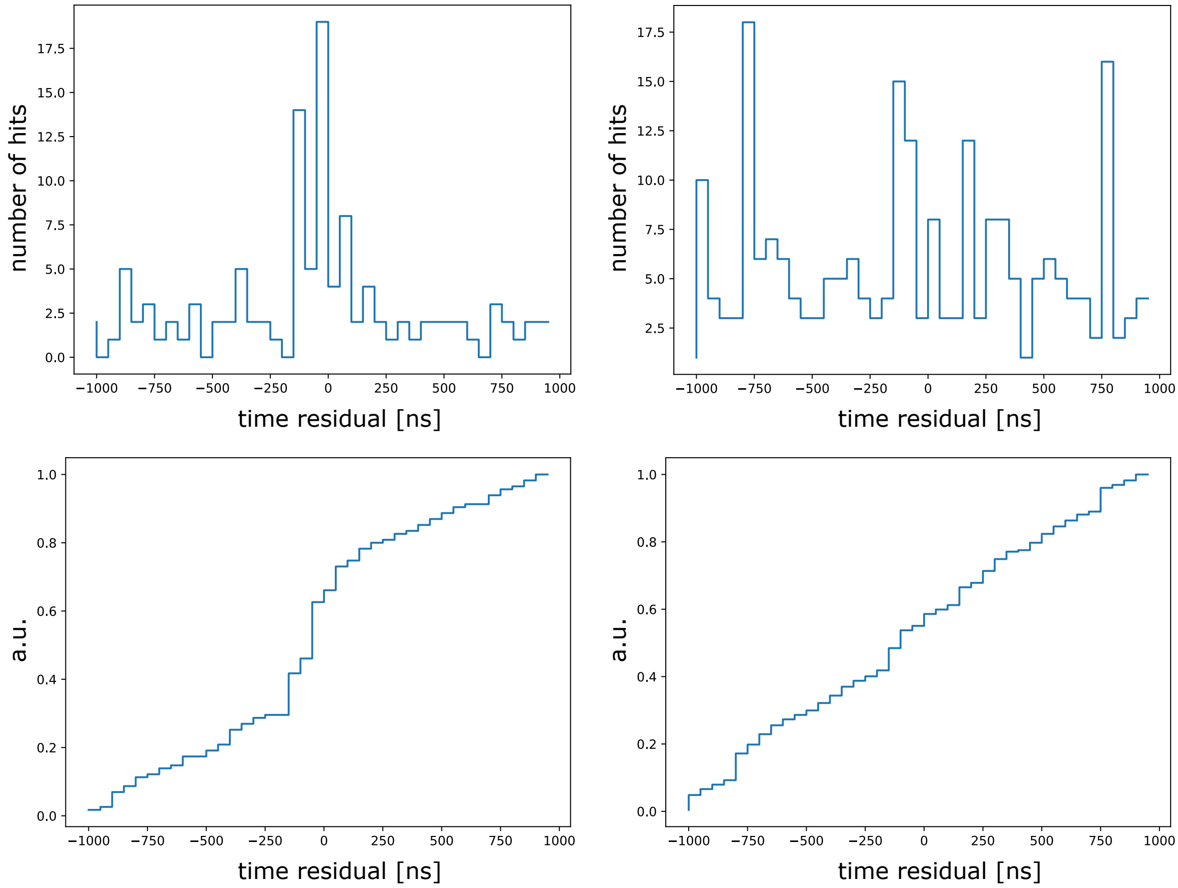

Figure 7.4: *Time residual distributions (top) for a typical shower (10 TeV ν_e CC event, left) and a track (290 TeV ν_μ CC event, right) and the respective cumulative distributions (bottom). Pictures by courtesy of Thomas Heid.*

teractions and tau neutrino CC events with an outgoing muon; all other neutrino events are defined as shower-like (see also Section 2.4). Both parameters provide very good discrimination power between atmospheric muons and shower-like events. However, track-like neutrino events reach significantly into the shower-like region because of the hadronic shower from the neutrino interaction that is detected for events occurring inside or near the instrumented volume.

The main bulk of parameters is given by SR3. Among the important ones are parameters that measure characteristics of the time residual[35] distribution in the range from -1000 to 1000 ns. A typical distribution is shown in Figure 7.4 (top) for both a shower and a track event. A first group of parameters is given by the mean, median, root mean square and other characteristics of the distribution. In the bottom of Figure 7.4, the corresponding cumulative distributions are shown. For a shower, the time residuals cluster around zero while for an elongated track the distribution is much broader. This also results in different slopes for the cumulative distributions in different time residual regions.

The second group of parameters is given by these slopes. For this purpose, the time residual range from -1000 ns to +1000 ns is divided into eleven regions given in Table 7.2. The slope for

---

[35] The time residuals are defined in Eq. (7.1).

region min. t_r [ns]	-1000						0	25	50	100	200
region max. t_r [ns]	-100	-50	-20	-10	0	1000					

Table 7.2: *Definitions of the eleven time-residual regions between -1000 ns and +1000 ns; six regions with a minimum time residual of -1000 ns and six regions with a maximum time residual of 1000 ns. (One region is defined from -1000 to 1000 ns.)*

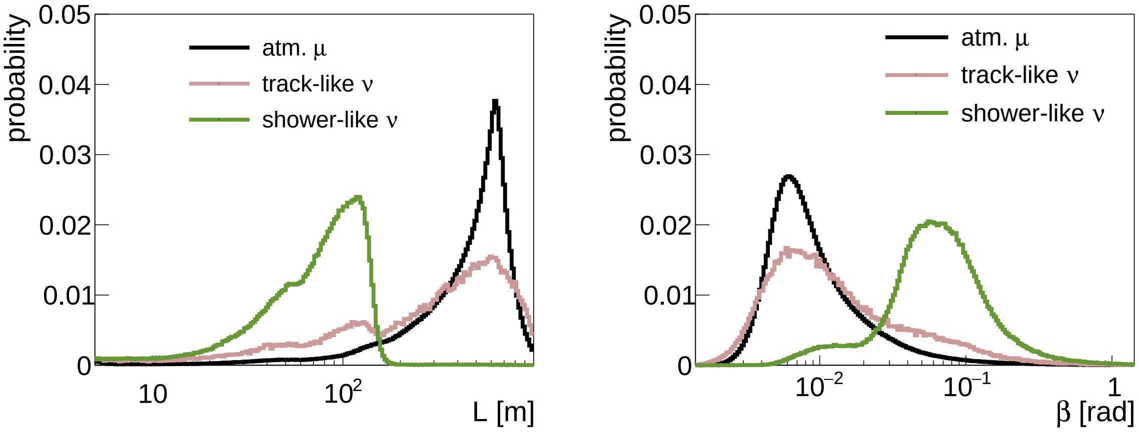

Figure 7.5: *PDFs of the reconstructed track length L (left) and the direction error β (right) for atmospheric muons, track-like and shower-like neutrino events.*

each region is determined via fitting a straight line. Further groups of parameters are given by the y-axis intercept of the corresponding lines and the χ^2 of the corresponding fits.

Additionally, the G parameter is defined as the following sum:

$$G = \frac{1}{N_{\text{hits}}} \sum_{i=1}^{N_{\text{hits}}} \exp\left\{ -\frac{t_{r,i}^2}{4.5\,\text{ns}^2} \right\}, \tag{7.6}$$

where N_{hits} is the number of selected hits and $t_{r,i}$ is the time residual corresponding to the i-th hit. The 4.5 ns^2 in the denominator of the exponent accounts for the time resolution of the PMTs. This parameter measures the agreement of the hit pattern with the assumed spherical light emission. The more the hit distribution deviates from this assumption the larger the time residuals and the smaller the value of G.

Lastly, also the vertex position determined at the pre-fit stage is provided as z-component and horizontal distance from detector centre, $z_{\text{pre-fit}}$ and $r_{\text{pre-fit}}$, respectively. For more details on the different parameters see [105].

From the track reconstruction algorithm, two parameters are especially useful for event discrimination: the reconstructed track length L and the error β on the reconstructed direction. In general, as shower events do not have a large elongation they get a smaller track length assigned than actual tracks. The error on the reconstructed direction is derived during the likelihood fit from the width of the likelihood function. It has in general higher values for showers due to their more spherical hit-pattern. The PDFs of these two parameters for atmospheric muons, track-like and shower-like

	SR1	SR2	SR3	TR
standard reconstruction parameters	6	6	6	6
other parameters	1	7	69	5

Table 7.3: *The number of reconstruction parameters provided by the shower reconstruction algorithms (SR) 1-3 and the track reconstruction algorithm (TR).*

neutrino events (definitions as above) are shown in Figure 7.5. Both show very good separation power.

In total, 106 parameters are provided by the reconstruction algorithms as detailed in Table 7.3. Before these parameters are used in Chapter 9 for the event classification, a preprocessing is performed as shown in the following chapter. This preprocessing includes also a method of finding the most useful parameters for the event classification, which also lead to the choice of parameters described here.

Chapter 8

Data preprocessing

The main purpose of the preprocessing as performed here is to find the reconstruction parameters most useful for event classification (the event classification is presented in Chapter 9). The different event classes that are to be distinguished are defined in Section 8.1. The method of finding the most useful parameters is based on histograms with a fixed number of bins. Therefore, it is necessary to define reasonable ranges for all considered parameters. This is discussed in Section 8.2.

A computational challenge is the large number of parameters. To reduce this number, correlations between the parameters have been investigated and redundant parameters have been sorted out. The corresponding method is presented in Section 8.3. Finally, in Section 8.4, the method for finding the most useful parameters is presented together with the corresponding results.

8.1 Event classes

In order to evaluate the sensitivity of ARCA, a shower and a track search are envisaged as also mentioned at the beginning of this part. Here, the signal and background event classes for both cases are defined. These classes are used later to find the most useful reconstruction parameters for their discrimination (Section 8.4).

The classes are defined as follows:

- Signal showers are defined as ν NC events and ν_e CC events with neutrino energy greater than 100 TeV.
- Signal tracks are defined as ν_μ CC events and ν_τ CC events where the outgoing tau decays into a muon. Both types of events are required to be up-going (zenith angle larger than 90°) and the neutrino energy is required to be greater than 200 TeV.
- In the shower search, the background is defined as all ν_μ CC and atmospheric muon events.
- In the track search, the background is defined as all ν NC and ν_e CC events as well as all atmospheric muon events.

The choices of signal and background energy regions are based on Figure 2.2 (p. 21). Event types not listed are ignored in order to achieve pure event samples.

These definitions are summarised in Table 8.1 together with the number of simulated events corresponding to each class.

	signal	background
shower search	ν NC, ν_e CC $E_\nu > 100\,\text{TeV}$	ν_μ CC, atm. μ
track search	ν_μ CC, ν_τ CC ($\tau \to \mu$) $E_\nu > 200\,\text{TeV}$, $\theta_\nu > 90°$	ν NC, ν_e CC, atm. μ

	signal	background
shower search	555 000	7 160 000
track search	214 000	8 920 000

Table 8.1: *Top: Definitions of event classes with neutrino energy E_ν, zenith angle θ_ν (defined in Section 7.3.1). Bottom: corresponding number of simulated events used for the training for the shower search and track search.*

8.2 Parameter ranges

In order to remove outliers and find the relevant range for a given parameter, an algorithm has been developed giving preliminary ranges. The algorithm also checks whether a linear or logarithmic scale is more suitable for the given parameter. To get to the final ranges, the results of the algorithm are checked individually and adjusted where necessary. The algorithm consists of the following steps:

1. Fill a histogram for the considered parameter with all simulated and weighted signal events. The bin number is chosen to be 100, the parameter range is chosen so that all simulated neutrino events are included.
2. Exclude bins at the lower edge until not more than 0.05% of the total signal event rate is removed. The lower edge of the new minimum bin is chosen as new minimum for the considered parameter. Do the same for the upper edge to get a new maximum for the parameter.
3. Repeat Step 1. However, the parameter range is now given from the minimum and maximum found in Step 2.
4. Repeat Steps 2 and 3 five times.
5. From the final histogram of Step 4, if the lower edge is positive, sum up the bin contents of the first seven bins. If this exceeds than one fifth of the total histogram content, use logarithmic parameter scale and repeat Steps 1 to 4 for the logarithmic-scale histogram.

The number of repetitions in Step 4 as well as the number of “seven bins” and “one fifth” in Step 5 have been chosen after some testing as they turned out to provide reasonable parameter ranges for most cases.

The minimum and the maximum of the final histogram are chosen as preliminary parameter range, neglecting at most 0.5% of the total signal event rate. As a last step, if the histogram contains too long tails so that the bulk of the signal event rates takes less than half the range, the parameter

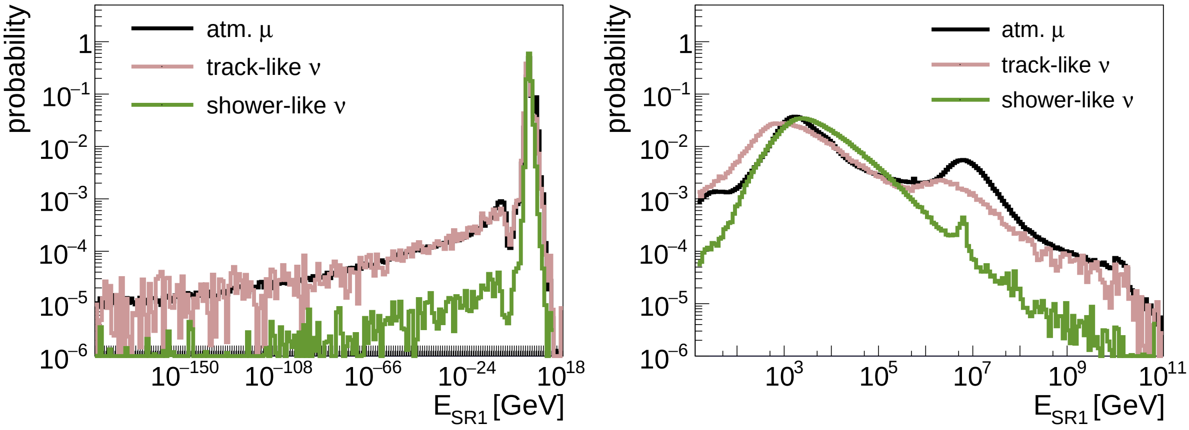

Figure 8.1: *PDFs of the reconstructed energy E_{SR1} of SR1 for atmospheric muons, track-like and shower-like signal neutrino events (definitions as in Section 7.3) for the initial (left) and final (right) parameter range. In the initial range, interesting structures visible in the final, relevant parameter range are hidden.*

range is adjusted. For the machine learning application (Chapter 9), events outside of the respective parameter ranges are ignored in the learning step.

An example of this procedure is illustrated in Figure 8.1 which shows PDFs for the reconstructed energy of SR1 (*shower reconstruction algorithm 1*) in the initial and final parameter range. Here, the lower edge had to be adjusted by eye because of the long tail of events with low reconstructed energy resulting from events with very few selected hits. The total signal event rate loss amounts to 1.1% in this case.

8.3 Removing redundant parameters

The purpose of removing redundant parameters is twofold. Firstly, using several redundant parameters in a classification application may reduce the efficiency [106], which is to be prevented; secondly, the aim is to reduce the computation time and thus increase the efficiency of the upcoming step of finding the most useful parameters (Section 8.4).

In order to remove redundant reconstruction parameters, correlations between the parameters are investigated. For each parameter, only events within the range determined in the previous section are considered. The following steps are performed:

1. For each parameter, generate a list of parameters strongly correlated with the given parameter. The correlation condition is $|\rho| > 0.95$ with ρ the correlation coefficient between two parameters.
2. Merge lists of those parameters that are correlated with each other (same condition as in Step 1) to get groups of correlated parameters[36]

---

[36] For instance for hypothetical parameters p_1, p_2, p_3, p_4, if p_1 is correlated with p_2 and p_3, and p_2 is correlated with p_1 and p_4, then those four parameters form a group of correlated parameters as each parameter is correlated with at least one other parameter in the group. (The list of parameters generated in Step 1 would be $\{p_2, p_3\}$ for p_1, $\{p_1, p_4\}$ for p_2, $\{p_1\}$ for p_3, and $\{p_2\}$ for p_4.)

$\lvert\rho\rvert$	$\chi^2_{-1000,0}$	$\chi^2_{-1000,-10}$	$\chi^2_{-1000,-20}$	$\chi^2_{-1000,-50}$
$\chi^2_{-1000,0}$	1	0.957	0.933	0.873
$\chi^2_{-1000,-10}$	0.957	1	0.993	0.946
$\chi^2_{-1000,-20}$	0.933	0.993	1	0.970
$\chi^2_{-1000,-50}$	0.873	0.946	0.970	1

Table 8.2: *Correlations between four correlated χ^2 parameters of SR3 (see also Section 7.3.2).*

parameter	highly correlated with	$\lvert\rho\rvert_{\text{min}}$
$\chi^2_{-1000,0}$	$\chi^2_{-1000,-10}$	0.873
$\chi^2_{-1000,-10}$	$\chi^2_{-1000,0}, \chi^2_{-1000,-20}$	0.946
$\chi^2_{-1000,-20}$	$\chi^2_{-1000,-10}, \chi^2_{-1000,-50}$	0.933
$\chi^2_{-1000,-50}$	$\chi^2_{-1000,-20}$	0.873

Table 8.3: *The list of parameters correlated with a given χ^2 parameter. Recall that a parameter appears in a list if the respective correlation coefficient is larger than 0.95 (absolute value).*

3. For each parameter in a group, find the minimum correlation coefficient $\lvert\rho\rvert_{\text{min}}$ between the considered parameter and each other parameter in the group (only absolute values of correlation coefficients are considered).

4. For each group, choose as representative the parameter with the largest $\lvert\rho\rvert_{\text{min}}$. The other parameters in the group are considered redundant and are neglected for further processing.

The correlation limit of 0.95 has been chosen after some testing as it gives reasonable results. Note that in order to qualify for the condition, the correlation limit needs to be fulfilled for all types of events.

Also note that in general, for two correlated parameters the lists constructed in Step 1 may contain different entries. Therefore the resulting group (Step 2) may contain several parameters whose absolute value of the correlation coefficient is smaller than 0.95.

The steps are in the following illustrated by an example with four correlated χ^2 parameters of SR3 (see Section 7.3.2). Table 8.2 shows the correlations among these parameters. The generated lists following from Step 1 are shown in Table 8.3. Note that none of these parameters has all other three parameters in its list. However, via the merging of Step 2 all four parameters form a group of correlated parameters (even though e.g. parameter $\chi^2_{-1000,0}$ and $\chi^2_{-1000,-50}$ only have a correlation of 0.873). The $\lvert\rho\rvert_{\text{min}}$ following from Step 3 are also listed in Table 8.3. As representative, $\chi^2_{-1000,-10}$ is chosen having the largest $\lvert\rho\rvert_{\text{min}}$ (Step 4).

Considering all available parameters, this procedure results in 11 independent groups of correlated parameters containing 52 parameters in total (4 from SR2, 48 from SR3). The other 54 parameters show no high correlation with any other parameter. As from each group one representative is chosen, 41 parameters are sorted out (mainly a subset of those generated from the time residual distribution of SR3 described in Section 7.3.2). Thus 65 parameters are left to be used

reco type	shower search	track search
SR1	r, z, θ	θ
SR2	$R_{\text{pre-fit}}$, I_R	z, $R_{\text{pre-fit}}$
SR3	T_{RMS}, $S_{-1000,-50}$, G	z, $z_{\text{pre-fit}}$, $r_{\text{pre-fit}}$, θ, E, $\chi^2_{100,1000}$, $\chi^2_{-1000,-50}$
TR	θ, β, L	θ

Table 8.4: *Most useful parameters according to the algorithm developed in this section for the shower search and the track search and subdivided into the reconstruction algorithm providing the respective parameters.*

for the next step of finding the most relevant parameters for event classification described in the following.

8.4 Most useful parameters

In order to find the most useful parameters for both the shower and track search, the distributions of events of the different classes with respect to the different parameters are investigated. This is done separately for both searches within the following steps:

1. Construct a two-dimensional histogram for each possible combination of parameters on the two axes. Having 65 parameters, this gives 2080 histograms. The histograms are filled with the signal and background events considered.
2. For each histogram, calculate the separation power P defined as

$$P = \sqrt{\sum_{i=1}^{N_{\text{bins}}} \frac{N_{S,i}^2}{N_{S,i} + N_{B,i}}} \tag{8.1}$$

   with N_{bins} the number of bins, $N_{S,i}$ and $N_{B,i}$ the number of signal and background events per year in the i-th bin, respectively.
3. For a given parameter, sum up the separation power of all histograms where this parameter is involved. Choose the parameter with the largest sum as a useful parameter.
4. Construct three-dimensional histograms filled with the signal and background events considered. The parameter chosen in the previous step is on the first axis, and all possible combinations of the remaining parameters are on the other two axes (giving 2016 histograms).
5. Repeat steps 2 and 3.
6. Construct d-dimensional histograms filled with the signal and background events considered, $d = p+2$ where p is the number of parameters chosen in the previous steps. These parameters are on the first p axes, and all possible combinations of the remaining parameters are on the remaining two axes.
7. Repeat the two previous steps until enough useful parameters are found.

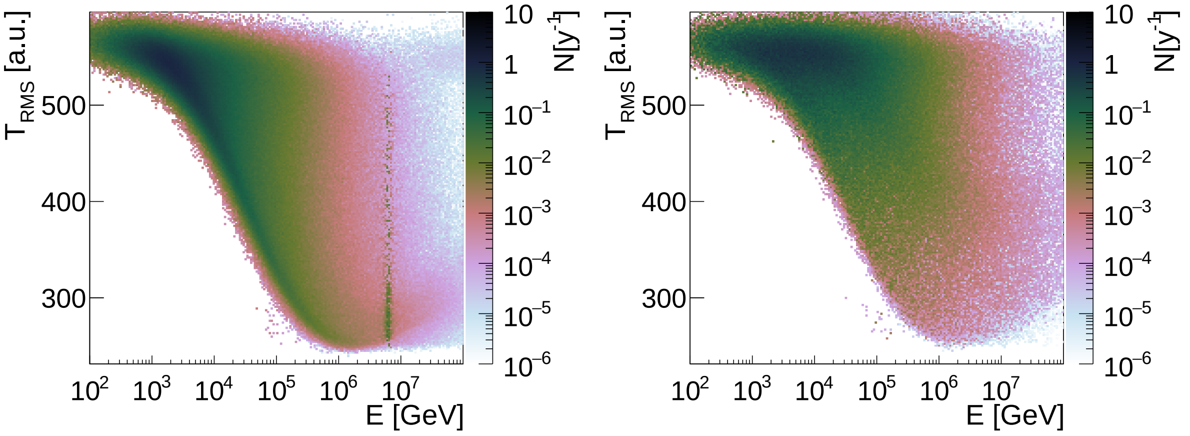

Figure 8.2: *Correlation between neutrino energy E and the root mean square T_{RMS} of the time residual distribution of SR3 for shower-like (left) and track-like signal events (right); definitions like in Section 7.3. It follows that in both cases, the value of T_{RMS} can approximately be translated into a minimum for the incident-neutrino energy that increases with lower values of T_{RMS}.*

In order to reduce computation time a random sample of 10% of all simulated events were used. Furthermore, to avoid binning effects, the bin number per dimension was set to ten for two dimensions and reduced by one for each additional dimension down to a minimum of three. This leads to a total bin number of nearly 200 000 for eleven dimensions. Since a further dimension would increase the total bin number to the order of simulated signal events in the shower search (see Table 8.1, p. 114), it was chosen to perform the last step until eleven useful parameters were found[37]. The small number of bins per dimension, however, makes the choice of appropriate parameter ranges, as performed in Section 8.2, very important.

Building this method up in a multi-dimensional way, as opposed to analysing each parameter solely in one dimension, allows further redundant parameters to be ignored implicitly. In addition, a "hidden" separation power, that a certain combination of parameters might have, can be found (an example are the components of the reconstructed vertex). In such a case, where a combination of two parameters has significantly higher separation power than all other combinations, both have been chosen for the construction of new histograms in Step 4. The result has then been compared to that of strictly following all steps, and the combination of parameters giving the better final result (higher separation power) has been chosen as most useful parameters.

As mentioned above, the whole procedure is performed for the shower and track searches separately. The most useful parameters found for each case are listed in Table 8.4. Note that for the shower search no reconstructed energy is used. This is because the used parameter T_{RMS} (root mean square of the time residual distribution of SR3) already exhibits a high anticorrelation with the neutrino energy of signal showers. In addition, there is also an anticorrelation with the neutrino energy of track-like events. This is illustrated in Figure 8.2.

For the track search, it is noteworthy that mainly standard reconstruction parameters (vertex, energy and zenith angle) are found. The only two non-standard parameters are $\chi^2_{100,1000}$ and $\chi^2_{-1000,-50}$ from SR3. The reason is that, contrary to the shower search, determining the topology of the

---

[37] The optimal number of parameters to be used for a machine learning algorithm depends highly on the respective problem and is hard to determine [106].

events is secondary; the main background of atmospheric muons is suppressed by considering the reconstructed direction and vertex (see also Section 7.3.1).

The next chapter describes how the parameters found in this section are used to discriminate the signal from background events with the help of a machine learning algorithm.

Chapter 9

Event classification

The aim of the classification is to separate signal from background events on a statistical basis. The classification is done with the help of boosted decision trees (BTDs) from the TMVA package [107] of the ROOT software framework [108]. After an early test of several machine learning algorithms, this one was chosen as it gave good results after a reasonable computation time as compared to the others. The algorithm is described in Section 9.1.

In general, a classifier based on machine learning takes training data to build up the underlying model (learning step). Here supervised learning is used, i.e. the desired output is known for the training data. After the learning has been performed, the result needs to be validated on data that have not been used for the training. The utilised validation techniques, cross validation and a resampling method, are described in Section 9.2.

As has been mentioned before (e.g. Section 8.1), two separate classifications are performed: a shower search where signal shower events have to be discriminated from all background events, and a track search where the same is done for signal track events. The results for both classifications are presented in Section 9.3 including a discussion of the classification output.

9.1 Boosted decision trees

The following description of boosted decision trees (BDT) is based mostly on the official TMVA documentation [107]. The BDT algorithm is based on binary decision trees. These classifiers are based on simple consecutive cuts on single variables with the goal to discriminate several classes. Here, two classes are used denoted as signal and background[38]. Thus a single decision tree possesses a binary tree structure as exemplarily depicted in Figure 9.1. Beginning with the root node, repeated decisions are made on a variable selected on each node according to an optimised cut value, leading to two further nodes. The variable and corresponding cut value are chosen as the ones that achieve the best discrimination between signal and background in the training data set. This is done for each node until a termination criterion is fulfilled. This leads to final leaf nodes within which the training events are distributed with a known distribution of the classes.

Afterwards, during application, single events end up in one of the leaf nodes based on the cuts at the intermediate nodes. These events are then classified as signal or background based on the majority of training events in the leaf node. Thus, taking into consideration all of the leaf nodes, the phase space is split into a large number of hyper cubes labelled as signal or background.

---

[38] Decision tree algorithms exist with the possibility to include more complex cuts including several variables and the distinction of more than two classes. For details see [109].

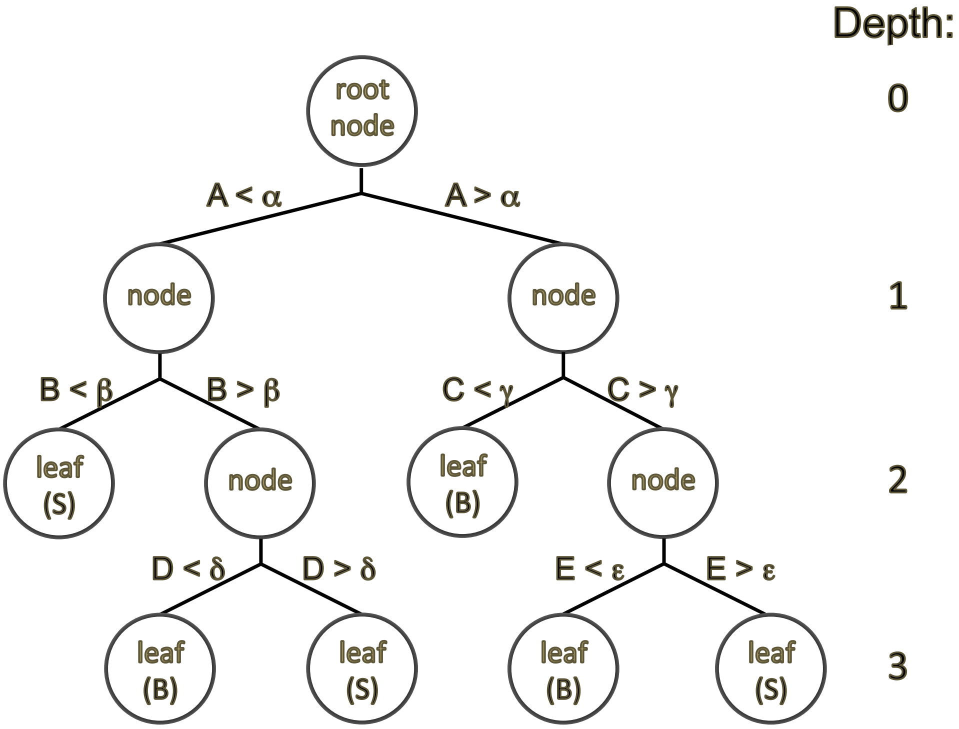

Figure 9.1: *Schematic view of a decision tree: beginning with the root node a series of cuts is applied to different parameters (Latin capital letters; greek letters represent the cut values) leading to further nodes and final leaf nodes which are labelled signal (S) or background (B) based on the majority of the training events in the corresponding leaf.*

In order to find the optimal variable and cut position at a node, each variable range is scanned with a given granularity. Different cuts are tested in order to opt for the best increase in separation power with respect to the parent node. For the scan, 20 steps are chosen representing a good compromise between computation time and resulting performance [107]. The separation power is measured with the so called *Gini Index* g:

$$g = p \cdot (1 - p), \tag{9.1}$$

where $p = N_S/(N_S + N_B)$ is the purity of a node given by the fraction of signal events over all events, with N_S and N_B being the number of signal and background events, respectively. The smaller the Gini Index the better the separation power. The combined separation power of two child nodes is given by the sum of their Gini Indices weighted by their relative fraction of events. The best combination of variable and respective cut position is the one that minimises the combined Gini Index.

Using a single decision tree has crucial shortcomings, among them the tendency to overtraining and instability (for details see e.g. [110]). These shortcomings are overcome by using a decision forest consisting of many single trees with strongly limited size. In the BDT algorithm the single trees in the forest are trained consecutively with the same data set. Events that got misclassified in the previous tree get “boosted” adaptively[39]: they are assigned a “boost weight” w for the training of

---

[39] Besides this adaptive boosting algorithm called AdaBoost [111,112], several other methods exist to create such a forest. For details see [113].

the next tree according to the misclassification rate ϵ:

$$w = \frac{1-\epsilon}{\epsilon}, \tag{9.2}$$

where ϵ is defined as the ratio of misclassified events over all events. Thus it holds $\epsilon \leq 0.5$ and $w \geq 1$. Assigning a response value of $\kappa = +1$ for signal and $\kappa = -1$ for background for a single tree, the response value of the decision forest is given by:

$$\kappa_{\text{tot}}(x) = \frac{1}{N_{\text{tot}}} \sum_{i=1}^{N_{\text{tot}}} \ln(w_i) \cdot \kappa_i(\boldsymbol{x}), \tag{9.3}$$

where N_{tot} is the total number of trees in the forest, w_i the boost weight used in the i-th tree and $\kappa_i(x)$ the response value of of the i-th tree for an event with input parameter values denoted by the vector $\boldsymbol{x}$. Furthermore, the learning rate as determined by the boosting can be tuned by changing the boosting weight w according to $w \rightarrow w^{\beta}$. The smaller β the smaller the learning rate. Here, β is kept at the default value from [107] of 0.5.

Having the forest of boosted trees, the phase space is now split very finely with a practically continuous distribution of the response value. Thus, depending on the response value κ_{tot}, events get classified as either background-like ($\kappa_{\text{tot}} < 0$) or signal-like ($\kappa_{\text{tot}} > 0$). The result for a complete set of events is then favourably represented by the distribution of the response value (see Section 9.3).

Further settings used for building up the forest are as follows: The maximum depth of the single trees is set to five which is two more than the TMVA standard setting and is done because of the relatively high number of training events[40]. The minimum number of training events in a leaf node is chosen to be 0.01% of the total data sample which corresponds roughly 770 or 910 events (see Table 8.1, p. 114). This means a node is not further split if any of these restrictions would be violated. The number of trees in the forest is chosen to be 300. No optimisation of these “meta parameters” has been performed.

9.2 Validation techniques

For the validation of a trained classifier a data set independent from the training data set is needed. However, the quality of a classifier increases the more data is available for training. Therefore, separating data from potential training data to use it for testing reduces the potential quality of the classifier. In order to keep this quality reduction small so-called cross validation is used. In order to get a handle on the error of the classification response and to smooth the output distributions, a resampling method is used. Both techniques are described in the following.

9.2.1 Cross validation

With cross validation it is possible to use all available data for training and for testing (or evaluation). This is achieved by training the classifier multiple times with different subsamples of the full data set. The final response value is then the mean of the single classifiers. Here, ten-fold cross validation is used which is illustrated in Figure 9.2 (left): the classifier is trained a total of ten times where the full

---

[40] A tree depth of five corresponds to a maximum of 32 leaf nodes. Thus, with the number of training events used here (see Table 8.1, p. 114) the mean number of events in a leaf node corresponds to roughly 250 000.

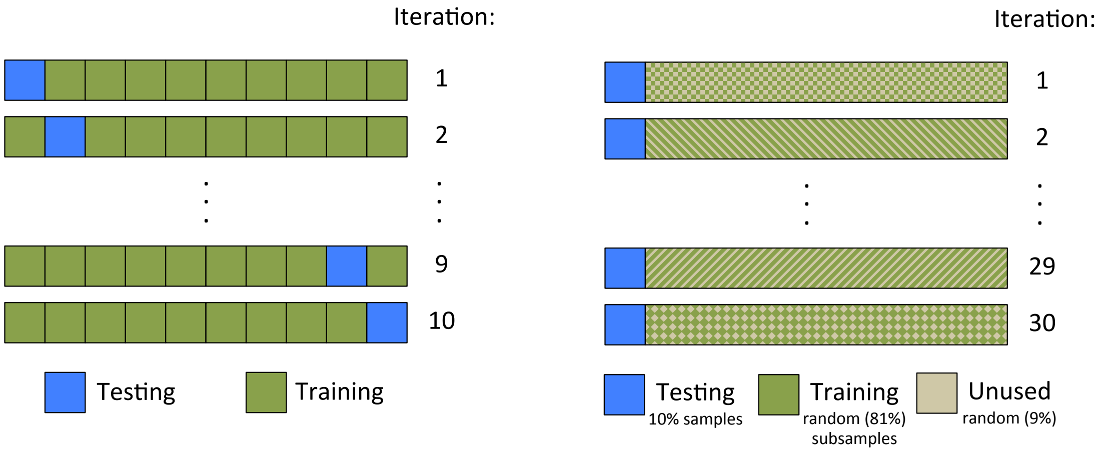

Figure 9.2: *Illustration of the used cross validation (left) and resampling method (right). One row represents the full data sample, testing and training samples are depicted as blue and green blocks, respectively. The unused data which is left from the random resampling (right) is illustrated as grey areas.*

data set is divided into ten subsamples of equal size. Each time a different combination of nine of the ten subsamples is used for training and the remaining sample for testing[41].

Recall that the classification output for the test samples are used for the sensitivity evaluation in the last part of this thesis. In an application with experimental data from detected events, the final response can be taken as the mean of the ten cross validation classifiers. This would also allow for the determination of a classification error on single events. Here, however, as every event is used only once for testing, an error estimation of the response value is impossible. In order to compensate for that, a resampling method is used as presented in the following.

9.2.2 Resampling

Resampling means that the classifier is trained multiple times with slightly different training samples[42]. Afterwards, the same testing sample is applied to all these trainings. From the differences in the responses for the single training events, the error can be estimated.

In this work, 30-fold resampling is used as illustrated in Figure 9.2 (right). In this process, 30 subsets are drawn randomly from the training sample, each 90% of the size of the full training sample. The classifier is then trained on each subset. In the application, for each event the response value of each of the 30 classifiers is used so that each event has to be down-weighted by 1/30. The result is a slighlty smeared and more continuous output distribution which is especially helpful to handle the tails of the distributions. This handling of the output is also called pull validation[43] [114].

In order to combine resampling and cross validation, the resampling is applied for each of the training samples used for cross validation. Therefore, 300 classifiers are trained in total and each single training uses 81% of the events used for the full classification (see also Table 8.1, p. 114).

---

[41] The optimal case to determine the mean classification accuracy would be to use N-fold cross validation, where N is the number of events in the full data set. I.e. the classifier is trained a total of N times on different combinations $N-1$ events, and the remaining event is used for evaluation. However, the computational requirements make this impossible.

[42] Note that the method employed here is similar to so-called bootstrapping or bagging [113].

[43] Other methods for handling the single outputs exist as e.g. taking a (weighted) mean. For details see e.g. [113].

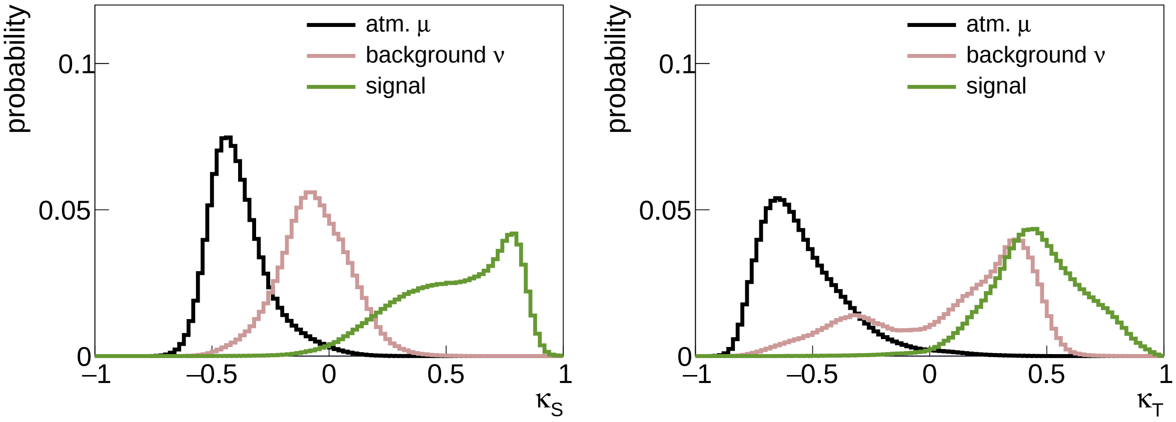

Figure 9.3: *Probability distribution functions for atmospheric muons, background and signal neutrinos for the shower search (left) and track search (right) with respect to the classifier output, κ_S and κ_T, respectively. For signal and background, the definition according to the respective training is used (see Table 8.1, p. 114).*

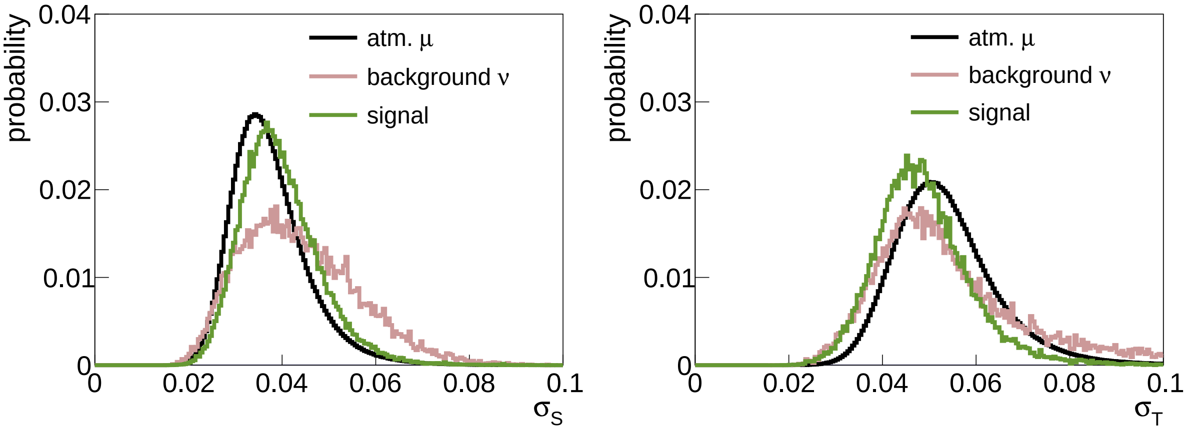

Figure 9.4: *Distribution of standard deviations for the shower search (σ_S, left) and track search (σ_T, right). Definitions as in Figure 9.3.*

9.3 Classification results

The resulting probability distribution functions with respect to the classifier output for both searches are shown in Figure 9.3 for atmospheric muons, background neutrinos and signal neutrinos as defined for the respective training (see Table 8.1, p. 114). In both cases, the atmospheric muons are very well separated from the signal neutrinos. The background neutrinos, however, accumulate near the centre. This is due to the fact that part of the background neutrino events have a similar topology as signal events. In the shower search, the muon neutrino CC events always produce a hadronic shower. If the event happens within the instrumented detector volume, the outgoing muon might leave undetected so that the event looks like a neutral-current event. In the track search, two bumps are visible for the background neutrinos corresponding to down-going (background-like, $\kappa_T < 0$) and up-going (signal-like, $\kappa_T > 0$) neutrinos. This means the large amount of atmospheric muons lead to a prioritising of the direction over topology in the classification.

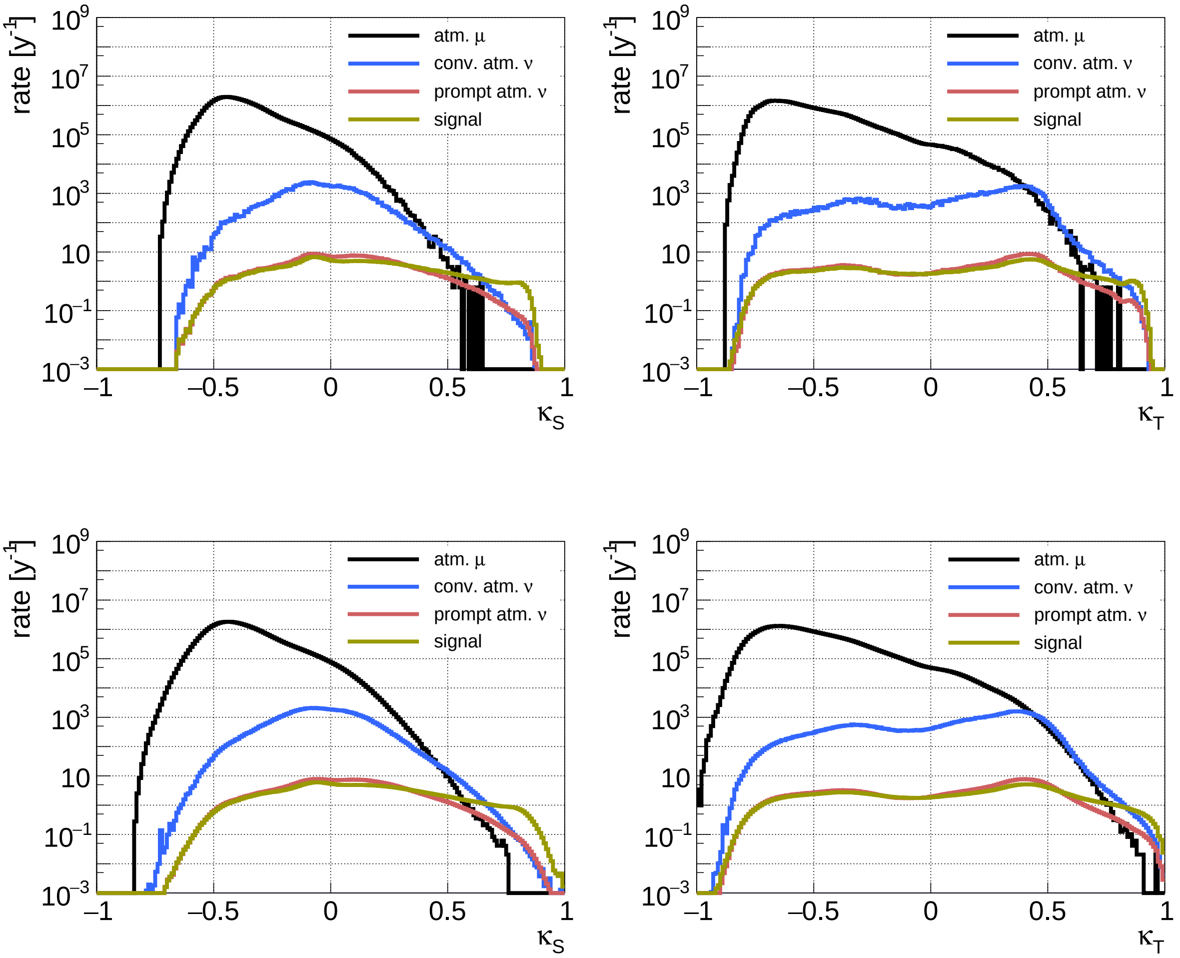

Figure 9.5: *ARCA event rate distributions (200 bins between −1 and 1) for atmospheric muons, conventional and prompt atmospheric neutrinos and signal neutrinos according to the IceCube flux (Eq. (2.7)) for the shower search (left) and the track search (right) as functions of the classifier outputs κ_S and κ_T, respectively, for a single resampling (top) and all 30 resamplings (bottom).*

The standard deviation $\sigma = \sqrt{\sigma^2}$ of the classifier output calculated from the resampling is illustrated in Figure 9.4 for both cases, again as PDFs for the different event classes. It is for each event calculated from the sample variance

$$\sigma^2 = \frac{1}{N-1} \sum_{i=1}^{N} (\kappa_i - \bar{\kappa})^2 \tag{9.4}$$

with $\bar{\kappa} = \sum_{i=1}^{N} \kappa_i / N$ as the mean, and the classifier outputs κ_i following from the $N = 30$ resamplings. The standard deviation is well below 0.1 for most events and has the mean near 0.04 for all three classes for both cases. The error on the mean can be calculated as $\sigma / \sqrt{N}$ with $N = 30$ as the number of resamplings. It thus has values below 1% for the majority of the events. These rather small values indicate that the different trainings are consistent with each other[44].

---

[44] Recall that for the different trainings of the classifiers, up to a quarter of the training events are different due to cross validation and resampling.

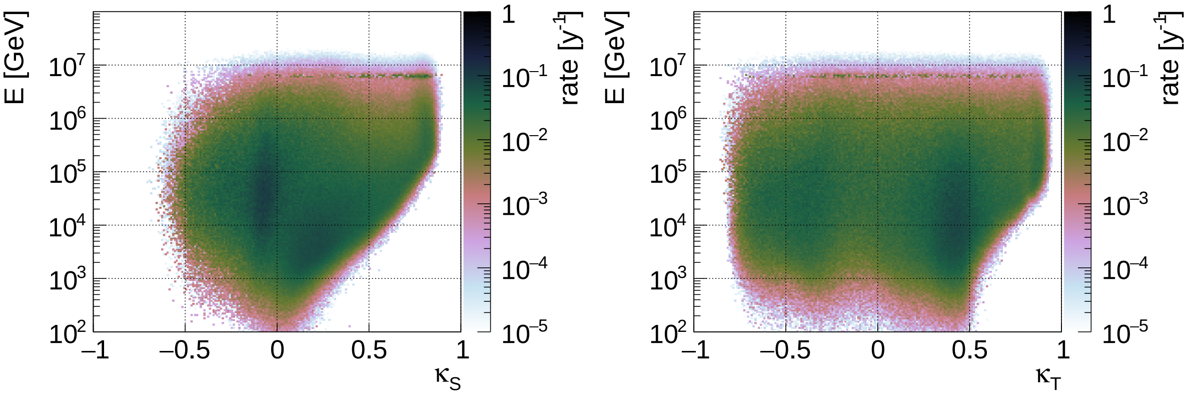

Figure 9.6: *Distribution of signal neutrino events versus classifier response and energy for the shower search (left) and the track search (right).*

For the evaluation of the ARCA sensitivity, the event rate distributions are important. They are shown in Figure 9.5 (bottom) for atmospheric muons, conventional and prompt atmospheric neutrinos and the IceCube signal flux.

For the shower search it can be seen that, even though the bunch of atmospheric muons and signal-like neutrinos are well separated (recall Figure 9.3), the signal event rate has an excess only in a rather small region ($\kappa_S \gtrsim 0.5$). In addition, a tail of atmospheric muons reaches even beyond $\kappa_S > 0.5$. These are very-high-energy muons passing the upper edge of the detector (an example is shown in Figure 3.5, page 41). Signal events in the background region ($\kappa_S < 0$) are caused by low-energy and track-like events. The separation of atmospheric and signal neutrinos above $\kappa_S = 0.5$ is mostly due to their different energy spectra.

In the track search there is also a clear excess of signal events above atmospheric muons. However, the excess above atmospheric neutrinos ($\kappa_T > 0.6$) is small and a separation of both event types is expected to be hard for the track search as compared to the shower search.

In order to illustrate the advantage of the utilised pull validation (as part of the resampling), the event rate distributions for a single sample are shown in the top of Figure 9.5. Comparing this with the final distributions shown in the bottom of this figure, it becomes obvious that statistical fluctuations are decreased and the atmospheric muons extend more smoothly into the signal-like regions in both cases. Recall that the atmospheric muons have a simulated livetime of roughly 3.3 years, leading to an event weight of 0.30/y per ARCA block which is much higher than the average weight of signal neutrino events ($3.0 \cdot 10^{-4}$/y per ARCA block). With the pull validation, a single atmospheric muon entry gets a weight of 0.01/y. As a consequence of this, the distributions are also slightly broader. However, the overall shape of every single distribution stays the same.

Discussion

In the following, a discussion of the classifier output is given in terms of correlations with neutrino observables (energy, zenith angle and containment as defined in Eq. (7.4)). For this purpose, Figures 9.6 to 9.8 show the distributions of signal neutrino events versus the classifier output and one of the observables (energy, zenith angle and containment, respectively) for both the shower and the track search.

The distribution versus energy (Figure 9.6) shows that for both classifiers, only high-energy

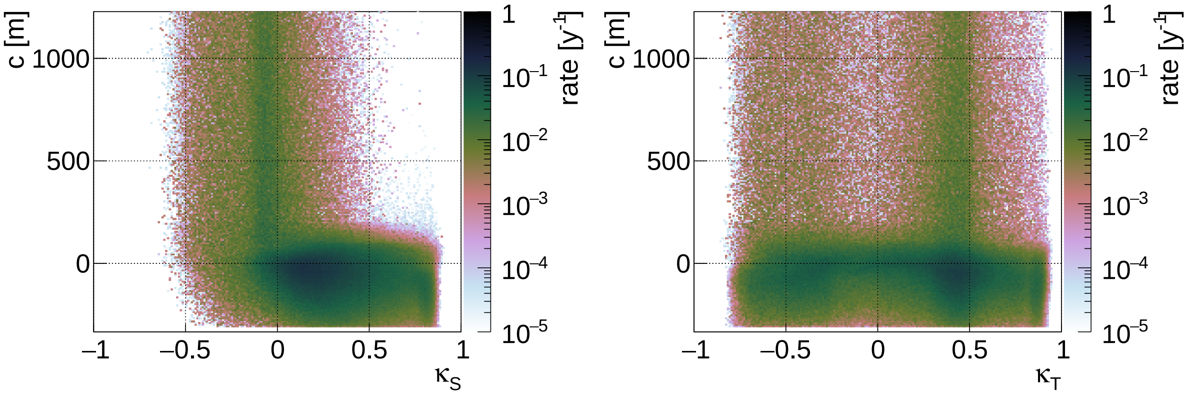

Figure 9.7: *Distribution of signal neutrino events versus classifier response and containment c (defined in Eq. (7.4)) for the shower search (left) and the track search (right). The smaller the containment, the shorter the distance of the interaction vertex to the detector boundary. Negative containment values correspond to events within the instrumented volume.*

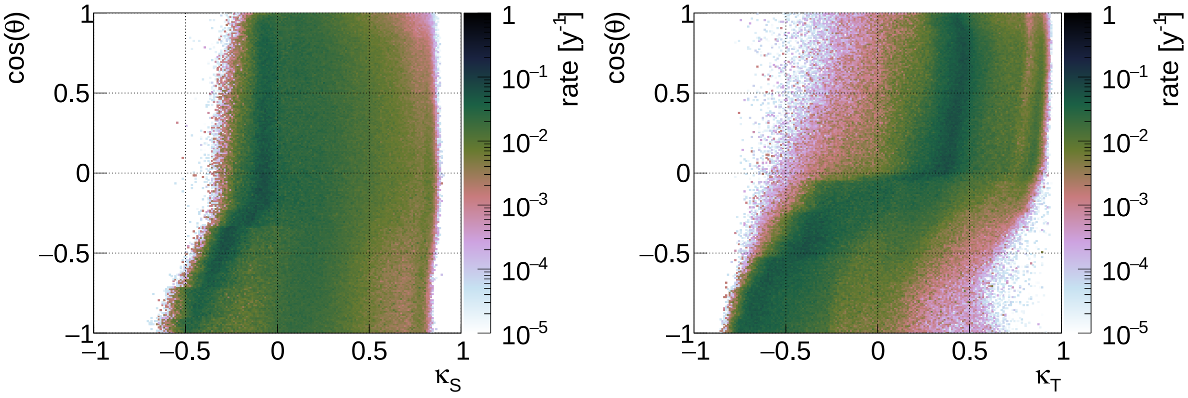

Figure 9.8: *Distribution of signal neutrino events versus classifier response and cosine of zenith angle $\cos\theta$ for the shower search (left) and the track search (right). Cosine values below zero correspond to events coming from above.*

events are assigned the largest response values as is expected from the definition of the different event classes (Table 8.1, p. 114).

In the background-like region (at low response values) for both classifiers, there are events of any energy. For the shower classifier, these are events outside the instrumented volume, especially ν_μ track events. This can also be seen when looking at the distribution versus containment (Figure 9.7). Mostly events near or within the instrumented volume ($c \lesssim 100\,\text{m}$) are assigned large response values for the shower search.

For the track search, there is no high correlation with the containment. This is expected since track events can reach the detector from far away. It can, however, be seen that many contained events are in the signal region of the track search, corresponding mainly to starting track events.

Looking at the distribution versus zenith angle (Figure 9.8) for the track search, there is a strong distinction between events coming from above (background-like) and events coming from below (signal-like). This is caused by the dominating background of atmospheric muons coming only from above which leads to a prioritisation of distinction in direction over distinction in energy.

The distribution versus zenith angle in the shower search shows that here events from above tend to be slightly more background-like. However, at the highest response values there are events from all directions.

In summary, both classifiers perform well and the resulting distributions are consistent with expectations. The distributions versus the classifier outputs will be used in the next part of this thesis to evaluate the sensitivity of ARCA to diffuse cosmic neutrino fluxes.

Part IV

ARCA diffuse flux sensitivity analysis

This part is about the evaluation of the sensitivity of ARCA to diffuse neutrino fluxes. In Chapter 10 this is done via performing a cut in the parameter space of the classifier outputs, and counting the events surviving the cut. In Chapter 11, the event rate distributions versus the shower classifier output are used to perform a so-called spectral fitting based on the maximum-likelihood principle. This procedure not only allows for an evaluation of the discovery potential but also of the sensitivity to the spectral properties of the signal flux.

Chapter 10

Cut-and-count analysis

The “cut-and-count” method allows for a fast evaluation of the discovery potential and a simple estimate of the numbers of events from the expected background and signal. Here, an optimal cut of the form $\kappa > x$ ($x \in$[-1,1]) on the response value κ from the classification described in Chapter 9 is determined that maximises the sensitivity to the respective signal flux. For each considered flux parameterisation a separate cut is set. This is done for both the shower search (SS) and track search (TS) separately and additionally for a combined search (CS) where an optimal combined cut on both classifier outputs is performed (e.g. $\kappa_T > x_T$ or $\kappa_S > x_S$) so that all events surviving either condition are counted. The former two allow for an investigation of the sensitivity for the two major event types, showers and tracks, while combining both increases the overall sensitivity.

As a reminder, the all-flavour signal fluxes considered are:

$$\Phi_E(E) = 3.6 \cdot 10^{-18} \cdot \left(\frac{E}{100\,\text{TeV}}\right)^{-2} \cdot \exp\left(-\frac{E}{3\,\text{PeV}}\right) \left(\text{cm}^2\,\text{s}\,\text{sr}\,\text{GeV}\right)^{-1}, \tag{10.1}$$

$$\Phi_C(E) = 6.7 \cdot 10^{-18} \cdot \left(\frac{E}{100\,\text{TeV}}\right)^{-2.5} \left(\text{cm}^2\,\text{s}\,\text{sr}\,\text{GeV}\right)^{-1}, \tag{10.2}$$

$$\Phi_T(E) = 2.7 \cdot 10^{-18} \cdot \left(\frac{E}{100\,\text{TeV}}\right)^{-2.13} \left(\text{cm}^2\,\text{s}\,\text{sr}\,\text{GeV}\right)^{-1}. \tag{10.3}$$

All fluxes assume a neutrino flavour ratio of 1 : 1 : 1 incident on Earth. For the further descriptions, these fluxes are assigned names: The first flux Φ_E will be called ‘evidence’ flux being the result of an IceCube analysis that gave first evidence to cosmic neutrinos. As a result of a combination of several IceCube searches, the second flux Φ_C will be named ‘combined’ flux. Finally the third flux Φ_T, highly in tension with Φ_C (see Section 2.1), will be called ‘tension’ flux.

General measures to quantify the sensitivity are briefly introduced in Section 10.1. The results of the cut-and-count method are presented in Section 10.2 while in Section 10.3 systematic uncertainties are discussed. Section 10.4 gives a conclusion including a comparison to previous ARCA sensitivity studies and to the IceCube results.

10.1 Sensitivity measures

A goal of ARCA is to confirm and investigate the cosmic neutrino signal flux as reported by the IceCube experiment [28]. Here, the term "confirm" has a clear definition: the p-value, which is defined as the probability that an observation is caused solely from the expected background, has to be 2.87×10^{-7} or lower. This value corresponds to the probability, given a normal distribution, to have an observation more than five standard deviations, or $5\,\sigma$, higher than the mean:

$$2.87 \cdot 10^{-7} = \frac{1}{\sqrt{2\pi}\,\sigma} \int\limits_{5\,\sigma}^{\infty} \exp\left(-\frac{x^2}{2\sigma^2}\right) \mathrm{d}x. \tag{10.4}$$

Therefore, this is often also called a $5\,\sigma$ discovery. Likewise, $N\,\sigma$ observations are defined for any value $N > 0$, and $N\,\sigma$ is called the significance. An observation with a significance of $3\,\sigma$, corresponding to a p-value of $1.35 \cdot 10^{-3}$, is referred to as evidence.

Given a signal hypothesis, an observation with at least a given significance s will only be achieved with a corresponding probability $p_s < 100\%$ depending on the signal and background hypotheses and resulting event numbers. In order to define the number of events that need to be detected, $p_s = 50\%$ is chosen.

If the expected signal flux is small so that observations consistent with background are expected, upper limits for the signal flux are placed. The upper limits are assigned a confidence level, e.g. 90%, so that a 90%-confidence-level upper limit is defined as the flux that would yield a higher observation in 90% of the cases when the same experiment would be repeated an infinite number of times. For a more detailed description of the principles of significance and upper limits, see e.g. Chapter 39 of [2].

In the following, sensitivity measures based on the general idea of significance and upper limits will be described briefly that will be used later to quantify the sensitivity resulting from the cut-and-count analysis.

Significance s after one ARCA year

Given a background and signal hypothesis, the cut-and-count procedure yields mean expected event numbers for the background μ_B and signal μ_S for one ARCA year[45]. The actual observed number of events then follows a Poisson distribution with mean $\mu_B + \mu_S$. The significance is calculated as described in the following.

The minimum number of events N detected with at least $p_s = 50\%$ probability is given by

$$\sum_{n=N}^{\infty} \frac{(\mu_S + \mu_B)^n}{n!} e^{-(\mu_S + \mu_B)} \geq 50\%. \tag{10.5}$$

The respective significance is given by translating the p-value given via

$$p = \sum_{n=N}^{\infty} \frac{\mu_B^n}{n!} e^{-\mu_B} \tag{10.6}$$

---

[45] One ARCA year corresponds to a full year of data taking with the full ARCA detector.

into the respective number of standard deviations, i.e. by solving

$$p = \frac{1}{\sqrt{2\pi}} \int_{s/\sigma}^{\infty} \exp\left(-\frac{x^2}{2}\right) \mathrm{d}x \tag{10.7}$$

for the significance s.

Expected time $T_{5\sigma}$ needed for a discovery

For a given cut, the mean expected event numbers are linear functions of the detector livetime. Therefore, the expected time $T_{5\sigma}$ needed for a $5\,\sigma$ discovery is determined by performing the calculations from Eq. (10.5) to Eq. (10.7) and scanning the time to get a significance of $5\,\sigma$. This is done here in steps of 0.01 years.

Model discovery potential after one ARCA year

The model discovery potential (MDP) [115] gives the flux normalisation[46] needed to achieve a discovery (observation with $5\,\sigma$ significance) after a given time, which is here chosen to be one year. Given the background-only hypotheses, the requirement of $5\,\sigma$ gives, via Eq. (10.6), the number of events N that needs to be detected. From Eq. (10.5) the minimum mean signal, μ'_S, needed for this observation is calculated. The MDP is then defined as

$$\text{MDP} = \frac{\mu'_S}{\mu_S}, \tag{10.8}$$

with μ_S being the mean from the signal hypothesis. The smaller the MDP the higher the sensitivity of an experiment.

Model rejection factor after one ARCA year

Finally, the model rejection factor (MRF) [116] is based on upper limits. Assuming the background-only hypothesis, an average upper limit $\bar{\mu}_{\text{up}}$ is calculated

$$\bar{\mu}_{\text{up}} = \sum_{n=0}^{\infty} \mu_{\text{up}}(n) \cdot \frac{\mu_B^n}{n!} e^{-\mu_B}, \tag{10.9}$$

i.e. an upper limit $\mu_{\text{up}}(n)$ is calculated for each possible observation n and weighted with the probability to observe this number of events from background only. The upper limits $\mu_{\text{up}}(n)$ are constructed via the method from Feldman and Cousins [117]. The MRF is then defined as

$$\text{MRF} = \frac{\bar{\mu}_{\text{up}}}{\mu_S}. \tag{10.10}$$

As with the MDP, the smaller the MRF the higher the sensitivity. MRF and MDP are closely related, for more details see [115].

---

[46] For the considered signal fluxes, the flux normalisations are 3.6 for Φ_E (Eq. (10.1)), 6.7 for Φ_C (Eq. (10.2)) and 2.7 for Φ_T (Eq. (10.3)) in units of $10^{-18} \cdot \left(\text{cm}^2\,\text{s}\,\text{sr}\,\text{GeV}\right)^{-1}$.

The cut is optimised for the significance s after one year for all searches and fluxes, the other sensitivity measures as determined from the same cut will be given for reference[47]. The optimal cut is determined by scanning the classification response in steps of 0.01. For each search and each of the considered signal fluxes, a separate optimisation is performed.

10.2 Results

The results are summarised in Table 10.1 and 10.2. Table 10.1 gives the optimal cut values for all considered signal fluxes and searches as well as the event numbers surviving the respective cuts for signal and the different background fluxes for one ARCA year. Table 10.2 gives the values of the sensitivity measures discussed above, together with the most sensitive energy range, i.e the neutrino energy range within which the central 90% of the signal events occur.

With the combined search, a discovery of the respective signal fluxes is possible in less than 1.4 ARCA years. The ‘evidence’ flux Φ_E and ‘tension’ flux Φ_T produce a very similar signal and are observed with a significance of $4.6\,\sigma$ and $4.3\,\sigma$, respectively, after one year. For the ‘combined’ flux Φ_C, a significance of $7.2\,\sigma$ is reached after one year. For each of the searches, Φ_T produces the weakest signal with event numbers of the order of ten per year while Φ_C produces the strongest signal with much higher signal event rates ranging from 40 (track search) to 70 (combined search) per year.

In the following subsections, the results will be described in more detail. In Section 10.2.1 further differences in the results for the different searches and considered signal fluxes are outlined by looking into the energy, zenith angle and interaction vertex distributions of the events surviving the cuts. The effective area and ratio of neutrino types after the cuts are discussed in Section 10.2.2. In Section 10.2.3, the achieved energy and zenith angle resolutions are described and Section 10.2.4 examines preliminarily the effect of the “self-veto”.

10.2.1 Event rate distributions

The optimal cut values are visualised in Figure 10.1 which shows the event rate distributions versus the classifier response of both the shower and track search in the signal region ($\kappa_S, \kappa_T > 0.5$) for all considered signal and background fluxes. From this Figure and Tables 10.1 and 10.2, it becomes clear that the shower search performs significantly better than the track search, and the combined search is only slightly better than the shower search.

In fact, the cuts for Φ_C are rather loose as compared to the other fluxes. This is due to the fact that Φ_C produces much more lower energy events than the other two fluxes, and these events are selected with such loose cuts. This becomes visible when looking at Figure 10.2 (left) which shows the expected event rate distributions over neutrino energy after the cuts of the combined search for the three signal fluxes. The event rate corresponding to Φ_C dominates over the other ones at almost all energies. The cut-off in Φ_E leads to a smaller event rate than Φ_T above about 3 PeV. This figure gives also an impression of the sensitive energy range in each case which starts at significantly lower energies for Φ_C (see also Table 10.2).

For Φ_E and Φ_T, the cuts for the combined search are dominated by the shower channel, indicated by the fact that the respective cut on the track-search classifier output is very hard with

---

[47] Note that the optimal cut would be slightly different for the different measures and would be a function of observation time.

Φ [1/(10^{18} cm^2 s sr GeV)]	search	cut	N_S	N_B	N_μ	N_c	N_p
Φ_E: $3.6 \cdot (E/100\,\text{TeV})^{-2} \cdot \exp(-E/3\,\text{PeV})$	SS	$\kappa_S > 0.67$	16.3	8.5	0.66	5.1	2.7
	TS	$\kappa_T > 0.75$	15.4	29	4.6	20	4.4
	CS	$\kappa_S > 0.68 \lor \kappa_T > 0.91$	16.0	7.8	0.51	4.7	2.6
Φ_T: $2.7 \cdot (E/100\,\text{TeV})^{-2.13}$	SS	$\kappa_S > 0.72$	10.7	3.3	0.17	1.8	1.4
	TS	$\kappa_T > 0.76$	12.1	25	3.6	17	3.9
	CS	$\kappa_S > 0.70 \lor \kappa_T > 0.94$	12.7	5.1	0.29	2.9	1.9
Φ_C: $6.7 \cdot (E/100\,\text{TeV})^{-2.5}$	SS	$\kappa_S > 0.55$	64	63	10	44	10
	TS	$\kappa_T > 0.71$	39	58	13	39	6.6
	CS	$\kappa_S > 0.55 \lor \kappa_T > 0.78$	70	75	11	52	11

Table 10.1: *The optimal cuts on the classifier output (3rd column) for one ARCA year for the considered fluxes (1st column) and the performed searches (2nd column: shower search (SS), track search (TS) and combined search (CS)) and the respective event numbers separated by signal N_S, total background N_B, atmospheric muons N_μ, atmospheric conventional neutrinos N_c and atmospheric prompt neutrinos N_p. Numbers are rounded based on uncertainties which are discussed in Section 10.3.*

Φ [1/(10^{18} cm^2 s sr GeV)]	search	MRF	MDP	$s\,[\sigma]$	$T_{5\sigma}$ [y]	central energy range
Φ_E: $3.6 \cdot (E/100\,\text{TeV})^{-2} \cdot \exp(-E/3\,\text{PeV})$	SS	0.39	1.18	4.5	1.21	46 TeV – 3.5 PeV
	TS	0.69	1.98	2.64	3.6	27 TeV – 1.9 PeV
	CS	0.38	1.12	4.6	1.20	50 TeV – 3.5 PeV
Φ_T: $2.7 \cdot (E/100\,\text{TeV})^{-2.13}$	SS	0.43	1.25	4.2	1.36	72 TeV – 7.4 PeV
	TS	0.81	2.36	2.16	4.9	28 TeV – 6.3 PeV
	CS	0.41	1.23	4.3	1.33	61 TeV – 7.2 PeV
Φ_C: $6.7 \cdot (E/100\,\text{TeV})^{-2.5}$	SS	0.243	0.69	7.0	0.52	13 TeV – 1.8 PeV
	TS	0.37	1.10	4.6	1.21	14 TeV – 1.1 PeV
	CS	0.234	0.68	7.2	0.49	12 TeV – 1.7 PeV

Table 10.2: *Continuation of Table 10.1: sensitivity measures as discussed in the beginning of this chapter (Section 10.1) and the energy range containing the central 90% of events caused by the respective signal flux. Numbers are again rounded based on uncertainties.*

$\kappa_T > 0.91$ and $\kappa_T > 0.94$, respectively. Here, looser cut values would increase the amount of background neutrinos disproportionately. In fact, in all three track searches the number of background events is significantly higher than the number of signal events as opposed to the other searches. However, in each case a very pure neutrino event sample is achieved, given by the number of neutrino events over the number of all events (neutrinos plus atmospheric muons). It is minimal for

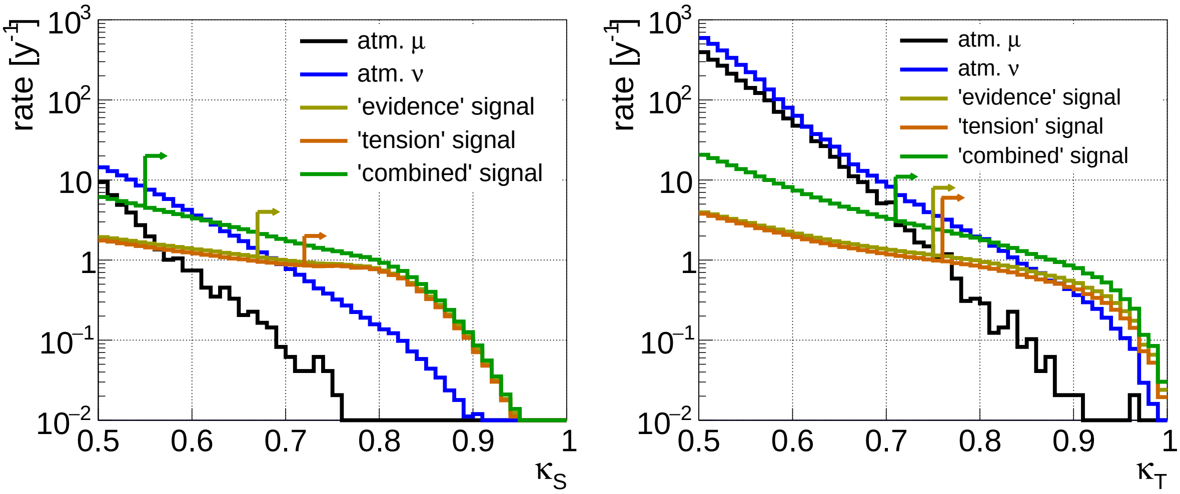

Figure 10.1: *Classifier response distribution for the shower search (left) and track search (right) for signal events of the three considered fluxes together with the background events of atmospheric muons and the sum of conventional and prompt atmospheric neutrinos. The optimal cuts for the two searches are indicated as vertical lines with arrows on top.*

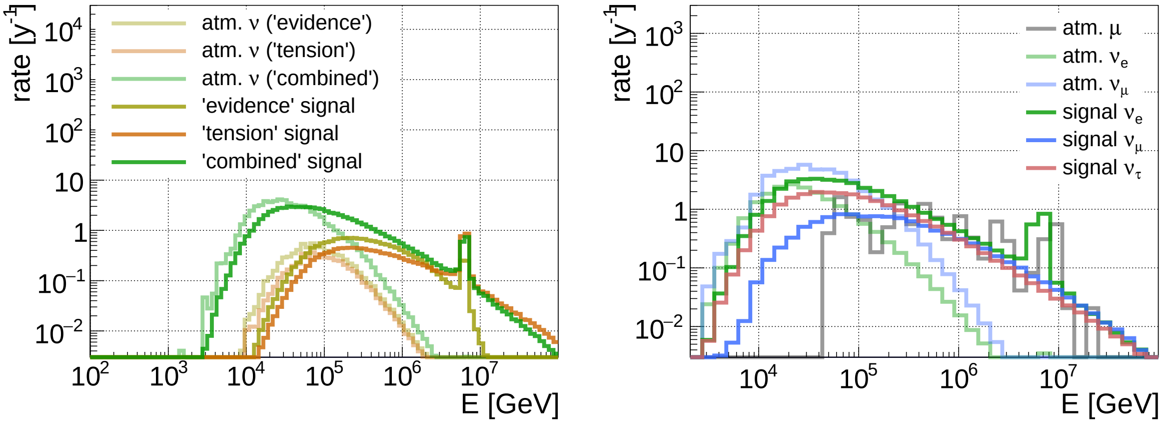

Figure 10.2: *Left: Event rates after the cuts of the combined search for the three considered IceCube signal fluxes as given in Eq. (10.1) to (10.3) together with the corresponding atmospheric neutrino background rates (sum of prompt and conventional). Right: Event rates separated by neutrino flavour for the signal flux Φ_C together with the atmospheric muon and neutrino background event rates (sum of prompt and conventional) after the cut of the combined search.*

Φ_C because of the rather loose cuts with 87% for the track search and 92% for the shower and combined search. For the hard cuts performed for Φ_E and Φ_T, it reaches values up to 99% for the shower search and 98% for the combined search.

Figure 10.2 (right) shows the event rate for Φ_C separated by neutrino flavours in the combined search together with the atmospheric neutrino and muon background. Atmospheric muons are present at energies exceeding 40 TeV and follow roughly the spectrum of the signal neutrinos. The number of atmospheric muons surviving the cut is rather low (118 simulated atmospheric muon events survive the cut, see also Table 10.5 in Section 10.3). It is also interesting to see that signal ν_μ events are much stronger suppressed than the other flavours until roughly 400 TeV, and start to

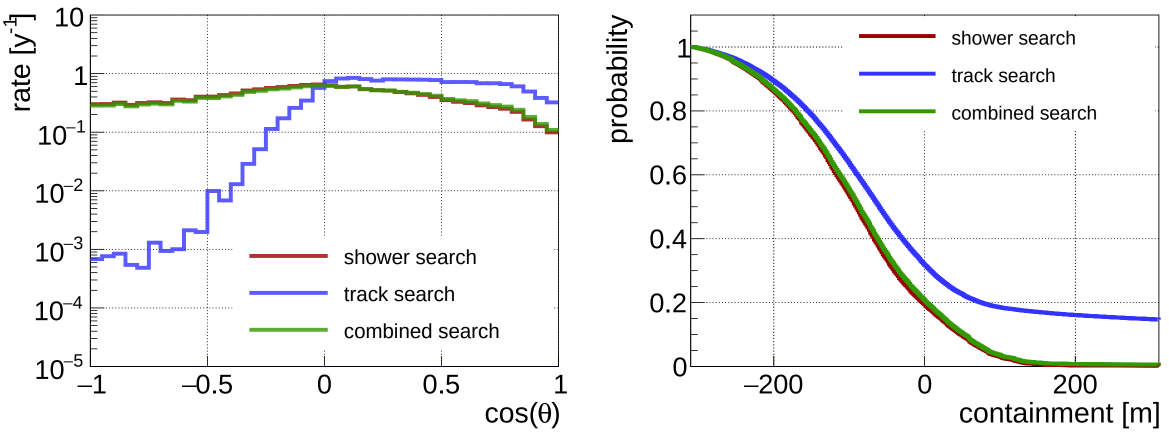

Figure 10.3: *Left: Event rate distribution versus cosine of zenith angle for the 'evidence' flux Φ_E (Eq. (10.1)) after the cuts of the different searches. Right: Normalised cumulative event rate distribution versus the containment for the 'tension' flux Φ_T (Eq. (10.3)) after the cuts of the different searches.*

dominate over the atmospheric ν_μ background at higher energies. Above 400 TeV, signal ν_μ and ν_τ events produce approximately the same event rate.

Figure 10.3 (left) shows the signal event rate distribution according to Φ_E versus the true neutrino zenith angle for the different searches. It becomes evident (as also discussed in Section 9.3) that the track search is only sensitive to events coming from below the horizon while the shower search and combined search are sensitive to events from all directions.

In order to get an impression of the event vertex distribution within and around the detector, Figure 10.3 (right) shows the normalised cumulative event rate distribution versus the containment[48] for the 'tension' flux for all three searches. As expected, the fraction of events outside the instrumented volume (containment > 0) is largest for the track search with roughly 33%. For the shower search, 20% of the events have their interaction vertex outside of the instrumented volume, namely 20%. Roughly 5% for the shower search are further away than 100 m, for the track search about 20%.

10.2.2 Effective area and expected neutrino ratio

From the effective area before and after a given cut, the suppression of the different neutrino flavours becomes evident. An example is shown in Figure 10.4 for the effective area as a function of neutrino energy in the case of the combined search for Φ_C. The right part of this figure visualises the acceptance which is for a given cut defined as the ratio of the effective areas after and before applying the cut. It can be seen that over the whole energy range muon neutrino events are suppressed by nearly one order of magnitude and more. This is caused by the large number of atmospheric muons and the high fraction of atmospheric muon neutrinos that need to be rejected with the cut. This results in similar effective areas for all flavours (except around the Glashow resonance due to $\bar{\nu}_e$ events) as can be seen in Figure 10.4 (left).

Looking at the acceptance for ν_e and ν_τ events, the sensitive energy range becomes evident. Above 100 TeV, the surviving fraction is around 50% (ν_e) and 30% (ν_τ). The shower events which are cut away are mainly events where the interaction happens at the edge of the can (recall also Figure 10.3 (right)) or where, in the case of a ν_τ CC interaction, the resulting tau decays into a

---

[48] For the definition of the containment see Eq. (7.4).

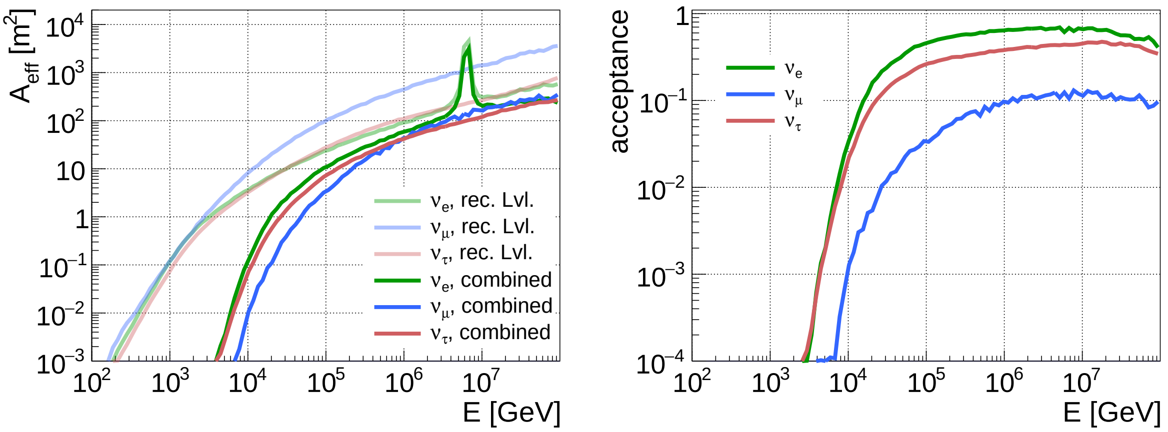

Figure 10.4: *Left: Effective area at reconstruction level (light colors) and after the cut for the different neutrino flavours versus neutrino energy for the combined search for Φ_C. It is averaged over zenith and azimuth angles and neutrinos and antineutrinos, and summed over interaction type (charged and neutral current). Right: Acceptance in terms of effective area, i.e. the ratio of effective area after the cut to effective area at reconstruction level (averaged in the same way as before).*

muon. Below 10 TeV, the suppression is larger than one order of magnitude and the acceptance approaches zero very fast at lower energies.

In general, for the shower searches muon neutrinos are even more suppressed (significantly more than one order of magnitude over the whole energy range) while for the track searches all neutrino flavours are suppressed by a similar amount (nearly one order of magnitude).

Table 10.3 shows the fractions of neutrino types contributing to the event rates of the different neutrino fluxes for the combined search for signal flux Φ_C also separated by interaction type and neutrino/antineutrino. It can be seen that the signal event sample is dominated by ν_e and ν_τ CC events with a total fraction of 75%. The total fraction of purely shower-like signal events (NC events of all types, ν_e CC events, and ν_τ events where the outgoing tau decays into a shower[49]) is around 88%. Thus, only 12% of the signal events exhibit a track.

The large fraction of ν_e CC events as compared to ν_e NC events is due to the fact that in the former case the total neutrino energy is deposited in the detector medium (recall Section 2.4) and the cuts favour events with large deposited energy. Thus, the steeper (softer) the neutrino flux spectrum, the larger (smaller) the ν_e CC/NC fraction. The fraction of neutrino to antineutrino events reflects the higher cross-section for the former event types.

For the events of the prompt atmospheric neutrino flux, the ratios are very similar to the signal ratios when only looking at ν_e and ν_μ events. The conventional atmospheric neutrinos exhibit very few antineutrino events and are dominated by muon neutrinos as expected from the different flux amplitudes (cf. Figure 2.2, p. 21).

10.2.3 Detector resolution

The cuts lead to good-quality neutrino event samples that allow for a representative analysis of the achieved resolutions of the event variables. Energy and direction resolutions following from *Shower*

---

[49] From the central energy range given in Table 10.2 with an upper limit of about 1.7 PeV for Φ_C in the combined search, it follows that the amount of taus with a track length significantly larger than 10 m is negligible. Thus ν_τ CC events with the tau decaying into a shower are treated as shower-like.

	ν_e				ν_μ				ν_τ			
atmospheric conventional neutrinos												
	19.3				80.7				–			
CC | NC	93.8		6.2		51.5		48.5		–		–	
$\nu \mid \bar{\nu}$	63.6	36.4	68.5	31.5	73.3	26.7	73.6	26.4	–	–	–	–
atmospheric prompt neutrinos												
	78.6				21.4				–			
CC | NC	91.7		8.3		62.8		37.2		–		–	
$\nu \mid \bar{\nu}$	55.4	44.6	58.3	41.7	57.4	42.6	57.6	42.4	–	–	–	–
cosmic neutrinos												
	53.0				15.1				31.8			
CC | NC	90.4		9.6		66.2		33.8		86.3 (91.7 | 8.3)		13.7	
$\nu \mid \bar{\nu}$	52.2	47.8	56.1	43.9	55.7	44.3	56.2	43.8	52.6	47.4	55.5	44.5

Table 10.3: *Expected neutrino fractions in % constituting the event rates for atmospheric conventional neutrinos, atmospheric prompt neutrinos and signal neutrinos according to the signal flux Φ_C of Eq. (10.2) after the respective cut of the combined search (compare Table 10.1). They are subgrouped by charged-current (CC) and neutral-current (NC) events and further by neutrinos (ν) and antineutrinos ($\bar{\nu}$) in a way so that the respective subgroup adds up to 100%. For ν_τ CC events also the fraction of events where the tau decays to a shower or to a muon are given in brackets in this order.*

Reconstruction Algorithm 1 (SR1) and from the track reconstruction algorithm (TR) are shown in Figure 10.5.

For ν_e CC events in the combined searches, the deviation between the reconstructed energy and the true neutrino energy is slightly less than 10% over most part of the relevant energy range for 68% of the events[50]. For 90% of the reconstructed events, the deviation is still less than 20%. Regarding the zenith angle of tracks originating from ν_μ CC events, the median resolution reaches values well below 1° and even down to 0.1° at very high energies. As the event samples for the combined search are a mixture of tracks and showers, a fine tuned event selection would have to be performed that selects pure showers and tracks to which these resolutions can be applied.

The bottom row of Figure 10.5 compares the SR1 zenith angle resolution of ν_e CC events versus neutrino energy (left) with that of ν events of all types versus the reconstructed energy of SR1 (right). In other words, the latter plot uses no Monte Carlo truth information for neutrino flavour and energy. Still for both cases a very good median resolution is achieved with values down to almost 1°. In addition, in nearly 90% of all events the angle is resolved better than 10°.

10.2.4 Self-veto effect

Finally, the simulations regarding the self-veto effect (Section 6.1), i.e. atmospheric neutrinos coming from above in coincidence with atmospheric muons from the same extensive air shower (EAS

---

[50] The 68% interval is chosen because it corresponds to the $\pm 1\,\sigma$ interval of a Gaussian distribution.

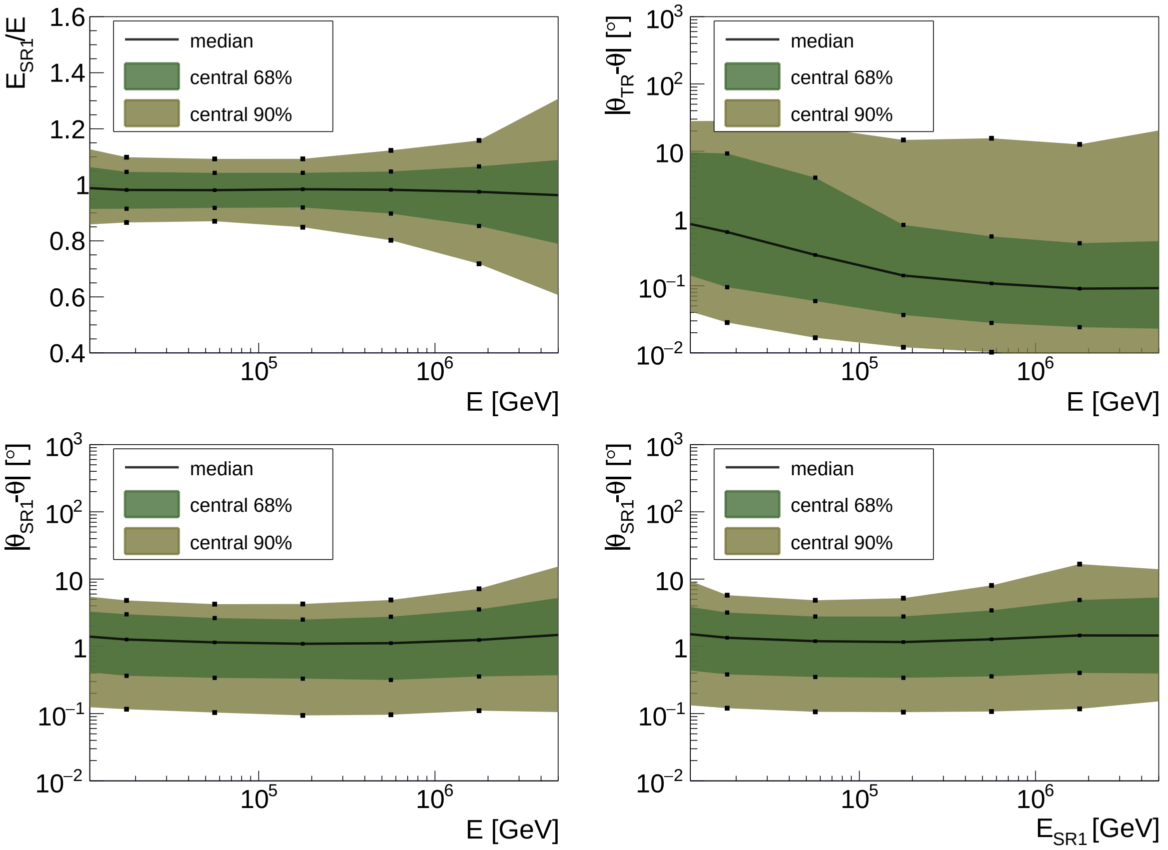

Figure 10.5: *Top left: Energy resolution according to SR1 for ν_e CC events after the cut of the combined search for Φ_C. Top right: Zenith angle resolution according to TR for ν_μ CC events after the cut of the track search for Φ_C. Bottom: Zenith angle resolution after the cut of the combined search for Φ_C for ν_e CC events (left) and neutrinos of all flavours for any interaction type (right) according to SR1. In each case the median is given as black line, the central 68% as green and the central 90% of the respective distributions as brown shaded area; two data points per energy decade, given as black squares, were determined for each of the respective quantiles.*

	conventional			prompt			sensitivity
flux	N_{rej}	N_{sim}	N_{tot}	N_{rej}	N_{sim}	N_{tot}	$s\,[\sigma]$
Φ_E	0.3	1.5 (20%)	4.7 (6.3%)	0.3	0.9 (37%)	2.6 (13%)	4.7 (+3.5%)
Φ_T	0.2	1.0 (21%)	2.9 (7.1%)	0.3	0.7 (40%)	1.9 (14%)	4.4 (+2.5%)
Φ_C	1.9	14 (14%)	52 (3.6%)	0.8	3.0 (29%)	11 (7.6%)	7.3 (+1.5%)

Table 10.4: *The effect of the self-veto for atmospheric conventional and prompt neutrinos for the cuts of the combined search regarding the three considered signal fluxes. The number of rejected events N_{rej} is compared to the number of events N_{sim} in the range of the EAS simulations (see text) and to the total number of the respective neutrino background events N_{tot} (also given in Table 10.1). In brackets, the event reduction resulting from the self-veto effect is given as a fraction (e.g. N_{rej}/N_{sim}). In the last column the new significance after one year is given (with its increase in brackets, compare Table 10.2). Numbers are rounded based on expected uncertainties as discussed in the next section.*

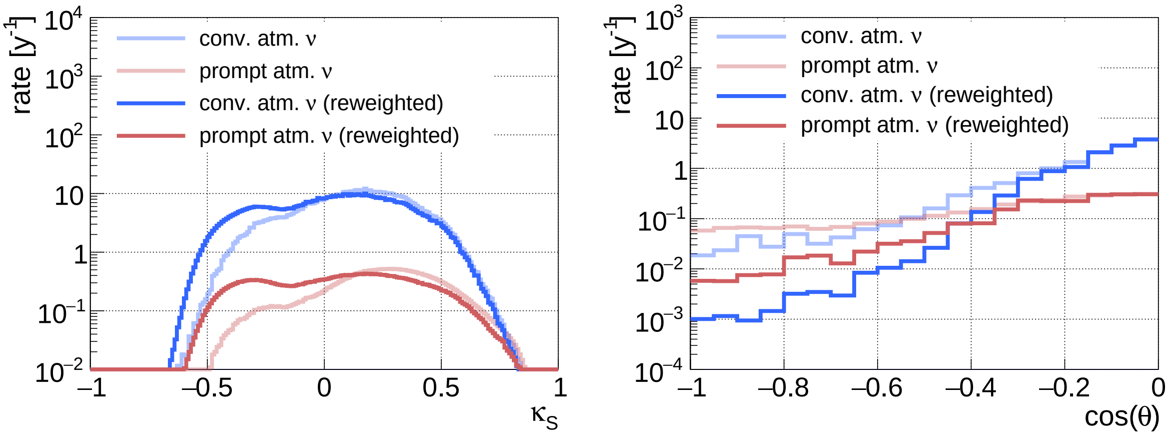

Figure 10.6: *The effect of the self-veto separated by conventional (blue) and prompt (red) atmospheric neutrinos with respect to the classifier response of the shower search (left), and with respect to the zenith angle (right) after the cut of the combined search with respect to Φ_C. Shown are the event rates within range of the EAS simulations before and after the reweighting as discussed in the text.*

simulations), are applied to the outcome of the cut-and-count analysis[51]. This effect is not applicable to the track search since this search rejects most events coming from above. For the shower search, however, being accompanied by atmospheric muons, such neutrinos are considered more background-like for the classification. The average classification response has therefore a lower value than for neutrinos unaccompanied by atmospheric muons. This is visible in Figure 10.6 (left) which shows the event rate distribution of atmospheric neutrinos versus the shower classifier output κ_S before and after the EAS-simulations reweighting. Considered are only events from above within the range of the EAS simulations (neutrinos with energies above 10 TeV and interaction vertices within the instrumented detector volume). Thus, a cut in the signal region rejects more of the atmospheric neutrino background than without the reweighting.

It becomes also clear, however, that the effect is rather small. For the combined search, the corresponding number of additionally rejected events and the respective event rate reductions are listed in Table 10.4. For the fluxes Φ_E and Φ_T, the reduction of events in the range of the EAS simulations reaches around 20% for the conventional and around 40% for the prompt flux. For the stronger flux Φ_C the reduction is in both cases roughly ten percentage points smaller. The resulting change in significance and its increase are listed in the table as well.

The reason why the fraction of rejected prompt neutrinos is higher than for conventional neutrinos becomes evident from Figure 10.6 (right). Here the event rates before and after the EAS-simulations reweighting are shown as a function of zenith angle. Since the probability to be accompanied by an atmospheric muon is much higher for neutrinos coming straight from above than for neutrinos from the horizon, the corresponding rejection is much higher, too (about 10% of the neutrinos survive the cut after the reweighting). However, the flux and thus the event rate of conventional neutrinos from above is much lower than for those coming from the horizon. For prompt neutrinos, the difference in event rate (before the reweighting) for neutrinos coming from above and from the horizon is much smaller. Hence, the total fraction of rejected events is higher after the reweighting for the prompt neutrinos.

The reason why the effect is smaller for the strong flux Φ_C is that much more lower-energy

---

[51] Recall that these simulations were not applied to the classification because of their preliminary status.

							atmospheric ν				
	signal ν			atm. μ			conv.		prompt		
flux	σ_{MC}	δ_{MC}	N_{sim}	σ_{MC}	δ_{MC}	N_{sim}	σ_{MC}	δ_{MC}	σ_{MC}	δ_{MC}	N_{sim}
Φ_E	0.06	0.4%	512 000	0.25	50%	9	0.13	2.7%	0.015	0.6%	161 000
Φ_T	0.13	1.1%	462 000	0.14	50%	7	0.09	3.1%	0.012	0.6%	147 000
Φ_C	0.20	0.29%	853 000	1.8	15%	118	1.0	1.9%	0.05	0.5%	265 000

Table 10.5: *The uncertainty σ_{MC} and relative error δ_{MC} (Eq. (10.11) and (10.12)) from the Monte Carlo simulations for signal, atmospheric muon and atmospheric conventional and prompt neutrino events for the combined search for the different signal fluxes (Eq. (10.1) to (10.3)) together with the number of simulated events N_{sim} surviving the respective cut (compare also Table 10.1, p. 137). For σ_{MC} and δ_{MC} the rounding rules of the particle data group are used (see Introduction of [2]) while N_{sim} is rounded to three significant digits.*

events survive the cuts (see also Figure 10.2) as compared to the other fluxes. The lower-energy atmospheric neutrinos coming from above are less likely to be accompanied by an atmospheric muon than higher-energy neutrinos [96]. This also adds to the effect that the reduction is larger for prompt neutrinos as here the spectral index is harder and the fraction of high-energy neutrinos is greater than for conventional neutrinos.

The rejection of events via the self-veto reduces to values below 10% in most cases (as also shown in Table 10.4) when all events surviving the cuts are taken into account[52].

Regarding sensitivity, the reweighting leads to an increase of the significance of 0.1 after one ARCA year, as also shown in Table 10.4. An extension of the EAS simulations to all detectable events, and including these in the classification, is expected to further increase the significance.

10.3 Systematic uncertainties

In the following, the impact of systematic uncertainties will be described, separated by uncertainties in the Monte Carlo simulations and uncertainties following from the assumed physics.

10.3.1 Monte Carlo uncertainties

Since the event numbers following from the Monte Carlo (MC) simulations are taken as means for the Poisson distributions discussed in Eq. (10.5) and (10.6), possible deviations from the true mean values have to be considered. The uncertainty σ_{MC} in the MC event number $N_{\text{MC}} = \sum_{i=1}^{N_{\text{sim}}} w_i$ can be calculated from the event weights[53] w_i of the events surviving the cut as follows

$$\sigma_{\text{MC}}^2 = \sum_{i=1}^{N_{\text{sim}}} w_i^2. \tag{10.11}$$

---

[52] This comprises events below 10 TeV, events outside the instrumented volume and events coming from below the horizon.

[53] Compared to Eq. (6.6) and (6.7), the weight for neutrino events is here transformed as $w_i \to w_i \Phi(E_i, \theta_i)/N_{\text{gen}}$.

where the sum runs over all simulated events N_{sim} of a given class (e.g. signal neutrinos or atmospheric muons). The relative error δ_{MC} is given by

$$\delta_{\text{MC}} = \sigma_{\text{MC}} \,/\, N_{\text{MC}} = \sqrt{\sum w_i^2} \,/\, \sum w_i, \tag{10.12}$$

where as above the sums run over the respective number of simulated events. For similar event weights, the relative error approaches $1 / \sqrt{N_{\text{sim}}}$ and gets small for large N_{sim}.

Table 10.5 lists the uncertainties and the relative errors for the different event classes for the combined search for the different signal fluxes together with the number of simulated events surviving the cuts. Many neutrino events survive the cuts so that the MC error in these cases is small. Both types of atmospheric neutrino fluxes share the same simulated events while the signal additionally comprises the tau neutrino events. For the signal and prompt neutrinos, the relative error has values around 1% and smaller while it is around 2-3% for the conventional atmospheric neutrinos. This is caused by the fact that the event rate of the conventional neutrinos is dominated by muon neutrinos of which fewer survive the cut but which have a high event weight (due to the large muon neutrino flux). The source of the largest MC uncertainty are the atmospheric muons. Here, only very few simulated events survive the cut so that the relative error takes values up to 50% for the searches to Φ_E and Φ_T.

In general however, it can be stated that the uncertainties are low. Taking into account all background uncertainties in quadrature leads to a relative uncertainty for the significance after one ARCA year of around 2% in all cases which is negligible compared to the systematic uncertainties discussed in the following section.

10.3.2 Physics systematics

The systematic uncertainties related to physics can be categorised into three groups which are described in the following: Non-simulated physics, detector uncertainties and background flux uncertainties.

Non-simulated physics

Several physics effects are not or only partly considered in the simulations, among them atmospheric muons below 10 TeV and neutrinos below 100 GeV and above 100 PeV. Looking for example at Figure 10.2 (p. 138), it becomes clear that these are negligible.

Among the phenomena which require in-depth investigations are the full self-veto effect, i.e. simulation of coincident atmospheric neutrinos and muons also outside of the instrumented volume, and the neutrino regeneration effect which happens on the neutrino's path through the Earth (see Section 2.3). For the self-veto effect also increased statistics are required [96]. Both effects will increase the sensitivity, though they are not further addressed here.

In addition, no prompt component of the atmospheric muons were simulated. Recent calculations [118] and measurements [119] show that this component becomes significant above around 1 PeV. These additional muons would reduce the sensitivity and also require further investigations.

Detector uncertainties

The detector uncertainties include everything related to the detector components and the surrounding medium. In particular, calibration uncertainties like positioning and orientation of the strings and

flux	Φ_E			Φ_T			Φ_C		
search	SS	TS	CS	SS	TS	CS	SS	TS	CS
conv.	15%	17%	15%	14%	17%	14%	17%	17%	17%
prompt	11%	5%	11%	14%	5%	13%	5%	4%	5%

Table 10.6: *Effect of the systematic uncertainties in the conventional and prompt atmospheric neutrino flux on the total background event rate.*

DOMs, as well as uncertainties in the PMTs, among them the timing or charge calibration. Important uncertainties of the detector medium are those of the light scattering and absorption lengths of the sea water around the detector. Most of these uncertainties have been studied to a large extent within the KM3NeT Letter of Intent [7] and have been proven to be negligible compared to the next group of uncertainties.

Background flux uncertainties

The background fluxes comprise atmospheric muons as well as the conventional and prompt atmospheric neutrinos. The uncertainty for the atmospheric muon flux is around 15% while that for the conventional neutrinos is taken to be ±25% [42]. Given the relatively small number of atmospheric muons surviving the cuts, it follows that the respective uncertainty is negligible compared to that of the conventional neutrinos. For the prompt flux, the uncertainty as given by Enberg [40] is used. It leads for all cuts of all searches to an asymmetric error of $^{+27\%}_{-41\%}$ in the prompt neutrino event rates.

Given the deviations to smaller event rates by σ_- and to higher event rates by σ_+, so that $\sigma_- = \sigma_+ = 0.25\,N_c$ for conventional, $\sigma_- = 0.41\,N_p$ and $\sigma_+ = 0.21\,N_p$ for prompt neutrinos with event number N_c and N_p, respectively, the relative error ε to the total number of background events $N_B = N_c + N_p + N_\mu$, with N_μ as the number of atmospheric muon events, is calculated as

$$\varepsilon = \frac{\sigma_- + \sigma_+}{2N_B}. \tag{10.13}$$

It is listed in Table 10.6 and it becomes clear that the uncertainty in the conventional neutrinos dominates in the track searches and in all searches for the signal flux Φ_C. In the shower and combined search, for flux Φ_E the prompt uncertainty is still a little smaller, but for Φ_T both uncertainties are of equal importance. In other words, the higher the sensitive energy range the more important the uncertainty of the prompt neutrino flux (because of its hard spectrum).

Combining both uncertainties in quadrature, the significance after one ARCA year has a relative uncertainty of around 10% for all searches and signal fluxes.

Figure 10.7 shows the significance and the probability to make a $5\,\sigma$ discovery over time for the combined search for all signal fluxes. In both cases also the uncertainties due to the prompt and atmospheric neutrino flux are shown. Each of the signal fluxes will be observed at $5\,\sigma$ level with more than 90% probability after three ARCA years, the strong ‘combined’ flux Φ_C already after less than one year.

Finally, it should be mentioned that the IceCube collaboration found a best-fit prompt component of zero with a 90%-confidence-level upper limit of 1.06 times the Enberg flux [28]. Assuming a

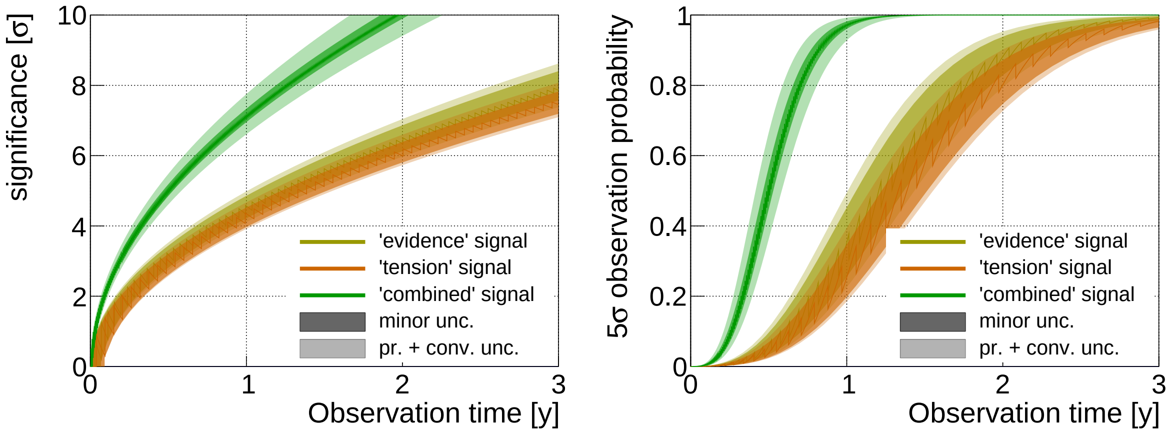

Figure 10.7: *Significance at 50% observation probability (left) and probability for a 5σ observation (right) over time for the different signal fluxes in the combined search including uncertainties from the conventional and prompt atmospheric neutrino flux. The graphs show the mean (i.e. without uncertainty) while the dark shaded bands show the minor of the two uncertainties (prompt for the 'evidence' flux Φ_E and 'combined' flux Φ_C, conventional for the 'tension' flux Φ_T) and the lightly shaded bands show the combined uncertainty.*

zero prompt component increases the mean significances after one ARCA year by roughly 5-15% (depending on the assumed signal flux).

10.4 Discussion and conclusion

In this chapter, the sensitivity of ARCA to three different cosmic neutrino fluxes was examined using a cut-and-count approach. A cut was placed on the classifier response for both the shower and track search as well as for a combined search. After the cut was applied, the number of events surviving the cut gave the expected number of signal and background events from which the discovery potential was determined. The sensitivity achieved is significantly higher in the shower search than in the track search – the combination of both is only slightly better than the shower channel alone. The results are summarised in Table 10.1 and 10.2 on page 137.

The signal fluxes considered are given by

$$\Phi_E(E) = 3.6 \cdot 10^{-18} \cdot \left(\frac{E}{100\,\mathrm{TeV}}\right)^{-2} \cdot \exp\left(-\frac{E}{3\,\mathrm{PeV}}\right) \left(\mathrm{cm}^2\,\mathrm{s}\,\mathrm{sr}\,\mathrm{GeV}\right)^{-1},$$

$$\Phi_C(E) = 6.7 \cdot 10^{-18} \cdot \left(\frac{E}{100\,\mathrm{TeV}}\right)^{-2.5} \left(\mathrm{cm}^2\,\mathrm{s}\,\mathrm{sr}\,\mathrm{GeV}\right)^{-1},$$

$$\Phi_T(E) = 2.7 \cdot 10^{-18} \cdot \left(\frac{E}{100\,\mathrm{TeV}}\right)^{-2.13} \left(\mathrm{cm}^2\,\mathrm{s}\,\mathrm{sr}\,\mathrm{GeV}\right)^{-1},$$

as published by the IceCube collaboration except that for Φ_E, which was used for the classification, the cut-off at 3 PeV was added to avoid a bias towards very-high-energy events.

With the combined search, the signal flux Φ_C is observed at the $5\,\sigma$ level with 50% observation probability after 0.49 ± 0.07 years in ARCA. For the flux Φ_E as initially published by the IceCube collaboration [3], the corresponding time needed is 1.20 ± 0.22 years. This is in comparison considerably less detector livetime than the IceCube collaboration used for their results[54]. One reason for this is that the event selection of the IceCube analysis was designed for events well contained within the detector volume while here the containment is of minor importance (roughly 20% of the events surviving the cut of the combined search are outside the instrumented volume). In addition the analyses presented here were optimised for the respective flux while the IceCube search was guided by theoretical predictions. With the respective event selection, the IceCube collaboration found 28 events in the two years of data with deposited energies greater than 30 TeV, of which 17 are consistent with cosmic origin. With ARCA and the search presented here, significantly more events are expected after two years of data: roughly 47 neutrino events with deposited energies similar to those of the events observed by IceCube, 32 of which of cosmic origin (see also Table 10.1, p. 137).

The achieved significance for the third considered flux Φ_T is very similar to that of Φ_E due to the similar spectral shape of the two fluxes. However, the respective track search result achieved here is slightly worse compared to that achieved in the respective IceCube publication [30] which was conducted in the track channel. This indicates room for improvement in the track search performed here. Recall that the methods described in Chapter 8 and 9 were developed and optimised for a shower channel analysis and afterwards applied for the track channel. Indeed, utilising the shower channel to search for this flux, a $5\,\sigma$ detection (50% observation probability) is possible within less than 1.5 years of ARCA. This is significantly less observation time than utilised in the respective IceCube analysis where $5.6\,\sigma$ were achieved with six years of data (four of which with the full IceCube

---

[54] The respective IceCube results achieving a detection at $4\,\sigma$ level were obtained with one year of data of the full detector (86 strings, 2011-2012) and one year of data during construction phase (79 strings, 2010-2011). Recall that the ARCA detector will roughly be of the same size as the full IceCube detector.

detector). It should be noted, however, that a track search is only sensitive to one hemisphere while a shower search is sensitive to the full sky.

Compared with previous cut-and-count analyses for the ARCA sensitivity as presented in the KM3NeT Letter of Intent [7], an increase in sensitivity in the shower channel is achieved, reducing the observation time needed for a $5\,\sigma$ discovery by roughly 10%. However, the results of the track channel could not be reached confirming that the track search performed here has room for optimisation. The starting point would be to include a dedicated muon energy estimator in the classification. Further steps could be to make a several-step classification where three major steps come to mind: 1) separating showers from tracks, 2) separating up-going from down-going tracks, 3) separating high-energy from low-energy tracks.

The main source of uncertainties are the systematics in the assumed background neutrino fluxes of atmospheric conventional and prompt neutrinos leading to an uncertainty of roughly ±15% (Φ_C) and ±18% (Φ_T) in the significance after one year observation time. In comparison to that, the uncertainties resulting from simulations are negligible with values around ±2%. All results presented here assume a prompt atmospheric neutrino flux according to Enberg. However, the IceCube collaboration found a best-fit prompt component of zero with a 90%-confidence-level upper limit of 1.06 times the Enberg flux [28]. Assuming a zero prompt component increases the predicted significances after one year of ARCA by roughly 5% for Φ_C and about 15% for Φ_T.

Besides the discovery potential, also the detector resolutions for the neutrino event samples surviving the cuts was investigated. The energy resolution to ν_e charged-current events is better than 10% for neutrino energies between 10 TeV and 1 PeV for 68% of the reconstructed events. The median zenith angle resolution is better than 1° for most of the events (independent of the topology) while it reaches values down to 0.1° for track events.

Finally, it should be mentioned that a cut-and-count analysis has several disadvantage: firstly, the cut has to be tuned to a given hypothesis and is evaluated afterwards. The different results of IceCube show, however, that the true flux of cosmic neutrinos still has many unknowns. Therefore, it is advisable to use a method that is independent of a certain signal hypothesis. Secondly, with a cut also many potential signal events are rejected that could still bear information about their origin. This information is lost when performing a cut. In the next chapter, an analysis is performed that counteracts these disadvantages, thereby increasing the discovery potential while also being sensitive to the spectral properties of the cosmic neutrino flux.

Chapter 11

Spectral sensitivity

In this chapter, the discovery potential of ARCA to diffuse cosmic neutrino fluxes and the sensitivity to different signal flux parameters is investigated with the help of a maximum-likelihood method. The principle of the method is described in Section 11.1 and consists of fitting the different event rate spectra to generated data. The method is therefore also called “spectral fitting”. The discovery potential achieved with this method is described in Section 11.2. Section 11.3 examines the sensitivity to signal flux parameters which is obtained via a small modification of the likelihood method. In Section 11.4 the potential to discriminate different signal flux models is discussed, and Section 11.5 investigates the sensitivity to the prompt atmospheric neutrino flux achievable with this method. Section 11.6 concludes with a summary and outlook.

The analyses described in this chapter focus on the ‘combined’ and ‘tension’ signal fluxes Φ_C and Φ_T as defined in Eq. (10.2) and (10.3), respectively. In addition, the analyses are based solely on the shower classifier described in Section 9.3. An inclusion of the track classifier would be part of future analyses.

11.1 Maximum likelihood method

For the spectral fitting, a binned maximum-likelihood approach[55] is used based on the classifier response distributions for the different event classes. They are shown in Figure 11.1 (left). With the help of the likelihood function given below, the distributions for signal and background are fitted to so-called pseudo-experiments. In a pseudo-experiment, event numbers are generated in each bin according to a Poisson distribution with mean as given by the sum of the respective bin contents of the considered distributions. Pseudo experiments are generated for the background hypothesis H_B (without signal), and for the signal hypothesis H_S (background plus signal). An example for generated event rate distributions from pseudo experiments is shown in Figure 11.1 (right) for both H_B and H_S.

The total likelihood L for a single pseudo experiment is given by the product of the single-bin likelihoods:

$$L = \prod_{i=1}^{N_{\text{bin}}} \frac{\mu_i^{n_i}}{n_i!} e^{-\mu_i} \tag{11.1}$$

---

[55] See e.g. [95] for a detailed description of maximum-likelihood methods.

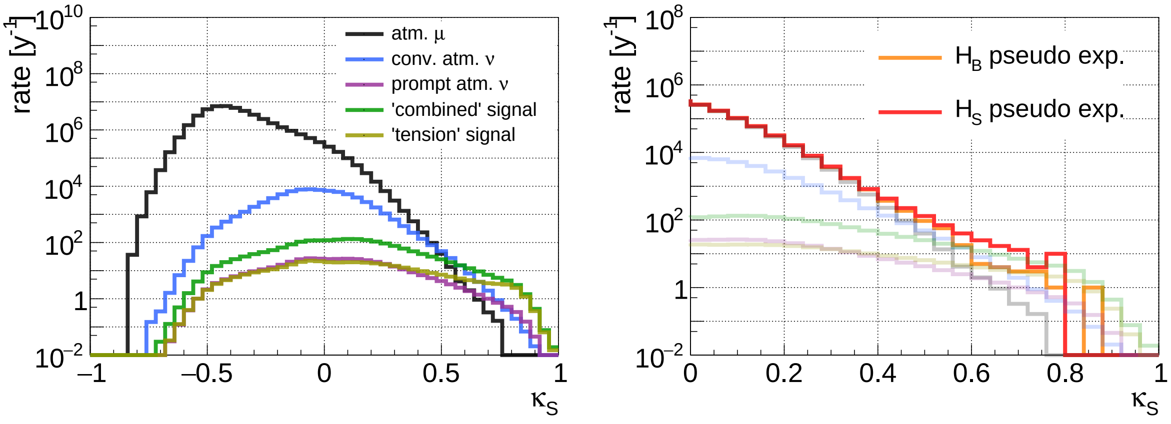

Figure 11.1: *Left: Event rate distributions versus the shower classifier response for the background flux and the 'combined' and 'tension' signal fluxes. Right: Event rate distributions zoomed in on the interesting signal range ($\kappa_S > 0$) for a single pseudo experiment in the background hypothesis H_B (orange) and signal hypothesis H_S (red) with the 'combined' flux as the signal. For comparison, the background and signal event rate distributions are shown in faint colors (see left figure).*

where n_i is the number of events generated in a pseudo-experiment, μ_i is the number of expected events in bin i, and N_{bin} is the total number of bins here chosen to be 50 in the range $-1 < \kappa_S < 1$. This choice is explained at the end of this section. The respective log-likelihood $\ln L$ is given as

$$\ln L = \sum_{i=1}^{N_{\text{bin}}} n_i \ln \mu_i - \mu_i - \ln n_i!. \tag{11.2}$$

In order to get the relative strengths of the background and signal fluxes present in the pseudo-experiment, they are fitted via their normalisations to produce the maximum (log-)likelihood. For this purpose, the expected number of events μ_i is written as

$$\mu_i = \sum_{\alpha} c_\alpha \, \mu_{i,\alpha} = c_{\text{s}} \, \mu_{i,\text{s}} + c_\mu \, \mu_{i,\text{m}} + c_{\text{c}} \, \mu_{i,\text{c}} + c_{\text{p}} \, \mu_{i,\text{p}} \tag{11.3}$$

where the c_α are the respective flux normalisations for signal ($\alpha = \text{s}$), atmospheric muons ($\alpha = \text{m}$), atmospheric conventional ($\alpha = \text{c}$) and prompt neutrinos ($\alpha = \text{p}$). The $\mu_{i,\alpha}$ are the respective expected event numbers in bin i given via the event rate histograms (Figure 11.1 (left)). The maximum-likelihood fit is then performed by varying the normalisations so that the maximum log-likelihood is produced, with the constraint that only non-negative values are allowed for any of the normalisations. Thus, the distributions for the flux normalisations when performing many pseudo experiments and fitting the normalisations are expected to be centred around unity. The only exception here is that for H_B, the signal normalisation c_{s} is expected to be close to zero instead.

In order to account for the known uncertainties of the background fluxes, further terms are added to the likelihood function that penalise deviations of the normalisation from their expected mean of unity. They are chosen to be Gaussian-shaped with widths σ_α equal to the respective systematic uncertainty listed in Table 11.1 (compare also Section 10.3). Note that the uncertainty on the prompt flux has thus been symmetrised in a conservative way. The log-likelihood then takes the form

$$\ln L(c_{\text{m}}, c_{\text{c}}, c_{\text{p}}, c_{\text{s}}) = \sum_{i=1}^{N_{\text{bin}}} \left[n_i \ln \left(\sum_{\alpha} c_\alpha \, \mu_{i,\alpha} \right) - \sum_{\alpha} c_\alpha \, \mu_{i,\alpha} - \ln n_i! \right] - \sum_{\alpha \neq \text{s}} \frac{(c_\alpha - 1)^2}{2\sigma_\alpha^2}, \tag{11.4}$$

σ_m	σ_c	σ_p
0.15	0.25	0.5

Table 11.1: *Systematic uncertainties as introduced in Eq. (11.4) assumed in the spectral fitting for the background fluxes: atmospheric muons σ_m, conventional atmospheric neutrinos σ_c and prompt atmospheric neutrinos σ_p.*

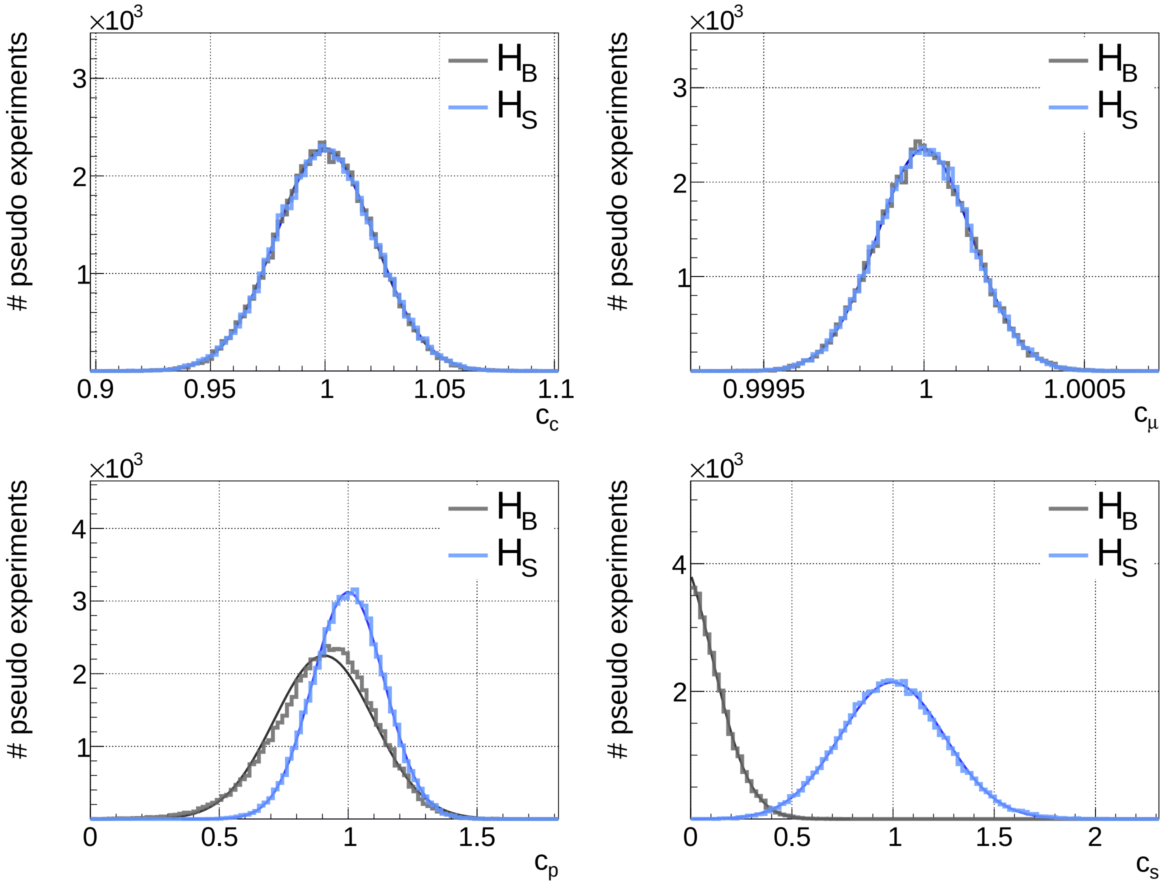

Figure 11.2: *Distributions of the normalisation factor for the atmospheric muon flux (top left), atmospheric conventional (top right) and prompt (bottom left) neutrino flux, and signal neutrino flux (bottom right) in case of the background-only hypothesis (H_B, black) and signal hypothesis (H_S, blue) assuming the 'tension' flux and one year of observation. Gaussians are fitted to all distributions (smooth lines). Normalisation factors smaller than 10^{-4} are neither shown in the plots nor used to fit the Gaussians.*

and is maximised with respect to the c_α.

In order to determine the sensitivity to a given signal flux, pseudo-experiments are generated for both the background hypothesis H_B and the signal hypothesis H_S. An example of the distributions of fitted normalisation factors after generating 60 000 pseudo experiments for both cases is shown in Figure 11.2 for one year of ARCA with the 'tension' signal flux of Eq. (10.2).

From the distributions of fitted c_s the probability to make an observation with a given minimum significance can be calculated[56]. Here, the H_S distribution determines the observation probability for

---

[56] See also Section 10.1 for the definition of significance.

a given c_s which in turn determines the significance as given by the H_B distribution (the probability, or p-value, to observe such a value or higher for c_s under the background hypothesis). The distributions can very well be described by Gaussian distributions which are fitted to them. The significance s at 50% observation probability, used to quantify the discovery potential of ARCA in the next section, is then given from the fitted Gaussians as:

$$s = \frac{\mu_S - \mu_B}{\sigma_B}, \tag{11.5}$$

where μ_S is the mean of the Gaussian for H_S, and μ_B and σ_B are the mean and standard deviation of the Gaussian for H_B. This relation follows from the definition of the significance and from basic properties of the Gaussian distribution (see e.g. [95]).

Looking at the distributions for the background normalisation also shown in Figure 11.2 it can be seen that for the atmospheric muons and conventional neutrinos the distributions for both hypotheses overlap completely. The large contribution of atmospheric muon events in the background-like region of the classifier response leads to a c_m distribution with a width of only about 10^{-4}. The distribution for the normalisation c_c of conventional neutrinos is constrained mainly by their event rate in the region around $\kappa_S = 0.5$ leading to a width of around 10^{-2}. In fact, the penalty term in the likelihood for both the atmospheric muons and conventional neutrinos has no significant influence on the fit. This is different for the prompt atmospheric neutrinos whose fitted-normalisation distribution is well constrained by the penalty term. In the case of the background hypothesis the distribution has a mean smaller than unity and has clear deviations from a Gaussian distribution. This is mainly due to the fact that the prompt contribution is so weak that the approximation of a Gaussian distribution is not well applicable.

In order to be able to compare different flux models as discussed in Section 11.3, the term 'signal strength' is defined as follows: given a signal hypothesis S_1 which is used to generate the pseudo experiments and another signal hypothesis S_2 whose spectrum is fitted to the generated data while the background normalisations are kept fix at $c_\alpha = 1$, S_2 is considered to have the same 'signal strength' as S_1 when the resulting distribution of the flux normalisation c_s has its mean at unity.

Finally, regarding the chosen number of bins used for the likelihood fit, it should be noted that the choice of 50 is a compromise between three different aspects. Firstly, a small bin number leads to a loss in separation power between the different distributions. Regarding the extreme case of only one bin, the separation power vanishes. Secondly, for a very high bin number statistical fluctuations in the Monte Carlo simulations have to be considered for bins with few Monte Carlo entries. In the extreme case where there is at maximum only one entry per bin, the respective sample variance goes to infinity. And thirdly, for bin numbers $\gtrsim 10$, the computation time needed for finding the maximum likelihood is mainly dictated by the number of bins as for each point in the likelihood parameter space the sum over all bins (Eq. (11.4)) has to be performed. The choice of 50 bins is a compromise between all three aspects allowing the statistical Monte Carlo uncertainties to be neglected while providing a good separation power: a choice of 100 number of bins increases resulting sensitivities only slightly (in the percent regime) but doubles the computation time needed.

The likelihood-method developed here represents a completely different approach compared to the cut-and-count method applied in the previous chapter, and will be used in the next section to

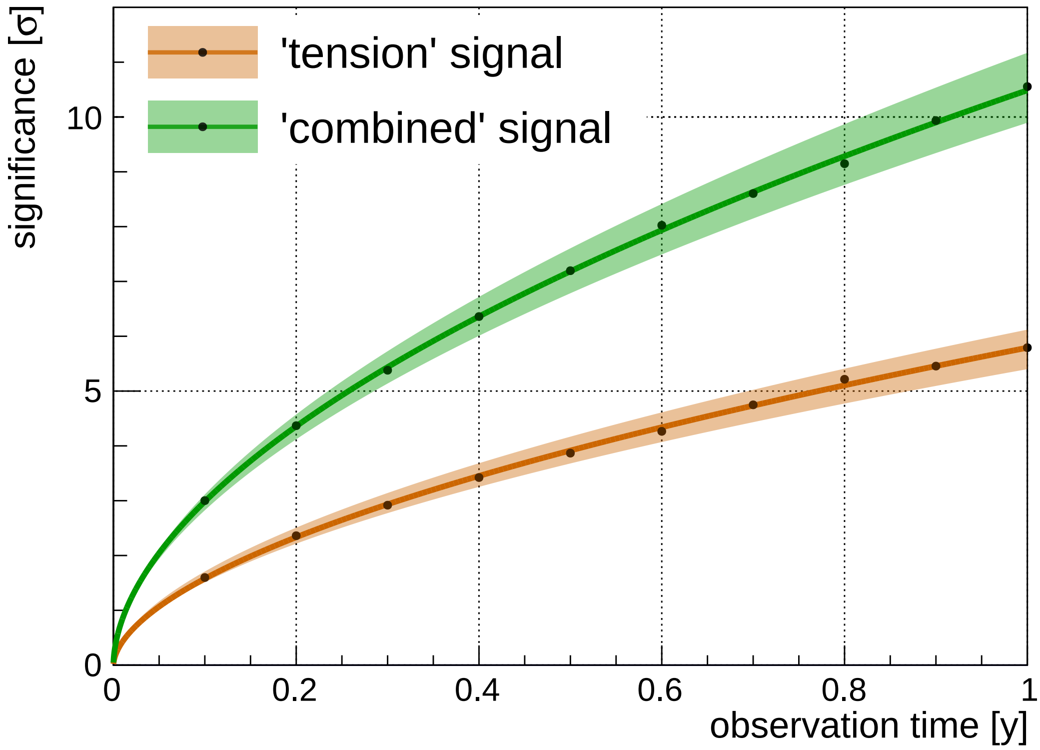

Figure 11.3: *Significance over ARCA time regarding the 'combined' flux (green) and the 'tension' flux (orange). To the generated points (black) a function is fitted (see text). Uncertainties resulting from background flux systematics are shown as bands.*

evaluate the discovery potential of ARCA in an unprecedented way. The advantage over the cut-and-count method is clear: the full spectral information of the signal events "encoded" in the shower classifier response is used – no information is lost.

11.2 Discovery potential

With the method developed in the previous section, the significance achieved with 50% observation probability is calculated for both the 'combined' and the 'tension' flux. It is shown as a function of ARCA observation time[57] in Figure 11.3 together with the uncertainties that follow from the systematic errors in the background fluxes. For each data point (shown as black dots) 60 000 pseudo experiments were generated for both the background and signal hypothesis. To the data points the following function:

$$f(t) = a \cdot t^b \tag{11.6}$$

is fitted via a and b, with t the ARCA time in years, so that a gives the significance after one ARCA year and b determines the rise of the significance. The result is for the 'combined' flux $a = 10.5\,\sigma$ and $b = 0.55$, and for the 'tension' flux $a = 5.79\,\sigma$ and $b = 0.56$.

---

[57] ARCA observation time, or 'ARCA time' for short, corresponds to the time during which the full ARCA detector is taking data.

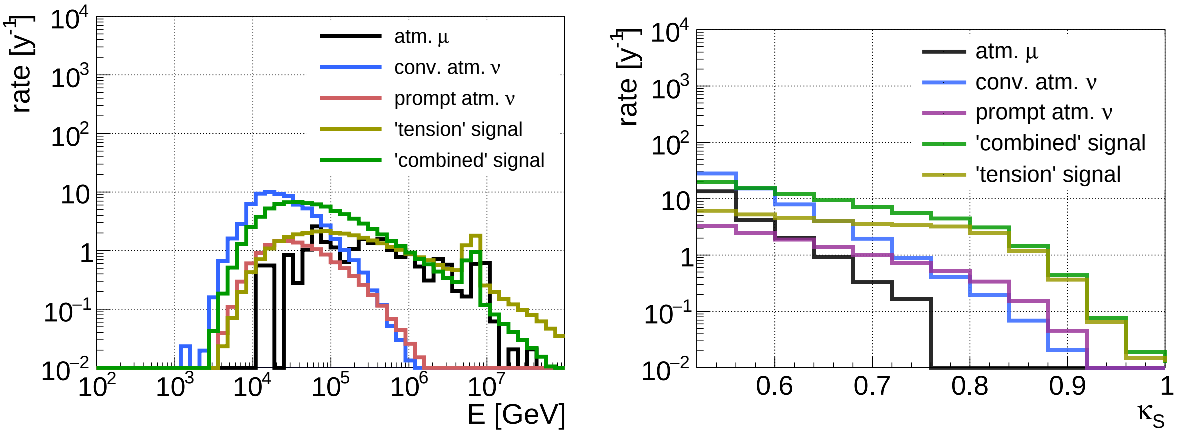

Figure 11.4: *Event rate distributions versus energy (left) and shower classifier response (right) after a cut of $\kappa_S > 0.52$ to reject muons with energies below 10 TeV.*

In the following, important uncertainties will be discussed and evaluated. The final results including uncertainties are summarised in Table 11.2 at the end of this section.

Important uncertainties

Considering the significance after one ARCA year (fitted a in Eq. (11.6)), the uncertainties resulting from the background fluxes amount to $^{+0.7\,\sigma}_{-0.6\,\sigma}$ for the 'combined' flux and $^{+0.33\,\sigma}_{-0.39\,\sigma}$ for the 'tension' flux. Only the dominating uncertainty is considered here which results from conventional atmospheric neutrinos for the 'combined' flux, and from prompt neutrinos for the 'tension' flux. In order to determine these uncertainties, pseudo experiments were generated where the normalisation of the background fluxes was changed by an amount given by the respective uncertainty (Table 11.1). The spectral fit was then performed in the same way as before, in particular the Gaussian-shaped penalty term of the likelihood (Eq. (11.4)) has been kept at the mean of unity.

However another important uncertainty has to be considered (the effect of which is not shown in Figure 11.3), namely atmospheric muons below 10 TeV which are not simulated. In order to be able to neglect such muons, a cut in the classifier response value must be performed that rejects most of these muons. The potential sensitivity loss due to these muons is estimated with a cut of $\kappa_S > 0.52$. The effect of the cut is shown in Figure 11.4. The left plot shows the event rate distributions versus energy after the cut. From this distribution the event rate of atmospheric muons below 10 TeV surviving the cut is estimated to be below 1/y and therefore negligible for the spectral fitting.

The resulting significance when constraining the spectral fitting to this parameter range (Figure 11.4 (right), bin size unchanged) is reduced by about 12% for the 'combined' flux from 10.5 σ to 9.2 σ after one ARCA year. For the 'tension' flux, the mean significance is reduced by about 7% from 5.79 σ to 5.37 σ.

Simulating the atmospheric muons below 10 TeV and thus knowing their classifier response values so that the strong cut can be released, might increase the sensitivity. For simplicity reasons, the reduced significance is therefore taken as the lower bound, and the initial significance as the upper bound for the respective uncertainty interval. In addition, the resulting uncertainty

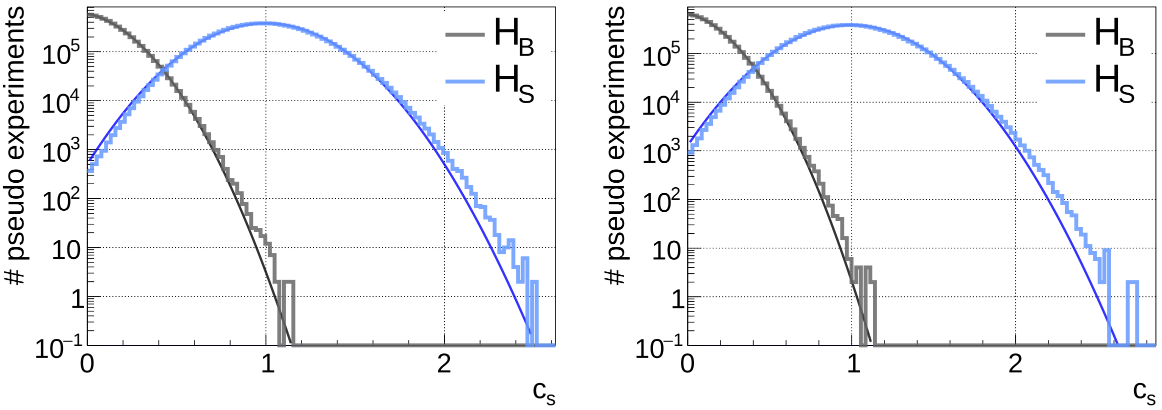

Figure 11.5: *The distribution of fitted c_s values after 10^7 pseudo experiments for the 'combined' (left) and the 'tension' signal flux (right). To both distributions a Gaussian is fitted (strong colours).*

interval is symmetrised so that the significance after one ARCA year (independent from the uncertainty in the atmospheric neutrinos) is then considered as $9.9\,\sigma \pm 0.6\,\sigma$ for the 'combined' flux and $5.58\,\sigma \pm 0.21\,\sigma$ for the 'tension' flux.

A further important uncertainty arises from the fits of the Gaussians that are used to determine the significance (see Eq. (11.5) and Figure 11.2). For the high significances achieved here, the tail of the c_s distribution for H_B is very important. A significance of $10\,\sigma$ corresponds to a p-value of about $8{\cdot}10^{-24}$ which means that on average 8 of 10^{24} pseudo experiments for H_B would result in a fitted signal normalisation greater than 1. Such a large number of pseudo experiments, which would be needed to rudimentarily confirm this result, is impossible to produce.

Therefore, only the observation times where a $5\,\sigma$ discovery is expected are checked, independently from the other uncertainties discussed above. Thus, the considered observation time is 0.25 ARCA years for the 'combined' signal flux hypothesis and 0.77 ARCA years for the 'tension' signal flux. A significance of $5\,\sigma$ corresponds to a p-value of $2.87 \cdot 10^{-7}$. Thus, roughly 3 out of 10^7 pseudo experiments would on average result in a fitted c_s value larger than $\mu_S \approx 1$ for H_S. Figure 11.5 shows the corresponding distributions for c_s for the 'combined' and 'tension' signal fluxes after 10^7 pseudo experiments. For better visibility of the tails, the y-axis is scaled logarithmically. It can clearly be seen that the tails are not very well represented by the fitted Gaussian.

In case of the 'combined' flux 25 experiments end up in a c_s value of greater than 1. This corresponds to a p-value of $2.5\cdot10^{-6}$ or a significance of $4.56\,\sigma$. For the 'tension' flux, 12 out of the 10^7 experiments have $c_s > 1$ corresponding to a significance of $4.72\,\sigma$. Thus, the significance reduces by about 9% for the 'combined' flux and 6% for the 'tension' flux. The reason for the larger effect in case of the 'combined' flux is assumed to be that the 'combined' flux produces a weaker signal after 0.25 years than the 'tension' flux after 0.77 years so that the "large-sample limit" and thus the assumption of a Gaussian distribution is more appropriate in the latter case. Thus in general, also the relative error of the significance is expected to get smaller over time as the sample size, i.e. the number of events contributing to the signal, increases. Again for simplicity reasons, the relative reduction is therefore taken as lower bound for this uncertainty, the unchanged significance as upper bound, and the interval is symmetrised. The significance after one year is then $10\,\sigma \pm 0.5\,\sigma$ for the 'combined' flux, and $5.63\,\sigma \pm 0.16\,\sigma$ for the 'tension' flux (independent from the other uncertainties).

		uncertainties [σ]		
signal flux	significance [σ]	atm. ν	atm. μ	method
Φ_E	5.82	-0.34 / $+0.38$	± 0.19	± 0.16
Φ_T	5.43	-0.33 / $+0.41$	± 0.20	± 0.15
Φ_C	9.4	-0.4 / $+0.7$	± 0.6	± 0.4

		uncertainties [σ]		
signal flux	time [y]	atm. ν	atm. μ	method
Φ_E	0.75	± 0.09	± 0.05	± 0.04
Φ_T	0.85	± 0.12	-0.06 / $+0.07$	-0.04 / $+0.05$
Φ_C	0.268	-0.028 / $+0.030$	-0.032 / $+0.039$	-0.022 / $+0.025$

Table 11.2: *Predicted significance after one ARCA year (top) and mean time needed for a 5σ discovery (50% observation probability; bottom) with the uncertainties following from the atmospheric background neutrinos (atm. ν), from the non-simulated low-energy atmospheric muons (atm. μ) and from the utilised method. The numbers are determined from the respective fits of the function given by Eq. (11.6).*

The expected significance after one ARCA year resulting from the combination of the discussed uncertainties is summarised in Table 11.2 together with the respective time needed for a 5σ discovery (50% observation probability) and corresponding uncertainties for the considered signal fluxes. For reference, also the results for the 'evidence' flux are given, which are similar to that of the 'tension' flux as expected from the results of the previous chapter.

Thus, after one ARCA year, a mean significance of more than 9σ is expected for the 'combined' flux, and more than 5σ for the 'tension' flux. Compared to the cut-and-count method developed in the previous chapter (considering the shower search), an increase of about 34% ('combined' flux) or 29% ('tension' flux) is achieved. The time needed for a 5σ discovery is in comparison reduced by about 48%, from 0.52 to about 0.27 years, for the 'combined' flux, and by 38% for the 'tension' flux from 1.36 to 0.85 years.

Besides the discovery of the cosmic neutrino flux, it is also important to determine its parameters. This is possible with a slight extension of the spectral fitting method as shown in the next section.

11.3 Sensitivity to signal flux parameters

Besides a (re)discovery of the cosmic neutrinos detected by the IceCube collaboration, a further goal of ARCA is to study the corresponding flux and to determine its spectral properties. This section investigates the capabilities of ARCA to determine these properties. For this purpose, three different signal flux models regarding the energy dependence are analysed: a simple power law (Section 11.3.2), a simple power law with a high-energy cut-off (Section 11.3.3), and a broken power law according to the two published IceCube fluxes which are in tension with each other

(Section 11.3.4). Section 11.3.1 gives a description of the measures used to quantify the sensitivity to the spectral parameters. Table 11.3 at the end of this section gives a summary of the results.

11.3.1 Sensitivity measures

The method used to investigate the sensitivity of ARCA to signal flux parameters is an extension of the likelihood method presented in Section 11.2. Given a signal flux depending on spectral parameters $\boldsymbol{\beta}$ (a set of one or more parameters, e.g. the spectral index and the flux normalisation), the signal mean $\mu_{i,\mathrm{s}} = \mu_{i,\mathrm{s}}(\boldsymbol{\beta})$ in bin i (Eq. (11.3)) is now a function of these parameters. Considering the flux normalisation as one of those parameters, and omitting the dependence on the background flux normalisations, the log-likelihood is then written as:

$$\ln L(\boldsymbol{\beta}) = \sum_{i=1}^{N_{\mathrm{bin}}} \left[n_i \ln \left(\mu_{i,\mathrm{s}}(\boldsymbol{\beta}) + \sum_{\alpha \neq \mathrm{s}} \mu_{i,\alpha} \right) - \mu_{i,\mathrm{s}}(\boldsymbol{\beta}) - \sum_{\alpha \neq \mathrm{s}} \mu_{i,\alpha} \right], \tag{11.7}$$

where the term $\ln n_i!$ irrelevant for the maximisation has also been omitted.

In order to determine the sensitivity to a given set of parameters $\boldsymbol{\beta}$, 2000 pseudo experiments for fixed values of the parameters are generated. The mean log-likelihood of all pseudo experiments is then calculated in the vicinity of these parameter values and a scan of the log-likelihood is performed (see e.g. [95] for a general description of this technique).

An example of such a likelihood scan is shown in Figure 11.6 where the 'combined' flux is assumed and the likelihood is scanned with respect to the spectral index and flux normalisation. The parameter values where the log-likelihood differs from the maximum by an amount of 1.15, 3.09 and 5.92 give the two-dimensional confidence contours containing the maximum likelihood in about 68%, 95% and 99% of all pseudo experiments[58], respectively. These intervals are also referred to as the two-dimensional $1\,\sigma$, $2\,\sigma$ and $3\,\sigma$ intervals as these correspond to the respective Gaussian confidence intervals. These contours are shown in white in the figure.

The conditional, one-dimensional log-likelihood scans of this example are shown in Figure 11.7. These give the maximum log-likelihood along a single parameter, i.e. for each value of that parameter the maximum likelihood as a function of the other parameter is computed. The corresponding curves in the two-dimensional plane are shown in light blue in Figure 11.6. In other words these curves give the conditional best-fit values for one parameter when the other parameter would be kept fix at a given value. They are helpful in visualising correlations between the parameters.

The parameter values where the conditional, one-dimensional log-likelihood differs from the maximum by an amount of 0.5, 2.0 and 4.5 give the one-dimensional confidence intervals containing the maximum likelihood in 68%, 95% and 99% of all pseudo experiments, respectively. Analogously to above, these intervals are also referred to as one-dimensional $1\,\sigma$, $2\,\sigma$, and $3\,\sigma$ intervals. These one-dimensional intervals are used in the following sections to quantify the sensitivity to the spectral parameters of a given signal flux.

In order to speed up the computation, the background normalisations are kept fixed. Checks have shown that fitting these parameters would increase the resulting uncertainties by roughly 10%.

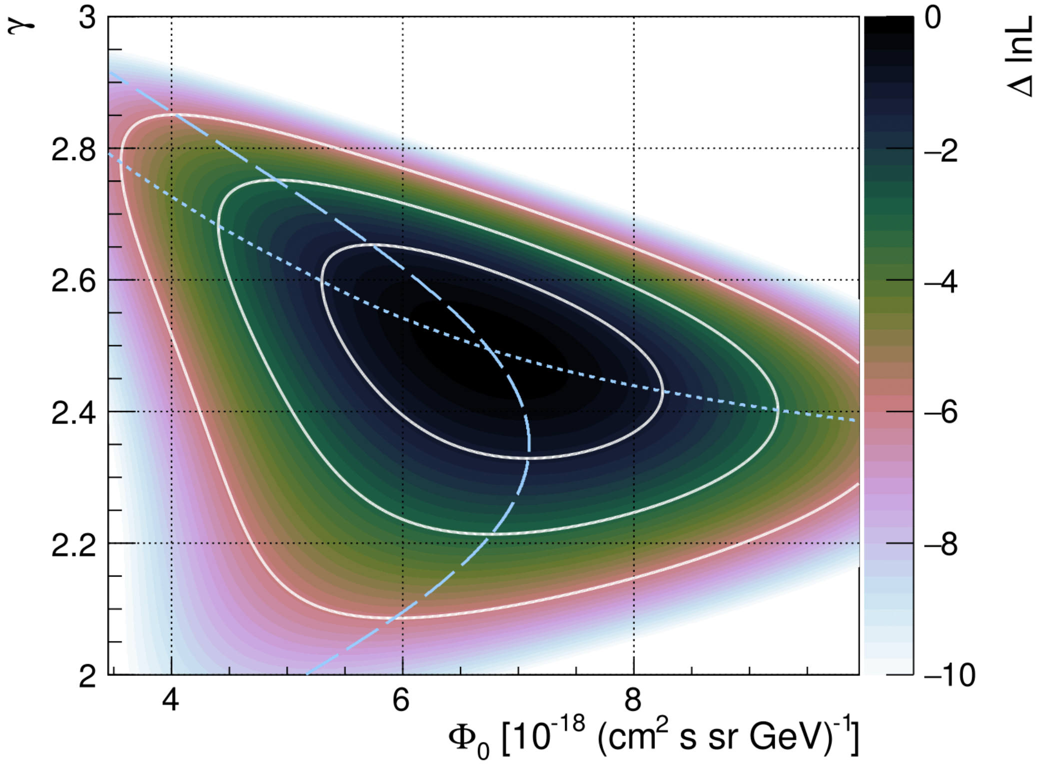

Figure 11.6: *Log-likelihood as a function of the flux normalisation Φ_0 and the spectral index γ after one ARCA year assuming the 'combined' signal flux. The colors correspond to the difference of the log-likelihood to the maximum log-likelihood $\Delta \ln L = \ln L - \ln L_{max}$. The white contours give the two-dimensional $1\,\sigma$, $2\,\sigma$ and $3\,\sigma$ intervals and the light blue curves give the conditional best-fit value for the spectral index (short dashed) and normalisation (long dashed) as a function of the respectively other parameter.*

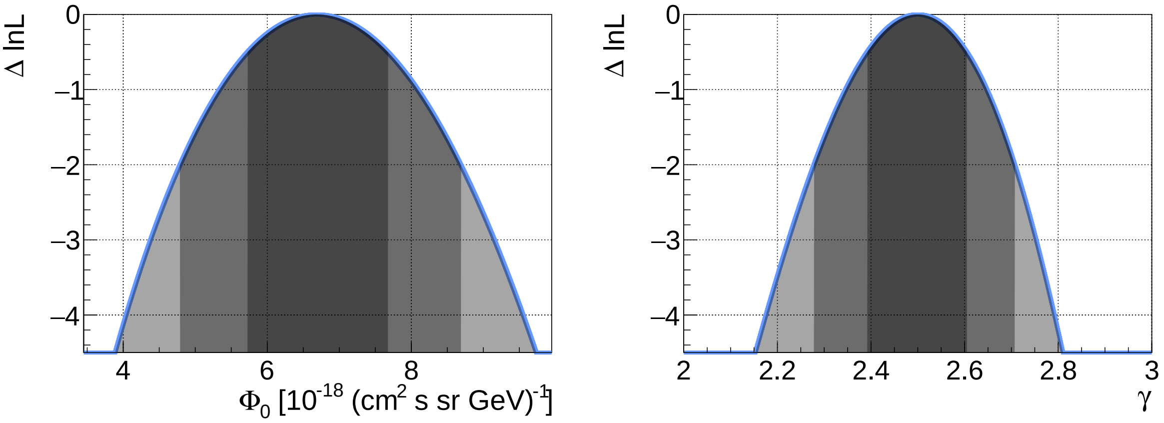

Figure 11.7: *Profile log-likelihood as a function of the flux normalisation Φ_0 (left) and the spectral index γ (right) after one ARCA year assuming the 'combined' signal flux. The y-axis shows the difference of the log-likelihood to the maximum log-likelihood $\Delta \ln L = \ln L - \ln L_{max}$. The shaded areas represent the one-dimensional $1\,\sigma$, $2\,\sigma$, and $3\,\sigma$ intervals.*

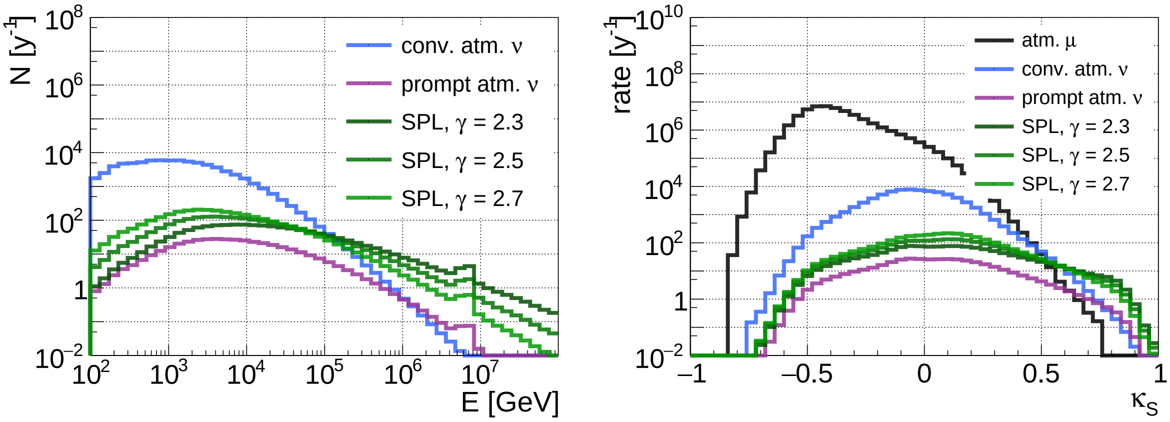

Figure 11.8: *Event rate distributions versus energy (left) and shower classifier response (right) for different spectral indices γ of the single-power-law (SPL) flux together with background distributions. The signal hypotheses are renormalised to produce the same 'signal strength' as the 'combined' flux.*

11.3.2 Single power law

The "single power law" model is described via:

$$\Phi(E) = \Phi_0 \cdot \left(\frac{E}{100\,\mathrm{TeV}}\right)^{-\gamma} \tag{11.8}$$

with energy E; the normalisation Φ_0 and spectral index γ are the spectral parameters to be analysed. Figure 11.8 shows examples for the resulting event rate distributions versus energy and classifier response for different values of the spectral index ($\gamma \in \{2.3, 2.5, 2.7\}$) and assuming for each case the same 'signal strength' (defined in Section 11.1) as the 'combined' flux (i.e. the normalisation Φ_0 is not fixed).

Pseudo experiments are generated according to the 'combined' flux, i.e. with $\Phi_0 = 6.7\,\mathrm{u}_\Phi$ and $\gamma = 2.5$, with flux unit $\mathrm{u}_\Phi := 10^{-18}\,(\mathrm{cm}^2\,\mathrm{s}\,\mathrm{sr}\,\mathrm{GeV})^{-1}$ that will also be used in the following sections. The resulting likelihood map around these parameter values for one ARCA year is shown in Figure 11.6, the corresponding one-dimensional profile likelihoods in Figure 11.7. From the likelihood map, it can be seen that the best-fit values are very close to those assumed as the signal hypothesis.

Furthermore, the correlation between both parameters can be investigated: the best-fit normalisation as a function of spectral index has a maximum of about $7\,\mathrm{u}_\Phi$ near $\gamma = 2.35$ and decreases for smaller and higher spectral indices. This means a higher (smaller) spectral index than 2.35, leading to a softer (harder) energy spectrum, increases the event rate at energies below (above) 100 TeV (recall Figure 11.8) in a way so that the best-fit normalisation gets smaller (in both cases). In other words, given $\Phi_0 = 7\,\mathrm{u}_\Phi$, events below 100 TeV dominate the spectrum if $\gamma > 2.35$, and events above 100 TeV dominate the spectrum if $\gamma < 2.35$. The corresponding profile likelihood (Figure 11.7 (right)) decreases as a consequence of the mismatch in the spectral shape.

The best-fit spectral index as a function of normalisation decreases monotonically and the corresponding profile likelihood decreases as the flux gets weaker (small normalisation) or stronger (large normalisation) than the best-fit flux.

---

[58] These numbers hold in the large sample limit, i.e. when the signal flux produces event rates large enough. This is here approximately true. A corresponding check has been performed.

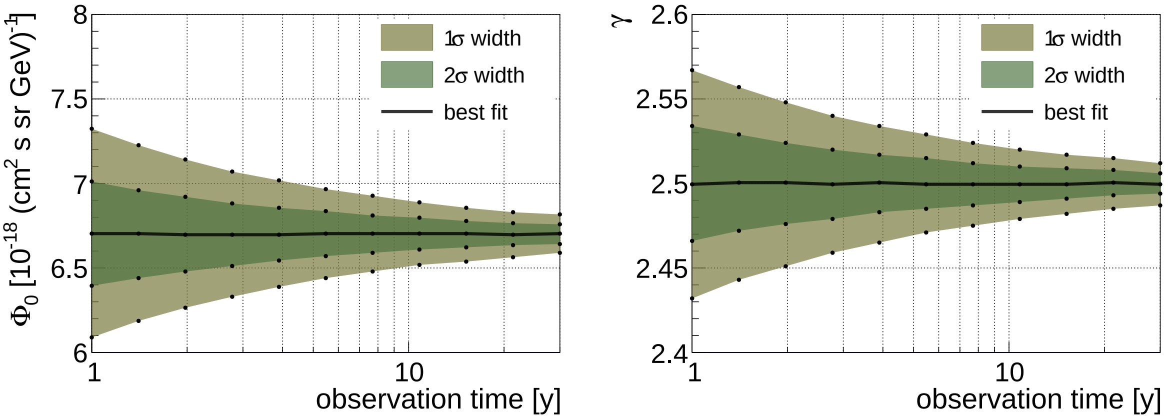

Figure 11.9: *Sensitivity to the flux normalisation (left) and spectral index (right) over time for the 'combined' flux Φ_C.*

The best-fit values of normalisation and spectral index and their respective uncertainty intervals are shown in Figure 11.9 as a function of ARCA observation time. The uncertainty intervals are close to symmetric around the best-fit values which can also be seen from the almost parabolic form of the one-dimensional likelihoods (Figure 11.7). The 1 σ-uncertainty in the normalisation reduces from ±1.0 u_Φ after one ARCA year to about ±0.30 u_Φ after ten ARCA years while the respective uncertainty for the spectral index reduces from ±0.10 to about ±0.03 in the same time period. The relative uncertainties after one ARCA year are therefore around 15% for the normalisation and 4% for the spectral index.

Assuming the 'tension' flux as signal flux with $\Phi_0 = 2.7\,\mathrm{u}_\Phi$ and $\gamma = 2.13$, producing a much weaker signal, the relative uncertainties are larger and not symmetric any more. The relative normalisation uncertainty after one ARCA year amounts to $^{+33\%}_{-48\%}$, the spectral index uncertainty to $^{+11\%}_{-16\%}$.

11.3.3 High-energy cut-off

In order to investigate the sensitivity to a potential cut-off in the signal spectrum, the following flux template is assumed:

$$\Phi(E) = \Phi_0 \cdot \left(\frac{E}{100\,\mathrm{TeV}}\right)^{-\gamma} \cdot \exp\left(-\frac{E}{E_C}\right). \tag{11.9}$$

The spectral parameters to be analysed are the flux normalisation Φ_0, spectral index γ and cut-off energy E_C. A modified 'tension' flux is introduced according to the 'tension' flux with $\Phi_0 = 2.7\,\mathrm{u}_\Phi$, $\gamma = 2.13$ and a cut-off added at $E_C = 3$ PeV. Figure 11.10 shows examples for the resulting event rate distributions versus energy and classifier response for $\gamma = 2.13$ and $E_C \in \{1\,\mathrm{PeV}, 3\,\mathrm{PeV}, 10\,\mathrm{PeV}\}$ with normalisation so as to produce the same 'signal strength' as the 'modified tension' flux. The different cut-off energies lead to only small changes in the distributions with respect to the classifier response. The sensitivity to the cut-off energy is therefore expected to be relatively small.

Considering as signal hypothesis the 'modified tension' flux, the generated two-dimensional likelihood scans for 10 ARCA years are shown in Figure 11.11. The left column shows the case when all three considered parameters are unconstrained so that for each point in the likelihood maps the maximum along the third parameter is given. In the right column, the respective third

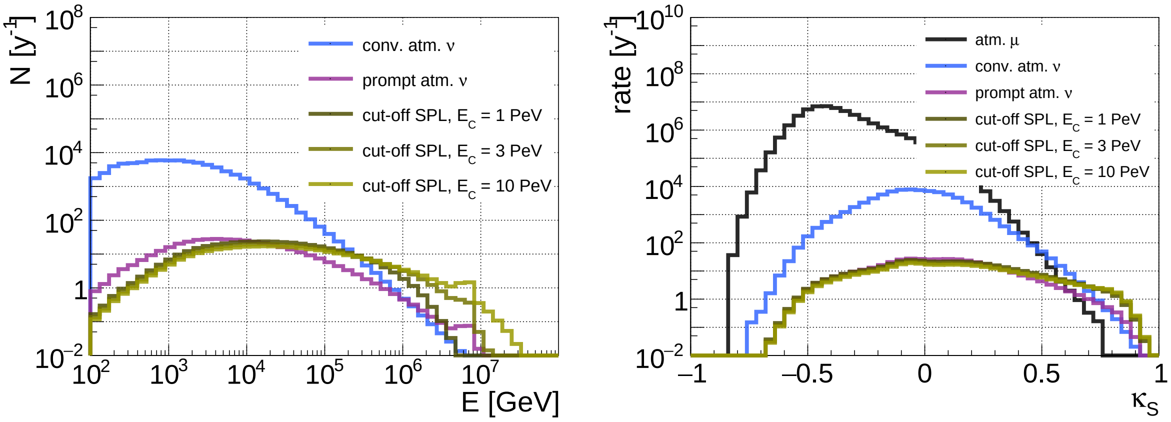

Figure 11.10: *Event rate distributions versus energy (left) and shower classifier response (right) for the single-power-law (SPL) model of the 'tension' flux with cut-offs added at different energies E_C together with background distributions. The signal hypotheses are renormalised to produce the same 'signal strength' as the 'tension' flux.*

parameter is fixed to its signal hypothesis value: $\Phi_0 = 2.7\,\mathrm{u}_\Phi$ (top), $\gamma = 2.13$ (middle), $E_C = 3\,\mathrm{PeV}$ (bottom).

It can be seen (top and middle row) that both a large spectral index (soft spectrum) and a small normalisation lead to the fitted cut-off energy tending to infinity, i.e. outside the sensitive energy range for ARCA for the considered signal strengths. Thus, in both cases the event rate at high energies reduces to an amount so that the sensitivity to a potential cut-off vanishes. However, for small spectral indices and large normalisations, the cut-off energy can be well constrained.

Looking also at the correlation between normalisation and spectral index (bottom row), it can be seen that there is hardly any distinction between a soft flux with small normalisation and a hard flux with large normalisation as long as there is the possibility of an (unconstrained) cut-off (bottom left). The classifier response can therefore not distinguish well between these different energy spectra.

Keeping all parameters unconstrained, the 1 σ contours reach in all cases outside of the considered range (recall that these maps are for 10 ARCA years) which shows that the sensitivity to the single parameters is small when all parameters are unconstrained. Figure 11.12 compares the sensitivity to the cut-off energy when all parameters are unconstrained to the case when the spectral index is fixed at $\gamma = 2.13$. In the latter case, the respective uncertainty for one ARCA year is $^{+0.76}_{-0.41}$ in the logarithm of the cut-off energy and reduces to $^{+0.17}_{-0.16}$ for 10 ARCA years. In the case of unconstrained parameters, the uncertainty is for most times greater than the considered cut-off energy range. After 30 ARCA years[59] the respective uncertainty amounts to $^{+0.49}_{-0.29}$ in the logarithm of the energy.

Fixing the spectral index at the generic value of 2.0, the best-fit cut-off energy changes from 3.0 PeV to 1.0 PeV and the respective logarithmic uncertainty reduces to $^{+0.35}_{-0.28}$. The best-fit cut-off energy gets smaller because of the harder spectrum, and the uncertainty reduces because of the best-fit cut-off energy being at smaller energies.

Uncertainties of the other considered parameters are summarised in Table 11.3.

---

[59] It should be kept in mind that 30 years of ARCA correspond to 10 years of the full, planned KM3NeT detector.

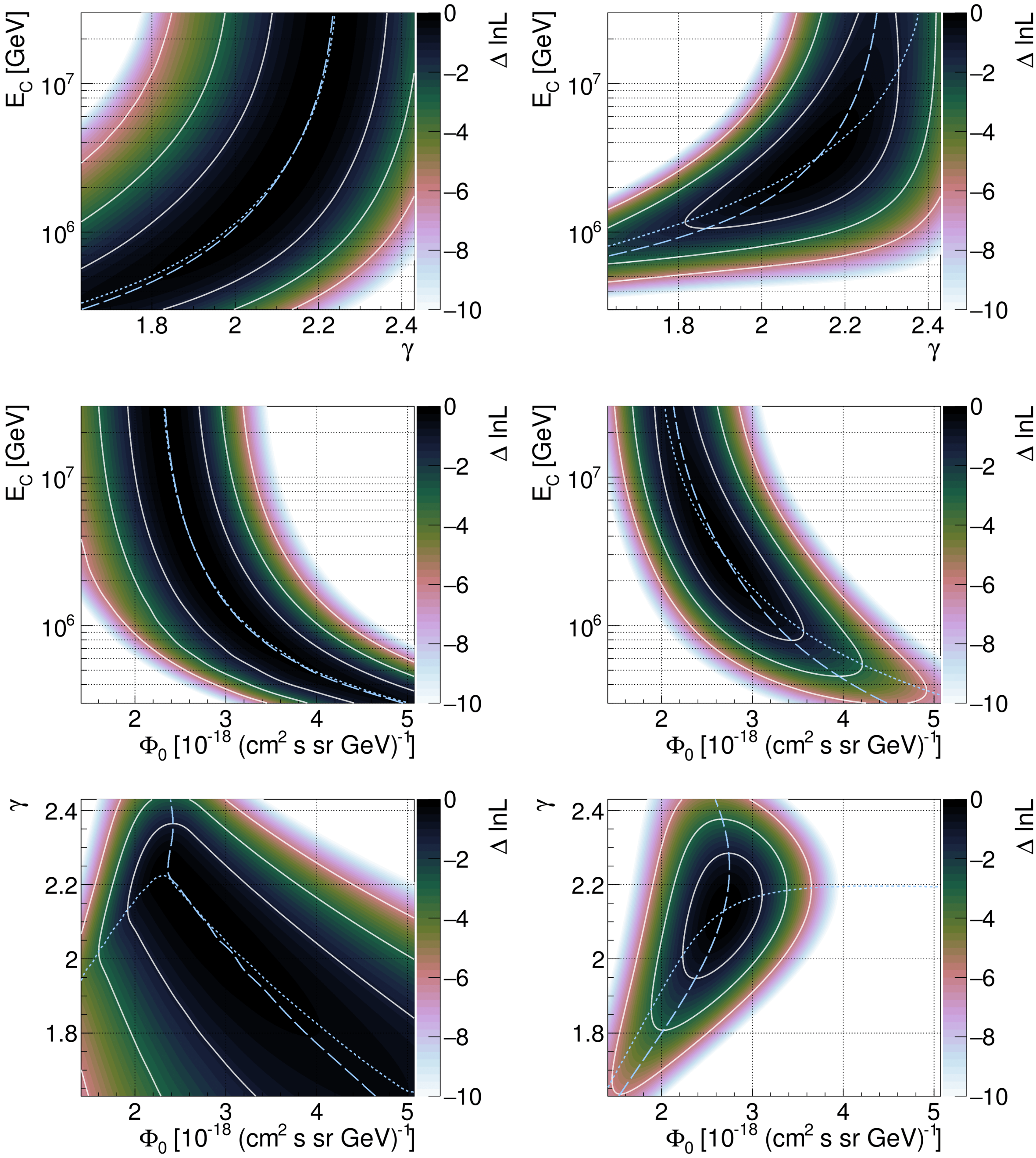

Figure 11.11: *Two-dimensional profile log-likelihood maps after 10 ARCA years assuming the 'combined' signal flux as a function of the three considered parameters: flux normalisation Φ_0, spectral index γ and cut-off energy E_C. Left: all parameters unconstrained. Right: the respective third parameter is fixed.*

11.3.4 Broken power law

In order to investigate the sensitivity to a possible break in a power-law flux, the following flux template is assumed:

$$\Phi(E) = \Phi_0 \cdot \begin{cases} \left(\frac{E}{100\,\text{TeV}}\right)^{-\gamma_1}, & \text{for } E < E_B \\ \left(\frac{E_B}{100\,\text{TeV}}\right)^{-\gamma_1+\gamma_2} \left(\frac{E}{100\,\text{TeV}}\right)^{-\gamma_2}, & \text{for } E \geq E_B \end{cases} \tag{11.10}$$

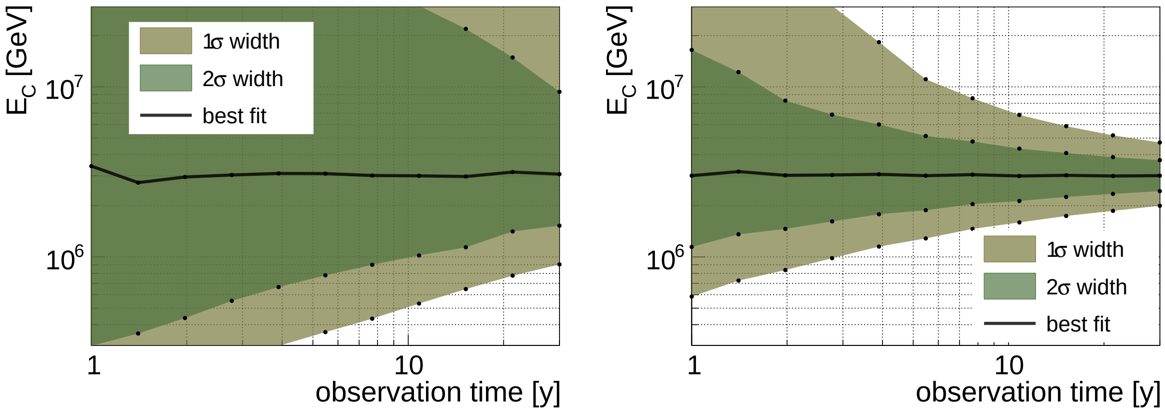

Figure 11.12: *Sensitivity to the cut-off energy over time with spectral index free (left) and fixed at 2.13 (right) during the fit under the 'tension' flux signal hypothesis with a cut-off added at 3 PeV.*

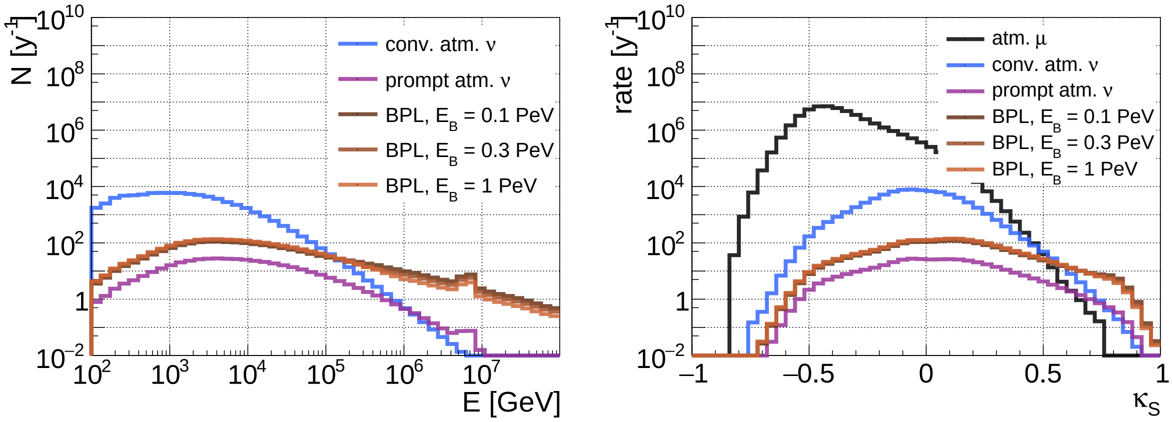

Figure 11.13: *Event rate distributions versus energy (left) and shower classifier response (right) for the broken-power-law (BPL) flux as described in the text with different break energies E_B together with background distributions. The signal hypotheses are renormalised to produce the same 'signal strength' as the 'combined' flux.*

with the flux normalisation Φ_0 as in the previous sections, spectral index γ_1 before the break, break energy E_B and spectral index γ_2 after the break. The former three parameters were investigated while the spectral index after the break has been kept constant during the likelihood investigation[60].

Two different signal hypothesis are assumed according to the published IceCube fluxes (recall Figure 2.1, p. 20). The first one is a combination of the 'combined' and 'evidence' flux and has therefore $\gamma_1 = 2.5$, $\gamma_2 = 2.0$ and $E_B = 300\,\text{TeV}$ which is the energy where both fluxes meet. The second signal hypothesis combines the 'tension' with the 'combined' flux with $\gamma_1 = 2.5$, $\gamma_2 = 2.13$ and $E_B = 1\,\text{PeV}$, which is again the energy where the corresponding fluxes meet. In both cases $\Phi_0 = 6.7\,\text{u}_\Phi$.

Examples of event rate distributions with $\gamma_1 = 2.5$, $\gamma_2 = 2.13$ and breaks at three different energies are shown in Figure 11.13. The different break energies, changed by half an order of magni-

---

[60] Tests have shown that varying the spectral index after the break enlarges the parameter space to an order of magnitude the investigation of which is out of the scope of this thesis.

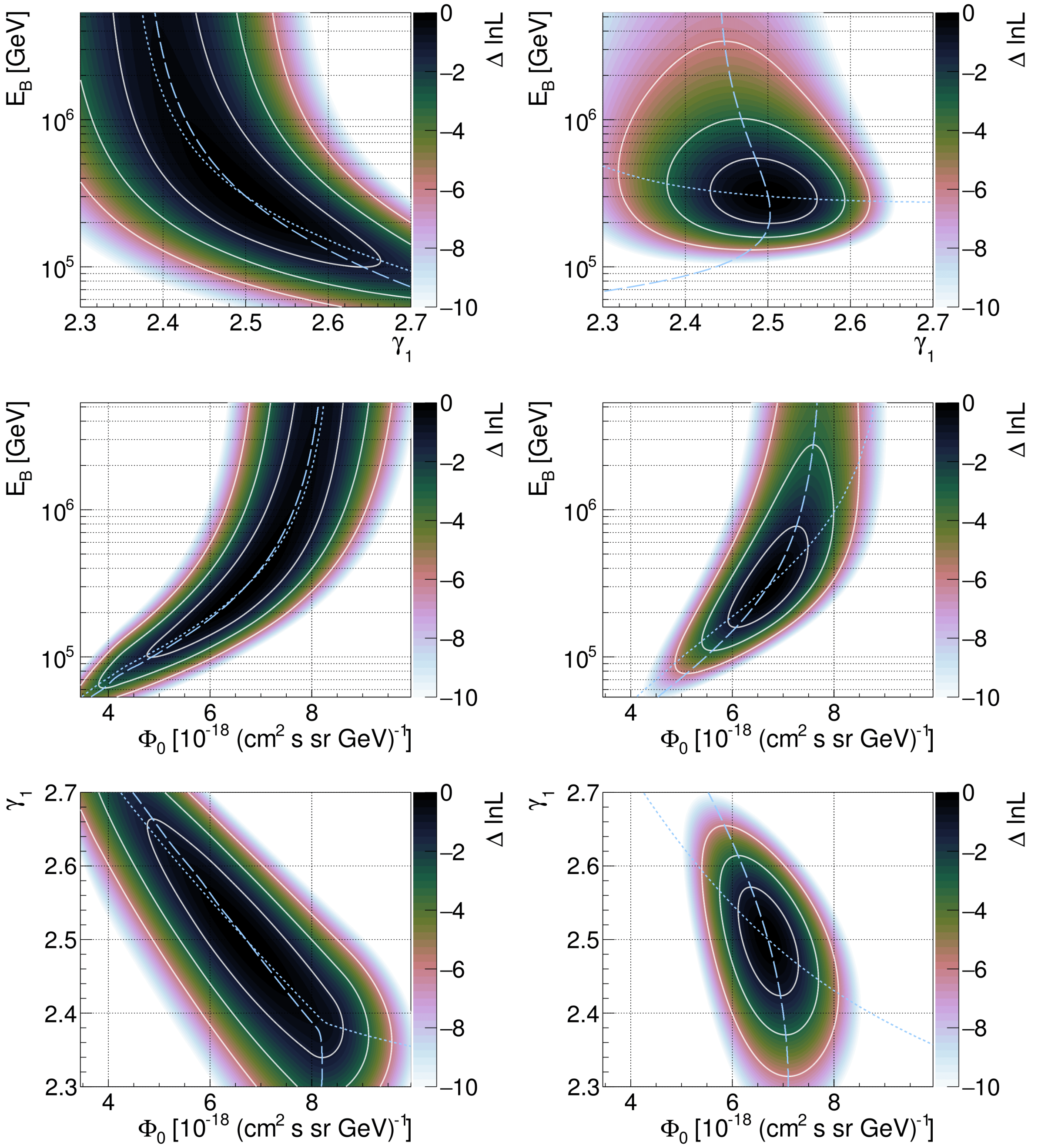

Figure 11.14: *Two-dimensional profile log-likelihood maps after 5 ARCA years assuming the 'combined' signal flux as a function of the three considered parameters: flux normalisation* Φ_0*, spectral index before the break* γ_1 *and break energy* E_B*. Left: all parameters unconstrained. Right: the respective third parameter is fixed.*

tude, lead to small changes in the distributions with respect to the classifier response. The respective sensitivity is therefore expected to be relatively small.

Considering the first signal hypothesis ($E_B = 300$ TeV), the corresponding likelihood scans for 5 ARCA years observation time are shown in Figure 11.14. The left column shows the case when all three considered parameters are unconstrained (as in Figure 11.11) where again for each point in the likelihood maps the maximum along the third parameter is given. In the right column, the respective third parameter is fixed to its signal hypothesis value: $\Phi_0 = 6.7\,\mathrm{u}$ (top), $\gamma_1 = 2.5$ (middle), $E_B = 300\,\mathrm{TeV}$ (bottom).

Looking at the correlations in the unconstrained case, it can be seen that for large fitted spectral indices (before the break) the break energy goes to smaller energies and is rather well constrained as opposed to small spectral indices. As the value of the first spectral index approaches that of the second one, the break energy tends to infinity – for $\gamma_1 = 2.13 = \gamma_2$ the break has no purpose any more. The best-fit normalisation changes with the other parameters in a way so that the event rates from energies before and after the break balance out.

If the normalisation is fixed, the best-fit spectral index as a function of break energy shows an interesting, totally different behaviour for $E_B \lesssim 300\,\mathrm{TeV}$ (top right figure). This is due to the fact, that the normalisation is fixed at 100 TeV (and not at smaller energies). As the break energy reaches this value, the flux at higher energies increases – at $E_B = 100\,\mathrm{TeV}$, the flux for $E > 100\,\mathrm{TeV}$ is completely independent of γ_1 (Eq. (11.10)). The increase of the flux at higher energies is compensated for via a reduction of the flux at lower energies which is achieved by a reduction of γ_1. For values of $\gamma_1 < 2.0 = \gamma_2$ (not considered here) and $E_B < 100\,\mathrm{TeV}$, the flux at energies above 100 TeV would reduce again. It can therefore be concluded that as long as $\gamma_1 > 2.0$ (as a function of E_B), a relevant part of the flux is below E_B. Furthermore, above $E_B \gtrsim 300\,\mathrm{TeV}$, γ_1 and E_B show no large correlation, i.e. the conditional best-fit cut-off energy is almost independent of γ_1. This also indicates that the flux above 300 TeV is of less relevance to the detected signal event rate than the flux below 300 TeV under the given hypothesis.

Keeping γ_1 fixed (middle right), it can be seen that there is a strong correlation between break energy and best-fit normalisation at low break energies which reduces at high energies where the break becomes more and more irrelevant. From the large tail of the log-likelihood at $E_B > 1\,\mathrm{PeV}$, it follows that the determination of the break energy would not be an easy task (i.e. even if both the spectral index before and after the break are fixed during the fit).

Figure 11.15 shows the sensitivity to the break energy over ARCA observation time comparing the cases of free and constrained γ_1 for both considered signal hypothesis. As expected from the likelihood maps, in the case where the break is at smaller energies, the uncertainties are much smaller. Even for unconstrained γ_1 the uncertainty after 10 ARCA years is smaller than 0.3 in the logarithm of the break energy for the considered signal hypothesis with $E_B = 300\,\mathrm{TeV}$. The uncertainties are reduced when γ_1 is fixed. They are summarised in Table 11.3.

11.3.5 Summary

The sensitivity to different spectral parameters for different signal flux models and signal hypothesis is summarised in Table 11.3 in terms of the relative $1\,\sigma$ uncertainty as given by the central 68% intervals. For the flux normalisation and spectral index this is the respective absolute deviation divided by the fitted mean, for the sensitivity to the cut-off and break energy it is the deviation in units of the decadic logarithm.

It becomes clear that in general, when the hypothetical signal flux is chosen according to the ‘combined’ flux the uncertainties are much smaller as compared to the ‘tension’ flux. The same is true for fitting two parameters versus fitting three parameters. For example, the smallest uncertainty to the flux normalisation is given for the single-power-law fit to the ‘combined’ flux (roughly ±5% after one ARCA year) while the largest one occurs for the fit of the “single-power-law with cut-

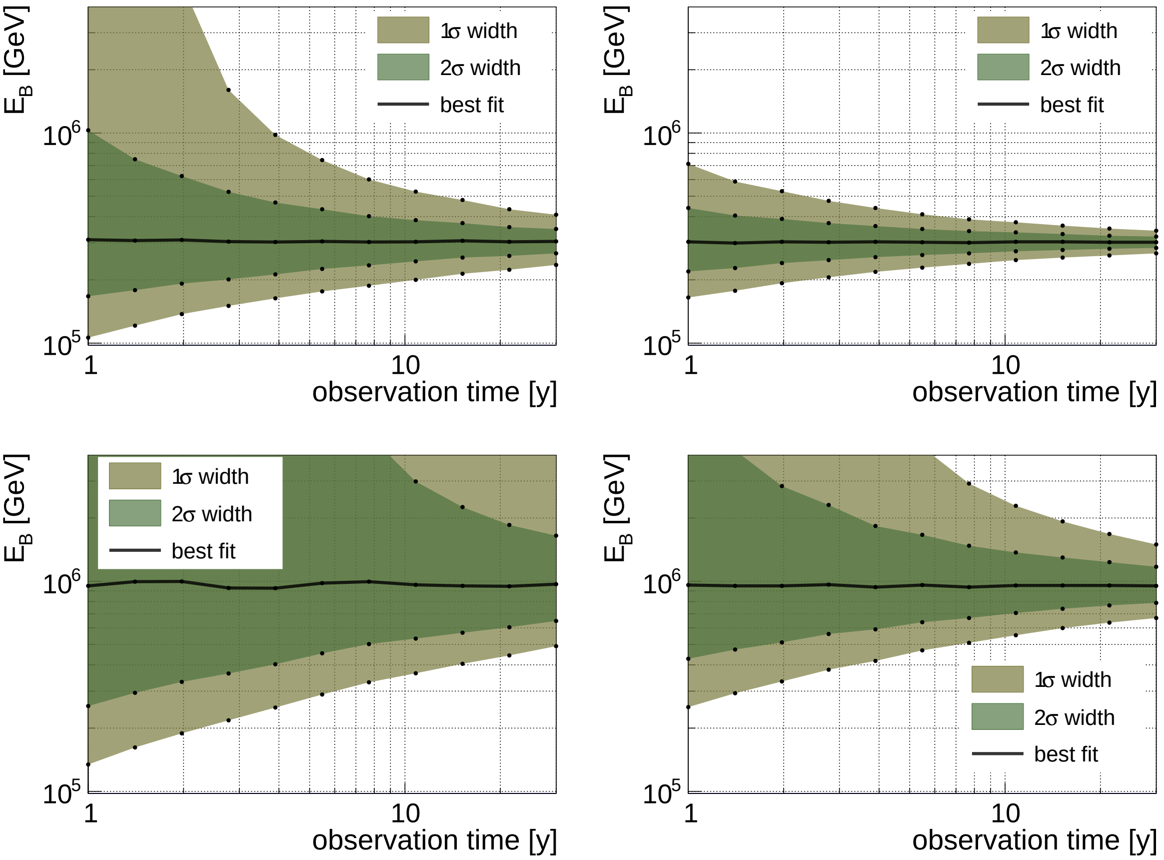

Figure 11.15: *Sensitivity to the break energy over time for free (left) and constrained γ_1 (right) for the signal hypothesis with $E_B = 300$ TeV and $\gamma_2 = 2.0$ (top) and $E_B = 1$ PeV and $\gamma_2 = 2.13$ (bottom).*

off" to the 'tension' flux ($^{+90\%}_{-22\%}$ after one ARCA year). When only two parameters are fitted, the normalisation uncertainties are around ±20% at most. The relative uncertainties to the spectral index for the single-power-law fit deviate by a factor of ten when the 'evidence' and 'tension' signal flux hypothesis are compared. For one ARCA year, they amount to roughly 1.4% in the former case and up to 16% in the latter case.

For the considered signal strengths and with the methods employed here, ARCA will only be sensitive to a high-energy cut-off around 3 PeV if the spectral index is rather hard with values around 2.0-2.1. For a softer spectrum the cut-off becomes undetectable. When the cut-off energy is fitted together with the spectral index and flux normalisation, it can only be limited towards lower energies. Fixing the spectral index leads to uncertainties of around half an order of magnitude after one ARCA year, which decrease to 10-16% in the logarithm of the energy after 11 ARCA years.

Considering a potential break in the spectrum of a cosmic diffuse neutrino flux, two hypotheses have been investigated according to combinations of the 'combined' flux with the 'evidence' and 'tension' flux. As a result, a spectral break at lower energies (here 300 TeV) would be much easier to identify than a break at higher energies (here 1 PeV). In the former case, the uncertainty to the break energy is around ±10% in the logarithm of the energy after 11 ARCA years reducing to ±5% when the spectral indices are kept fix during the fit. For the break at 1 PeV, the uncertainty increases to $^{+49\%}_{-26\%}$, or $^{+16\%}_{-13\%}$ when the spectral indices are kept fix.

flux model	hypothesis	varied parameters	relative 1 σ uncertainty [%] after					
			1 y		10.8 y		30 y	
single power-law (Eq. (11.8))	$\Phi_0 = 6.7\,\mathrm{u}_\Phi$	Φ_0	-4.6	+4.6	-1.4	+1.4	-0.92	+0.82
	$\gamma = 2.5$	γ	-1.3	+1.4	-0.42	+0.42	-0.22	+0.26
	$\Phi_0 = 2.7\,\mathrm{u}_\Phi$	Φ_0	-49	+34	-12	+11	-7.2	+6.6
	$\gamma = 2.13$	γ	-16	+11	-3.8	+3.4	-2.3	+2.0
single power-law with cut-off at $E_C = 3$ PeV, $\Phi_0 = 2.7\,\mathrm{u}_\Phi$ (Eq. (11.9))	$\gamma = 2.13$	Φ_0	-22	+90	-14	+20	-8.7	+11
		γ	n.a.	+8.3	-6.8	+5.4	-3.9	+3.3
		E_C	-110	n.a.	-47	n.a.	-30	+48
	$\gamma = 2.13$	Φ_0	-20	+21	-6.0	+6.3	-3.5	+3.7
		E_C	-42	+74	-15	+16	-9.1	+9.1
	$\gamma = 2.0$	Φ_0	-21	+22	-6.9	+6.6	-4.3	+3.9
		E_C	-30	+43	-9.9	+13	-6.1	+7.3
broken power-law with $\Phi_0 = 6.7\,\mathrm{u}_\Phi$, $\gamma_1 = 2.5$, γ_2 fixed (Eq. (11.10))	$\gamma_2 = 2.0$ $E_B = 300$ TeV	Φ_0	-14	+14	-4.3	+3.9	-2.5	+2.3
		γ_1	-3.1	+3.1	-0.87	+0.94	-0.52	+0.54
		E_B	-27	+52	-9.3	+10	-5.7	+5.9
	$\gamma_2 = 2.13$ $E_B = 1$ PeV	Φ_0	-13	+9.5	-4.1	+4.4	-2.6	+2.5
		γ_1	-2.4	+2.9	-0.99	+0.91	-0.55	+0.56
		E_B	-57	n.a.	-26	+49	-18	+23
	$\gamma_2 = 2.0$	Φ_0	-5.5	+5.4	-1.7	+1.6	-0.92	+1.0
	$E_B = 300$ TeV	E_B	-14	+16	-4.5	+4.5	-2.7	+2.7
	$\gamma_2 = 2.13$	Φ_0	-5.4	+5.3	-1.7	+1.6	-1.0	+0.92
	$E_B = 1$ PeV	E_B	-35	n.a.	-13	+16	-8.1	+9.1

Table 11.3: *Relative 1 σ uncertainties to the parameters of the different flux models under the given hypotheses after 1, 10.8 and 30 ARCA years. In some cases the uncertainty is larger than the considered parameter range (n.a.). The relative statistical error on the given values following from the maximum likelihood method is below 5%.*

In general the uncertainty intervals, mostly asymmetric for one ARCA year, are getting more and more symmetric with increasing ARCA time. The uncertainties after 30 ARCA years are valid for the full KM3NeT detector which is planned to be three times the size of ARCA and to be operated at least for 10 years. The uncertainties are still relatively large at that time in the case of the ‘tension’ flux hypothesis and when more than two parameters are fitted. Thus it should be envisaged to develop more sophisticated methods to increase the respective sensitivity. A starting point could be

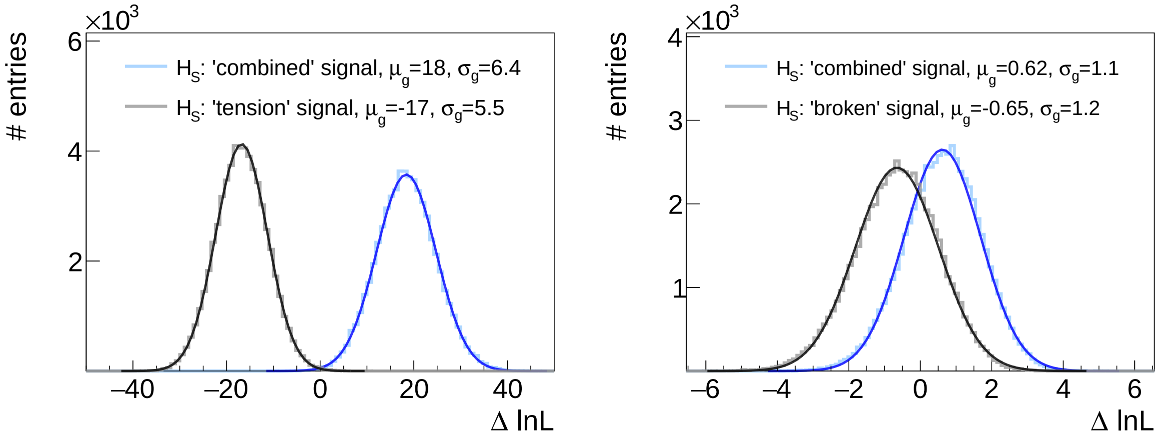

Figure 11.16: *Distribution of the log-likelihood-ratio when the 'combined' and 'tension' flux (left), and the 'combined' and 'broken' flux (right) are assumed as signal hypotheses. Gaussians are fitted to the distributions, their means μ_g and variances σ_g are given in the legend.*

to include the reconstructed energy in the likelihood fitting (i.e. not only the classifier response).

Besides determining the parameters of the cosmic flux, another important problem is the question which of the considered model fits best to measured data and how the different models can be discriminated. This will be the topic of the next section.

11.4 Discrimination of different fluxes

In this section, the potential of ARCA to discriminate different flux models is investigated. For this purpose, the log-likelihood ratio is considered as test statistics based on the log-likelihood $\ln L_S$ given in Eq. (11.4) where now the index denotes a certain signal hypothesis. The log-likelihood-ratio $\ln LR$ for two different hypotheses S_1 and S_2 is then defined as:

$$\ln LR := \ln(L_1/L_2) = \ln L_1 - \ln L_2 \tag{11.11}$$

If S_1 is the true hypothesis, L_1 will tend to have a larger value than L_2, i.e. the event rate distributions under S_1 tend to be more in agreement with the generated data than the distributions under S_2. Thus, the log-likelihood-ratio will in general be larger than zero. If S_2 is the true hypothesis it is vice versa.

Pseudo experiments are then generated under both hypotheses and the distributions of the log-likelihood-ratio for both hypotheses are compared. Note that no fitting is performed in this case, i.e. all normalisations and parameter are kept fix. Examples of such distributions for one ARCA year are shown in Figure 11.16. From the distributions, a discrimination power between the two considered models can be calculated in three different ways.

The first (second) one of them is given by the probability p_1 (p_2) that under the true hypothesis S_1 (S_2) the log-likelihood-ratio has an outcome smaller (greater) than the median under the other hypothesis S_2 (S_1). I.e. the observation probability for such a value of the log-likelihood-ratio or a more extreme one is 50% under the other hypothesis. The probability p_1 (p_2) is again translated to the corresponding significance s_1 (s_2) in units of σ. Figure 11.16 shows that the distributions can well be described by Gaussians. From these the corresponding significances are calculated as

$$s_1/\sigma = \frac{\mu_1 - \mu_2}{\sigma_1} \tag{11.12}$$

$$s_2/\sigma = \frac{\mu_1 - \mu_2}{\sigma_2} \tag{11.13}$$

where μ_1 (μ_2) and σ_1 (σ_2) are the mean and standard deviation, respectively, of the Gaussian under hypothesis S_1 (S_2). Their values are also given in the figure.

The third measure s_3 of the discrimination power is calculated from the Gaussians as

$$s_3/\sigma = \frac{\mu_1 - \mu_2}{\sqrt{\sigma_1^2 + \sigma_2^2}} \tag{11.14}$$

which (translated to the corresponding p-value) can be interpreted as the probability that both hypotheses give a similar outcome for the likelihood ratio, i.e. that either both (small p-value) or neither (large p-value) of the hypotheses would be excluded in an experiment.

A small value for s_1 (s_2), e.g. smaller than $2\,\sigma$, means that hypothesis S_2 (S_1) is compatible with S_1 (S_2). A high value for s_3, say greater than $5\,\sigma$, means that they are not.

Two cases of flux discrimination are considered here as shown in Figure 11.16. Firstly, the discrimination between the 'combined' and the 'tension' flux: From the values given in the figure, it follows that both fluxes should very well be distinguishable in ARCA with $s_1 = 5.5\,\sigma$, $s_2 = 6.4\,\sigma$ and $s_3 = 4.1\,\sigma$.

The second case concerns the 'combined' flux and a broken-power-law flux as discussed in Section 11.3.4 and given via Eq. (11.10) with $\gamma_1 = 2.5$, $\gamma_2 = 2.13$ and $E_B = 1$ PeV. The respective measures for the discrimination power have values of $s_1 = 1.2\,\sigma$, $s_2 = 1.1\,\sigma$ and $s_3 = 0.78\,\sigma$, i.e. with the methods developed in this thesis it will not only be difficult to find a potential break in the signal flux but also to discriminate such a flux from a simple single-power-law flux.

It has again to be considered that the distributions are not perfectly described by Gaussians (see the end of Section 11.2), so that the actual significance values for the discrimination power after one ARCA year will be about 5-10% smaller than given above.

11.5 Sensitivity to the prompt atmospheric neutrino flux

In order to investigate the capabilities of ARCA to determine the normalisation of the prompt atmospheric neutrino flux, the likelihood method described in Section 11.1 was used. The precision on the prompt flux determination is derived from the distribution of fitted prompt normalisations c_p (see Figure 11.2, p. 153). Here, the prompt normalisation is now allowed to vary freely in the fit, i.e. without the penalty term in the likelihood (Eq. (11.4)). Example distributions for c_p in that case are shown in Figure 11.17 both for the 'combined' and 'tension' signal flux hypothesis. The figure illustrates that in the former case the distribution is much broader originating from the similar flux shapes of the prompt and the signal flux.

To enhance the sensitivity, the EAS simulations[61] (Section 6.1) are used. Thus, atmospheric neutrino events are reweighted as described in Section 6.3. In addition, instead of one-dimensional distributions with respect to the shower classifier response κ_S, here also the reconstructed zenith

---

[61] Due to the preliminary status of these simulations, these simulations were not considered in the other sections of this chapter.

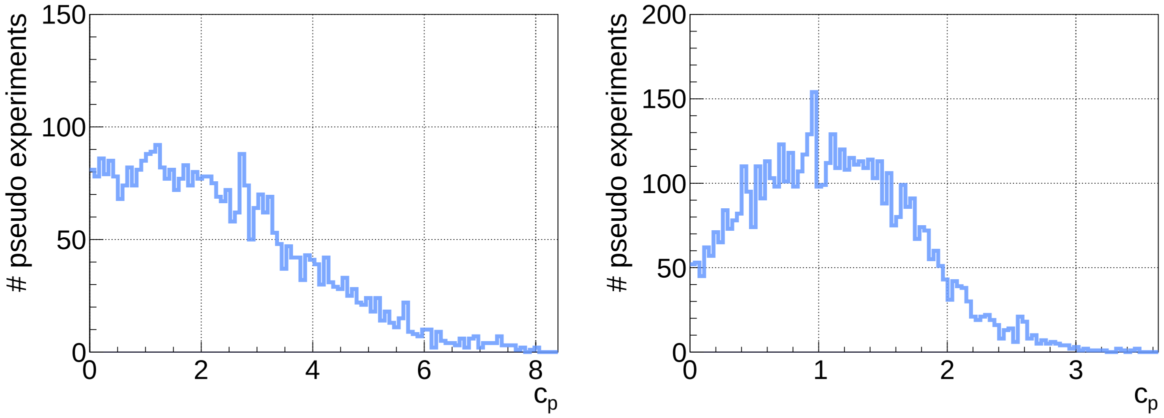

Figure 11.17: *Distribution of the prompt-flux normalisation factor in case of the ‘combined’ (left) and ‘tension’ (right) signal flux hypothesis for five ARCA years (6000 pseudo experiments each).*

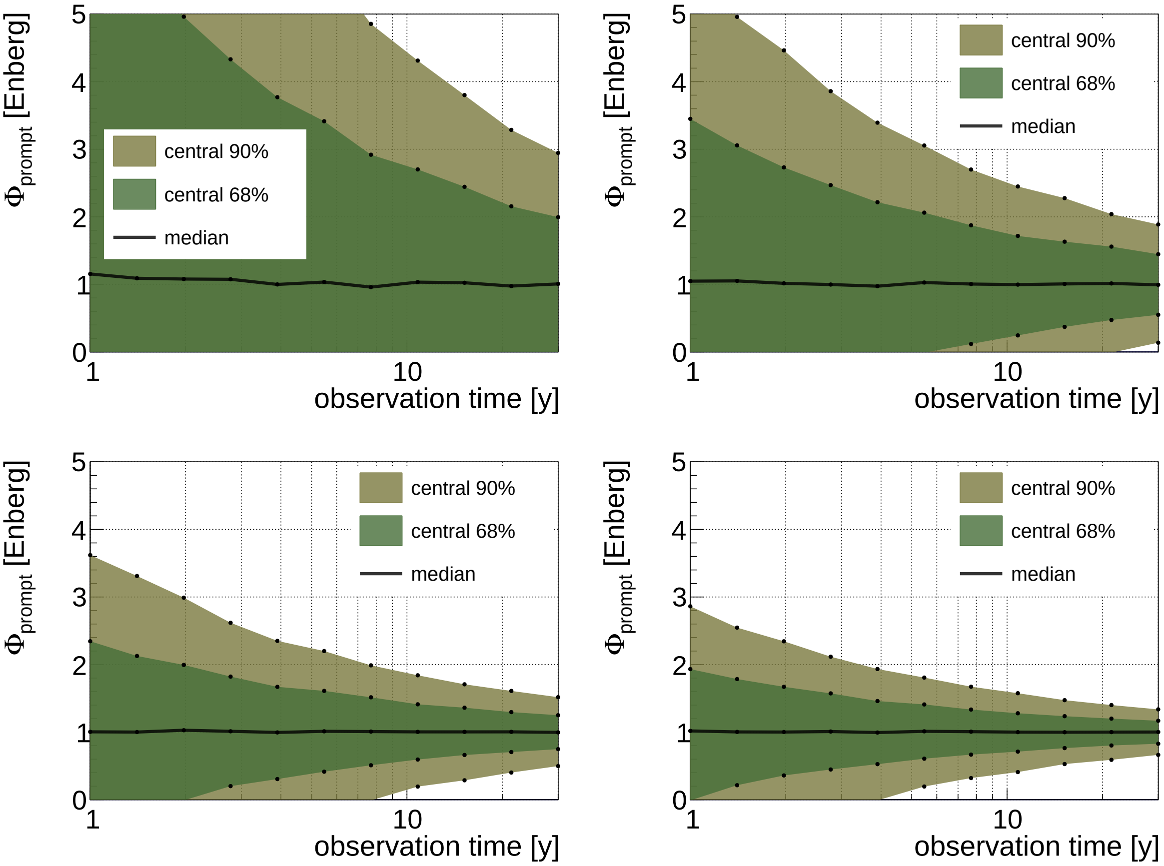

Figure 11.18: *Sensitivity to the prompt flux normalisation over ARCA time under the ‘combined’ (top) and ‘tension’ (bottom) signal flux hypothesis without (left) and with (right) use of the EAS simulations.*

angle θ_1 of *Shower Reconstruction Algorithm 1* is used to generate two-dimensional distributions versus θ_1 and κ_S. This is done because of the zenith-angle-dependent self-veto effect (see also Figure 10.6, p. 143). Tests have shown that this further increases the sensitivity – the shower classifier response alone does not differentiate well between different zenith angles. To avoid too fine binning and a large computation time, the number of bins is chosen to be 20 with respect to κ_S and 10 with respect to θ_1. Thus, the sum in Eq. (11.4) runs over 200 bins.

The precision of the determination of the prompt flux normalisation is assessed via the central 68% interval of the resulting c_p distribution. It is shown over time together with the respective central 90% interval in Figure 11.18 for the two cases of the 'combined' and 'tension' signal flux hypothesis. In addition the respective sensitivities reached with and without the use of the EAS simulations are compared. It can be seen that after ten ARCA years the uncertainty without the EAS simulations is about $^{+1.8}_{-1.0}$ under the 'combined' flux hypothesis and ±0.4 under the 'tension' flux hypothesis both in units of the Enberg [40] prompt flux. Utilising the EAS simulations, they reduce to about ±0.8 and ±0.2, respectively.

This result shows that the self-veto effect is very important in determining the prompt atmospheric neutrino flux. The sensitivity is compatible with that of the IceCube experiment which achieved with 5-6 ARCA years of data a respective uncertainty of around 1 in the 'combined' analysis [28] (providing the 'combined' flux) and around 0.5 in the analysis that provided the 'tension' flux [30], both in units of the Enberg flux.

It should be noted, however, that a possible degradation of the sensitivity to the prompt flux due to systematic uncertainties of the other background fluxes has not been investigated here. Also, the analysis presented here has not been optimised to determine the prompt neutrino flux. A dedicated study and the inclusion of comprehensive EAS simulations are expected to increase the sensitivity. Both aspects would be part of future analyses.

11.6 Summary

In this chapter, the discovery potential of ARCA to a diffuse, isotropic cosmic neutrino flux has been investigated with the help of a maximum likelihood method based on event rate distributions with respect to the shower classifier output. The method has been extended in order to analyse the sensitivity to the cosmic flux parameters, to investigate the capabilities of discriminating different flux models and to determine the sensitivity to the prompt atmospheric neutrino flux.

The achieved significance with 50% observation probability for one observation year of ARCA is $9.4\,\sigma\,^{+0.7\,\sigma}_{-0.4\,\sigma}$ (atm. ν) $\pm\,0.6\,\sigma$ (atm. μ) $\pm\,0.4\,\sigma$ (method) to the 'combined' flux Φ_C and $5.5\,\sigma\,^{+0.4\,\sigma}_{-0.3\,\sigma}$ (atm. ν) $\pm\,0.2\,\sigma$ (atm. μ) $\pm\,0.2\,\sigma$ (method) to the 'tension' flux Φ_T, both recently published by the IceCube collaboration [28,30] (they are given in Eq. (10.2) and (10.3) on page 133). In both cases a neutrino flavour ratio of $\nu_e : \nu_\mu : \nu_\tau = 1:1:1$ incident on Earth is assumed. The uncertainty estimations include missing simulations (atm. μ), systematics from the background fluxes (atm. ν) and estimated systematics inherent to the employed method. Missing simulations refer here to non-simulated atmospheric muons below 10 TeV. The mean significance after one year is increased by about 30% for both fluxes as compared to the cut-and-count method utilised in the previous chapter (see also Section 10.4).

Compared to previous ARCA sensitivity studies [7] in the shower channel, where a different maximum-likelihood method was employed after several cuts, the observation time needed for a detection with $5\,\sigma$ significance (50% observation probability) is reduced by about 25% for Φ_E, and roughly 50% for Φ_C. The main reason for this is that no strict event selection has been applied. This makes it possible to exploit the information carried by signal events below 50 TeV which are cut away in the previous study and which are especially important for the soft spectrum of Φ_C. It should be considered, however, that the fluxes as published by the IceCube collaboration are only valid in a limited energy range. This has not been considered here, instead the flux is assumed to be valid down to lowest energies where atmospheric neutrinos dominate the spectrum. Future studies will show if this assumption is justified or if the signal flux changes at lower energies leading to a possible degradation of the sensitivity. This holds especially for the soft spectrum of Φ_C.

Regarding the sensitivity to the parameters of the cosmic flux, it is clear that such parameters are easier to determine for the rather strong flux Φ_C than for Φ_T. Assuming a single power law as given by these fluxes, the relative uncertainty to the spectral index is of the order of 1% for Φ_C and 10% for Φ_T after one year observation time. For the flux normalisation the relative uncertainty is around 5% (Φ_C) or greater than 30% (Φ_T) after the same time.

In order to investigate the sensitivity to a potential cut-off at high energies, an exponential cut-off at 3 PeV was added to the 'tension' flux Φ_T. When all parameters are varied during the maximum-likelihood fit, a significant detection of the cut-off will not be possible with the methods employed here during the expected minimum lifetime of ARCA of 10 years. The resulting increase of the parameter space also increases the uncertainties to the spectral index and flux normalisation by a factor of up to two. A significant detection of the cut-off will only be possible if one of the other parameters is fixed during the maximum-likelihood fit. Then, the uncertainty on the cut-off energy is about half an order of magnitude after one ARCA year and reduces to about 10-15% in the common logarithm of the energy after ten years.

Considering a possible break in the cosmic neutrino flux as motivated by the different fluxes published by IceCube, results show that with the signal strengths given by these fluxes a break is easier detectable when it occurs at lower energies (between 100 TeV and 1 PeV) as compared to higher energies (above 1 PeV). The uncertainty to the break energy E_B after ten years of ARCA is around 10% for a break at lower energies ($E_B = 300$ TeV) and $^{+49\%}_{-26\%}$ for $E_B = 1$ PeV. Here, the spectral index after the break has been kept fix during the fit while, in additional to the break energy, the spectral index before the break and the flux normalisation have been varied.

The analyses regarding the discrimination of different flux models show that it will be difficult to discriminate a single power law flux form a flux with a break, especially when the break happens at high energies. However, the discrimination of the two published fluxes Φ_C and Φ_T will be possible with a significance of more than $3\,\sigma$ after one observation year. Thus a few years of ARCA observation will be very helpful in solving the tension between these two flux hypothesis.

It should be noted though, that for the discrimination analyses as well as for the investigation of the signal flux parameters, the background fluxes were kept fix during the maximum-likelihood fit (as opposed to the discovery potential investigation). Allowing the background contributions to vary during the fit is expected to increase the uncertainties.

Furthermore, it should be recalled that the utilised shower classifier was trained only to separate high-energy shower events from all other event types. No further optimisation has been performed for constraining the parameters of the diffuse cosmic neutrino flux. Future analyses are therefore expected to increase the sensitivity via a dedicated optimisation. A starting point could be the inclusion of the reconstructed energy in the maximum-likelihood fit.

The sensitivity to the prompt flux normalisation achievable with the developed method has been investigated in terms of the Enberg flux [40]. It has been shown that the 'self-veto' effect is an essential ingredient in being able to determine the prompt neutrino flux. Furthermore, the shape of the cosmic neutrino flux plays an important role: the more the shape between the prompt and cosmic neutrino flux differ, the greater the sensitivity to the prompt neutrino flux. This is because neutrinos from the lower hemisphere (where no 'self-veto' effect is present) can more easily be exploited to constrain the prompt flux. The uncertainties to the prompt flux normalisation after one ARCA observation year correspond to around ±80% when the 'combined' signal flux Φ_C is assumed and around ±20% with the 'tension' signal flux. Note that also here, an increase in sensitivity is expected with a dedicated optimisation which would for example be achievable with the inclusion of full 'self-veto' simulations in a dedicated classifier.

Finally as already mentioned before, for the studies presented in this chapter only the shower channel has been considered via utilising the shower classifier output. With an inclusion of an optimised identifier for signal track events, there is further potential for an increase of sensitivities in future studies.

Part V

Conclusion and outlook

This thesis presents contributions to the simulation and analysis of both detectors, ORCA and ARCA, of the future neutrino telescope KM3NeT. For the ORCA detector, the susceptibility of neutrino oscillation characteristics to uncertainties in the neutrino oscillation parameters and in the Earth model has been investigated in the relevant neutrino energy range of 1-20 GeV for atmospheric neutrinos travelling through the Earth. The focus was on how the ability of ORCA to measure the neutrino mass hierarchy is affected.

In order to quantify the impact of the different oscillation parameters, they have been varied within their $3\,\sigma$ uncertainty ranges. The absolute and cumulative differences occurring as a consequence of these variations have been investigated.

The uncertainties of the mixing angle θ_{12} and the small mass squared difference Δm^2_{21} are found to be negligible, while those of the other two mixing angles θ_{13} and θ_{23} and the CP phase δ_{cp} have a considerable impact. The largest effect is observed for the large mass squared difference Δm^2_{31}. On the other hand, ways of reducing the uncertainties of θ_{23} and Δm^2_{31} have been pointed out, thus increasing the potential sensitivity to the neutrino mass hierarchy. Regarding θ_{23}, the ability to distinguish electron from tau neutrinos will be very helpful while Δm^2_{31} can be constrained by exploiting oscillation maxima and minima above neutrino energies of 10 GeV.

Concerning the impact of parameters describing the Earth's interior, Earth model parameters have been changed on a per-Earth-layer basis. Considered parameters were the density, the position of the layer boundaries and the steepness of the density jumps at the layer boundaries. As sophisticated error estimations for such parameters are scarce, the variations have been done within a range considered conservative to get an impression of their effect on the oscillation probabilities.

The lower mantle and outer core being the largest layers, changes in the parameters describing these two layers have the largest effect. In particular, variations of the density in these layers of more than about 5% begin to have a significant effect resulting in a change of oscillation probabilities by around 10%. This should be considered in future sensitivity studies as the combination of matter density and electron fraction uncertainties may reach this value. Shifting the border between these layers by around 50 km produces significant changes which is, however, a value much larger than known uncertainty estimates. A smoothing of the sudden density jumps between two layers has an overall negligible effect on the oscillation probabilities.

These results were valuable input to initial feasibility and sensitivity studies of the ORCA experiment (see also the KM3NeT Letter of Intent [7]).

Furthermore, a method has been derived to interpolate oscillation probabilities in the eight-dimensional parameter space given by the six oscillation parameters and the kinetic parameters of neutrino energy and zenith angle. For detailed sensitivity studies, these oscillation probabilities need to be known to a high precision. The ultimate goal is the reduction of the computing time needed for ORCA sensitivity studies which are dominated by the calculation of the oscillation probabilities.

The formulae used for the interpolation have been derived based on Taylor expansions around given data points. They show high flexibility as the number of data points used for the expansion can be chosen freely and the order of the expansion is only limited by the chosen number of data points. At the same time a very high precision is achievable depending on the chosen number of data points and order of the expansion while the density of generated data points can be kept rather low.

The final result of this study was an estimate for the total number of pre-calculated data points needed to interpolate the full 3σ space of the oscillation parameters with a precision better than 10^{-3} (i.e. difference between true and interpolated oscillation probability). However, this number requires large computational resources. Therefore, several possibilities for improvement have been identified. Among them is the optimisation of the grid of data points in the eight-dimensional parameter space, as for example for most parameters it holds that more points are needed at low energies and fewer at high energies. This will not only reduce the required computing time but also the required disk space.

Regarding the final computation time needed during the sensitivity studies, the equation of motion for calculating the oscillation probabilities then has to be solved only once in advance for a given set of parameter values. From this point on, they would be interpolated on the fly from the given data. Comparing both methods the average time needed to calculate the oscillation probability for a single point in the parameter space is reduced by at least three orders of magnitude.

Regarding the planned ARCA detector of KM3NeT, the sensitivity to the cosmic neutrino flux as measured by the IceCube collaboration was examined using two different methods: a cut-and-count approach and a spectral fitting method based on the maximum-likelihood principle. Both analyses were based on the output of a boosted-decision-tree classifier, a machine learning algorithm used to distinguish signal neutrino events from the background of atmospheric muons and atmospheric neutrinos. A dedicated preprocessing has been developed to identify the event reconstruction parameters most suitable for this classification. Optimised for the shower channel, the same procedure has also been applied to the track channel. Applying a cut-and-count method, this lead to a shower search, a track search and a combined search.

The cut-and-count method consisted of determining a cut in the classifier output that optimises the sensitivity to the hypothetical cosmic neutrino fluxes. After this cut, event numbers are counted to determine the sensitivity based on Poisson statistics. The achieved sensitivity turned out to be significantly higher in the shower search than in the track search – the combination of both is only slightly better than the shower channel alone.

With the combined search, the strongest of the considered signal fluxes [28] is observed at the 5σ level with 50% observation probability after 0.49 ± 0.07 years of ARCA observation time. The uncertainty results from systematics of the conventional atmospheric neutrino flux which dominates the uncertainty of the final result. The weakest considered flux [30] is detected with the same significance after 1.30 ± 0.23 years. Here, the uncertainty is dominated by the prompt component of the atmospheric neutrino flux. Considering the similar size of the ARCA and IceCube detector, these predicted times for ARCA are in both cases considerably less than needed by IceCube for their results. A major reason for this is that here no veto-layers are used so that events outside and near the borders of the instrumented detector volume contribute significantly to the expected event rate. For the weakest considered flux roughly 34 neutrino events with energies greater than 60 TeV are expected after two years of data taking, 24 (71%) of which of cosmic origin. For the strongest flux implying a different optimal cut, about 280 neutrino events are expected above 10 TeV after two years, 130 (48%) of which of cosmic origin.

The main source of uncertainties are the systematics in the assumed background neutrino fluxes of conventional and prompt atmospheric neutrinos, leading to an uncertainty of the order of ±15% in the significance after one year observation time. The systematic uncertainties in the significance resulting from Monte Carlo simulations are negligible with values around ±2%. All results presented here assume a conventional atmospheric neutrino flux according to Honda [39] and a prompt atmospheric neutrino flux according to Enberg [40]. Results from IceCube favour a vanishing prompt component which would increase significances reported here by a few percent.

Compared with previous cut-and-count analyses for the ARCA sensitivity as presented in the KM3NeT Letter of Intent [7], an increase in sensitivity in the shower channel is achieved, reducing the observation time needed for a $5\,\sigma$ discovery by roughly 10%. However, the respective results in the Letter of Intent of the track channel analysis could not be reached implying that the track search performed here requires an individual optimisation. One possibility could be to perform a multi-step classification.

Besides the discovery potential, also the detector resolutions for the neutrino event samples surviving the cuts of the combined search were investigated. The energy resolution for ν_e charged-current events is better than 10% for neutrino energies between 10 TeV and 1 PeV for 68% of the events. The median zenith angle resolution is better than 1° for most of the events while it reaches values down to 0.1° for track events.

In order to improve the sensitivity and to investigate the capabilities of ARCA to determine the parameters describing an isotropic cosmic neutrino flux, a spectral fitting method has been developed and applied. With this method, the strongest considered signal flux is in ARCA detected with a significance of $9.4\,\sigma\,^{+0.7\,\sigma}_{-0.4\,\sigma}$ (atm. ν) $\pm\,0.6\,\sigma$ (atm. μ) $\pm\,0.4\,\sigma$ (method), the weakest considered flux with $5.5\,\sigma\,^{+0.4\,\sigma}_{-0.3\,\sigma}$ (atm. ν) $\pm\,0.2\,\sigma$ (atm. μ) $\pm\,0.2\,\sigma$ (method), with 50% observation probability for one observation year of ARCA. The mean significance after one year is increased by about 30% for both fluxes as compared to the cut-and-count method. The uncertainty estimations include the dominating sources of uncertainty: missing simulations (atm. μ), systematics from the background fluxes (atm. ν) and estimated systematics inherent to the employed method. Missing simulations refer here to non-simulated atmospheric muons below 10 TeV.

It was possible to reduce the observation time needed for a detection with $5\,\sigma$ significance at 50% observation probability by about 25% (weak flux) or 50% (strong flux) compared to previous ARCA sensitivity studies [7] in the shower channel. The main reason for this is that in contrast to this previous study where a different maximum-likelihood method was employed after several cuts, here no strict event selection has been applied. This allows exploiting the information carried by low energy signal events (below 50 TeV) which are rejected in the previous study and which are of high importance for a flux with a soft spectrum.

Assuming a single-power-law signal spectrum, the spectral index is determined with less than 2% accuracy after one year of ARCA given the strongest signal flux. For the weakest signal flux, an accuracy of around 15% is achieved after one year. In addition the sensitivity to a potential cut-off or break in the cosmic neutrino spectrum was investigated. The sensitivity depends highly on the energy of the cut-off or break. Fixing the spectral index while fitting for the respective energy and assuming a cut-off or break above 1 PeV yields uncertainties of around half an order of magnitude or more. The uncertainties get larger when all parameters are allowed to vary during the fit. It should be considered, however, that the applied method was not optimised to determine these spectral parameters so that future analyses might achieve increased sensitivity.

Finally, also the capabilities to discriminate different signal fluxes have been investigated having in mind that the strongest and weakest signal fluxes published by IceCube are in tension with each other at a significance of more than 3σ. This tension should be resolvable with ARCA within a few years of data taking. This tension might however be caused by an anisotropy present in the cosmic neutrino flux which has not been investigated here. Respective studies as well as a check for the capabilities to determine the cosmic neutrino flavour ratio are excellent candidates for follow-up analyses. Furthermore, a dedicated inclusion of the track channel for these studies is of high interest.

The studies have shown that the ARCA detector allows for an investigation of cosmic neutrinos with unprecedented sensitivity. The sensitivity will further be improved considering the full KM3NeT detector which will be thrice the size of ARCA regarding the investigation of cosmic neutrinos. The successful operation of the KM3NeT experiment will therefore significantly expand our knowledge about neutrinos, their cosmic origin, and thus about the origin of highest-energy cosmic rays.

List of Abbreviations

AGAD Averaged Global Absolute Differences

AGED Averaged Global Effective Differences

AGN Active Galactic Nucleus

ANTARES Astronomy with a Neutrino Telescope and Abyss environmental RESearch

AMANDA Antarctic Muon And Neutrino Detector Array

ARCA Astroparticle Research with Cosmics in the Abyss

BDT Boosted Decision Tree

CC Charged Current

CORSIKA COsmic Ray SImulations for KAscade. Software to simulate of extensive air showers.

CS Combined Search

CP CP-symmetry stands for the combined symmetry of charge conjugation (C) and parity (P). A complex CP phase indicates violation of CP-symmetry.

CPU Central Processing Unit

DIS Deep-Inelastic Scattering

DOM Digital Optical Module

DU Detection Unit

EAS Extensive Air Shower

GAD Global Absolute Difference

GED Global Effective Difference

GENHEN GENerator of High-Energy Neutrinos. Monte Carlo simulation software for high-energy neutrino interactions.

GRB Gamma Ray Burst

HPC High Performance Computing

IH Inverted Hierarchy

KM3NeT km^3-sized Neutrino Telescope

LAD Local Absolute Difference

LED Local Effective Difference

MC Monte Carlo

MDP Model Discovery Potential

MGAD Maximum Global Absolute Difference

MGED Maximum Global Absolute Difference

MLAD Maximum Local Effective Difference

MLED Maximum Local Effective Difference

MRF Model Rejection Factor

MSW resonance After Mikheyev, Smirnov and Wolfenstein.

NC Neutral Current

NH Normal Hierarchy

ORCA Oscillation Research with Cosmics in the Abyss

PDF Parton Distribution Function, Probability Density/Distribution Function

PINGU Precision IceCube Next Generation Upgrade

PMNS matrix After Pontecorvo, Maki, Nakagawa and Sakata.

PMT Photomultiplier Tube

PREM Preliminary Reference Earth Model

QCD Quantum Chromodynamics

RMS Root Mean Square

SNR Supernova Remnant

SR Shower Reconstruction algorithm

SS Shower Search

TR Track Reconstruction algorithm

TS Track Search

WIMP Weakly Interacting Massive Particles

List of Figures

List of Tables

Bibliography

[1] V. F. Hess, "Über Beobachtungen der durchdringenden Strahlung bei sieben Freiballonfahrten." *Physikalische Zeitschrift* 13 (November, 1912) 1084–1091.

[2] Particle Data Group Collaboration, C. Patrignani *et al.*, "Review of Particle Physics." *Chin. Phys.* C40 no. 10, (2016) 100001.

[3] IceCube Collaboration, M. G. Aartsen *et al.*, "Evidence for High-Energy Extraterrestrial Neutrinos at the IceCube Detector." *Science* 342 (2013) 1242856, `arXiv:1311.5238`.

[4] W. Pauli, "Offener Brief an die Gruppe der Radioaktiven bei der Gauvereinstagung zu Tübingen." in *Open letter to the group of radioactive people at the Gauverein meeting in Tübingen*. 1930.

[5] C. L. Cowan *et al.*, "Detection of the Free Neutrino: a Confirmation." *Science* 124 (1956) 103–104.

[6] Super-Kamiokande Collaboration, Y. Fukuda *et al.*, "Evidence for Oscillation of Atmospheric Neutrinos." *Phys. Rev. Lett.* 81 (1998) 1562–1567, `arXiv:hep-ex/9807003`.

[7] KM3Net Collaboration, S. Adrián-Martínez *et al.*, "Letter of Intent for KM3NeT 2.0." *J. Phys.* G43 no. 8, (2016) 084001, `arXiv:1601.07459`.

[8] Z.-z. Xing and S. Zhou, "Neutrinos in Particle Physics, Astronomy and Cosmology." *Zhejiang University Press, Hangzhou* (2011).

[9] P. Lipari, M. Lusignoli, and D. Meloni, "Flavor composition and energy spectrum of astrophysical neutrinos." *Phys. Rev. D* 75 (Jun, 2007) 123005.

[10] KM3NeT Collaboration, A. Trovato, "KM3NeT/ARCA sensitivity and discovery potential for neutrino point-like sources." *EPJ Web Conf.* 116 (2016) 04006.

[11] E. Waxman and J. N. Bahcall, "High-energy neutrinos from astrophysical sources: An Upper bound." *Phys. Rev.* D59 (1999) 023002, `arXiv:hep-ph/9807282`.

[12] K. Mannheim, R. J. Protheroe, and J. P. Rachen, "On the cosmic ray bound for models of extragalactic neutrino production." *Phys. Rev.* D63 (2001) 023003, `arXiv:astro-ph/9812398`.

[13] V. Berezinsky, A. Gazizov, M. Kachelrieß, and S. Ostapchenko, "Restricting UHECRs and cosmogenic neutrinos with Fermi-LAT." *Physics Letters B* 695 no. 1-4, (2011) 13–18.

[14] E. Fermi, “On the Origin of the Cosmic Radiation.” *Phys. Rev.* 75 (1949) 1169–1174.

[15] R. Blandford and D. Eichler, “Particle Acceleration at Astrophysical Shocks: A Theory of Cosmic Ray Origin.” *Phys. Rept.* 154 (1987) 1–75.

[16] K. Kotera, D. Allard, and A. V. Olinto, “Cosmogenic Neutrinos: parameter space and detectabilty from PeV to ZeV.” *JCAP* 1010 (2010) 013, `arXiv:1009.1382`.

[17] D. Gaggero *et al.*, “The gamma-ray and neutrino sky: A consistent picture of Fermi-LAT, Milagro, and IceCube results.” *Astrophys. J.* 815 no. 2, (2015) L25, `arXiv:1504.00227`.

[18] M. Su, T. R. Slatyer, and D. P. Finkbeiner, “Giant Gamma-ray Bubbles from Fermi-LAT: AGN Activity or Bipolar Galactic Wind?.” *Astrophys. J.* 724 (2010) 1044–1082, `arXiv:1005.5480`.

[19] Pierre Auger Collaboration, J. Abraham *et al.*, “An upper limit to the photon fraction in cosmic rays above 10^{19} eV from the Pierre Auger Observatory.” *Astropart. Phys.* 27 (2007) 155–168, `arXiv:astro-ph/0606619`.

[20] U. F. Katz and C. Spiering, “High-Energy Neutrino Astrophysics: Status and Perspectives.” *Prog. Part. Nucl. Phys.* 67 (2012) 651–704, `arXiv:1111.0507`.

[21] IceCube Collaboration, A. Achterberg *et al.*, “First Year Performance of The IceCube Neutrino Telescope.” *Astropart. Phys.* 26 (2006) 155–173, `arXiv:astro-ph/0604450`.

[22] IceCube Collaboration, M. G. Aartsen *et al.*, “Atmospheric and Astrophysical Neutrinos above 1 TeV Interacting in IceCube.” *Phys. Rev.* D91 no. 2, (2015) 022001, `arXiv:1410.1749`.

[23] IceCube Collaboration, M. G. Aartsen *et al.*, “Observation of High-Energy Astrophysical Neutrinos in Three Years of IceCube Data.” *Phys. Rev. Lett.* 113 (2014) 101101, `arXiv:1405.5303`.

[24] IceCube Collaboration, Schönwald, A. and Brown, A. M. and Mohrmann, L., “Search for diffuse astrophysical neutrinos with cascade events in the IceCube-59 detector.” in *Proceedings, 33rd International Cosmic Ray Conference (ICRC2013).* 2013. `arXiv:1309.7003`.

[25] IceCube Collaboration, M. G. Aartsen *et al.*, “Search for neutrino-induced particle showers with IceCube-40.” *Phys. Rev.* D89 no. 10, (2014) 102001, `arXiv:1312.0104`.

[26] IceCube Collaboration, M. G. Aartsen *et al.*, “Evidence for Astrophysical Muon Neutrinos from the Northern Sky with IceCube.” *Phys. Rev. Lett.* 115 no. 8, (2015) 081102, `arXiv:1507.04005`.

[27] IceCube Collaboration, M. G. Aartsen *et al.*, “Search for a diffuse flux of astrophysical muon neutrinos with the IceCube 59-string configuration.” *Phys. Rev.* D89 no. 6, (2014) 062007, `arXiv:1311.7048`.

[28] IceCube Collaboration, M. G. Aartsen *et al.*, “A combined maximum-likelihood analysis of the high-energy astrophysical neutrino flux measured with IceCube.” *Astrophys. J.* 809 no. 1, (2015) 98, `arXiv:1507.03991`.

[29] IceCube Collaboration, M. G. Aartsen *et al.*, "The IceCube Neutrino Observatory - Contributions to ICRC 2015 Part II: Atmospheric and Astrophysical Diffuse Neutrino Searches of All Flavors." in *Proceedings, 34th International Cosmic Ray Conference (ICRC 2015)*. `arXiv:1510.05223`.

[30] IceCube Collaboration, M. G. Aartsen *et al.*, "Observation and Characterization of a Cosmic Muon Neutrino Flux from the Northern Hemisphere using six years of IceCube data." *Astrophys. J.* 833 no. 1, (2016) 3, `arXiv:1607.08006`.

[31] Baikal Collaboration, I. A. Belolaptikov *et al.*, "The Baikal underwater neutrino telescope: Design, performance and first results." *Astropart. Phys.* 7 (1997) 263–282.

[32] Baikal Collaboration, Z. A. Dzhilkibaev, "Search for a diffuse flux of high-energy neutrinos with the Baikal neutrino telescope NT200." `arXiv:0909.5562`.

[33] E. Andres *et al.*, "The AMANDA neutrino telescope: Principle of operation and first results." *Astropart. Phys.* 13 (2000) 1–20, `arXiv:astro-ph/9906203`.

[34] IceCube Collaboration, A. Achterberg *et al.*, "Multi-year search for a diffuse flux of muon neutrinos with AMANDA-II." *Phys. Rev.* D76 (2007) 042008, `arXiv:0705.1315`. [Erratum: Phys. Rev.D77,089904(2008)].

[35] ANTARES Collaboration, M. Ageron *et al.*, "ANTARES: the first undersea neutrino telescope." *Nucl. Instrum. Meth.* A656 (2011) 11–38, `arXiv:1104.1607`.

[36] ANTARES Collaboration, L. A. Fusco, "Searches for diffuse fluxes of cosmic neutrinos with the ANTARES telescope." *EPJ Web Conf.* 121 (2016) 05013.

[37] IceCube Collaboration, M. G. Aartsen *et al.*, "Search for astrophysical sources of neutrinos using cascade events in IceCube." `arXiv:1705.02383`.

[38] IceCube Collaboration, M. G. Aartsen *et al.*, "The contribution of Fermi-2LAC blazars to the diffuse TeV-PeV neutrino flux." *Astrophys. J.* 835 no. 1, (2017) 45, `arXiv:1611.03874`.

[39] M. Honda *et al.*, "Calculation of atmospheric neutrino flux using the interaction model calibrated with atmospheric muon data." *Phys. Rev.* D75 (2007) 043006, `arXiv:astro-ph/0611418`.

[40] R. Enberg, M. H. Reno, and I. Sarcevic, "Prompt neutrino fluxes from atmospheric charm." *Phys. Rev.* D78 (2008) 043005, `arXiv:0806.0418`.

[41] C. G. S. Costa, "The prompt lepton cookbook." *Astropart. Phys.* 16 (2001) 193–204, `arXiv:hep-ph/0010306`.

[42] A. Fedynitch, J. Becker Tjus, and P. Desiati, "Influence of hadronic interaction models and the cosmic ray spectrum on the high energy atmospheric muon and neutrino flux." *Phys. Rev.* D86 (2012) 114024, `arXiv:1206.6710`.

[43] S. Schonert, T. K. Gaisser, E. Resconi, and O. Schulz, "Vetoing atmospheric neutrinos in a high energy neutrino telescope." *Phys. Rev.* D79 (2009) 043009, `arXiv:0812.4308`.

[44] T. K. Gaisser, K. Jero, A. Karle, and J. van Santen, "Generalized self-veto probability for atmospheric neutrinos." *Phys. Rev.* D90 no. 2, (2014) 023009, `arXiv:1405.0525`.

[45] B. Pontecorvo, "Mesonium and anti-mesonium." *Sov. Phys. JETP* 6 (1957) 429. [Zh. Eksp. Teor. Fiz.33,549(1957)].

[46] B. Pontecorvo, "Neutrino Experiments and the Problem of Conservation of Leptonic Charge." *Sov. Phys. JETP* 26 (1968) 984–988. [Zh. Eksp. Teor. Fiz.53,1717(1967)].

[47] Z. Maki, M. Nakagawa, and S. Sakata, "Remarks on the Unified Model of Elementary Particles." *Prog. Theor. Phys.* 28 (1962) 870–880.

[48] SNO Collaboration, Q. R. Ahmad *et al.*, "Direct Evidence for Neutrino Flavor Transformation from Neutral-Current Interactions in the Sudbury Neutrino Observatory." *Phys. Rev. Lett.* 89 (2002) 011301, `arXiv:nucl-ex/0204008`.

[49] KamLAND Collaboration, T. Araki *et al.*, "Measurement of Neutrino Oscillation with KamLAND: Evidence of Spectral Distortion." *Phys. Rev. Lett.* 94 (2005) 081801, `arXiv:hep-ex/0406035`.

[50] G. L. Fogli *et al.*, "Global analysis of neutrino masses, mixings and phases: entering the era of leptonic CP violation searches." *Phys. Rev.* D86 (2012) 013012, `arXiv:1205.5254`.

[51] Z.-z. Xing, "New formulation of matter effects on neutrino mixing and CP violation." *Phys. Lett.* B487 (2000) 327–333, `arXiv:hep-ph/0002246`.

[52] L. Wolfenstein, "Neutrino Oscillations in Matter." *Phys. Rev.* D17 (1978) 2369–2374.

[53] L. Wolfenstein, "Neutrino Oscillations and Stellar Collapse." *Phys. Rev.* D20 (1979) 2634–2635.

[54] S. P. Mikheev and A. Y. Smirnov, "Resonance Amplification of Oscillations in Matter and Spectroscopy of Solar Neutrinos." *Sov. J. Nucl. Phys.* 42 (1985) 913–917. [Yad. Fiz.42,1441(1985)].

[55] E. K. Akhmedov, S. Razzaque, and A. Yu. Smirnov, "Mass hierarchy, 2-3 mixing and CP-phase with Huge Atmospheric Neutrino Detectors." *JHEP* 02 (2013) 082, `arXiv:1205.7071`. [Erratum: JHEP07,026(2013)].

[56] A. M. Dziewonski and D. L. Anderson, "Preliminary reference Earth model." *Phys. Earth Planet. Interiors* 25 (1981) 297–356.

[57] E. K. Akhmedov, "Parametric resonance of neutrino oscillations and passage of solar and atmospheric neutrinos through the earth." *Nucl. Phys.* B538 (1999) 25–51, `arXiv:hep-ph/9805272`.

[58] R. Gandhi, C. Quigg, M. H. Reno, and I. Sarcevic, "Neutrino interactions at ultrahigh energies." *Phys. Rev. D* 58 (Sep, 1998) 093009.

[59] A. Connolly, R. S. Thorne, and D. Waters, "Calculation of High Energy Neutrino-Nucleon Cross Sections and Uncertainties Using the MSTW Parton Distribution Functions and Implications for Future Experiments." *Phys. Rev.* D83 (2011) 113009, `arXiv:1102.0691`.

[60] R. Gandhi, C. Quigg, M. H. Reno, and I. Sarcevic, “Ultrahigh-energy neutrino interactions.” *Astropart. Phys.* 5 (1996) 81–110, `arXiv:hep-ph/9512364`.

[61] A. Bhattacharya, R. Gandhi, W. Rodejohann, and A. Watanabe, “The Glashow resonance at IceCube: signatures, event rates and pp vs. $p\gamma$ interactions.” *JCAP* 1110 (2011) 017, `arXiv:1108.3163`.

[62] I. F. M. Albuquerque, J. Lamoureux, and G. F. Smoot, “Astrophysical Neutrino Event Rates and Sensitivity for Neutrino Telescopes.” *Astrophys. J. Suppl.* 141 (2002) 195–209, `arXiv:hep-ph/0109177`.

[63] P. A. Čerenkov, “Visible Radiation Produced by Electrons Moving in a Medium with Velocities Exceeding that of Light.” *Phys. Rev.* 52 (Aug, 1937) 378–379.

[64] KM3NeT Collaboration, S. Adrián-Martínez *et al.*, “Deep sea tests of a prototype of the KM3NeT digital optical module.” *Eur. Phys. J.* C74 no. 9, (2014) 3056, `arXiv:1405.0839`.

[65] KM3NeT Collaboration, S. Adrián-Martínez *et al.*, “The prototype detection unit of the KM3NeT detector.” *Eur. Phys. J.* C76 no. 2, (2016) 54, `arXiv:1510.01561`.

[66] K. Collaboration, “KM3NeT official website.” 2016. `http://www.km3net.org`.

[67] G. Carminati, A. Margiotta, and M. Spurio, “Atmospheric MUons from PArametric formulas: A Fast GEnerator for neutrino telescopes (MUPAGE).” *Comput. Phys. Commun.* 179 (2008) 915–923, `arXiv:0802.0562`.

[68] Y. Becherini, A. Margiotta, M. Sioli, and M. Spurio, “A Parameterisation of single and multiple muons in the deep water or ice.” *Astropart. Phys.* 25 (2006) 1–13, `arXiv:hep-ph/0507228`.

[69] J. A. Formaggio and G. P. Zeller, “From eV to EeV: Neutrino Cross Sections Across Energy Scales.” *Rev. Mod. Phys.* 84 (2012) 1307–1341, `arXiv:1305.7513`.

[70] C. Rott, A. Taketa, and D. Bose, “Spectrometry of the Earth using Neutrino Oscillations.” *Sci. Rep.* 5 (2015) 15225, `arXiv:1502.04930`.

[71] A. W. Hofmann *et al.*, “Mantle geochemistry: the message from oceanic volcanism.” *Nature* 385 no. 6613, (1997) 219–229.

[72] Jones, E. and others, “SciPy: Open source scientific tools for Python.” 2001-2017. `http://www.scipy.org/`.

[73] A. C. Hindmarsh, “ODEPACK, A Systematized Collection of ODE Solvers.” *IMACS Transactions on Scientific Computation* 1 (1983) 55–64.

[74] IceCube PINGU Collaboration, M. G. Aartsen *et al.*, “Letter of Intent: The Precision IceCube Next Generation Upgrade (PINGU).” `arXiv:1401.2046`.

[75] P. Toale. Private Communication.

[76] F. Capozzi *et al.*, “Neutrino masses and mixings: Status of known and unknown 3ν parameters.” *Nucl. Phys.* B908 (2016) 218–234, `arXiv:1601.07777`.

[77] B. A. Bolt, “The Precision of Density Estimation Deep in the Earth.” QJRAS 32 (Dec., 1991) 367.

[78] U. S. N. A. O., *Astronomical Almanac for the Year 2017 and Its Companion, the Astronomical Almanac Online*. Admiralty Nautical Almanacs. U.S. Government Printing Office. `http://asa.usno.navy.mil/`.

[79] M. Lindner, T. Ohlsson, R. Tomas, and W. Winter, “Tomography of the Earth’s core using supernova neutrinos.” *Astropart. Phys.* 19 (2003) 755–770, `arXiv:hep-ph/0207238`.

[80] W. Winter, “Atmospheric neutrino oscillations for Earth tomography.” *Nucl. Phys.* B908 (2016) 250–267, `arXiv:1511.05154`.

[81] H. Kerner and W. von Wahl, *Mathematik für Physiker, Kapitel 9.4*. Springer-Verlag, 2013.

[82] G. Fischer, *Lineare Algebra*. vieweg studium, 2005.

[83] M. Jongen. Private Communication.

[84] ANTARES Collaboration, A. Margiotta, “Common simulation tools for large volume neutrino detectors.” *Nucl. Instrum. Meth.* A725 (2013) 98–101.

[85] P. Antonioli *et al.*, “A Three-dimensional code for muon propagation through the rock: Music.” *Astropart. Phys.* 7 (1997) 357–368, `arXiv:hep-ph/9705408`.

[86] S. Jadach, J. H. Kuhn, and Z. Was, “TAUOLA: A Library of Monte Carlo programs to simulate decays of polarized tau leptons.” *Comput. Phys. Commun.* 64 (1990) 275–299.

[87] G. Ingelman, A. Edin, and J. Rathsman, “LEPTO 6.5: A Monte Carlo generator for deep inelastic lepton-nucleon scattering.” *Comput. Phys. Commun.* 101 (1997) 108–134, `arXiv:hep-ph/9605286`.

[88] H. L. Lai *et al.*, “Global QCD analysis and the CTEQ parton distributions.” *Phys. Rev.* D51 (1995) 4763–4782, `arXiv:hep-ph/9410404`.

[89] D. Heck *et al.*, “CORSIKA: A Monte Carlo code to simulate extensive air showers.”. `https://www.ikp.kit.edu/corsika/`.

[90] R. Brun, F. Bruyant, M. Maire, A. C. McPherson, and P. Zanarini, *GEANT 3: user’s guide Geant 3.10, Geant 3.11; rev. version*. CERN, Geneva, 1987. `http://cds.cern.ch/record/1119728`.

[91] D. Bailey, *Monte Carlo tools and analysis methods for understanding the ANTARES experiment and predicting its sensitivity to dark matter*. PhD thesis, Oxford U., 2002.

[92] C. M. F. Hugon, “GEANT4 simulation of optical modules in neutrino telescopes.” *PoS* ICRC2015 (2016) 1106.

[93] KM3NeT Collaboration, S. Adrián-Martínez *et al.*, “Expansion cone for the 3-inch PMTs of the KM3NeT optical modules.” *JINST* 8 (2013) T03006.

[94] J. Reubelt, *Hardware studies, in-situ prototype calibration and data analysis of the novel multi-PMT digital optical module for the KM3NeT neutrino telescope (in preparation)*. PhD thesis, Friedrich-Alexander Universität Erlangen-Nürnberg, 2018.

[95] W. J. Metzger, *Statistical methods in data analysis*. Nijmegen Univ. Fys. Lab., Nijmegen, 2002. `http://cds.cern.ch/record/482882`.

[96] KM3NeT Collaboration, T. Heid, C. James, and K. Pikounis, "Self-veto approaches to reject atmospheric neutrinos in KM3NeT/ARCA." *PoS* ICRC2015 (2016) 1067.

[97] KM3NeT Collaboration, A. Trovato, E. Drakopoulou, and P. Sapienza, "Muon track reconstruction and muon energy estimate in the KM3NeT/ARCA detector." *PoS* ICRC2015 (2016) 1114.

[98] KM3NeT Collaboration, D. Stransky *et al.*, "Reconstruction of cascade-type neutrino events in KM3NeT/ARCA." *PoS* ICRC2015 (2016) 1108.

[99] KM3NeT Collaboration, C. Kopper, "A software framework for KM3NeT." *Nucl. Instrum. Meth.* A602 (2009) 107–110.

[100] A. Heijboer (2014). Internal note: KM3NeT_ASTRO_2014_001.

[101] L. Ambrogi, T. Chiarusi, and M. Spurio (2013). Internal note: ANTARES-Phys-2013-007.

[102] F. Folger, *Search for a diffuse cosmic neutrino flux using shower events in the ANTARES neutrino telescope*. PhD thesis, Friedrich-Alexander Universität Erlangen-Nürnberg, Erlangen, 2014.

[103] A. Heijboer, *Track reconstruction and point source searches with ANTARES*. PhD thesis, Amsterdam U., 2004. `https://www.nikhef.nl/~t61/thesis.shtml`.

[104] B. D. Hartmann, *Reconstruction of Neutrino-Induced Hadronic and Electromagnetic Showers with the ANTARES Experiment*. PhD thesis, Friedrich-Alexander Universität Erlangen-Nürnberg, 2006. `arXiv:astro-ph/0606697`.

[105] T. Heid, *Neutrino flavour identification in KM3NeT (in preparation)*. PhD thesis, Friedrich-Alexander Universität Erlangen-Nürnberg, 2017.

[106] S. B. Kotsiantis, D. Kanellopoulos, and P. E. Pintelas, "Data preprocessing for supervised leaning." *International Journal of Computer Science* 1 no. 2, (2006) 111–117.

[107] A. Hoecker *et al.*, "TMVA: Toolkit for Multivariate Data Analysis." *PoS* ACAT (2007) 040, `arXiv:physics/0703039`.

[108] R. Brun and F. Rademakers, "ROOT - An Object Oriented Data Analysis Framework." in *AIHENP'96 Workshop, Lausane*, vol. 389, pp. 81–86. 1996.

[109] W.-Y. Loh, "Classification and regression trees." *Wiley Interdisciplinary Reviews: Data Mining and Knowledge Discovery* 1 no. 1, (2011) 14–23.

[110] L. Rokach and O. Maimon, *Data mining with decision trees: theory and applications*. World scientific, 2014.

[111] Y. Freund and R. E. Schapire, “A desicion-theoretic generalization of on-line learning and an application to boosting.” in *European conference on computational learning theory*, pp. 23–37, Springer. 1995.

[112] Y. Freund and R. E. Schapire, “Experiments with a new boosting algorithm.” in *Icml*, vol. 96, pp. 148–156. 1996.

[113] T. G. Dietterich, *Ensemble Methods in Machine Learning*, pp. 1–15. Springer Berlin Heidelberg, 2000. `http://dx.doi.org/10.1007/3-540-45014-9_1`.

[114] IceCube Collaboration, M. G. Aartsen *et al.*, “The IceCube Neutrino Observatory - Contributions to ICRC 2015 Part IV: Searches for Dark Matter and Exotic Particles.” `arXiv:1510.05226`.

[115] G. C. Hill *et al.*, “Examining the balance between optimising an analysis for best limit setting and best discovery potential.” in *Statistical Problems in Particle Physics, Astrophysics and Cosmology (PHYSTAT 05): Proceedings, Oxford, UK, September 12-15, 2005*, pp. 108–111.

[116] G. C. Hill and K. Rawlins, “Unbiased cut selection for optimal upper limits in neutrino detectors: The Model rejection potential technique.” *Astropart. Phys.* 19 (2003) 393–402, `arXiv:astro-ph/0209350`.

[117] G. J. Feldman and R. D. Cousins, “A Unified approach to the classical statistical analysis of small signals.” *Phys. Rev.* D57 (1998) 3873–3889, `arXiv:physics/9711021`.

[118] A. Fedynitch, R. Engel, T. K. Gaisser, F. Riehn, and T. Stanev, “Calculation of conventional and prompt lepton fluxes at very high energy.” *EPJ Web Conf.* 99 (2015) 08001, `arXiv:1503.00544`.

[119] IceCube Collaboration, M. G. Aartsen *et al.*, “Characterization of the Atmospheric Muon Flux in IceCube.” *Astropart. Phys.* 78 (2016) 1–27, `arXiv:1506.07981`.

Danksagung

Ich möchte all jenen von ganzem Herzen danken, die diese Arbeit möglich gemacht haben. Darunter meine Betreuer Uli Katz, Clancy James und Thomas Eberl, die jederzeit (sofern anwesend) sowohl eine offene Tür als auch ein offenes Ohr hatten.

Außerdem gebührt Prof. Dr. Ulrich Katz und PD Dr. Ira Jung-Richardt Dank für das Anfertigen der Gutachten.

Desweiteren bin ich meinen Korrekturlesern Uli, Clancy, Thomas, Macarena, Kerstin, Robert, Stefan, Lew, Tom, Jürgen, Michael und Gerd außerordentlich dankbar. Wer weiß wie diese Arbeit ohne sie aussehen würde...

Der ECAP-Neutrinogruppe danke ich für die gute, fruchtvolle Unterhaltung während und auch außerhalb diverser Meetings.

Natürlich danke ich auch meinen Zimmergenossen Lew, Jonas und Tom, ohne die das Forschen wahrscheinlich nicht einmal halb so viel Spaß gemacht hätte und auch nur halb so erfolgreich gewesen wäre.

Freilich sollen auch all meine Freunde herzlichst bedankt sein, die mir zu gegebener Zeit die nötige Ablenkung verschafft haben.

Und zu guter Letzt danke ich meiner Familie in höchstem Maße, insbesondere Aurélie und Anisa Nova (Glieba)!